Study of the Evolution of Velocity and Magnetic Fields in the Solar Atmosphere

A thesis submitted in partial fulfilment of the requirements for the degree of

Doctor of Philosophy

by

Hirdesh Kumar

(Roll No. 17330014)

Under the Supervision of

Dr. Brajesh Kumar

Associate Professor

Udaipur Solar Observatory

Physical Research Laboratory, Udaipur, India.

DISCIPLINE OF PHYSICS

INDIAN INSTITUTE OF TECHNOLOGY GANDHINAGAR

2023

Dedicated to

my parents

Declaration

I declare that this written submission represents my ideas in my own words and where others ideas or words have been included, I have adequately cited and referenced the original sources. I also declare that I have adhered to all principles of academic honesty and integrity and have not misrepresented or fabricated or falsified any idea/data/fact/source in my submission. I understand that any violation of the above will be cause for disciplinary action by the Institute and can also evoke penal action from the sources which have thus not been properly cited or from whom proper permission has not been taken when needed.

Date: **Hirdesh Kumar**

Roll No: 17330014

CERTIFICATE

It is certified that the work contained in the thesis titled "**Study of the Evolution of Velocity and Magnetic Fields in the Solar Atmosphere**" by **Hirdesh Kumar (Roll No. 17330014)**, has been carried out under my supervision and this work has not been submitted elsewhere for a degree or diploma. I have read this dissertation, and in my opinion, it is fully adequate, in scope and quality, for the degree of Doctor of Philosophy.

Date:

Dr. Brajesh Kumar
Associate Professor
Udaipur Solar Observatory
Physical Research Laboratory
Udaipur 313001, India

Acknowledgement

I would like to start by expressing my sincere and deep gratitude to my PhD supervisor, Dr. Brajesh Kumar, for his guidance and support throughout my PhD tenure. I thank him for the patience and confidence that he showed in me. I express my sincere gratitude to my Doctoral Studies Committee (DSC) members, Prof. Nandita Srivastava (USO), Prof. Shibu K. Mathew (USO) and Prof. Shashi K. Ganesh (PRL), for their valuable comments and suggestions during my seminars and PRL review.

I extend my gratitude to Dr. Anil Bhardwaj, Director, PRL, Ahmedabad, for providing me with timely administrative help and the necessary facilities to carry out my research work. I am also thankful to Dr. Bhushit G. Vaishnav, Head of Academic Services, for his support with academic matters. I also express my gratitude to the PRL academic committee for reviewing my progress in research periodically and for their timely feedback. I appreciate the cooperation of administration and library staff members at Udaipur Solar Observatory (USO), Udaipur, PRL, Ahmedabad and IIT, Gandhinagar.

I am sincerely thankful to my collaborator Prof. S. P. Rajaguru (IIA, Bengaluru) for discussions related to in-depth understanding of the different wave dynamics in the lower solar atmosphere and teaching me the diagnostic diagram technique. I am also thankful to Prof. Shibu K. Mathew for explaining the line scan observations using the Narrow Band Imager (NBI) instrument installed with the Multi-Application Solar Telescope (MAST) operational at USO, Udaipur and various data reduction procedures to estimate the chromospheric line-of-sight Dopplergrams. Thanks also to Dr. A. Raja Bayanna (USO) for helping me in understanding the adaptive optics (AO) system installed with the MAST. I also express my sincere thanks to the MAST team members.

I am very much thankful to all the helpful people who helped me during my tough time, i.e. COVID-19 illness. Thanks to Dr. Brajesh Kumar, Prof.

Nandita Srivastava, and Prof. Shibu K. Mathew for being in touch with me during my COVID-19 isolation period. I am deeply thankful to my junior, Mr. Yogesh Kumar Maurya (SRF), for bringing life-saving stuffs (medications, fruits and other materials). Thanks also to Ms. Pallavi Arvind Singh, ma'am, and Dr. Arvind Singh for preparing my diet plan for fast recovery from the post-Covid-19 complications.

I am thankful to my seniors Dr. Rahul Yadav, Dr. Alok Ranjan Tiwari, Dr. Kuldeep Pandey, Dr. Sardar Singh Rao and my colleagues Abhijit Kayal, Neeraj, Sushant, Vipin, Aravind, Abhay, Shivani, Alka, Satyajeet, Ankit, Anshika, Deepak, Suraj and my juniors Yogesh, Sandeep Sharma, Sandeep Dubey for their help and company at USO and PRL. Thanks also to all the residents of USO staff quarters for their support and invitations on various occasions.

Finally, I owe my deepest gratitude to my parents, who have given me the freedom necessary to concentrate on my research. I must say that being away from home, I have missed innumerable opportunities to be with family members, but they have always been by my side all the time.

Hirdesh Kumar

Abstract

In 1962, Leighton, Noyes and Simon discovered velocity oscillations on the photosphere of the Sun at Mt. Wilson Observatory in the USA using a spectroheliograph. These oscillations were interpreted as the superposition of millions of individual acoustic modes generated beneath the photosphere via turbulent convection and trapped inside the Sun. The oscillatory motions showed a dominant period of 5-minutes with a maximum velocity amplitude of 500 m s^{-1}. In 1972, Wolf suggested that solar flares could stimulate free modes of oscillations of the entire Sun. Solar flares are highly energetic events in the solar atmosphere that take place within a few minutes to hours and release an enormous amount of energy in the electromagnetic spectrum and consist of accelerated charged particles. During the bombardment of highly energetic charged particles on the chromosphere, some of these particles and downward propagating shock strike the solar photosphere thereby generating acoustic events like sunquakes or seismic emissions. Kosovichev and Zharkova (1998), for the first time, discovered the seismic emissions from an X2.2 class flare on July 9, 1996, in the active region NOAA 7978. This phenomenon was identified as a "sunquake". Moreover, apart from the back reaction of charged particles and shock, Hudson et al. (2008a) suggested that abrupt changes in Lorentz force (namely the "magnetic jerk") can also induce seismic emission in the sunspots accompanying major solar flares. However, Qiu and Gary (2003) had suggested and later on, it was found that line profiles are prone to getting distorted in the flaring locations during solar flares, which could affect the measurements of the Doppler velocity and magnetic fields. Therefore, we have investigated seismic emissions in the sunspots away from flaring locations accompanying major solar flares. These locations are considered to be free from any flare-related contaminations in the observational data. We construct acoustic power maps in 2.5–4 mHz band from photospheric Doppler velocity observations obtained during pre-, spanning and post-flare epochs and

overplot contours of H_α flare ribbons and hard X-ray footpoints in 12–25 keV band. We have identified seismic emission locations within sunspots and away from the flaring sites. Our detailed analysis shows an abrupt and persistent change in photospheric magnetic fields in the seismic emission locations in the range of 50–100 Gauss within a period of 10–20 minutes. Also, we find that the estimated change in Lorentz force of the order of 10^{21} dyne is sufficient to induce seismic emission in the sunspots during the major solar flares. Our investigation provides evidence that abrupt changes in the magnetic fields and associated impulsive changes in the Lorentz force could be the driving source for these seismic emissions in the sunspots during solar flares. It is crucial to study the seismic emission in the sunspots during solar flares because these excess wave energies propagate up in the solar atmosphere in the magnetized regions and thereby may contribute to the heating of the solar active region atmospheres.

Additionally, the trapped low-frequency acoustic waves beneath the solar photosphere in acoustic cavities are considered to leak along the inclined magnetic fields due to the reduction in acoustic cut-off frequency. The propagation of these low-frequency acoustic waves in the small-scale magnetic fields is important in terms of their contribution to the heating of the lower solar atmosphere. Moreover, acoustic waves interact with highly structured magnetic fields of the solar atmosphere in complex ways. Observational studies of such interactions and the magnetohydrodynamic waves that result from them are essential for the energetics of the solar atmosphere and recovering the background thermal and magnetic structures. The plasma $\beta \approx 1$ surfaces and the magnetic canopy in the solar atmosphere play decisive roles in propagation of these waves. The high-frequency fast mode waves are refracted at $\beta \approx 1$ in the higher atmosphere and are known to cause high-frequency acoustic halos around the sunspots. Thus, we analyze the propagation of low-frequency acoustic waves into the solar chromosphere within small-scale inclined magnetic fields over a quiet-magnetic network region utilizing photospheric and chromospheric Dopplergrams obtained from the

Helioseismic and Magnetic Imager (HMI) onboard Solar Dynamics Observatory (SDO) and the Multi-Application Solar Telescope (MAST) operational at the Udaipur Solar Observatory, respectively. In view of the stochastic excitation of acoustic waves and their intermittent interaction with the background magnetic fields, we use the wavelet technique to detect these episodic signals. We report a one-to-one correspondence between the presence of oscillatory signals (2.5–4 mHz band) in the photospheric and the chromospheric wavelet power spectra, which are associated with the leakage of photospheric oscillations into the chromosphere. In addition to this, chromospheric power maps also show the presence of high-frequency acoustic halos around relatively high magnetic concentrations, which indicate the refraction of high-frequency fast mode waves around $v_A \approx v_s$ layer in the solar atmosphere.

The internal or atmospheric gravity waves (IGWs) are generated by turbulent subsurface convection overshooting or penetrating locally into a stably stratified medium. This is a normal response generated by a gravitationally stratified medium to any perturbations from its equilibrium position and buoyancy acting as a restoring force. Gravity waves in the solar atmosphere are now increasingly recognized as an important contributor to the dynamics and energetics of the lower solar atmosphere. While propagating energy upwards, their characteristic negative phase shift over height is a well-recognized observational signature. Since their first detailed observational detection and estimates of energy content, several studies have explored their propagation characteristics and interaction with magnetic fields and other wave modes in the solar atmosphere. Recently, numerical simulations have shown that gravity waves are suppressed or scattered and reflected back into the lower solar atmosphere in the presence of magnetic fields. Here, we present a study of the atmospheric gravity wave dispersion diagrams utilizing intensity observations that cover photospheric to chromospheric heights over different magnetic configurations of quiet-Sun (magnetic network regions), a plage, and a sunspot, as well as velocity observations within the photospheric layer over a quiet and a sunspot region. In order to investigate the propagation characteristics, we construct two-height intensity - intensity and velocity - velocity cross-spectra and study phase and coherence signals in the wavenumber - frequency dispersion diagrams and their association with background magnetic fields. We derive signatures of association between magnetic fields and much-reduced phase shifts over height from intensity-intensity and velocity-velocity phase and coherence diagrams, both indicating suppression/scattering of gravity waves by the magnetic fields and thereby provide a qualitative observational verification of numerical simulations of such phenomena.

Thus, in this thesis we have investigated the evolution of velocity and magnetic fields in the solar atmosphere with an emphasis to understand the propagation of waves in the lower solar atmosphere.

Keywords: Sunspots, magnetic fields, quiet-Sun, flares, photosphere, chromosphere, oscillations.

Contents

List of Figures

List of Tables

Chapter 1

Introduction

1.1 The Sun: Our understanding

The Sun is the nearest star to our Earth; therefore, its proximity allows us to study its features with high spatial and temporal resolution in detail. The Sun is regarded as the *'Rosetta Stone'* of astronomy where different physical phenomena can be studied and verified. It has an extreme effect on space weather and Earth's climate. Hence, its study is crucial for understanding the behaviour of stars, cosmic plasma and from the astrophysics perspective. Generally, solar phenomena have been classified into two classes: quiet and active. The *quiet Sun* is defined as a static, spherically symmetric ball of plasma for which the magnetic field is negligible, and properties depend on a first approximation of the radial distance from the centre (considered constant in space and time) (Priest 2014, p. 4). The *active Sun* consists of transient phenomena, such as pores, sunspots, filaments, prominences, solar flares and coronal mass ejections, which are overlapped in the quiet atmosphere and owe their existence to the magnetic fields (i.e., solar activity in which phenomena occur within finite time scale) (Priest 2014, p. 4). The Sun is a main-sequence star of spectral type G2V with radius ($R_\odot$) $\approx 6.955\times 10^8$ m, mass ($M_\odot$) $\approx 1.99\times10^{30}$ kg, surface gravity ($g_\odot$) ≈ 274 m s^{-2}, and luminosity

($L_\odot$) $\approx 3.86\times10^{26}$ W. The Sun is about 3.3×10^5 times more massive than the Earth, 109 times larger in radius, and surface gravity is 27 times greater. The mean distance from the Sun to the Earth is 1.496×10^{11} m (1 AU = 215 $R_\odot$), and light takes around 8 minutes to reach Earth's surface (Priest 2014, p. 5). Like other stars, the Sun probably originated in the gravitational collapse of a huge, tenuous interstellar gas cloud approximately 4.6×10^9 years ago. It may have been triggered by the compression of a nearby supernova explosion, a collision between two clouds, a shock wave propagating with the Galaxy's spiral arm, or the thermal instability of the interstellar medium. Currently, the Sun is in a hydrostatic equilibrium state (Foukal 2004, p. 433).

1.2 Structure of the Sun

The Sun has different layers that define its structures, like the Earth. However, unlike the Earth, the Sun is entirely gaseous and has no solid surface. Nevertheless, the Sun is entirely made of gas, and the density and temperature of the gas change drastically as it moves from the centre to the outer atmosphere.

1.2.1 Solar Interior

The interior of the Sun is hidden under the light of the sphere (i.e., photosphere). Consequently, it is impossible to see beneath the photosphere even utilizing the most powerful telescopes in visible, X-rays or radio wavelengths. The observed features on the photosphere, like granulations, pores, dark sunspots, their motions and solar activity cycle indicate dynamics inside the Sun. The 'standard solar model' (SSM; Bahcall et al. (1982)), helioseismology (Leibacher et al. 1985), and solar neutrino observations (Bahcall et al. 2001) have significantly contributed to building up the current picture of the internal structure of the Sun. Solar interiors have been modeled and compared with the observed properties by varying the model parameters to match the observations. The interior of the Sun mainly

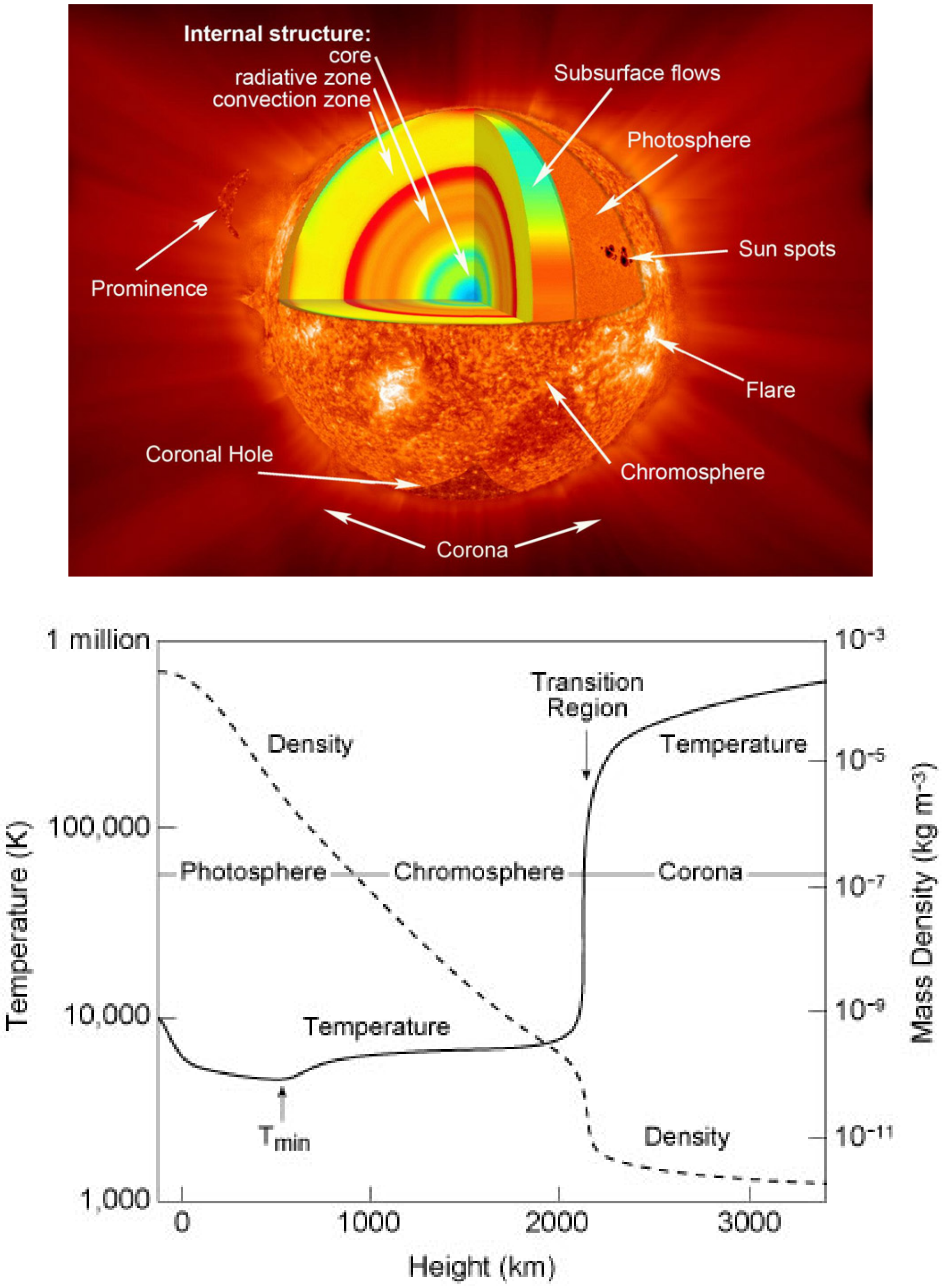

Figure 1.1: *Top panel*: shows the solar interior, features at the surface and in the atmosphere of the Sun (Source: https://scied.ucar.edu/learning-zone/sun-space-weather/sun-regions. *Bottom panel*: demonstrates the plot of temperature and density variation from the photosphere to the corona (Source: Lang (2008)).

includes core, radiative zone and convection zone (c.f. top panel of Figure 1.1). The core, which is 25 % of the total solar radius ($R_\odot$), has a temperature around 1.5×10^7 K, and a density of 1.6×10^5 kg m^{-3} (Priest 2014, p. 6), where nuclear fusion reaction generates the energy in the form of gamma rays photons. Above the core, there is radiative zone which spans from 0.25 $R_\odot$ to 0.70 $R_\odot$. The photons (generated in the core) are absorbed and re-emitted several times in the radiative zone leading to lower energy photons. The temperature drops from approximately 7×10^6 K at the base of the radiative zone to 2×10^6 K at the top of the radiative zone. The high density ($\approx 2\times10^4$ kg m^{-3}) in the radiative zone of the Sun leads to a small mean free path of the photons ($\approx 9.0\times10^{-2}$ cm). Therefore, these photons, in practice take approximately 170,000 years to cross it (Mitalas and Sills 1992). It indicates that if the energy generation process is stopped, the Sun will continue to shine for millions of years. The outer layer of the solar interior is convection zone, extending from 0.70 $R_\odot$ to 1.0 $R_\odot$. A thin layer known as Tachocline separates the radiative and convection zone. It is believed that it plays a key role in generating and storing the toroidal magnetic fields. As one moves outward from the radiative zone, opacity rises and increases the magnitude of $(-dT/dr)_R$. It is approximately 0.70 $R_\odot$, where convective instability sets in (Priest 2014, p. 12). In the convection zone, energy is transported through the convection rather than radiation. The large convective cells formed in the convection zone rise from the base of the convection zone and reaches a position where the opacity is no longer sufficient to hold the escape of the radiation. The plasma expands, radiates, and cools and, in so doing, loses its buoyancy and descends (Priest 2014, p. 12). The signature of convective cells can be traced on the photosphere of the Sun in the form of granulations, mesogranulations, and supergranulations etc.

1.2.2 Solar Atmosphere

The solar atmosphere is defined as a part of the Sun from which photons can escape directly into space. It consists mainly of three layers, i.e., photosphere, chromosphere, and corona, with varying physical properties. The photosphere of the Sun is a visible layer from which most of the visible light is emitted at 5000 Å wavelength. In the model, photosphere is defined as a region of $\approx$ 500 km thickness from $\tau_{5000} = 1$ (where τ is optical depth at 5000 Å) to the temperature minimum height (Priest 2014, p. 30). We observe different solar features, viz. granulation, meso-granulation, supergranulation, oscillations, faculae, pores, and sunspots on the photosphere as shown in the top panel of Figure 1.1. On the photospheric layer of the Sun, temperature decreases from approximately 6000 K to 4000 K. During a total solar eclipse, a thin reddish annulus is seen around the rim of the photosphere, known as the chromosphere (colour-sphere). This layer is highly dynamic, optically thin in a visible, near-ultraviolet and near-infrared continuum; however, optically thick in strong spectral lines (Priest 2014, p. 6). In the chromosphere and higher atmosphere, different physical phenomena are frequently observed like spicules, plages, magnetic networks, filaments, prominences, solar flares etc. The corona is the outermost part of the solar atmosphere. Between the chromosphere and the corona, there is a thin layer known as the transition region. In this region, thermodynamic variables change dramatically. Corona spans from the top of transition region to out into the heliosphere. This layer's temperature is of the order of $\approx$ 1000000 K. The density of the plasma decreases from the photosphere to the corona. Nevertheless, above the photosphere, temperature decreases till $\approx$ 500 km, then slowly increases till $\approx$ 2000 km. Further, there is a sudden increase in the temperature at the transition region layer and continues into the corona. The bottom panel of Figure 1.1 depicts the temperature (solid black curve) and density (dashed curve) variation above the photosphere into the corona. The cause of high temperature of the solar atmosphere is assigned to be the 'coronal heating' problem (Grotrian 1939; Edlén 1943).

1.3 Solar velocity oscillations

The possibility of the presence of oscillations in the solar atmosphere was theoretically suggested by Whitney (1958). Subsequently, Leighton et al. (1962) discovered velocity oscillations on the photosphere of the Sun by measuring the shift of spectral line profiles. They provided evidence of the oscillatory motions on the photosphere and the existence of patches or wave packets, both in space and time. Further, Evans and Michard (1962); Noyes and Leighton (1963); Simon and Leighton (1964); Orrall (1965); Gonczi and Roddier (1969) also found similar periodic oscillations in their observational data obtained from different instruments. Here, these oscillations are demonstrated in the top panel of Figure 1.2 as blue and red tiny patches, where blue regions are moving towards us whereas the red areas are moving away from us. The fact that the observed oscillations are stronger near the disk centre while weaker near the limb suggests that the motions are radial, i.e., inward and outward. At a given location, these oscillations exhibit a quasi-sinusoidal variation with an amplitude of a few hundreds of m s^{-1} and the incoherent superposition of these million modes gives rise to the dominant period of around 5 min. The estimated size of each patch was found to be of the order of a few kilometers.

After a long period of the observational report of these oscillations, Ulrich (1970) and Leibacher and Stein (1971) provided a theoretical explanation of the source of these oscillations. The oscillations we see in the photosphere of the Sun are due to the acoustic waves generated and trapped in the interior of the Sun. These waves are produced by turbulent convection within and near the top boundary layers of the convection zone, and they resonate to form p-mode (pressure driven) oscillations. As these waves propagate towards the deep interior of the Sun, they

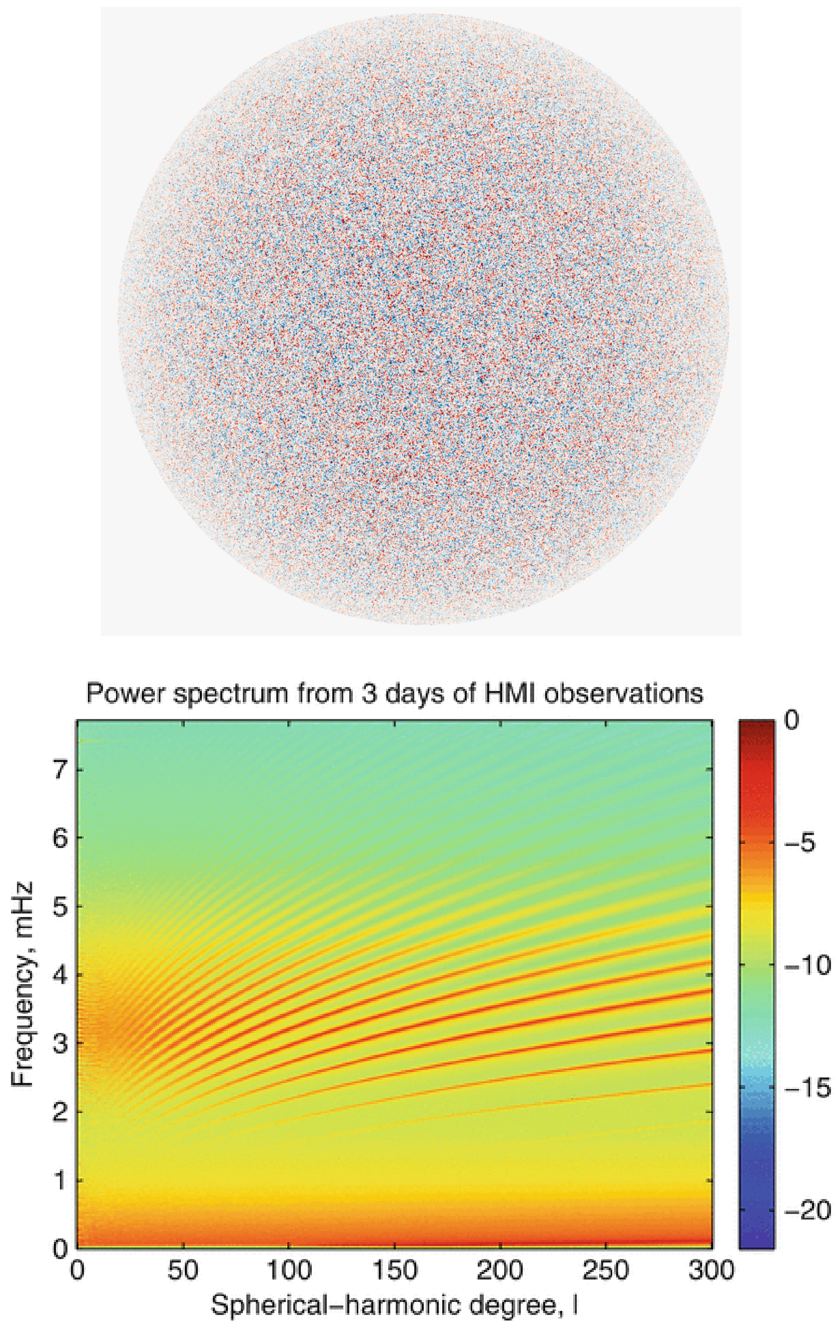

Figure 1.2: *Top panel*: Illustrations of 5-min oscillations in the full disk running difference of Dopplergrams obtained from the Helioseismic and Magnetic Imager (HMI) instrument onboard Solar Dynamics Observatory (SDO) spacecraft. *Bottom panel*: The power spectrum derived from high-cadence full disk velocity observations obtained from the the HMI instrument onboard SDO spacecraft (Source: Hanasoge (2015)).

refract (direction of motion bent) due to the increase of sound speed; as temperature increases towards the core, consequently, return to the surface. However, outward propagating acoustic waves reflect off the photosphere (where the density decreases rapidly). Thus, these waves are trapped inside cavities beneath the solar surface that forms from the small density of the photosphere and high temperature inside the Sun. These trapped waves set the Sun vibrating in millions of different modes. Ulrich (1970) concluded that, these standing acoustic waves may exist along discrete lines (ridges) in the $k_h - \omega$ diagnostic diagram (where k_h is horizontal wavenumber, and ω is the angular frequency). These predicted ridges were first observed by Deubner (1975) with the Domeless Coudé Telescope at Capri. The bottom panel of Figure 1.2 shows the power as a function of l and ν (where ν is the cyclic frequency of the oscillations, l is the angular degree, and λ_h is the horizontal wavelength in megameters). It is to be noted that $k-\omega$ power spectra exhibit ridge structure well beyond the photospheric cut-off frequency of $\nu_{ac} = 5.3$ mHz (Libbrecht 1988), and that is not due to the trapped resonant p-modes in the interior but are understood to be due to an atmospheric interference between waves directly from the subsurface sources and those refracting back from the solar interior (Kumar et al. 1990; Kumar and Lu 1991).

1.4 Solar magnetic fields

The photosphere of the Sun exhibits dark structures ranging from a spatial scale of a few meters to kilometres, known as magnetic networks, pores, sunspots etc. These magnetized structures are a sheet of high magnetic concentration and are considered to be responsible for the different physical phenomena occurring in the solar atmosphere. The magnetic field of the solar surface is measured by the Zeeman effect from the magnetic sensitive spectral lines (Hale 1908). Generally, a dynamo mechanism operating at the base of the convection zone of the Sun is considered as the source of the magnetic field (Solanki et al. 2006). It is known

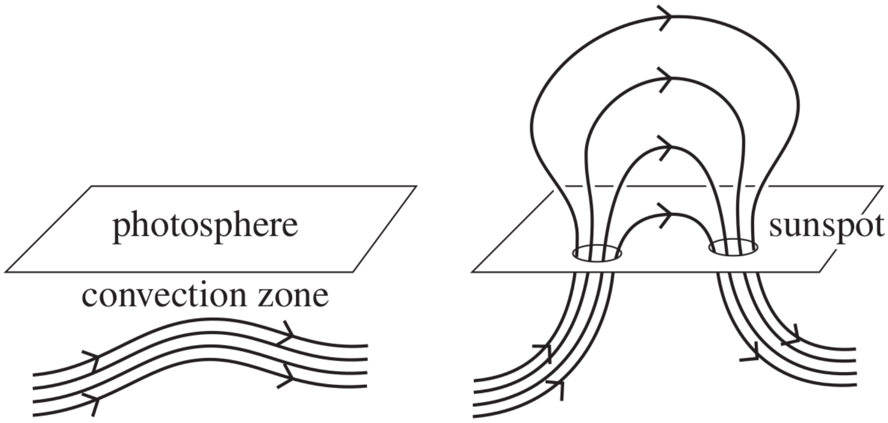

Figure 1.3: Illustration of a magnetic flux tube emergence from the solar surface due to magnetic buoyancy and formation of a bipolar sunspot (Source: Priest (2014)).

that active regions or sunspots manifest the bundle of flux tubes which were already concentrated before emerging into the photosphere (Zwaan 1978, 1987). Due to the strong differential rotation in the tachocline region, it plays an essential role in generating the toroidal magnetic flux. Further, toroidal magnetic flux emerge into the photosphere due to magnetic buoyancy and gives rise to the formation of bipolar active regions (Parker 1955). Figure 1.3 shows the formation of a sunspot via the emergence of a magnetic flux tube in the photosphere.

Most of the Sun's activity is considered to be associated with the sunspots and sunspot's groups which comprise magnetic flux of the order of $\approx 10^{21}$ Mx to 10^{22} Mx, respectively (Priest 1984; Wiegelmann et al. 2014). However, much of the flux in ARs in the form of smaller magnetic concentrations compared to sunspots is organized in the form of pores or, most commonly, magnetic elements. These features are characterized by the absence of a penumbra, which carries fluxes of the order of 10^{20} Mx to 10^{21} Mx (Thomas and Weiss 2004; Wiegelmann et al. 2014). Moreover, the photosphere also illustrates the distinct magnetic fields consisting of small magnetic flux elements on a wide range of spatial scales and separated by a relatively non-magnetized plasma. The measured magnetic flux

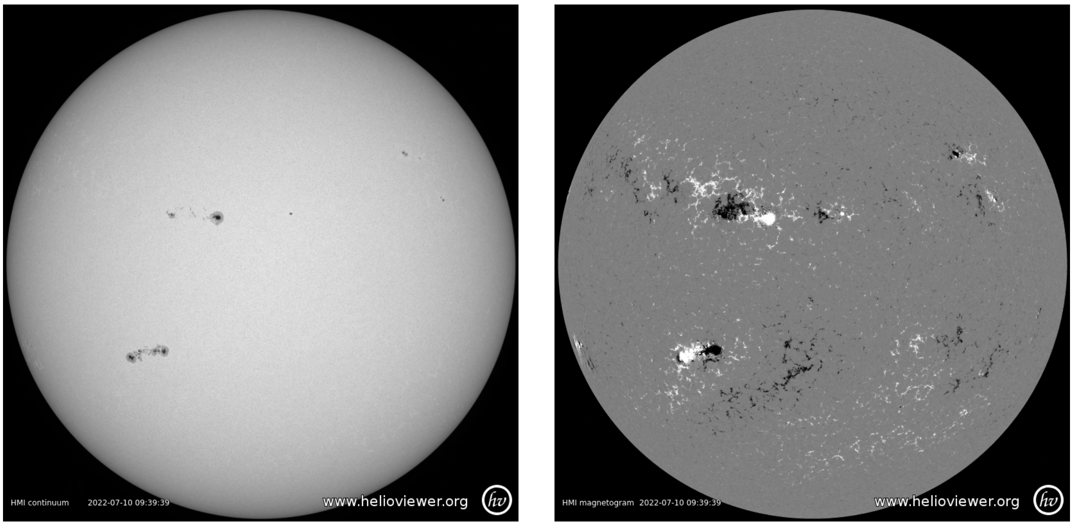

Figure 1.4: Photospheric continuum intensity image (*left panel*) obtained from the Helioseismic and Magnetic Imager (HMI) instrument aboard Solar Dynamics Observatory (SDO) depicting dark structures known as sunspots and pores, whereas the *right panel* shows the photospheric line-of-sight magnetogram obtained from the HMI instrument aboard SDO in which black and white patches indicate negative and positive polarity of magnetic fields (Source: `https://helioviewer.org`).

in the smallest network elements are of the order of 10^{17} Mx, whose life is only a few tens of minutes (Foukal 2004, p. 264). Nevertheless, the study of sunspots suggests that the number of sunspots follows a cyclic variation of around 11 years, known as the sunspot cycle or activity cycle (Schwabe 1844). The top panel of Figure 1.5 shows the yearly averaged sunspot number variation over the last 400 years. During the Maunder minimum, sunspots were less observed compared to the solar maximum (c.f. top panel of Figure 1.5). Moreover, temporal variation of sunspots shows that during the beginning of the solar activity, mostly sunspots occur at $\pm$ 35° heliographic latitudes. However, at the end of solar activity, location of sunspots move towards lower latitudes. This interesting behavior is mostly known as the Butterfly diagram. The bottom panel of Figure 1.5 shows that mostly sunspots have the same magnetic polarity pattern in one hemisphere in one solar activity cycle. In the other hemisphere, the orientation is reversed. Notably, during the transition to the next solar cycle, the polarity of the paired sunspots reverse their sign. It is also depicted in the bottom panel of Figure 1.5 that the global magnetic field also changes its polarity, and two sunspot cycles make one magnetic cycle of a period of 22 years.

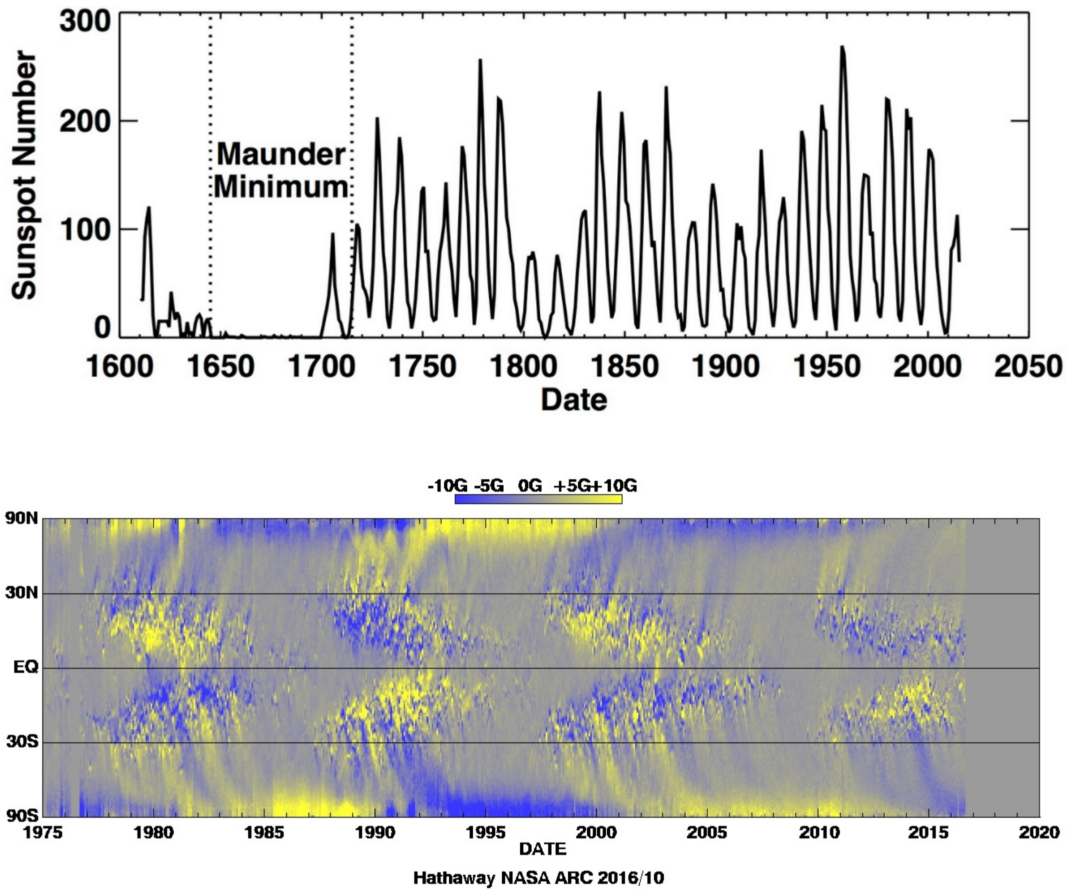

Figure 1.5: Plot showing the variation of sunspot numbers (*top panel*) during the last 400 years. *Bottom panel*: The butterfly diagram shows the distribution of longitudinal averaged surface magnetic field (Source: D. Hathaway /NASA/MSFC).

1.5 Magnetohydrodynamic waves

The waves are the prime candidates for transferring mass and energy over a long distance. The variety of different wave spectra allows communication from all kinds of mediums. Electromagnetic waves can propagate through solid, liquid, gas, plasma, and vacuum. However, mechanical waves can only propagate through a medium. Longitudinal acoustic waves can propagate via a medium through compressions and rarefactions. Magnetic fields also induce different kinds of hydrodynamic wave components. These magnetohydrodynamic (MHD) waves depend on the properties of the magnetic fields of the medium. All the waves mentioned above are present in the Sun and its atmosphere. As the magnetic fields cover the atmosphere of the Sun over the magnetic network, plage, pore and sunspot regions, MHD waves may play a crucial role in transporting energy and heating the atmosphere of the Sun.

In the absence of a background magnetic field, the supported plasma modes are acoustic waves (sound waves), which are generated due to pressure gradient, i.e., pressure is the restoring force. These waves are isotropic (i.e., speed is independent of the propagation direction) and non-dispersive. Nevertheless, magnetic fields support different types of waves. Interestingly, some of these waves have similarities with acoustic waves. These waves can be highly anisotropic because their propagation characteristics depend on the alignment of the wave vector with the direction of background magnetic fields (B_0), and the plasma β (Jess et al. 2015).

To explore the properties of waves in a magnetized plasma, consider the linearized ideal MHD equations (i.e., continuity, momentum, energy and induction) as follows:

$$\frac{d\rho}{dt} + \rho \boldsymbol{\nabla} \cdot \boldsymbol{v} = 0, \tag{1.1}$$

$$\rho \frac{d\boldsymbol{v}}{dt} = -\boldsymbol{\nabla} P + \frac{(\boldsymbol{\nabla} \times \boldsymbol{B}) \times \boldsymbol{B}}{\mu} - \rho g, \tag{1.2}$$

$$\frac{d}{dt}\left(\frac{p}{\rho^{\gamma}}\right) = 0, \tag{1.3}$$

$$\frac{\partial \boldsymbol{B}}{\partial t} = \boldsymbol{\nabla} \times (\boldsymbol{v} \times \boldsymbol{B}), \tag{1.4}$$

$$\boldsymbol{\nabla} \cdot \boldsymbol{B} = 0. \tag{1.5}$$

Now, consider small perturbations about static equilibrium ($v_0 = 0$), where $\rho = \rho_0 + \rho_1$, $\boldsymbol{v} = \boldsymbol{v}_1$, $p = p_0 + p_1$, and $\boldsymbol{B} = \boldsymbol{B}_0 + \boldsymbol{B}_1$ (subscript 0 for equilibrium state, whereas 1 is for perturbed state). Further replacing all these variables in equations 1.1 - 1.5 and considering the plane wave solution for the perturbed quantities, like $\boldsymbol{v}_1, \boldsymbol{B}_1, \rho_1, p_1 \propto e^{i(\boldsymbol{k}\cdot\boldsymbol{x}-\omega t)}$, (where $\boldsymbol{k}$ is the wavevector, and $\boldsymbol{x}$ is position vector) and after solving them there are two possibilities exist: (i) $\boldsymbol{k}\cdot\boldsymbol{v}_1 = 0$ corresponds to the incompressible case, and (ii) $\boldsymbol{k}\cdot\boldsymbol{v}_1 \neq 0$ that corresponds to compressible case. From (i), we obtain the following relation in terms of phase speed ($v_{ph} = \frac{\omega}{k}$) (where $k = |\boldsymbol{k}|$),

$$v_{ph}^2 = \frac{\boldsymbol{B}_0^2 cos^2(\theta)}{\mu_0 \rho_0}, \tag{1.6}$$

$$v_{ph}^2 = v_A^2 cos^2(\theta), \tag{1.7}$$

where, θ is the angle between wavevector $\boldsymbol{k}$, and background magnetic fields $\boldsymbol{B}_0$, which is an isotropic, non-dispersive wave, and the restoring force is only magnetic tension. This is the phase speed of the Alfven wave, where $v_A = \frac{|B_0|}{\sqrt{\mu_0 \rho_0}}$ (Alfvén 1947).

For the case (ii) i.e., compressible case ($\boldsymbol{k}\cdot\boldsymbol{v}_1 \neq 0$) system of equations give following dispersion relation,

$$v_{ph}^4 - (v_S^2 + v_A^2)v_{ph}^2 + v_S^2 v_A^2 cos^2(\theta) = 0. \tag{1.8}$$

Equation 1.8 has two solutions in terms of the square of the phase speed, i.e.,

$$v_{ph}^2 = \frac{1}{2}(v_S^2 + v_A^2) + \frac{1}{2}(v_S^4 + v_A^4 - 2v_S^2 + v_A^2 cos(2\theta))^{1/2}, \tag{1.9}$$

and

$$v_{ph}^2 = \frac{1}{2}(v_S^2 + v_A^2) - \frac{1}{2}(v_S^4 + v_A^4 - 2v_S^2 + v_A^2 cos(2\theta))^{1/2}, \tag{1.10}$$

The Equations 1.9, and 1.10 correspond to two magneto-acoustic wave modes: the fast mode (Eqn. 1.9), and the slow mode (Eqn. 1.10). In summary, in linearized ideal MHD for a homogeneous plasma, three different waves exist. The slow and fast magnetoacoustic and Alfven wave. The phase speed of these waves are well organized viz., $0 \leq v_{slow} \leq v_A \leq v_{fast}$. The phase speed ($v_{ph}$) of magnetoacoustic waves in equation 1.8 depends on angle, θ (where θ is the angle between wave propagation direction and magnetic fields), and on the ratio of v_S and v_A, which can be written in terms of plasma β ($\beta = \frac{2}{\gamma}\frac{v_S^2}{v_A^2}$). The restoring force for the two magnetoacoustic waves is a combination of total pressure (gas and magnetic pressure) and magnetic tension, whereas the Alfven wave is incompressible and is only supported by the magnetic tension (Jess et al. 2015). Table 1.1 provides information on the propagation of these waves in different plasma β environments.

1.5.1 Plasma β regimes and mode conversion in the solar atmosphere

As discussed in Section 1.4, the propagation characteristics of magnetoacoustic waves depend on plasma β and θ (angle between wave vector ($\boldsymbol{k}$) with magnetic

Table 1.1: Table represents the phase speed of slow, fast and Alfven waves for a uniform unbounded plasma (Jess et al. 2015).

		$\beta > 1, v_A < v_S$	$\beta < 1, v_A > v_S$
$\boldsymbol{k} \cdot \boldsymbol{v}_1 = 0$	$\boldsymbol{k} \vert\vert B_0$	Alfven wave, $v_{ph}^2 \approx v_A^2$	Alfven wave, $v_{ph}^2 \approx v_A^2$
	$\boldsymbol{k} \perp B_0$	Alfven wave does not propagate	Alfven wave does not propagate
$\boldsymbol{k} \cdot \boldsymbol{v}_1 \neq 0$		Fast wave, $v_{ph}^2 \approx v_S^2$ magnetic and kinetic pressure in phase	Fast wave, $v_{ph}^2 \approx v_A^2$ magnetic and kinetic pressure in phase
	$\boldsymbol{k} \vert\vert B_0$	Slow wave, $v_{ph}^2 \approx v_A^2$ magnetic and kinetic pressure out of phase	Slow wave, $v_{ph}^2 \approx v_S^2$ magnetic and kinetic pressure out of phase
	$\boldsymbol{k} \perp B_0$	Fast wave, $v_{ph}^2 \approx v_S^2$ magnetic and kinetic pressure in phase slow wave does not propagate	Fast wave, $v_{ph}^2 \approx v_A^2$ magnetic and kinetic pressure in phase slow wave does not propagate

fields). The plasma β of the region defines the dominating force, either plasma pressure (p_g) or the magnetic pressure (p_B) in the medium:

$$\beta = \frac{p_g}{p_B} = \frac{2}{\gamma} \cdot \frac{c_s^2}{v_A^2}, \tag{1.11}$$

where c_s^2 and c_A^2 are the sound and Alfven speed, respectively. The gas and magnetic pressure ratio (plasma β) can also describe the dominating regime. Moreover, in a sunspot region at the photosphere, the plasma β decreases by some magnitude at the transition from a sunspot's penumbra to the dark umbral core. The magnetized solar atmosphere can be categorized into three plasma β regions:

Low-β: In the $\beta << 1$ regime, magnetic pressure dominates the plasma pressure. Due to high magnetic field strength and low gas density, the Alfven velocity exceeds the sound speed.

High-β: Here, gas pressure dominates the magnetic pressure. Therefore, the dynamics and magnetic structures are governed by the motion of plasma.

Plasma $\beta \approx 1$: This is the layer which separates the regions of two different forces. At this regime, magnetic and plasma pressure are in equilibrium. Thus, Alfven's speed is approximately equal to the sound speed. This regime is very crucial for the mode conversion of magnetoacoustic waves. Between the high and low β domain, conversion of waves (fast and slow) occurs. In the quiet Sun, plasma $\beta \approx 1$ layer is situated around the chromosphere. However, in the magnetized solid structure viz. pores, sunspots, this region lies below the chromospheric height (Gary 2001).

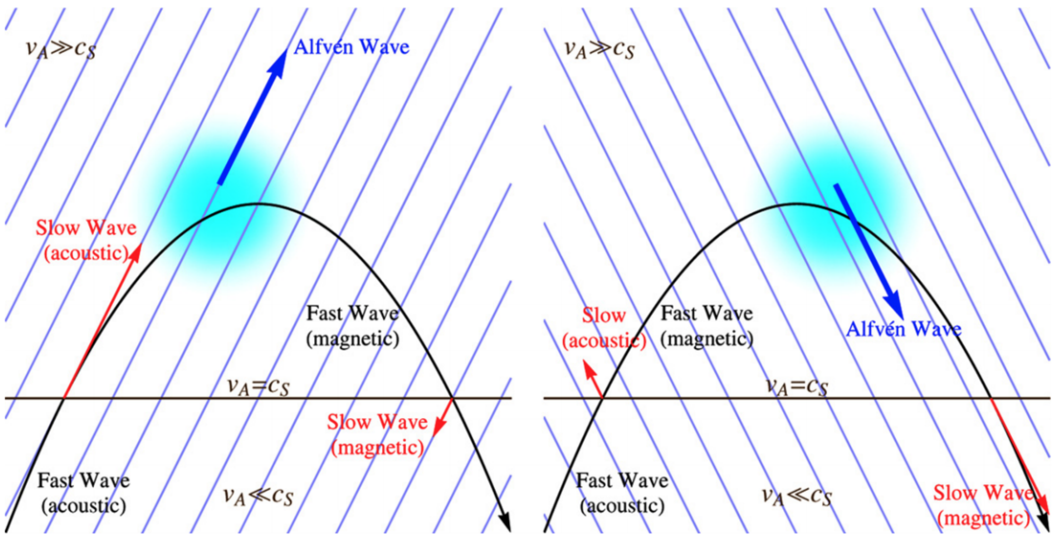

Figure 1.6: Schematic diagram depicting the propagation of waves in an inclined magnetic field region and various mode conversions and reflections of the wave as they enter into the solar atmosphere. Magnetic field lines (pale blue) are oriented out of the plane and shown in the projection. A solid black horizontal line represents the region where sound and Alfven's speed are equal. It separates low β (upper region) from the high β (lower region) regime. (Source: Khomenko and Cally (2012)) .

Figure 1.6 demonstrates the propagation of fast wave in the inclined magnetic field regions (pale blue colour), which are oriented out of the plane and shown in the projection. The orientation is measured by the inclination angle θ from vertical and varying within $0° < \theta < 90°$ whereas azimuth angle ϕ ($0° < \phi < 180°$) is estimated clockwise from the plane of wave propagation. Here, two regions are shown, $\phi < 90°$ in the left panel whereas $\phi > 90°$ in the right panel. Solid black horizontal line represents the equipartition layer, which separates $v_S = v_A$ region. At this junction, the wave splits into a slow wave (guided along magnetic field lines) as depicted by the red color and a fast magnetically dominated wave (black color). The upward propagating fast wave does not reach into the chromosphere in the $c_S < v_A$ region and reflects back to the photosphere somewhere above the equipartition layer. The preliminary cause of this behavior is the vertical and horizontal gradient of Alfven speed, which leads to the refraction of waves. The Alfven speed is influenced due to the change in the density in the sunspot region. The value of Alfven speed is changed several orders of magnitude in the vertical and horizontal directions both (Khomenko and Collados 2006). At the reflection region, as shown by a fuzzy blob, the fast wave partially converts into an Alfven wave depending on the inclination of background magnetic fields and wave vector (Khomenko and Cally 2012). However, slow (acoustic) waves continue propagating into the higher atmosphere along the magnetic field lines and dissipate energy via shock formation. Moreover, downward propagating high-frequency fast mode waves are believed to cause high-frequency acoustic halos around sunspots (Khomenko and Collados 2009).

1.6 Solar atmospheric gravity waves

As mentioned in Section 1.4, compressibility provides restoring force for generating the acoustic (sound) waves. Similarly, gravitational acceleration also provides restoring force, which generates waves driven by buoyancy force known as gravity waves. The gravity waves in the solar atmosphere can be understood in terms of the Schwarzschild criterion for convective instability.

Consider a plasma parcel, which is moving at an angle θ with respect to vertical. If the density of the plasma parcel is greater than the surroundings, it will fall back because of heaviness. Assume that motion is sufficiently slow so that the plasma parcel will remain in pressure equilibrium with the surrounding atmosphere. In this case, the density difference between parcel and surrounding can be written from the perfect gas law at constant pressure in terms of $\frac{\delta\rho}{\rho} = -\frac{\delta T}{T}$. Also, assuming motion is so fast, there is no energy exchange between the parcel and the surrounding atmosphere, i.e. motion is adiabatic. These assumptions are reasonable whenever the time scale of energy exchange is long compared to sound travel time across the parcel (Stix 2004, p. 238). In this case, the temperature difference between the parcel and surroundings is given as (Leibacher and Stein 1981)

$$dT = \left(\frac{dT}{dz}\bigg|_{Adiab.} - \frac{dT}{dz}\bigg|_{Atmos.} \right) \cdot x \cdot cos\theta, \tag{1.12}$$

From Newton's equation of the motion

$$\rho \frac{\partial^2 x}{\partial t^2} = -\delta\rho \cdot g \cdot cos\theta, \tag{1.13}$$

or

$$\frac{\partial^2 x}{\partial t^2} = -\omega^2 x = -\frac{\delta\rho}{\rho} \cdot g \cdot cos\theta, \tag{1.14}$$

$$= -\frac{1}{T} \left(\frac{dT}{dz}\bigg|_{Atmos.} - \frac{dT}{dz}\bigg|_{Adiab.} \right) \cdot x \cdot g.cos^2\theta, \tag{1.15}$$

Hence,

$$\omega^2 = N_{BV}^2 cos^2\theta, \tag{1.16}$$

where the buoyancy or Brunt-Väisälä frequency is given as

$$N_{BV}^2 = \left[\frac{g}{T} \left(\frac{dT}{dz}\bigg|_{Atmos.} - \frac{dT}{dz}\bigg|_{Adiab.} \right) \right]. \tag{1.17}$$

This is the natural frequency (c.f. Equation 1.17) of oscillation of a plasma parcel displaced from its equilibrium position in a gravitational field. When $N_{BV}^2 > 0$ the atmosphere is stably stratified, and plasma parcel experiences harmonic oscillations. However, in the case of $N_{BV}^2 < 0$ parcel feels a force in the direction of its displacement, and the perturbation grows exponentially. Whereas $N_{BV}^2 = 0$ atmosphere remains in adiabatic equilibrium, neither convection nor buoyancy oscillations can occur (Mihalas and Mihalas 1995a, p. 202). It must be noted that acoustic waves have only a characteristic speed, whereas gravity waves have only a characteristic frequency. Gravity waves can propagate less than this critical frequency (Leibacher and Stein 1981). Gravity waves of a given frequency propagate at an angle with respect to vertical given as $cos\theta = \frac{\omega}{N_{BV}}$. A broad spectrum of excitation of gravity waves would be very dispersive, with different frequency components propagating in different directions. The energy flux in an internal gravity wave (IGW) is radially outwards from the source, which is in the direction of the particle motions but perpendicular to the direction of phase propagation. This has a curious consequence that for the downward phase propagation, there is upward energy propagation (Lighthill 1978, Chapter 4).

1.7 Acoustic-gravity wave spectrum

The propagation of waves in a compressible, stably stratified medium in a gravitational field as the atmosphere of the Sun, or the Earth or a star, can be driven by both restoring forces, viz. compressibility and buoyancy. These forces can induce oscillations of plasma parcel slightly displacing from its equilibrium position. Thus the behavior of waves becomes more complicated than in a homogeneous medium. Due to the preferred direction of the force of gravity, propagation characteristics becomes anisotropic. The speed of waves depends on k or ω; hence these waves are dispersive. The stratification of the atmosphere imposes a cut-off frequency below which gravity modified acoustic waves can not propagate and thus restricts the region in the $k_h - \omega$ diagnostic diagram. Buoyancy force gives rise to new types of propagating waves, i.e. gravity waves. These two waves occupy different regimes in the $k_h - \omega$ diagnostic diagram along with a band of the evanescent region. Acoustic-gravity waves become essential because they are ubiquitous in terrestrial and solar atmosphere and also exist in stellar atmosphere (Mihalas and Mihalas 1995a). The behavior of the acoustic-gravity waves can be derived from the analysis of dispersion relation given as (Vigeesh et al. 2017):

$$k_z^2 = \frac{(\omega^2 - \omega_{ac}^2)}{c_s^2} - \frac{(\omega^2 - N^2)k_h^2}{\omega^2}, \tag{1.18}$$

where ω is the angular frequency, c_s is sound speed, N is the Brunt-Väisälä frequency, ω_{ac} is acoustic cutoff frequency, and k_h is the horizontal wavenumber ($k_h^2 = k_x^2 + k_y^2$). For an iso-thermal atmosphere, the acoustic cut-off frequency is a function of sound speed and density scale height i.e. $\omega_{ac} = c_s/2H_\rho$. Nevertheless, in the non-isothermal case like that of the solar atmosphere, the gradient in temperature also modifies the cutoff frequency (Deubner and Gough 1984), which is given by $\omega_{ac}^2 = c_s^2/4H_\rho^2(1-2dH_\rho/dz)$. The maximum frequency of gravity waves is set by the Brunt-Väisälä frequency (N) which is for the iso-thermal atmosphere is $N = \sqrt{(\gamma-1)}g/c_s$, whereas for non-isothermal atmosphere $N^2 = g(1/H_\rho - g/c_s^2)$ (Deubner and Gough 1984). The dispersion Equation 1.18 distinguishes different wave behavior in the $k_h - \omega$ diagnostic diagram. Two different wave

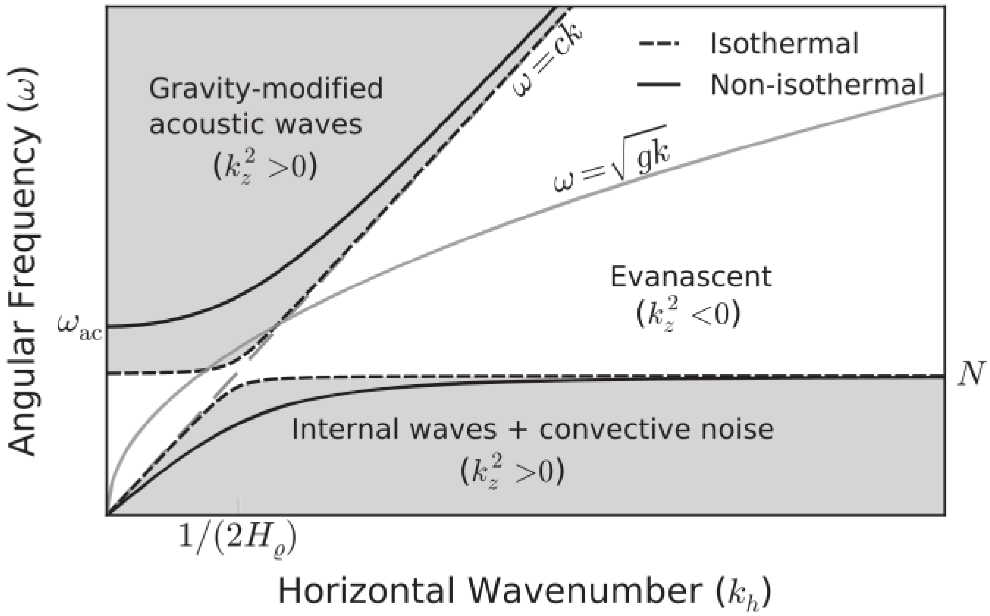

Figure 1.7: Schematic of a $k_h - \omega$ diagnostic diagram, demonstrating different wave propagation regimes in a compressible, gravitationally stratified medium for a given height. The dark shaded area demarcate the regions of vertical propagation of gravity and acoustic waves. The dashed black and solid lines represent the propagation boundaries obtained from isothermal and non-isothermal cut-off frequencies. The solid grey curve represents the dispersion curve of the surface gravity wave. The long dashed grey line denotes the dispersion curve for Lamb wave (Source: Vigeesh et al. (2017)).

regimes in the $k_h - \omega$ diagram can be obtained by putting $k_z^2 = 0$ in Equation 1.18, where $k_z^2 > 0$ isolate vertically propagating region from evanescent regime ($k_z^2 < 0$) (Leibacher and Stein 1981). A schematic diagram of such phenomena for a compressible, gravitationally stratified medium for a given height is shown in Figure 1.7. In this figure, solid black lines mark the regions of internal gravity wave regime (lower one) and gravity modified acoustic wave regime (upper one) for non-isothermal atmosphere, whereas dashed boundaries are for the iso-thermal atmosphere. The solid grey curve represents the fundamental mode (surface gravity wave), and the dashed grey curve denotes the Lamb wave, representing the horizontal propagation of acoustic waves.

1.8 Solar flares and their effect on photospheric velocity oscillations

Solar flares are the most catastrophic events in the solar atmosphere. They can release the energy of the order of 10^{32} erg within a few minutes to a few hours. Solar flares emit radiation in the whole electromagnetic spectrum, from radio to γ rays and highly energetic accelerated charged particles in the interplanetary medium. The flares are a consequence of the rapid release of previously stored magnetic energy as inductive magnetic fields due to electrical currents flowing into the corona (Fletcher et al. 2011). It was suggested long ago that solar flares can stimulate free oscillation modes of the entire Sun (Wolff 1972a).

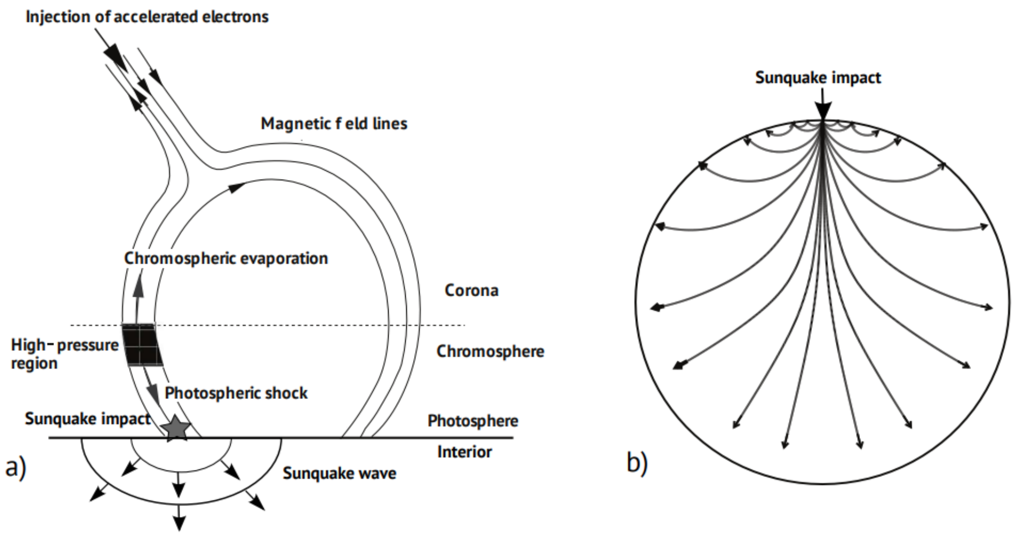

Figure 1.8: Schematic illustrates the formation of a sunquake from a 'thick target' model of solar flares. Panel (a) shows the injection of highly energetic charged particles into a magnetic flux tube which heats the chromosphere and creates a high-pressure region resulting in the chromospheric evaporation and a shock travelling to the photosphere responsible for the sunquake. Panel (b) represents the ray paths of acoustic waves generated by shock hitting on the solar surface. These acoustic waves travel deep inside the Sun and reflect back to the surface resulting in the sunquake ripples (Source: Kosovichev (2015)).

Figure 1.8 demonstrate the 'thick target model' of solar flare (panel a), and the

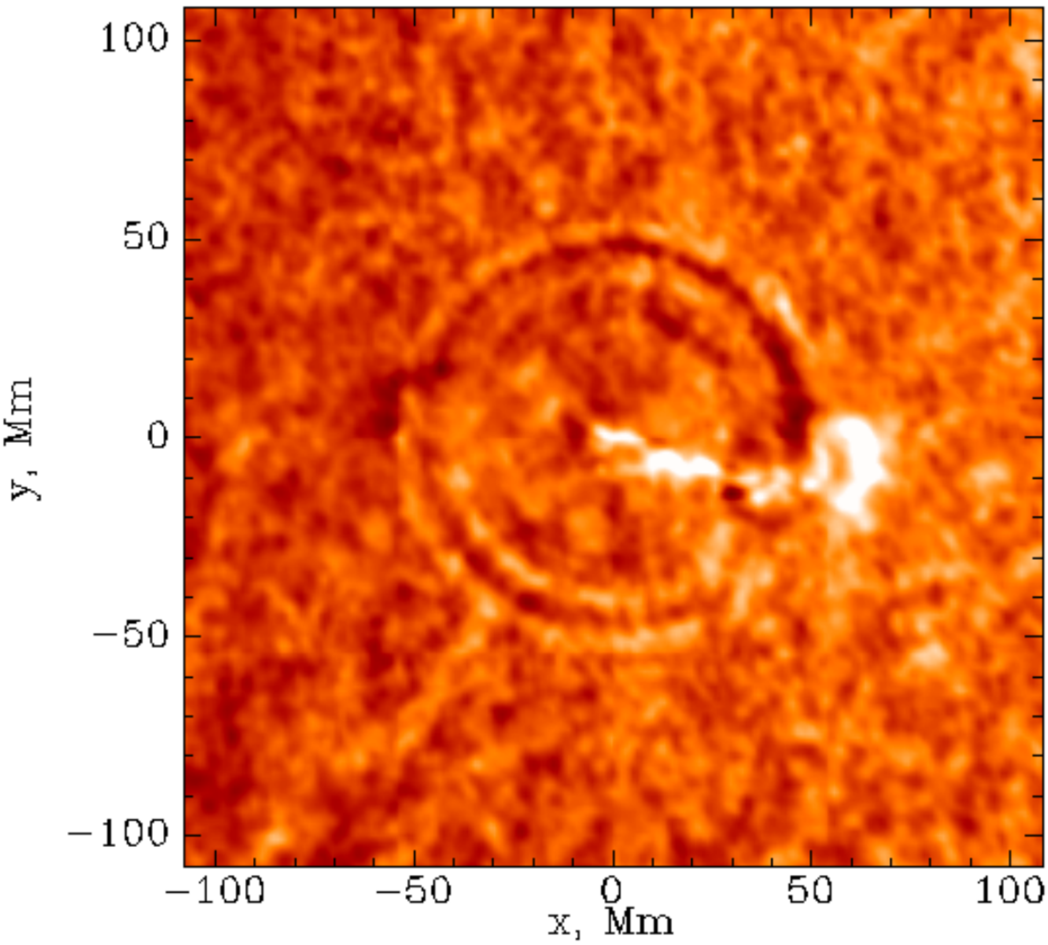

Figure 1.9: Illustration of sunquake ripples in the velocity image obtained from the Michelson Doppler Imager instrument onboard Solar and Heliospheric Observatory spacecraft during an X-class solar flare (Source: Kosovichev and Zharkova (1998)).

formation of a sunquake is shown in the panel *b*. According to this model, a strong compression of the lower chromosphere is generated due to the back bombardment of high energetic charged particles on the chromosphere during the course of solar flares. This compression produces chromospheric evaporation and a downward propagating shock wave, which hits the photosphere and yields seismic response (Kosovichev 2015). Panel *b* of Figure 1.8 shows the generation of acoustic waves due to the impact of shock on the photosphere. These waves propagate downward and reflect the surface due to the high temperature inside the Sun. They appear on the solar surface as a circular ripples known as sunquake. Figure 1.9 shows the ripples observed in the velocity image obtained from the MDI instrument onboard the SOHO spacecraft during an X2.6 class solar flare that occurred on July 9 1996, which was termed as 'sunquake' (Kosovichev and Zharkova 1998). However, it is to be noted that all the solar flares do not produce sunquake-like ripples, but they generate enhancement in a compact region known as 'seismic emission' in the active regions (Lindsey and Donea 2008). The investigation of seismic emissions in the sunspots accompanying solar flares are also essential for the understanding of the propagation of magnetoacoustic waves in the solar atmosphere.

1.9 Motivation and Organization of the Thesis

The objective of this thesis is to study the evolution of velocity and magnetic fields in the solar atmosphere in different magnetic structures, such as sunspots, pores and magnetic network regions, in the quiet phase as well as during dynamical activities like solar flares with an emphasis to understand the propagation of waves in the lower solar atmosphere. Since the discovery of solar oscillations (5-min) (Leighton et al. 1962) on the photosphere of the Sun, significant studies have been done to understand the evolution of velocity oscillations in the flaring locations accompanying solar flares (Kosovichev and Zharkova (1998); Donea and Lindsey (2005); Donea et al. (2006); Moradi et al. (2007); Kumar and Ravindra (2006); Zharkova and Zharkov (2007); Venkatakrishnan et al. (2008); Maurya and Ambastha (2009); and Kumar et al. (2016a)). Moreover, earlier investigations also suggest that photospheric line profiles could be distorted in the flaring locations due to the change in local thermodynamic conditions (Qiu and Gary (2003); Abramenko and Baranovsky (2004); Maurya and Ambastha (2009); Maurya et al. (2012); and Raja Bayanna et al. (2014a)). Thus, the observed changes in the velocity and magnetic fields in flaring locations could be contaminated, and there is always a reliability issue. However, the locations away from the flaring sites are considered to be free from any flare-related contamination in the observational data. Therefore, using the abovementioned approach, it is essential to examine the evolution of velocity and magnetic fields in the sunspots during major solar flares.

Additionally, the trapped acoustic waves beneath the solar photosphere are considered to leak along the inclined magnetic fields due to the reduction in the cut-off frequency. The propagation of these low-frequency acoustic waves in the small-scale magnetic fields is important in terms of their contribution in the heating of lower solar atmosphere. Moreover, the interaction of acoustic waves with the background magnetic fields leads to various magnetohydrodynamic waves, which are essential to study from the perspective to understand different physical phenomena taking place in the solar atmosphere like refraction and reflection of waves and mode conversion etc. Nevertheless, the gravity waves in the solar atmosphere are also now recognized as a potential candidate to heat the lower solar atmosphere. While propagating energy upwards, their characteristic negative phase-shift over height is a well-recognized observational signature (Straus et al. 2008). Recent simulations found that these waves are scattered/suppressed and refracted in the presence of background magnetic fields (Vigeesh et al. 2017, 2019; Vigeesh and Roth 2020). Hence, we investigate the observational signatures of the influence of magnetic fields on the phase propagation of gravity waves in different magnetic configurations in the lower solar atmosphere.

Some specific problems related to the evolution of velocity and magnetic fields in sunspots accompanying major solar flares and the propagation of waves in the lower solar atmosphere have been addressed in this thesis. The motivation behind these studied are as follows.

- Investigation of seismic emissions accompanying major solar flares in sunspot regions away from flare ribbons or hard X-rays foot points, which are considered to be free from any flare-related artefacts in the measurements of velocity and magnetic fields. It is essential to study the seismic emissions appearing in sunspot regions during flares because these excess wave energies propagate up in the solar atmosphere in the magnetized regions and thereby may contribute to the heating of the solar active region atmosphere.

• Propagation of acoustic waves from photosphere to chromosphere in a magnetic network region and their interaction with the background magnetic fields, utilizing two height velocity observations. Observational studies of such interactions and magnetohydrodynamic waves that result from them are essential not only for the energetics of the solar atmosphere but also for understanding the different physical phenomena occurring in the solar atmosphere and recovering the background thermal and magnetic structures.

• The internal or atmospheric gravity waves (IGWs) are generated by turbulent subsurface convection overshooting or penetrating locally into a stably stratified medium. These waves are now increasingly recognized as an important contributor to the dynamics and energetics of the lower solar atmosphere. Recently, numerical simulations have shown that gravity waves are suppressed or scattered and reflected into the lower solar atmosphere in the presence of magnetic fields. We have investigated the effect of magnetic fields on the propagation characteristics of gravity waves over different magnetic configurations, viz. sunspots, plages, and a quiet Sun.

Based on the work carried out to accomplish the objective mentioned above, the thesis is arranged into six chapters. A brief summary of them is as follows:

Chapter 1: Introduction

In this chapter, we have discussed the interior and atmosphere of the Sun and photospheric velocity oscillations followed by a discussion on the solar magnetic fields. This chapter also includes descriptions of the generation of different mechanical waves, their propagation into the lower solar atmosphere, and the effect of different physical properties in the medium. Here, we have also outlined the effect of solar activity like solar flares on the photospheric velocity oscillations and present a summary of the motivation and organization of the thesis.

Chapter 2: Observational data and processing

This chapter provides the details of the observations taken from ground- and space-based telescopes to accomplish the objective of the thesis. The techniques used in reducing the Ca II 8542 Å line scan observations obtained from the Narrow Band Imager with the Multi-Application Solar Telescope operational at Udaipur Solar Observatory, along with the estimation of chromospheric line-of-sight velocity, are described. The primary data sources for this thesis are the Multi-Application Solar Telescope (MAST), Interferometric BIdimensional Spectropolarimeter (IBIS) instrument mounted at the Dunn Solar Telescope (DST), Global Oscillation Network Group (GONG), Solar Dynamics Observatory (SDO), Reuven Ramaty High Energy Spectroscopic Imager (RHESSI), and Geostationary Operational Environmental Satellite (GOES).

Chapter 3: Seismic emissions accompanying major solar flares

In this chapter, we study acoustic (seismic) emissions accompanying major solar flares in different active regions. In this work, we investigate the evolution of magnetic fields and Lorentz force in the seismic emission locations in the sunspots during major solar flares. We have constructed acoustic power maps in 2.5 – 4 mHz band from photospheric velocity and overplot H_α flare ribbon contours and hard X-rays foot points, to identify the seismic emission locations away from flaring locations. Our investigations show a step-like change in the magnetic fields of the order of 50 – 100 G within a duration of 10 – 20 minute. The change in Lorentz force of the order of 10^{21} dyne has been found sufficient to enhance seismic emissions. We also present the implications of this work in this chapter.

Chapter 4: Study of the interaction of acoustic waves with the small scale magnetic fields

In this chapter, we present an analysis of the propagation of low-frequency acoustic waves into the chromosphere along the small-scale inclined magnetic fields of a magnetic network region utilizing photospheric and chromospheric velocity observations. We also discuss the formation of high frequency acoustic halos caused by the magnetohydrodynamic waves resulting from the interaction of acoustic waves with the background magnetic fields.

Chapter 5: Investigation of the propagation of gravity waves in the magnetized regions in lower solar atmosphere

In this chapter, we present detailed analysis of the propagation of gravity waves in the different magnetized regions, viz. magnetic network regions, plages, and sunspots in the lower solar atmosphere. We analyse $k_h - \omega$ phase and coherence diagrams utilizing two height intensity-intensity and velocity-velocity observations. Here, we find that gravity waves are suppressed/scattered or reflected in the magnetized regions compared to quiet regions. These findings are qualitatively in agreement with the recent simulations done by Vigeesh et al. (2017, 2019); Vigeesh and Roth (2020).

Chapter 6: Summary and future prospects

This chapter provides the summary of the work done, highlighting the significant findings and their implications in the above chapters and the scope for future work.

Chapter 2

Observational Data and Processing

2.1 Introduction

The solar atmosphere ranging from the photosphere to the higher corona, exhibits different features like magnetic network regions, pores, sunspots, faculae, plages, filaments, and prominences etc. These regions are considered higher magnetic field strength sheets confining themselves at different spatial scales. All these magnetic phenomena consist of three-dimensional magnetic structures ranging from the deep photosphere to the higher solar atmosphere. These magnetized regions show various physical phenomena in several ways such as oscillations, magnetohydrodynamic waves, solar transients like flares and eruptions, etc. The investigation of all these associated phenomena necessarily requires multi-height observations. This purpose is fulfilled with the combined observations of the solar atmosphere from space and ground-based instruments. Here, in order to accomplish the motivations of this thesis, we have acquired observational data from ground-based and space-borne observatories, which sample different layers in the solar atmosphere. We have extensively utilized these observations to achieve the scientific objectives mentioned in Chapter 1. The advantage of using the observations from space is that we can get uninterrupted continuous observations. At the same time, the ground-based observations suffer from the seeing effect, which degrades the quality of the images. Albeit, all types of observations are not possible from space as yet. Hence, we have to rely on ground-based observations too.

In the following, first we describe the observations obtained from ground-based observatories followed by their data reduction process and later focus on the space-borne instruments.

2.2 The Multi-Application Solar Telescope (MAST)

The Multi-Application Solar Telescope (MAST: Mathew (2009a); Venkatakrishnan et al. (2017a)) is a 50 cm off-axis Gregorian Solar telescope operational at the Udaipur Solar Observatory, Udaipur, India (c.f. Figure 2.1). This telescope was built and installed by M/s Advanced Mechanical and Optical Systems (AMOS), Belgium. The MAST is situated on an island in the middle of the Lake Fatehsagar of Udaipur, Rajasthan (c.f. Figure 2.2). The sky conditions at Udaipur are pretty favorable for solar observations. A large water body surrounding the telescope decreases the amount of heating of the surface layers. That decreases the air mass turbulence and improves the image quality and seeing. The telescope is designed to provide near diffraction-limited observations equipped with adaptive optics. The MAST's maximum circular field-of-view (FOV) is 6 arcmins, and diffraction-limited resolution is 0.310 arcsec at Fe I 6173 Å wavelength. The major science goal of the MAST is to understand the velocity and magnetic fields in the small and large-scale magnetic configurations. In addition, it also aims at the understanding of emerging flux regions, which are thought to be the site of the origin of explosive phenomena, i.e. flares and coronal mass ejections, and the evolution of velocity and magnetic fields in the pores and sunspots and their relations with the moving magnetic features etc. These scientific goals can be achieved by obtaining the measurements of the magnetograms (scalar and vector) and Dopplergrams from the near-simultaneous observations of the photosphere and chromosphere of the Sun. In order to accomplish the aforementioned scientific goals, the following back-end instruments are developed at USO:

Figure 2.1: The Island Observatory of Udaipur Solar Observatory (USO), located in the middle of lake Fatehsagar at Udaipur, India. The MAST observational facility of USO is housed inside the collapsible dome shown on the left hand side in the figure.

- Narrow-band imager
- Imaging Spectro-polarimeter
- Multi-Slit Spectro-polarimeter
- Littrow spectrograph
- Adaptive optics system

Figure 2.2: The *top left panel* shows the MAST observational facility pointing towards the Sun, whereas the *top right panel* shows the collapsible dome housing this telescope. *Bottom panel* shows the back-end instruments on an optical table including adaptive optics, narrow-band imager and polarimeter (Source: Venkatakrishnan et al. (2017a)).

2.2.1 Brief description of Narrow Band Imager (NBI)

An imager optimized with two wavelengths is integrated with the telescope to obtain near-simultaneous observations of the photosphere and the chromosphere. Two voltage-tunable lithium niobate Fabry-Perot (FP) etalons and a set of interference blocking filters have been used to develop the Narrow Band Imager (NBI: Raja Bayanna et al. (2014b); Mathew et al. (2017a)). These two etalons are used in tandem for the photospheric observations in Fe I 6173 Å absorption spectral line. However, only one of the etalons is used for the chromospheric observations in Ca II 8542 Å absorption spectral line.

The FP etalon is a simple interferometer which works on the principle of multiple reflections between two closely spaced partially reflecting surfaces. A simple FP etalon consists of two partially reflecting surfaces separated by a distance d, forming a cavity as shown in Figure 2.3. Every time a part of the incident light is

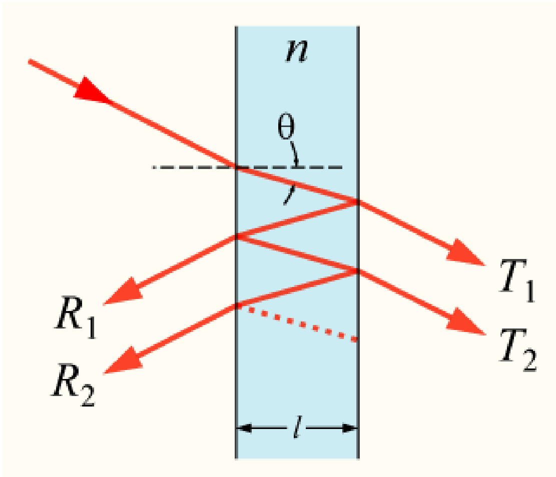

Figure 2.3: Schematic represents the multiple reflections in the Fabry-Perot etalon. The $l = d$ is the optical thickness (Source: https://en.wikipedia.org/wiki/Fabry).

transmitted and reaches the second surface, a portion of the light is transmitted, and the remaining part is reflected. The transmitted or reflected light coming out of the cavity combine constructively when the number of waves in the cavity is an integer for a specific wavelength (wavelength fits an integer number of times in the cavity).

The transmitted intensity through the etalon is described by the Airy formula,(Born and Wolf 1999),

$$I_t = \frac{I_i}{1 + Fsin^2(\delta/2)}. \tag{2.1}$$

Here, I_t and I_i are the transmitted and incident intensities, and F is the reflectivity finesse given by $4r/(1-r)^2$, where r is the reflectivity of the coated surface. The phase shift (δ) between two consecutive transmitted beams is given by $4\pi\mu d\cos(\theta)/\lambda$, whereas μ is the refractive index of the medium, d is the spacing between the surfaces, θ is the angle of incidence within the medium concerning the optical axis, and λ is the wavelength. The condition for the transmission channel for any given wavelength λ is given by $2\mu d\cos(\theta) = m\lambda$, where m is the order of interference. Figure 2.4 shows the Ca II 8542 Å spectral line (black colour) obtained from the BASS2000 solar survey archive, and the overplotted red profile represents the FP channel. The distance between two transmitted peaks is known as the free-spectral range (FSR), which is defined as $\lambda^2/2\mu d$. The transmission peak position of FP profile can be changed by changing the refractive index of the medium, or thickness, or the angle of incidence. As mentioned, the FP etalon comprises lithium niobate crystal and a set of interference filters. The electro-optic property of this crystal can be utilized for wavelength tuning. In the MAST, we tune the FP etalon at different wavelength positions by changing the refractive index from the voltage. Additional details are discussed in the articles of Raja Bayanna et al. (2014b), and Mathew et al. (2017a). Utilizing the capability of the NBI with the MAST, we have scanned the Ca II 8542 Å line profiles at different wavelength positions. Figure 2.5 shows the Ca II spectral line profile (black thin, full width at half maximum (FWHM) = 2 Å) and contribution function (thick profile) estimated in quiet Sun atmosphere, suggesting that it covers a broader height range in the solar atmosphere (Cauzzi et al. 2008). However, we do not scan the complete line profile; we restrict ourselves to within $\pm$ 1.38 Å from the line centre by applying a voltage of the order of $\pm$ 3000 volts (Mathew et al. 2017a). Moreover, we do not cover the wavelength mentioned earlier because of the safety of the FP etalon. We have observed a magnetic network region in the chromosphere of the Sun in Ca II 8542 Å line in the disk center on 21 May, 2020. Figure 2.6 shows the Ca II line profile scanned at 15 different wavelength positions (plus symbols) within a temporal cadence of 15 s. We have also observed a medium size sunspot in Ca II line at 41 locations at a spectral sampling of 25 mÅ and temporal cadence of 60 s (c.f. Figure 2.7) on 05 February, 2022. The core of the Ca II line map the middle chromosphere around h = 1400 - 1500 km, and the wings sample almost the photosphere (Cauzzi et al. 2008).

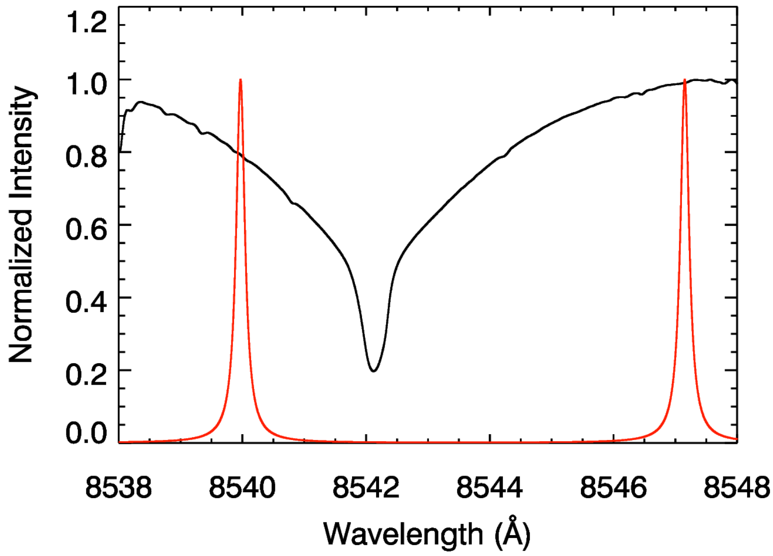

Figure 2.4: Plot represents the Ca II 8542 Å spectral line (black colour) obtained from BASS2000 solar survey archive, while overplotted red colour profile shows the Fabry-Perot channel having a full width at half maximum of 170 mÅ.

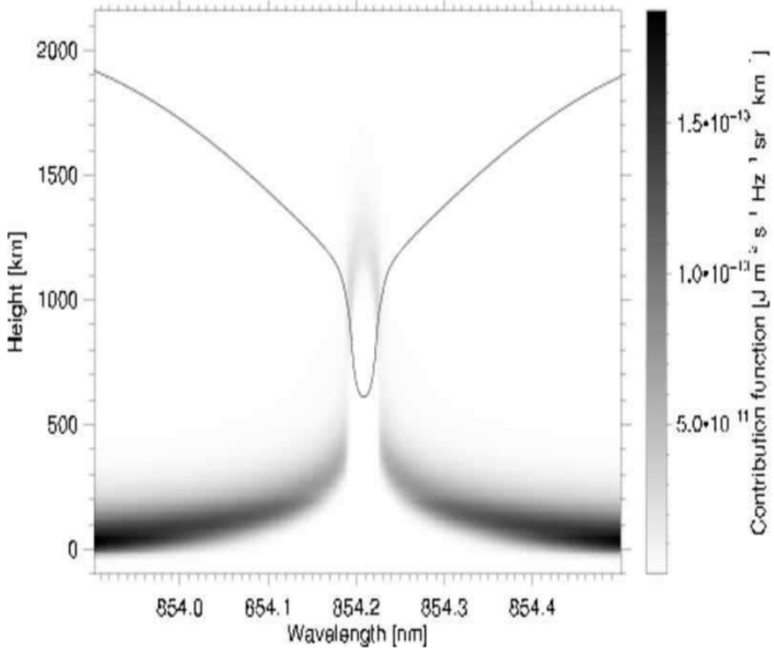

Figure 2.5: Plot represents the Ca II 8542 Å spectral line (black colour), while overplotted thick profile shows contribution function estimated in a plane-parallel, hydro-static average quiet-Sun atmosphere. Here, height zero corresponds to the level at which optical depth (τ) in the continuum at 500 nm is unity (Source: Cauzzi et al. (2008)).

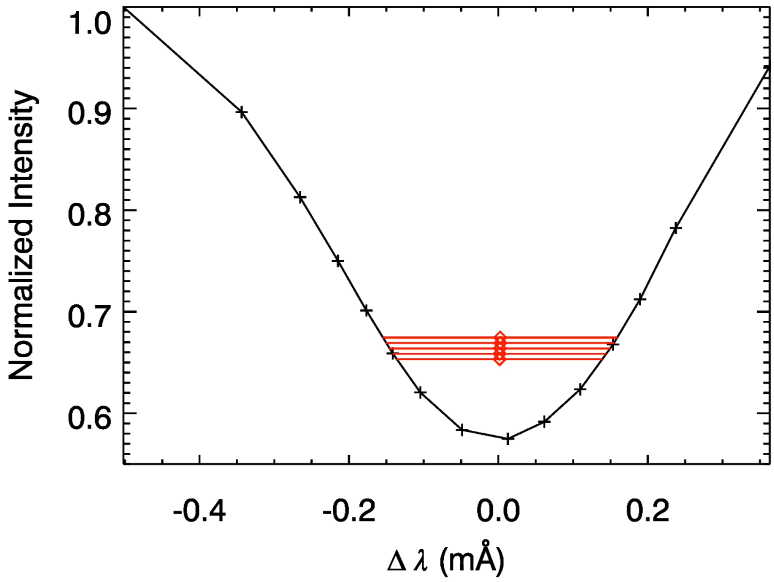

Figure 2.6: Plot represents the Ca II 8542 Å spectral line profile with 5 bisector points (red colour) and plus symbols indicate the wavelength positions where the line profile has been scanned by the narrow-band imager with the MAST.

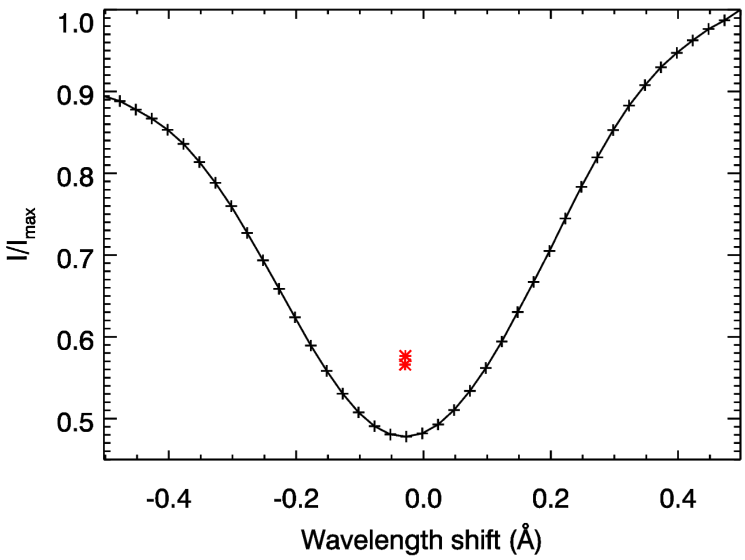

Figure 2.7: Plot represents the Ca II 8542 Å spectral line profile with 2 bisector points (red colour) and plus symbols indicate the wavelength positions where the line profile has been scanned by the narrow-band imager with the MAST.

2.2.2 MAST data reduction

The line scan observations obtained from the NBI with the MAST are subjected to the dark and flat corrections, before constructing the chromospheric line-of-sight Dopplergrams.

Dark correction: Astronomical CCDs used for the observations are so sensitive that even without illuminating the CCD surface, one gets a nonzero output signal. The output signal created by the CCD chip without exposure to photons is known as dark current. It results from thermal electrons in the pixels, voltage offsets in the CCD electronics and noise generated by the electronics. The rate of thermal electrons depends on the CCD's temperature and each pixel's impurities. Since the CCD pixels have different impurities, each element will accumulate electrons at a different rate. This can cause a faint pattern on images acquired with the CCD. Albeit this pattern is not due to light, it is difficult to determine which pixel intensity was due to light and which was due to dark current. Luckily, the thermal electrons accumulate at a constant rate for a given CCD temperature for each pixel. This indicates that this effect can be measured, and its contributions can be subtracted from the recorded images. In practice, during the observations, one should take a dark frame of the CCD under the same conditions as when taking data, with the only difference being that the beam of sunlight is blocked somewhere in the optical path. In order to reduce noise in the single dark frame, 50-100 dark images were usually taken and subsequently averaged. The resulting dark frame is almost free of noise and contains only the information about the dark counts of each CCD pixel.

Flat-field correction: In a common image processing method, a flat-field image should be made by taking a picture of an evenly illuminated scene which does not show any intensity variation. The flat-field image shows only the inherent variances in intensity values across the CCD array due to differences in the photosensitivity or dust specks on the CCD surface or vignetting in the optical system. In the solar observations, the homogeneous illumination of the detector is achieved by a rapid random swinging of the telescope by around 10 arcmins in all directions so that the field of view moves around the solar disk centre, avoiding sunspots and pores. By collecting many images on the CCD during this time and averaging them, one expects to smear any information about the solar surface and to have a CCD flat-field image. It is important to take flat fields when the CCD is in the same position in the optical setup as in the observations to avoid flat fielding artefacts on the dust particles on the CCD surface because of a different beam cone. In our observations, a flat field image consists of more than 200-300 images. Finally, using the Equation 2.2, we do dark and flat corrections from the line scan observations. Figures 2.8 and 2.9 show the dark and flat corrected intensity image of a quiet and a sunspot region, respectively.

$$I_c = \frac{(I_o - I_{ad}) \times (mean(I_{af} - I_{ad}))}{(I_{af} - I_{ad})}, \tag{2.2}$$

where I_c is corrected intensity image, I_o is observed intensity image, I_{ad} is average of dark images, and I_{af} is average of flat images.

Estimation of line-of-sight Doppler velocity:

We have used the bisector method (Gary 2005) on dark and flat corrected line scan observations to get the line-of-sight (LOS) Doppler velocity. Figure 2.6 shows the Ca II 8542 Å line profile obtained from the average intensity over full FOV over a quiet region as shown in the right panel of Figure 2.8. Here, plus symbols represent locations where line profiles have been scanned from the NBI with the MAST, and red horizontal lines in the core of Ca II line represent the bisector points. Figure 2.5 shows that Ca II 8542 Å line covers a broader height range. The bisector points in the core of Ca II spectral line (within ± 0.14 - 0.16 Å) sample the lower chromosphere around h = 900 - 1100 km. Similarly, bisector

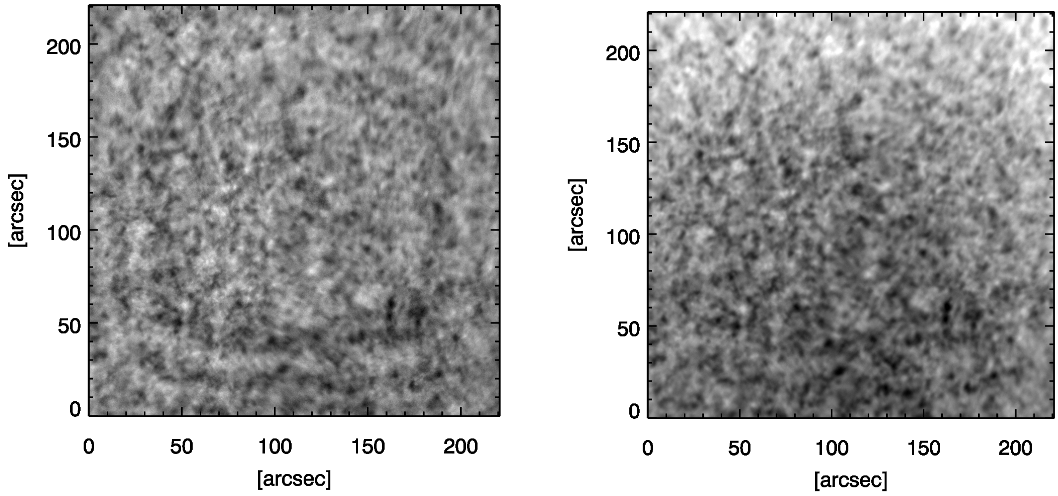

Figure 2.8: *Left panel*: A sample map of the Ca II intensity image of a quiet magnetic network region at a wavelength of 8541.7 Å observed with narrow-band imager on 21 May 2020, without dark and flat corrections. *Right panel*: same as *left panel* but after doing dark and flat corrections.

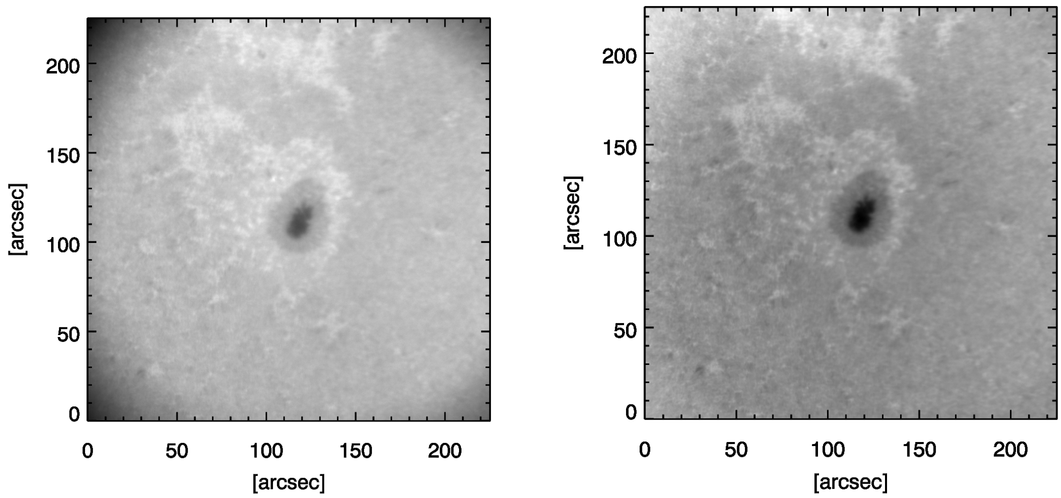

Figure 2.9: *Left panel*: A sample map of the Ca II intensity image of a sunspot at a wavelength of 8541.6 Å observed with narrow-band imager on 05 February 2022, without dark and flat corrections. *Right panel*: same as *left panel* but after doing dark and flat corrections.

method have been used to obtain LOS Doppler velocity of chromosphere over a sunspot (c.f. Figures 2.7, and 2.11). After taking the average of all these bisector points, we obtained the map of $\delta\lambda$.

Although, we also need to do the wavelength shift correction from the map of

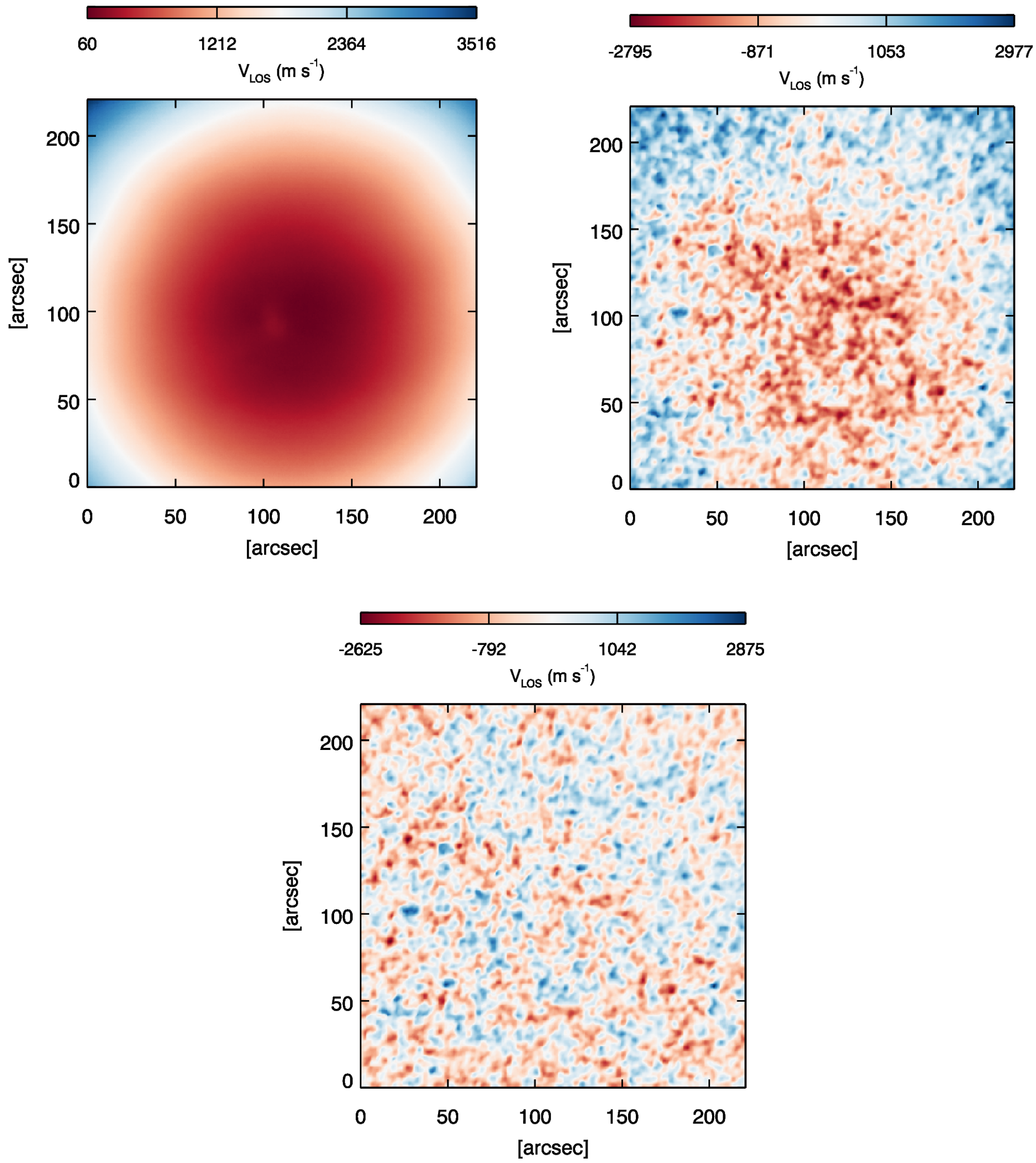

Figure 2.10: A sample map of velocity originated from wavelength shift (*top left panel*), and without wavelength shift corrected velocity map (*top right panel*). *Bottom panel* shows the Doppler velocity map of a quiet region after wavelength shift corrections.

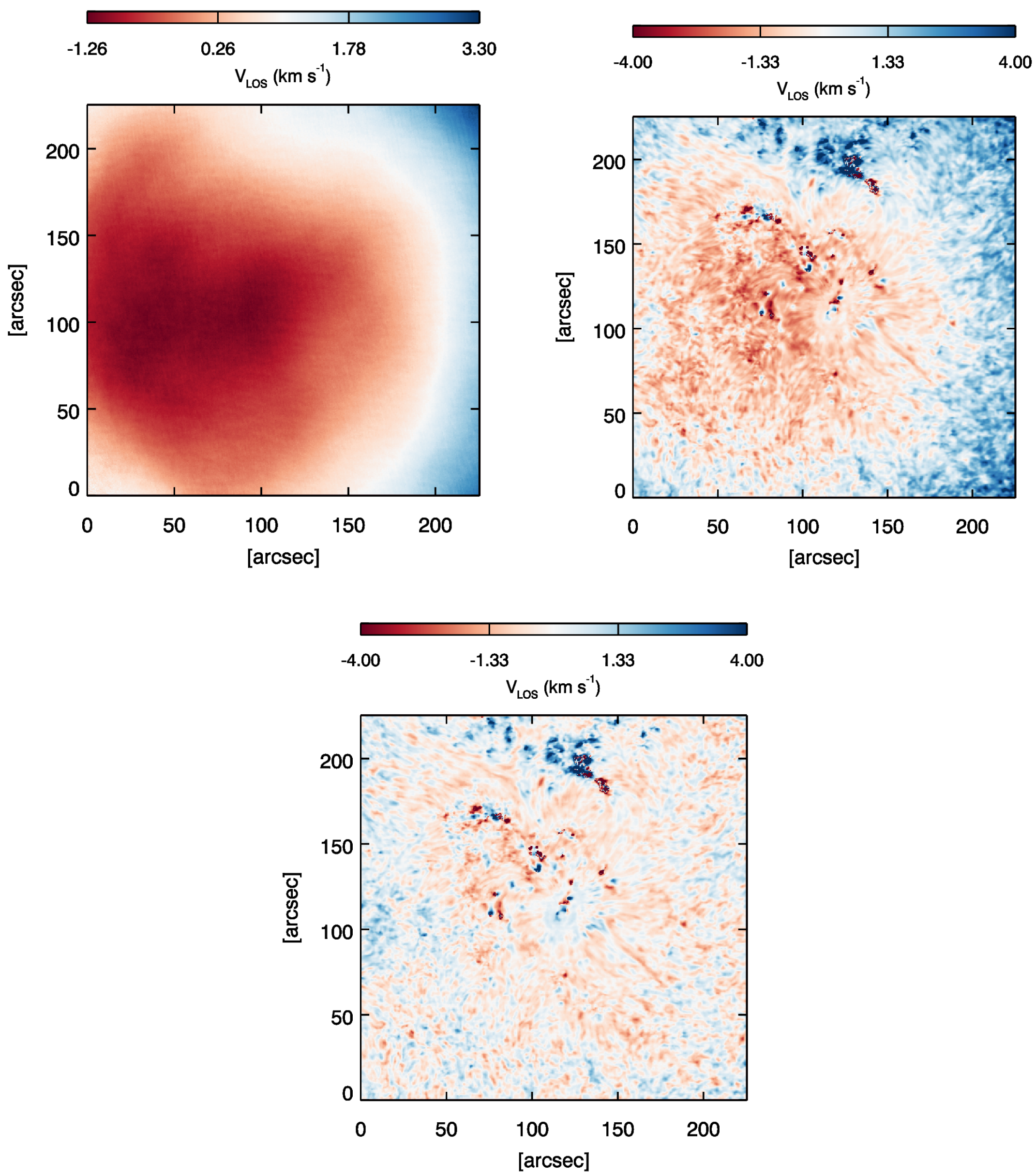

Figure 2.11: Same as Figure 2.10 but for a sunspot region. The bad pixels indicate the distorted line profiles locations.

$\delta\lambda$, which is implemented as follows. As mentioned earlier, we use NBI with the MAST to scan the line profile at different wavelength positions. For this purpose, we change the applied voltage to the FP system which changes the crystal's refractive index and consequently it scans the line profile. However, the FP channel also shifts due to the incident angle (θ) of the light relative to the optical axis. In order to remove the shift caused by the incident angle θ of the light, we use a diffuser and scan the line profile in the same way as for acquiring the actual data. From these data, we construct a map of $\delta\lambda_{shift}$ to get the information about the shift induced by the incident angle of light. The top left panel of Figure 2.10 shows the velocity map caused by the shift of incident angle (θ), while the top right panel shows the map of velocity constructed from the bisector method before removing the wavelength shift. Here, it clearly shows the effect of the shift produced by the incident angle of the light (θ). The bottom panel of Figure 2.10 shows the wavelength shift corrected line-of-sight (LOS) Doppler velocity image of the chromosphere in Ca II line used in our analysis. Figure 2.11 shows the LOS Doppler velocity maps in Ca II line with and without wavelength shift corrections estimated from the bisector method over a sunspot region. The bad pixels in the umbra and in the plage regions represent the locations of distorted line profiles.

2.3 Interferometric Bidimensional Spectrometer (IBIS)

The Interferometric Bidimensional Spectrometer (IBIS; Cavallini (2006)) is an imaging spectrometer instrument installed at the Dunn Solar Telescope (DST) at Sacramento Peak, New Mexico. It is composed of a series of two Fabry-Perot interferometers and a set of narrow-band interference filters. The sunlight enters the instrument; a beam splitter feeds it to two channels, one for context observations in continuum intensity and the other for narrow spectral band imaging. In both the channels, interference filters limit the transmitted spectral range. However, in the broad-band channel, the filters have a bandwidth of several nanometers. The pre-filters in the narrow-band channel have a centered transmission on a spectral line and allow a bandwidth of only 0.3 nm or 0.5 nm in the case of Ca II 8542 Å line. Cavallini (2006) and Reardon and Cavallini (2008) presented the detailed characterizations of the IBIS instrument. It has a circular field-of-view of 80 arcsec in diameter. It provides two dimensional solar spectroscopic observations of photosphere and chromosphere at high spatial, spectral and temporal resolutions. It observes the Sun in 560 – 860 nm wavelength range and acquires images over a CCD of 1024×1024 pixels^2 with a spatial scale of around 0.098 arcsec per pixel. Here, we have utilized imaging spectropolarimetry observations of a medium size sunspot (NOAA AR10960) located near the disk centre on June 08, 2007 in the photospheric Fe I 6173 Å absorption line.

Figure 2.12: The Richard B. Dunn Solar Telescope at Sacramento Peak, New Mexico, USA. (Source: National Solar Observatory, AURA, Inc.)

2.4 Global Oscillation Network Group (GONG)

The Global Oscillation Network Group (GONG: Harvey et al. (1988)) is a community-based project specially designed for the detailed investigations of the internal structure and dynamics of the Sun using helioseismic techniques. There are six ground-based telescopes located around the world (c.f. Figure 2.13) to obtain near-continuous observations of the Sun, namely (i) Learmonth Solar Observatory in Western Australia, (ii) High Altitude Observatory at Mauna Loa in Hawaii, USA, (iii) Big Bear Solar Observatory in California, USA (iv) Cerro Tololo Inter-american Observatory in Chile, (v) Observatorio del Teide in the Canary Islands, (vi) Udaipur Solar Observatory in India.

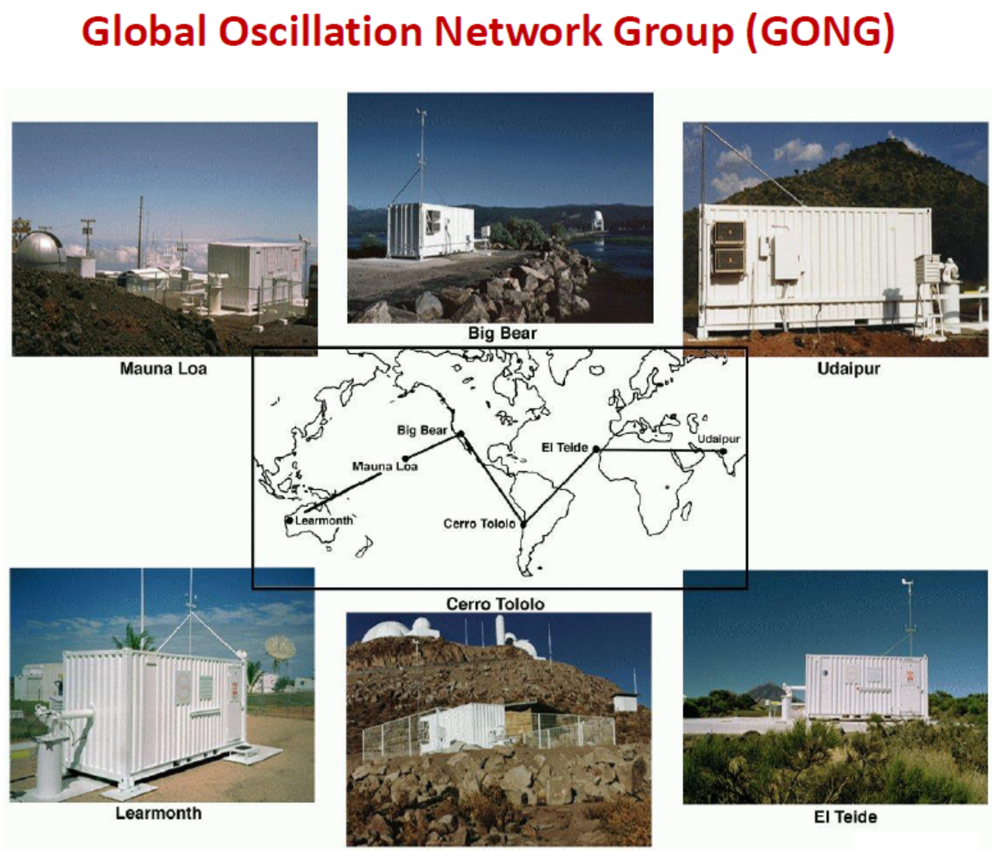

Figure 2.13: Figure demonstrates the six stations of the GONG instruments located over the globe for the continuous observations of the Sun (Source: https://gong.nso.edu/).

It observes the photosphere of the Sun in Ni I 6768 Å absorption line and works on the principles of phase shift interferometry. These instruments acquire full disk photospheric Dopplergrams, line-of-sight magnetograms, and continuum intensity images at a cadence of 60 s with a spatial sampling of 2.5 arcsec per pixel.

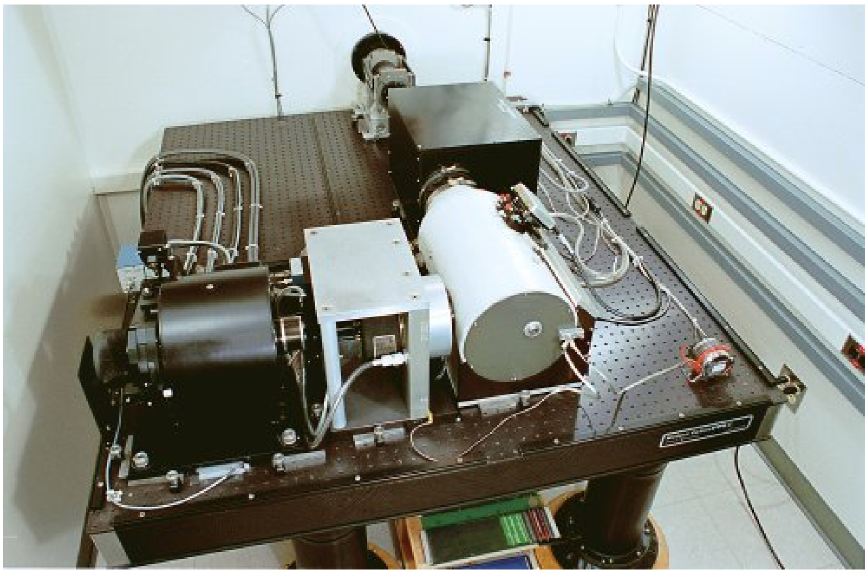

Figure 2.14: Fiure shows the layout of the GONG instruments placed on the optical table (Source: https://gong.nso.edu/instrument/).

Figure 2.14 shows the layout of the instrument placed on the optical table. The GONG instruments were upgraded to GONG+ (Harvey et al. 1998) by replacing the existing CCD camera of 256×256 pixels^2 with a new CCD camera having 1024×1024 pixels^2 for a better spatial resolution observations. Further, in 2010, GONG+ instruments were upgraded to GONG++ with the addition of the H_α telescope to provide near continuous observations for use in the space weather applications (Harvey et al. 2011). Since then, the GONG++ network is providing full disk chromospheric observations in the H_α 6562.8 Å line at a cadence of one minute and spatial sampling of $\approx$ 1 arcsec per pixel apart from other photospheric observables. In our analysis, we have used H_α intensity observations to obtain the flare ribbon information.

2.5 Solar Dynamics Observatory (SDO)

The Solar Dynamics Observatory (SDO: Pesnell et al. (2012) is a spacecraft of NASA's Living with a Star (LWS) program, which was launched on 11 February

2010 from Kennedy Space Centre in Florida. The main objective of the SDO is to study how the Sun creates solar activity and drives space weather, the dynamic conditions in space which influence the whole solar system. It also includes measurements of the interior of the Sun and how the Sun's magnetic field is generated, structured, and converted into extremely violent solar events, which are responsible for the space weather. Additionally, it also aims to understand the hot plasma of the solar corona and extreme ultraviolet irradiance of the Sun that is a key driver to the structure and composition of the upper atmosphere of the Earth. This observatory contains three different instruments: (1) Helioseismic and Magnetic Imager (HMI: Scherrer et al. (2012)), (2) Atmospheric Imaging Assembly (AIA: Lemen et al. (2012)), (3) Extreme ultraviolet Variability Explorer (EVE: Woods et al. (2012)).

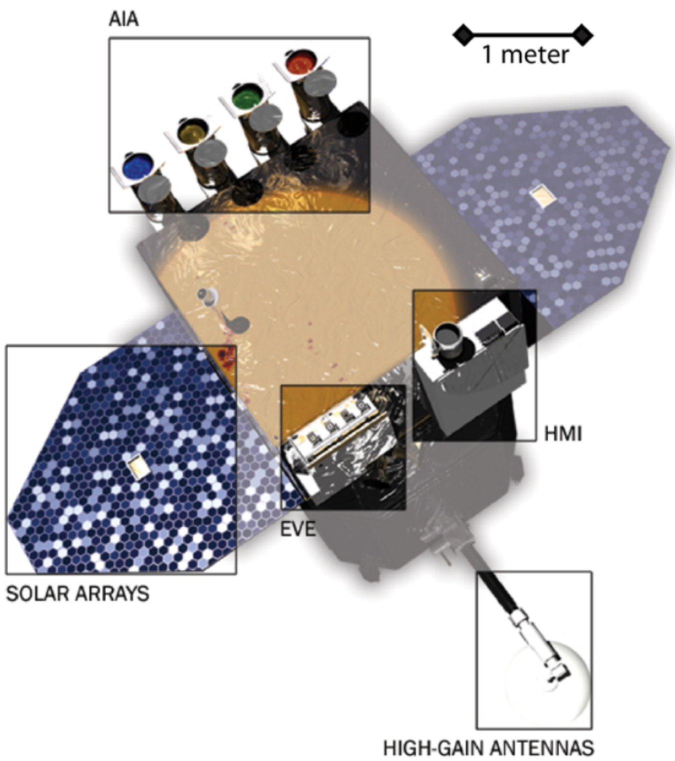

Figure 2.15: The SDO spacecraft with its instruments (Source: Pesnell et al. (2012)).

2.5.1 Helioseismic and Magnetic Imager Instrument (HMI)

The HMI instrument onboard the SDO spacecraft was built at the Lockheed Martin Solar and Astrophysics Laboratory (LMSAL) in collaboration with Stanford University as a part of the Stanford Lockheed Institute for Space Research collaboration. It has been observing the photosphere of the Sun in Fe I 6173 Å absorption line since 2010. This line's Lande-factor ($g_{eff} = 2.5$) is high, which increases its suitability to measure the magnetic fields. The HMI instrument is built around an optical filter composed of a front window, a blocking filter, a five-stage Lyot filter, and two Michelson interferometers (Couvidat et al. 2012d). It produces a narrow band transmission profile, with a Full Width at Half maximum (FWHM) of 76 mÅ. It uses two 4096×4096 pixels CCD cameras with mechanical shutters and control electronics having a pixel size of 0.5 arcsec. Other details of the HMI instrument are given in Table 2.1. The Images are recorded in a sequence of tuning and polarizations at a cadence of 4 sec in both of these cameras (See for more details `http://hmi.stanford.edu/Description/HMI_Overview.html`). One of the cameras is dedicated to 45 s Doppler and LOS magnetic fields observables, while the second is to vector magnetic field observations. The HMI instrument provides full-disc (4096×4096 pixel images), Dopplergrams, line-of-sight (LOS) magnetograms, intensitygrams and vector magnetic fields at a spatial resolution of 1 arcsec. It samples Fe I 6173 Å neutral line at six wavelength positions around the line centre. The LOS observables are generated at every 45 s, mainly Dopplergrams, LOS magnetograms, continuum intensitygrams, line depth and Fe I line width. These observables are produced using the 12 filtergrams taken at six different wavelength positions with two polarizations, i.e. left circular polarization (LCP) and right circular polarization (RCP) (Couvidat et al. 2012a). From the LCP and RCP observations in order to derive the full disk maps of LOS magnetic fields and Dopplergrams, an MDI-like algorithm is applied at every pixel (for more details, refer to (Couvidat et al. 2012a)). All these data products are publically available on http://jsoc.stanford.edu/ajax/lookdata.html as **hmi.V_45s** (Dopplergram), **hmi.M_45s** (LOS magnetogram), **hmi.Ic_45s** (continuum intensity), **hmi.Lw_45s** (line width), and **hmi.Ld_45s** (line depth) for different scientific investigations. As mentioned above, other information related to the observables is given in Table 2.2.

Table 2.1: The specifications of the HMI instrument.

Central wavelength	Fe I 6173.3 Å±0.1
Filter bandwidth	76 mÅ±10 mÅ
Filter tuning range	680±68 mÅ
Central wavelength drift	<10mÅ during in any 1 hour
Field of view	2000 arcsec
Angular resolution	better than 1.5 arcsec
Field of view	2000 arcsec
Detector resolution	0.50±0.01 arcsec/pixel
Field of view	2000 arcsec
Focus adjustment range	±4 depths of focus
Pointing jitter reduction factor	>40 db with servo bandwidth >30 Hz
Image stabilization offset range	>14 arcsec in pitch and yaw
Pointing adjustment range	> 200 arcsec in pitch and yaw
Dopplergram cadence	45 sec
Camera image cadence	4 sec
Timing	<1 μs stability, <100 ms absolute
Science telemetry allocation	<55 Mbps/s
Instrument design lifetime	> 5.3 years

The HMI instrument is made of combinations of a Lyot filter along with two Michelson interferometers. Moreover, there is a set of 10th-order retarders between these two instruments, λ /2, λ /4, and λ /2, respectively. Further, a beam splitter divides the light between two 4096×4096 pixels^2 CCDs. These cameras acquire full disc images of the Sun at a pixel size of 0.5 arcsec. The first camera, also known as the Doppler camera, is dedicated to the measurement of left and right circular polarization, I±V, at six wavelength positions along the Fe I 6173 Å line. From these observations, full disc maps of LOS Dopplergrams and LOS magnetograms are produced at 45 s. The second camera, hereafter referred to as

Table 2.2: The HMI observations.

Doppler Velocity	
Cadence	45 s
Precision	13 m/s
Zero point accuracy	0.05 m/s
Dynamic range	±6.5 km/s
Line-of-Sight Magnetic field	
Cadence	45 s
Precision	10 G
Zero point accuracy	0.05 G
Dynamic range	±4 kG
Continuum intensity	
Cadence	45 s
Precision	0.3%
Accuracy pixel to pixel	0.1%
Vector Magnetic field	
Cadence	90 s
Precision:	
Polarization	0.22%
Sunspots (1kG< $\|B\|$<4kG)	
$\|B\|$	18 G
Azimuth	0.6°
Inclination	1.4°
Quiet Sun (0.1KG< $\|B\|$<2kG)	
$\|B\|$	220 G
Total flux density	35 G
Azimuth	15°
Inclination	18°

the vector camera, measures the full Stokes vector $\boldsymbol{I} = (\boldsymbol{I}, \boldsymbol{Q}, \boldsymbol{U}, \boldsymbol{V})$ at the same wavelength positions as the first camera. Now, these observed Stokes profiles are fitted by nonlinear least-squares fitting algorithms which use the analytical profiles obtained from the radiative transfer equation solved by the assumptions of the Milne-Eddington atmospheric model (Landolfi and Landi Degl'Innocenti 1982). The Very Fast Inversion of the Stokes Vector (VFSIV; Borrero et al. (2011)) algorithm is used by the HMI team to invert the Stokes profiles, which provides magnetic field components to the solar physics community. The magnetic fields obtained from the above procedure have the so-called 180° ambiguity problem, which arises because the direction of the horizontal component of the magnetic fields is not resolved due to azimuthal angle retrieval from the inversion of Stokes vectors. The HMI's science team use minimum-energy method (Metcalf (1994), and Leka et al. (2009)) to resolve 180° ambiguity problem. After doing all the data processing of Stokes vectors, the HMI team provides vector magnetograms at the standard pipeline[1] in the spherical coordinates, namely radial (B_r), azimuthal (B_p) and zenith component (B_t). Further, these field vectors in the spherical coordinates are approximated to B_z, B_x and -B_y in cartesian coordinates, respectively (Gary and Hagyard 1990).

2.5.2 Atmospheric Imaging Assembly Instrument (AIA)

The AIA instrument onboard the SDO spacecraft was designed to study solar emissions from the transition region to corona. It consists of four telescopes, which provide full-disc images (4096×4096 pixels^2) with a spatial resolution of 1.5 arcsec. It observes the atmosphere of the Sun in Ultra-Violet (UV) to extreme ultraviolet (EUV) wavelength range with a 12-second temporal cadence. The AIA instrument observes the outer atmosphere of the Sun in seven EUV filters at 94 Å, 131 Å, 171 Å, 193 Å, 211 Å, 304 Å and 335 Å, two UV filters at 1600 Å and 1700 Å and one white light filter at 4500 Å wavelengths. The temporal cadence of EUV observations is 12 s, 24 s for UV and 3600 s for a white light filter. For further details of the instruments, please refer to the Table and article of Lemen et al. (2012).

[1]http://jsoc.stanford.edu/ajax/lookdata.html

Table 2.3: The AIA observations.

Channel (Å)	Primary Ions	Region of Atmosphere	Char. Log(T)
4500	Continuum	Photosphere	3.7
1700	Continuum	Temperature minimum, Photosphere	3.7
304	He II	chromosphere, transition region	4.7
1600	C IV-cont	transition region, upper photosphere	5.0
171	Fe IX	quiet corona, upper transition region	5.8
193	Fe XII, XXIV	corona and hot flare plasma	6.2, 7.3
211	Fe XIV	active region corona	6.3
335	Fe XVI	active region corona	6.4
94	Fe XVIII	flaring corona	6.8
131	Fe VIII, XXI	transition region, flaring corona	5.6, 7.0

2.6 GOES soft X-ray observations

The Geostationary Operational Environmental Satellite (GOES) is a joint effort of the National Aeronautics and Space Administration (NASA) and the National Oceanic and Atmospheric Administration (NOAA), which formally began in 1975. The X-ray Sensors aboard GOES provide continuous observations of solar X-ray flux. Each satellites have two sensors, which measure the disc-integrated X-rays flux[2] in two different wavelengths i.e. 0.5–4 Å and 1–8 Å bands. Both of the channels of GOES 13–15 satellites observe simultaneously and provide data at a cadence of $\approx$ 2 sec. We have used GOES observations in the 1–8 Å band to identify the transient solar activities, viz. solar flares and their impact on different physical parameters like Doppler velocity and magnetic fields.

2.7 RHESSI hard X-ray observations

The Reuven Ramaty High Energy Solar Spectroscopic Imager (RHESSI; Lin et al. (2002)) is a Small Explorer (SMEX) mission of NASA, which was launched on 05 February 2002. The primary objective of the RHESSI instrument is to un-

[2] http://goes.ngdc.noaa.gov/data/

derstand the basic science behind particle acceleration and energy release accompanying solar flares. It is accomplished by imaging and spectroscopy of hard X-ray/gamma-ray continua emitted by energetic electrons and of gamma-ray lines produced by energetic ions (Lin et al. 2002). This instrument is designed to image solar flares in soft X-rays ($\approx$ 3 keV) to gamma rays ($\approx$ 17 MeV) energy bands with a high spatial resolution as $\approx$ 2.3 arcsec and a full-Sun field-of-view having a spectral resolution of $\approx$1–10 keV FWHM over 3 keV–17 MeV. The RHESSI imaging is based on a Fourier transform technique, which uses a set of nine Rotating Modulation Collimators (RMCs), consisting of a pair of widely separated grids. Images are reconstructed from the set of measured Fourier components in exact mathematical analogy to the multi-baseline radio interferometry. The raw data were obtained from the RHESSI data site[3] for different events. We have used the Pixon method (Hurford et al. 2002) to construct HXR maps for different events analyzed in the work. It provides reconstructed images at a spatial and temporal resolutions of 4 arcsec pixel^{-1} and 1 min, respectively. In our analysis, we have used 12–25 keV energy band to get the information on hard X-ray footpoints during the solar flares.

2.8 Summary and Conclusions

In this chapter, we discussed observational data obtained from various ground- and space-based instruments to achieve the objectives of this thesis. We have presented the data reductions of the Ca II 8542 Å line scan observations of a quiet and a sunspot region obtained from the NBI with the MAST operational at the Udaipur Solar Observatory, Udaipur India. Here, we also discuss working procedure of the NBI instrument with the MAST. In order to construct the chromospheric line-of-sight Doppler velocity from Ca II 8542 Å line scan observa-

[3] ftp://hercules.ethz.ch/pub/hessi/data/

tions, we have used bisector method. Further, we discuss about the wavelength shift corrections and methodology to perform the wavelength shift corrections from Doppler velocity maps before proceeding to the scientific analysis of chromospheric line-of-sight Dopplergrams. We have also extensively utilized data obtained from the HMI and AIA instruments onboard the SDO spacecraft. In addition to that, we have also used data from the IBIS/DST, GONG, GOES and RHESSI instruments. We have utilized SSW pacakages to handle the data obtained from the space based instruments. We have also written our own IDL programs to handle the MAST observations.

Chapter 3

Seismic Emissions Accompanying Major Solar Flares

3.1 Introduction

Solar flares are the magnetized events in the solar atmosphere, in which previously-stored magnetic energy of the order of 10^{27}–10^{32} ergs are released into the solar atmosphere in the form of thermal radiation, mass motion and accelerated charged particles within few minutes to an hour. During solar flares, the back bombarded charged particles gyrate along the magnetic field lines and generate gyrosynchrotron emissions (Hudson and Ohki 1972). The bremsstrahlung radiation generated by deaccelerating charged particles while striking the chromospheric plasma produces hard X-rays (Brown 1971). Wolff (1972b) suggested that large solar flares could also stimulate free global oscillations in the Sun. Much later, Fisher et al. (1985) proposed that during solar flares, the bombardment of charged particles on the chromospheric layers heats the chromospheric plasma and, as a result, chromospheric evaporation into the corona takes place. Further, the downward settlement of the condensed material can launch a shock on the photosphere, thereby delivering large momentum to the photospheric layers (Fisher 1989) and this high amount of energy can excite the acoustic waves inside the Sun. Kosovichev and Zharkova (1998) reported the first instance of flare-induced seismic emission in the Sun during an X 2.6 class solar flare, which occurred on 9 July 1996, utilizing the data from the Michelson Doppler Imager (MDI; Scherrer et al. (1995)) instrument aboard the Solar and Heliospheric Observatory (SOHO; Domingo et al. (1995)) spacecraft. They identified this phenomenon as a "sunquake". Later on, there are several others cases reported by Donea and Lindsey (2005), Donea et al. (2006), Moradi et al. (2007) and Kumar and Ravindra (2006), in which they have found acoustic emissions accompanying different classes of solar flares. Zharkova and Zharkov (2007) investigated acoustic emissions in a proton-rich solar flare, and they explained these enhancements as due to the back-reaction of the shock driven by high energetic charged particles impinging on the solar photosphere during the flare. Furthermore, Venkatakrishnan et al. (2008) observationally found that these high energetic charged particles can reach up to the photosphere from the chromosphere in about 1 minute and thus could be responsible for enhancing the velocity oscillations. Hudson et al. (2008b) proposed another mechanism, known as "magnetic jerk", which could be responsible for the generation of seismic waves in the sunspots, apart from the back-reaction of shock and high energetic charged particles on the solar photosphere.

It is well known that during solar flares, magnetic fields of the corona change and the signatures of those appear in the form of the temporal evolution of the photospheric magnetic fields. Changes in the magnetic fields occur within a short time before the flare, during the flare, and after the flare epochs. Patterson and Zirin (1981) was the first to report the rapid, short-term changes (transient changes) in the magnetic fields during solar flares. Further, Patterson (1984) illustrated that these observed transient changes in the magnetic fields could be due to emission in the core of the spectral line, which is used to obtain the information of the magnetic fields. In addition, Qiu and Gary (2003) discussed the possibility of change in line profiles during a transient polarity reversal observed in the photospheric magnetic field measurements obtained from the MDI instrument aboard SOHO. Wang (1992) and Wang et al. (1994, 2002) reported abrupt and permanent changes in the evolution of magnetic fields in the flaring region during the different classes of solar flares using the data from Big Bear Solar Observatory. Later on, extensive analysis done by Sudol and Harvey (2005) and Petrie and Sudol (2010) of X- and M-class solar flares using the line-of-sight magnetic fields data obtained from the GONG instruments, showed abrupt and permanent changes in the magnetic fields in the flaring locations within 10-minute duration with a median magnitude of 100 Gauss. In addition, Kumar et al. (2016b) also found abrupt and persistent changes in line-of-sight magnetic fields at different locations in the active region during an M6.5 class solar flare using the data from the HMI/SDO, which are considered to be due to the re-organization of coronal magnetic fields.

The Lorentz force dominantly governs the solar corona compared to other forces, viz. gravity and gas-pressure (Fisher et al. 2012). It is believed that photospheric or sub-photospheric flows produce magnetic stress in solar active regions, which generates the Lorentz force and magnetic free energy in the active regions. However, during the solar flares, magnetic stress of the active regions is released, resulting in a Lorentz force impulse affecting the solar photosphere, which can change the configuration of the magnetic field (Hudson 2000). Hudson (2000) also conjectured that abrupt release of previously stored magnetic energy would lead to magnetic implosion and subsequently there could be contraction and collapse of magnetic loops towards the photosphere. Further, they have suggested that an abrupt radial Lorentz force will act on the photosphere due to the magnetic implosion. It was proposed by Hudson et al. (2008b), and Fisher et al. (2012) that an impulsive change in Lorentz force acting on the photosphere can induce seismic emission in the sunspots during solar flares. The change in radial and horizontal components of Lorentz force acting on the solar photosphere within a temporal window of δt introduced by Fisher et al. (2012) are as follows:

$$\delta F_{r,interior} = \frac{1}{8\pi} \int_{A_{ph}} dA(\delta B_r^2 - \delta B_h^2), \tag{3.1}$$

and

$$\delta F_{h,interior} = \frac{1}{4\pi} \int_{A_{ph}} dA\delta(B_r B_h), \tag{3.2}$$

where B_r and B_h are the radial (vertical) and horizontal (i.e., transverse) components of vector magnetic fields, respectively, δF_r & δF_h are the changes in radial and horizontal components of Lorentz force acting on the solar interior, dA is the elementary surface area over the photosphere and A_{ph} represents the area of the photospheric domain containing the active region. The sign of Equations 3.1 and 3.2 have been reversed as compared to Equations 9, and 10 of Fisher et al. (2012) in order to estimate the force acting on the photosphere. It is to be noted that Petrie (2014) further discussed the application of formulation introduced by Fisher et al. (2012) within a subdomain of an active region. Petrie (2014) suggested that these expressions could be used in a sub-domain of the active region at the photosphere if the horizontal length scale of the structure is much more than 300 km and the magnetic field strength is greater than 630 G at the height of the observations.

Moreover, transient changes in the magnetic fields and Doppler velocity in flaring locations are found to be associated with the distortions in the line profiles (Maurya et al. 2012). The detailed investigations done by Raja Bayanna et al. (2014a) observed distortions in the two circular polarization states of light, the Left Circular Polarization (LCP) and the Right Circular Polarization (RCP) observations, in the flaring locations which depicted transient changes in Doppler velocity and line-of-sight magnetic fields during an X-class flare, using the line profile observations from the HMI instrument aboard the SDO spacecraft. They concluded that observed transient changes in Doppler velocity and magnetic fields in the flaring locations are prone to artefacts in the measurements.

In this Chapter, we present a detailed analysis of seismic emission in the sunspots away from the flare ribbons and hard X-ray foot-points accompanying major solar flares. Such acoustic enhancements are supposed to be free from any flare-related contamination in the observational data. In the following Sections, we first describe the data analysis techniques and selection criteria for choosing the active regions for our investigations. This is followed by methods of analysis and the results obtained. Finally, we summarize our results in Section 3.5.

3.2 Observational Data and Analysis Procedure

In order to investigate the seismic emissions in the sunspots accompanying major solar flares, we have used photospheric Dopplergrams, continuum intensity, line-of-sight magnetograms at a cadence of 45 s and vector magnetograms (B_x, B_y, B_z) at a cadence of 135 s acquired from the HMI instrument onboard SDO spacecraft. For the chromospheric flare ribbons and hard X-ray footpoints (12–25 keV band) information, we have utilized chromospheric H_α intensity observations from the GONG network and RHESSI spacecraft, respectively. The disk integrated solar flux variations in 1–8 Å obtained from GOES have been utilized to get the information of solar flares. The details of the various instruments are presented in Chapter 2. To accomplish our scientific goal, we have adopted selection criteria to choose active regions, which are as follows:

(i) We have selected only those active regions which have produced M- and X-class solar flares.

(ii) The active regions, which are within 40° latitude and longitude of the solar disk, have been analyzed because p-mode oscillations are radial and dominated near the disk centre. Thus, as we go away from the disk centre, these oscillations suffer from the projection effect.

(iii) We have restricted our analysis to only those active regions in which magnetic field strength is less than 3000 Gauss and the Doppler velocity does not exceed $\pm$ 6 km s^{-1}, including the orbital velocity of the spacecraft. It is to be noted that in the active regions where the total Doppler velocity exceeds $\pm$ 8.5 km s^{-1} or the magnetic field strength is more than $\pm$ 3800 Gauss, the Fe I 6173 Å spectral line can go outside the observing window in the HMI instrument thereby causing saturation problem in the observational data (Couvidat et al. 2012b).

On applying the aforementioned selections criteria, we have investigated eight active regions, the details of which are given in the Table 3.1.

Table 3.1: Details of the active regions (ARs) used in our analysis and information related to the flare evolution as seen in GOES soft X-ray (1–8 Å band).

ARs NOAA	Location on the disk	Flare class	Date	Start time (UT)	Peak time (UT)	Decay time (UT)
11158	S28W17	X2.2	2011 February 15	01:44	01:56	02:06
11261	N15W35	M6.0	2011 August 03	13:17	13:48	14:10
11882	S06E28	M2.7	2013 October 28	14:46	15:01	15:04
11882	S06E28	M4.4	2013 October 28	15:07	15:15	15:21
12222	S20W31	M6.1	2014 December 04	18:05	18:25	18:56
12241	S09W09	M6.9	2014 December 18	21:41	21:58	22:25
12242	S21W24	X1.8	2014 December 20	00:11	00:28	00:58
12297	S16E13	X2.0	2015 March 11	16:11	16:22	16:29
12371	N13W06	C3.9	2015 June 22	17:20	17:27	17:33
12371	N13W06	M6.5	2015 June 22	17:39	18:23	18:23

3.3 Evolution of velocity oscillations in the sunspots during flares

We have analyzed photospheric line-of-sight Dopplergrams to identify any seismic emissions in the sunspots during the flares. Here, we discuss the analysis procedure and results of the active region NOAA 11158; however, a brief overview of important results related to other active regions is also presented. The remaining results are provided in the Appendix of the thesis.

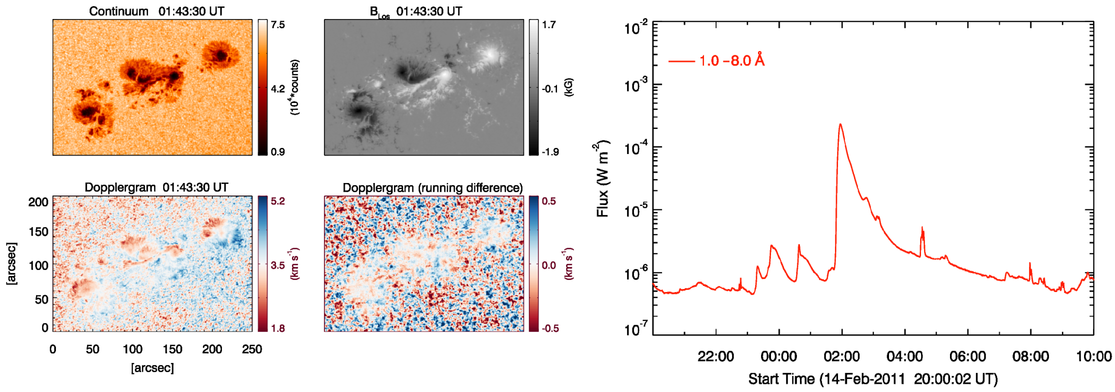

Figure 3.1: *Left panel*: Sample images of the active region NOAA 11158 showing I_c image (*top left*), photospheric B_{LOS} magnetic fields (*top right*), Dopplergram (*bottom left*) and running difference of Doppler images (*bottom right*) acquired from the HMI instrument onboard SDO spacecraft on 2011 February 15. *Right panel*: Plot shows the temporal evolution of disk-integrated solar flux in 1–8 Å band during an X2.2 class flare on 2011 February 15, obtained from GOES.

The active region NOAA 11158 produced several flares during its passage on the solar disk. This was the first active region of Solar Cycle 24, which produced an X2.2 class flare on 2011 February 15, around 01:44 UT (c.f. right panel of Figure 3.1). We have used the tracked photospheric Dopplergrams at a cadence of 45 s (c.f. bottom left panel of Figure 3.1) obtained from the HMI instrument onboard the SDO spacecraft. In order to study the p-mode oscillations, we have applied a two-point backward difference filter which removes the slowly varying

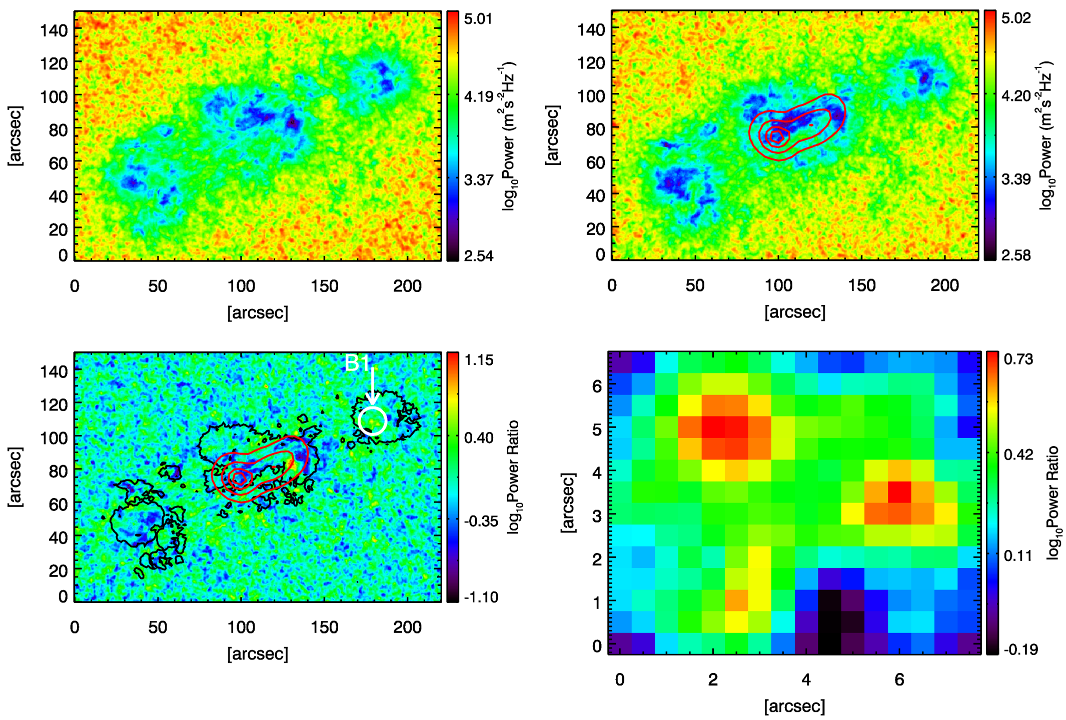

Figure 3.2: *Top left panel*: Acoustic power map of active region NOAA 11158 in 2.5 – 4 mHz band estimated over 2 hour duration for pre-flare epoch. *Top right panel*: Same as shown in the *left panel* but for spanning the flare. *Bottom left panel*: Ratio of power maps estimated for spanning and pre-flare epochs. Here, black contours represent the outer boundary of the sunspot penumbra obtained from continuum intensity image whereas the red contours represent hard X-ray foot-points at 25, 50, 75 and 90% of its maximuum as observed in 12–25 KeV band from the RHESSI spacecraft. *Bottom right panel*: Illustrates the blow-up region of '$B1$' enhanced location in the sunspot as indicated in the power map ratio.

features from the Dopplergrams. Those filtered Dopplergrams are then subjected to fast Fourier transform (FFT) for estimating the power spectrum at each pixel. Following this, we construct power maps in the frequency range 2.5–4 mHz band (p-mode oscillations) for pre-flare and spanning flare epochs (c.f. top panels of Figure 3.2). These acoustic power maps (c.f. top panels of Figure 3.2) depict that there is a suppression of p-mode power in the sunspot regions as compared to the quiet-Sun. Further, we have overplotted the hard X-ray contours from RHESSI instrument in the 12–25 KeV energy band on the spanning flare power map (c.f.

top right panel of Figure 3.2) at 25, 50, 75, and 90% of its maximum level in order to identify the hard X-ray foot-point locations. Earlier work (Zharkova and Zharkov (2007), Venkatakrishnan et al. (2008) and references therein) shows that high energetic charged particles can reach up to the photosphere and induce p-mode oscillations beneath the hard X-rays foot points and flaring ribbons. However, line profiles are prone to getting distorted in the flaring/hard X-ray footpoints locations due to the change in local thermodynamics conditions as mentioned above (Qiu and Gary (2003), Maurya et al. (2012), and Raja Bayanna et al. (2014a)). Therefore, we have looked for only those acoustically enhanced locations in the sunspots which are away from HXR footpoints and flare ribbons.

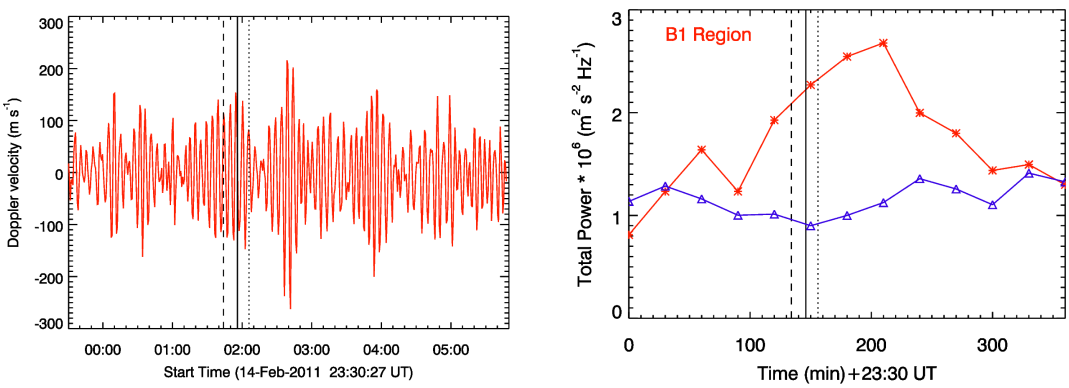

Figure 3.3: *Left panel*: Plot in red colour shows the temporal evolution of Doppler velocity at a cadence of 45 s in the '$B1$' location of active region NOAA 11158. The dashed, solid and dotted vertical lines represent onset, peak and decay time of the flare. *Right panel*: Plot showing the temporal evolution of integrated acoustic power over the '$B1$' location (red colour with asterisks) whereas that shown in blue colour with triangles represents evolution of total power in an unaffected region in the same sunspot. It is to be noted that there is a time offset of about $\pm$ 30-minutes between the acoustic power variation and the GOES flare-time.

Although, by visualization of these two power maps (c.f. top panel of Figure 3.2), it is difficult to infer any adequate changes in the acoustic power in the sunspot regions during the flare. As a result, we have taken the ratio of these two power maps (spanning flare to pre-flare) as shown in the bottom left panel of Figure 3.2.

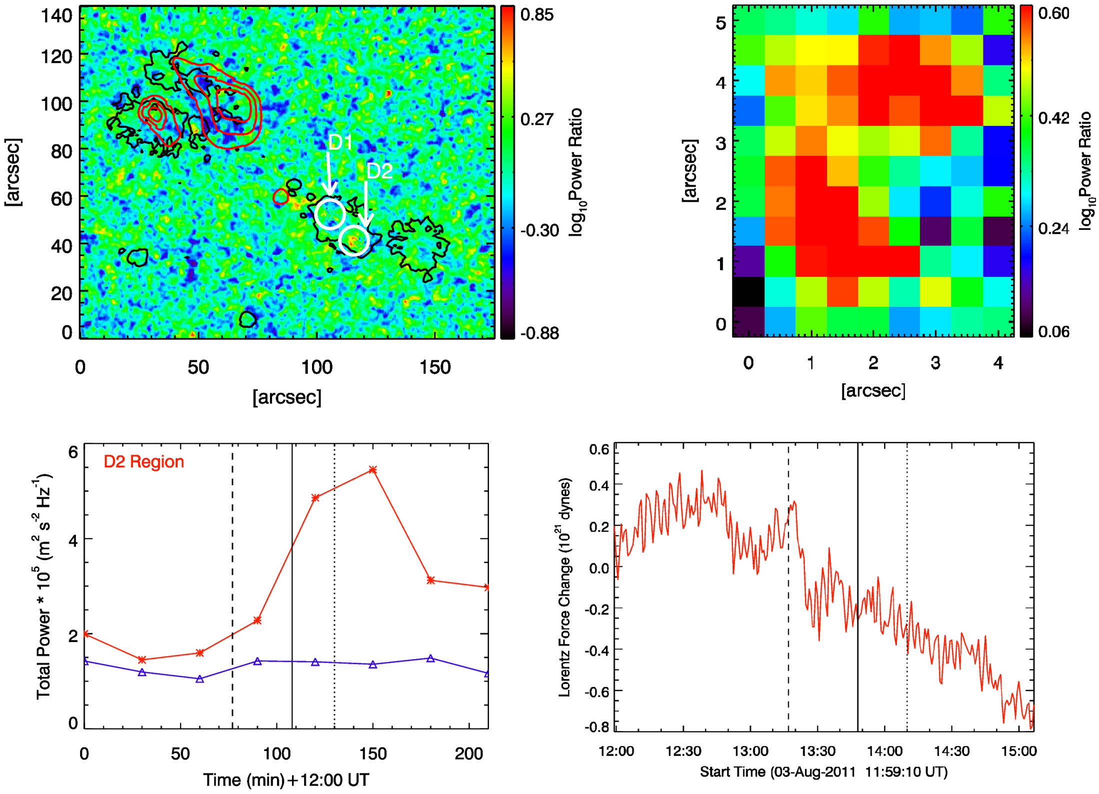

Figure 3.4: A brief illustration of important results obtained for the active region NOAA 11261. *Top left panel*: This illustrates the ratio of acoustic power maps estimated for spanning flare and pre-flare epochs in the 2.5–4 mHz band. Here, black contours represent the outer boundary of the sunspot penumbra obtained from continuum intensity image whereas the red contours represent flare-ribbon locations from Hα chromospheric intensity observations at 70, 80 and 90 % of its maximum value as observed from the GONG instrument. *Top right panel*: Illustrates the blow-up region of '$D2$' enhanced location in the sunspot as indicated in the power map ratio. *Bottom left panel*: Plots showing the temporal evolution of integrated acoustic power over the '$D2$' location (red colour with asterisks) whereas that shown in blue colour with triangles represents evolution of total power in an unaffected region in the same sunspot. It is to be noted that there is a time offset of about $\pm$ 30-minutes between the acoustic power variation and the GOES flare-time. *Bottom right panel*: Plot in red colour shows the temporal evolution of change in radial (i.e., upward) component of Lorentz force in the '$D2$' location. The dashed, solid and dotted vertical lines represent the onset, peak and decay time of the flare. The remaining maps and plots have been provided in the Appendix.

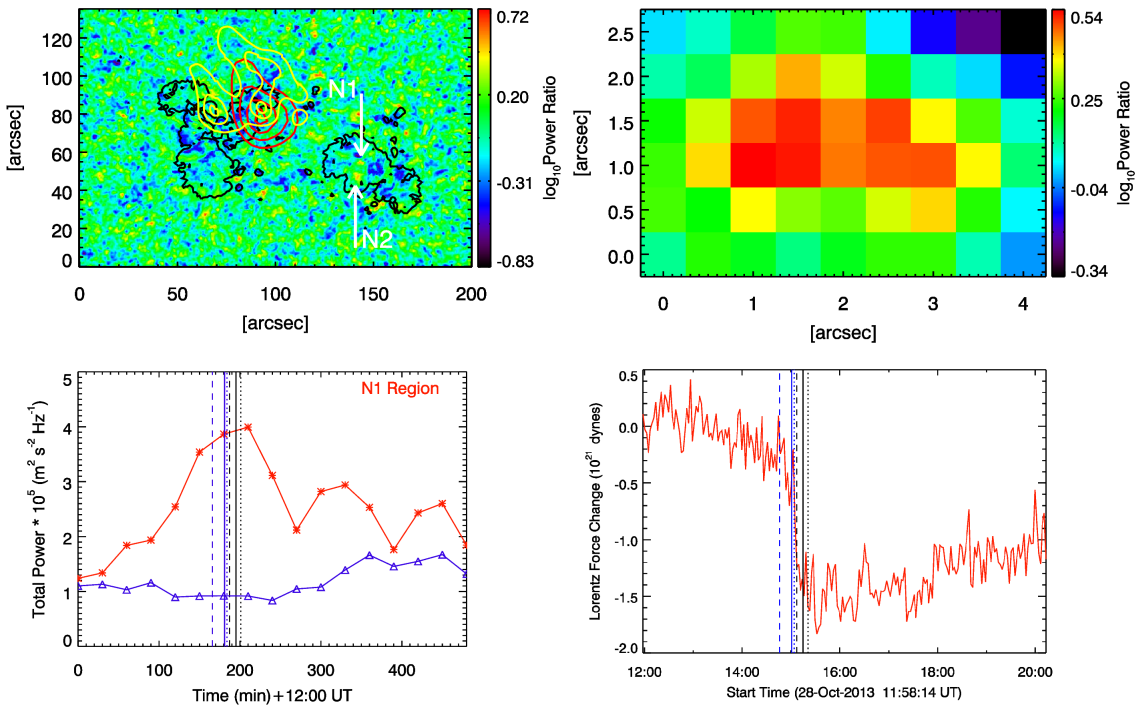

Figure 3.5: Same as Figure 3.4, but for '$N1$' location of active region NOAA 11882. It is to be noted that there is a time offset of about ± 30-minutes between the acoustic power variation and the GOES flare-time in the *bottom left panel*. The bottom right panel illustrates the change in horizontal (i.e., transverse) component of Lorentz force in the aforementioned location. The dashed, solid and dotted blue and black vertical lines represent the onset, peak and decay time of M2.7 and M4.4 class flares, respectively. The remaining maps and plots have been provided in the Appendix.

Again, we have over-plotted hard X-ray foot-point contours (red colour) in 12–25 keV band obtained from the RHESSI instrument on this power map ratio. In addition, we have also overplotted contours of the outer boundary of the sunspot penumbra (black colour) from the HMI continuum intensity image on the power map ratio. Further, we have selected the acoustically enhanced '$B1$' location in the sunspot, away from the flaring regions. The blow-up region of the '$B1$' location shows an enhancement in power ratio in patches (c.f. bottom right panel of Figure 3.2). The temporal evolution of Doppler velocity in '$B1$' location shows enhancement in p-mode velocity oscillations after the solar flare (c.f. left panel

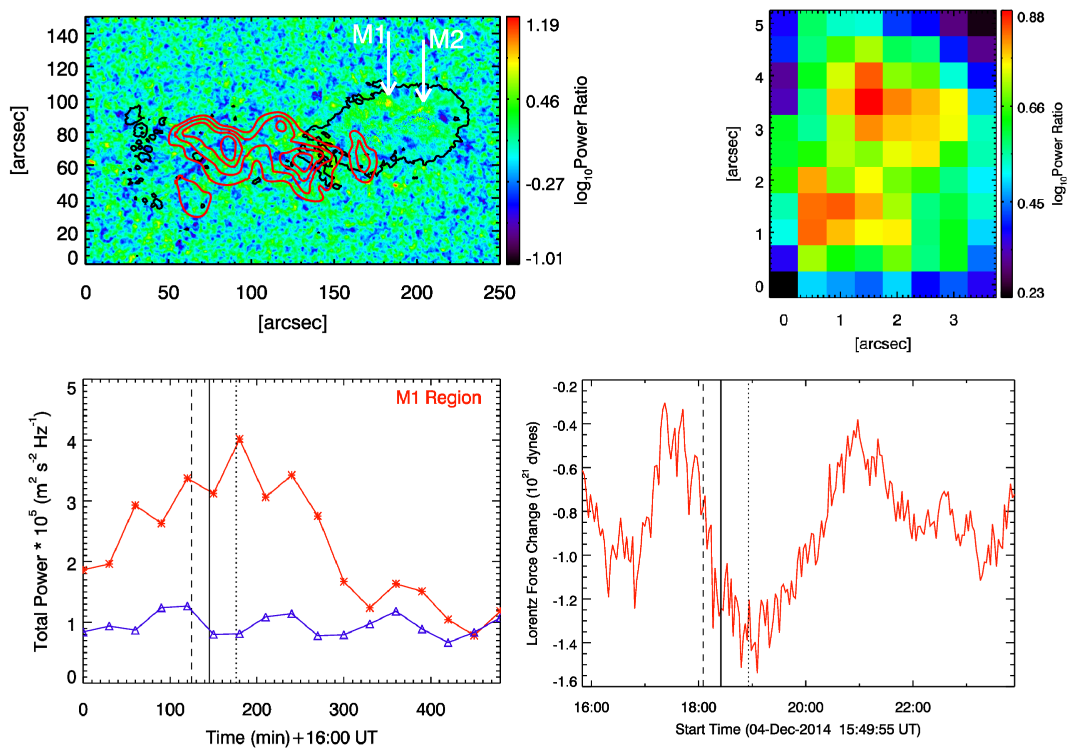

Figure 3.6: Same as Figure 3.4, but for '$M1$' location of active region NOAA 12222. It is to be noted that there is a time offset of about $\pm$ 30-minutes between the acoustic power variation and the GOES flare-time in the *bottom left panel*. The *bottom right panel* illustrates the change in radial (i.e., upward) component of Lorentz force in the aforementioned location. The remaining maps and plots have been provided in the Appendix.

of Figure 3.3). Additionally, We have examined the temporal evolution of total power integrated over the '$B1$' region as shown in red colour with asterisks in the right panel of Figure 3.3. This is done by estimating the power spectrum for a 1-hour duration and then shifting it for every 30-minutes during the observation period. Thus, it will have a time offset of about $\pm$ 30-minutes relative to the flare's onset, peak and decay time. The temporal evolution of total power over '$B1$' location demonstrates significant enhancement spanning the flare. On the other hand, the plot shown in blue colour with triangles representing the evolution of total power for an unaffected region in the same sunspot shows normal evolution over the whole duration. Similar analysis have been performed on the

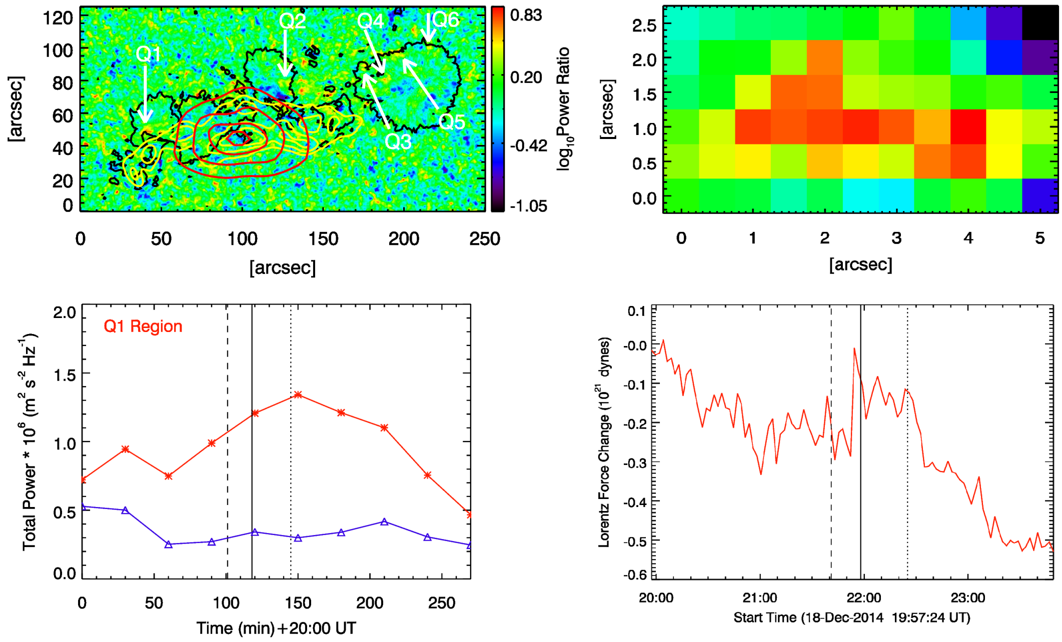

Figure 3.7: Same as Figure 3.4, but for '*Q*1' location of active region NOAA 12241. It is to be noted that there is a time offset of about ± 30-minutes between the acoustic power variation and the GOES flare-time in the *bottom left panel*. The *bottom right panel* illustrates the change in horizontal (i.e., transverse) component of Lorentz force in the aforementioned location. The remaining maps and plots have been provided in the Appendix.

active regions listed in the Table 3.1. A brief illustration of the results of other active regions are shown in the Figures 3.4, 3.5, 3.6, 3.7, 3.8, 3.9, and 3.10. We have also estimated percentage change in the total power of the regions showing acoustic enhancement in sunspots in power map ratios of the active regions considered in our analysis. All the seismic emission regions and corresponding percentage changes in total power spanning the flare are listed in Table 3.2, showing significant variations. In order to investigate the cause of seismic emissions in the sunspot regions away from flaring locations, we examine the evolution of magnetic fields and changes in the Lorentz force as suggested by Hudson et al. (2008a) and described above.

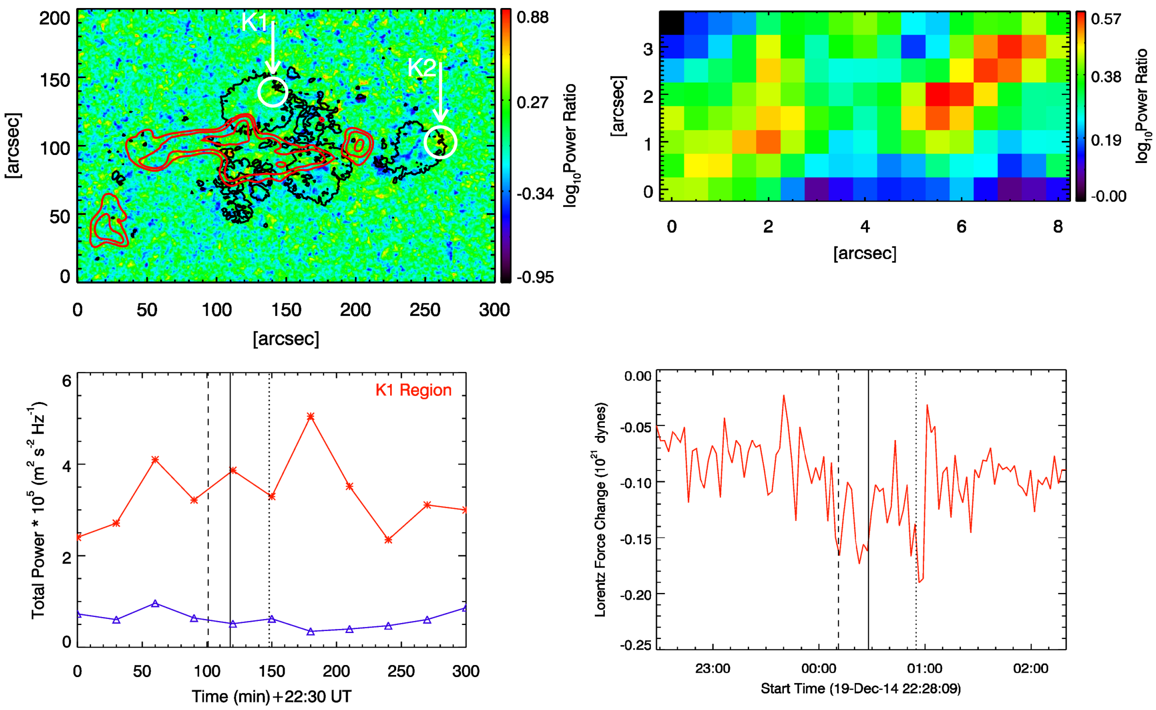

Figure 3.8: Same as Figure 3.4, but for '$K1$' location of active region NOAA 12242. It is to be noted that there is a time offset of about $\pm$ 30-minutes between the acoustic power variation and the GOES flare-time in the *bottom left panel*. The *bottom right panel* illustrates the change in horizontal (i.e., transverse) component of Lorentz force in the aforementioned location. The remaining maps and plots have been provided in the Appendix.

3.4 Changes in the photospheric magnetic fields in the sunspots during flares

We have analyzed sequences of tracked line-of-sight magnetograms at a cadence of 45 s and vector magnetograms at a cadence of 135 s obtained from the HMI instrument onboard the SDO spacecraft in order to examine the evolution of magnetic fields corresponding to the seismic emission regions in the sunspots accompanying the flares. The left panel of Figure 3.11 represents the temporal evolution of line-of-sight magnetic fields over the '$B1$' location. Here, we find that before the flare, the magnetic field is normally evolving, while there is an

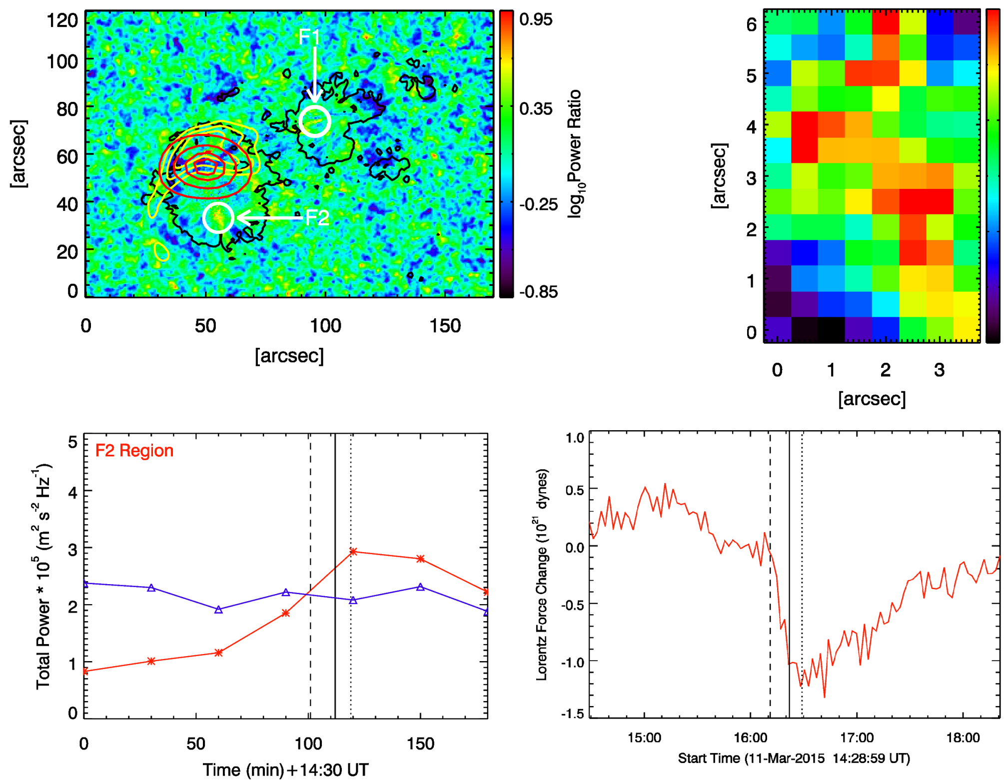

Figure 3.9: Same as Figure 3.4, but for '$F2$' location of active region NOAA 12297. It is to be noted that there is a time offset of about ± 30-minutes between the acoustic power variation and the GOES flare-time in the *bottom left panel*. The *bottom right panel* illustrates the change in horizontal (i.e., transverse) component of Lorentz force in the aforementioned location. The remaining maps and plots have been provided in the Appendix.

abrupt change in the magnetic field of the order of 80–90 Gauss within a period of 10–20 minutes spanning the flare, and after the flare, there is a normal evolution. Moreover, the temporal evolution of transverse components of vector magnetic fields over '$B1$' location depicts a step-like change of the order of 60–70 Gauss within 10–20 minutes during the flare (c.f. right panel of Figure 3.11). We have done a similar analysis of magnetogram data for the seismic emission locations for other active regions, which are mentioned in Table 3.1. The temporal evolution of magnetic fields corresponding to seismic emission locations in all active regions shows similar changes in the magnetic fields. These results have been provided

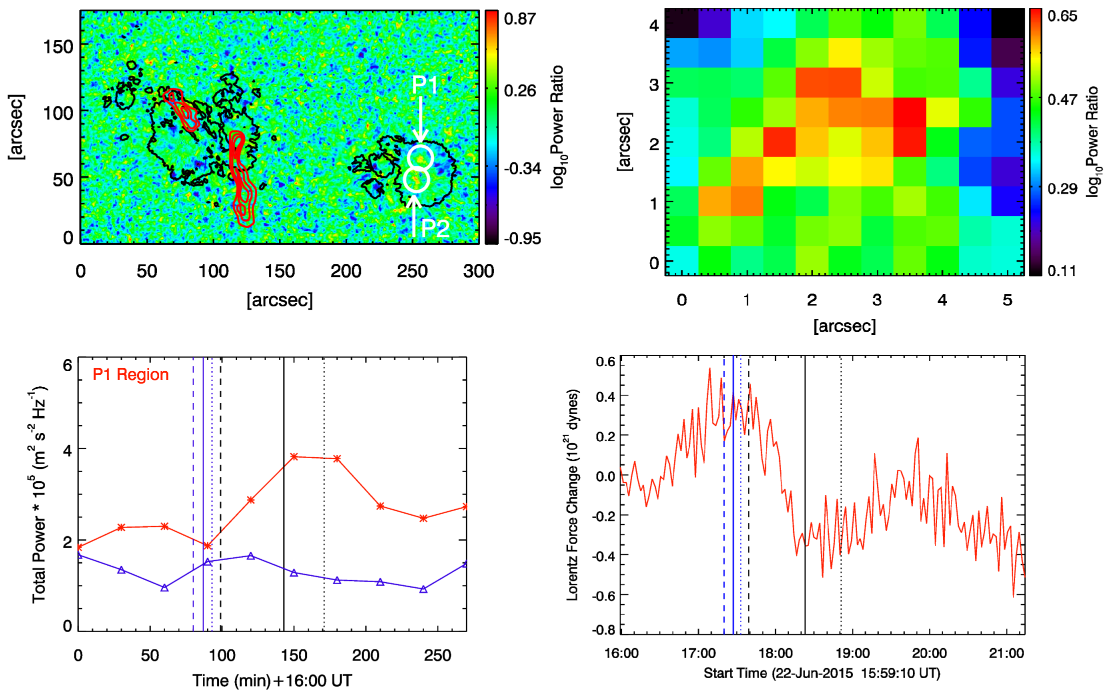

Figure 3.10: Same as Figure 3.4, but for '$P1$' location of active region NOAA 12371. It is to be noted that there is a time offset of about $\pm$ 30-minutes between the acoustic power variation and the GOES flare-time in the *bottom left panel*. The *bottom right panel* illustrates the change in radial (i.e., upward) component of Lorentz force in the aforementioned location. The dashed, solid and dotted blue and black vertical lines denote the onset, peak and decay time of C3.9 and M6.5 class flares, respectively. The remaining maps and plots have been provided in the Appendix.

in the Appendix.

As described in Section 3.1, we have examined changes in both the components of Lorentz force utilizing the Equations 3.1 and 3.2. Figure 3.12 shows the temporal evolution of change in radial and horizontal components of Lorentz force over '$B1$' location. These plots demonstrate an abrupt change in the radial component of Lorentz force and step-like change in the horizontal component of Lorentz force of the order of 10^{21} dynes within 10–20 minutes duration spanning the flare. Similar changes in the Lorentz force corresponding to the analysis of other active

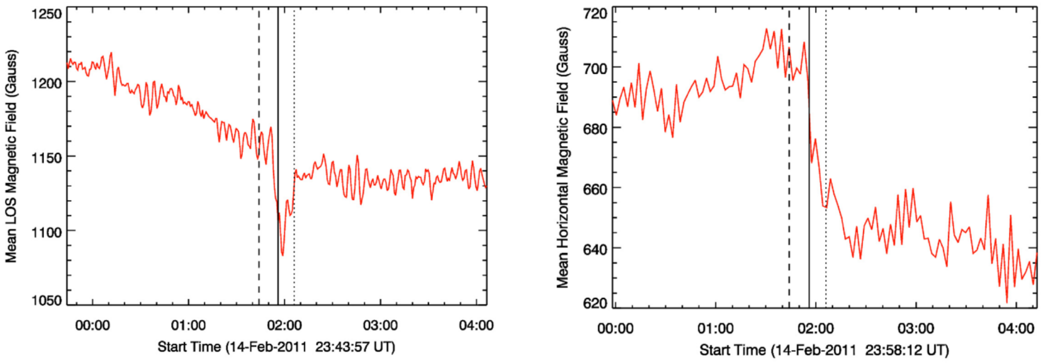

Figure 3.11: *Left panel*: Plot in red colour shows the temporal evolution of line-of-sight magnetic fields at a cadence of 45 s in the '$B1$' location of active region NOAA 11158. *Right panel*: Plot in red colour shows the temporal evolution of horizontal (i.e., transverse) component of vector magnetic fields at a cadence of 135 s in the '$B1$' location. The dashed, solid and dotted vertical lines represent the onset, peak and decay time of the flare.

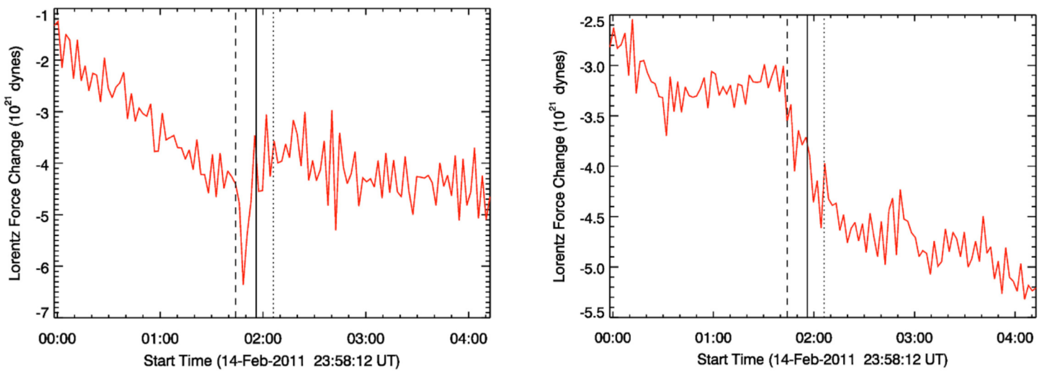

Figure 3.12: *Left panel*: Plot in red colour shows the temporal evolution of change in radial (i.e., upward) component of Lorentz force in the '$B1$' location of the active region NOAA 11158. *Right panel*: Same as shown in the left panel but for change in horizontal (i.e., transverse) component of Lorentz force in the aforementioned location. The dashed, solid and dotted vertical lines represent the onset, peak and decay time of the flare.

regions (c.f. Table 3.2) have been found, which are in close approximation to the estimates of Hudson et al. (2008b) and Fisher et al. (2012). The plots of change in Lorentz force for the other active regions are shown in Figures 3.4 to 3.10 and are also provided in the Appendix.

Table 3.2: Details of the active regions (ARs) and flare produced, identified seismic emission locations in the sunspots, observed changes in the total power and estimated changes in Lorentz force corresponding to the seismic emission locations accompanying the flares.

ARs	Flare class	Seismic emission locations	Change in power (percent)	Change in Lorentz Force (dynes)
NOAA 11158	X2.2	$B1$	≈ 113	$\approx 2.0 \times 10^{21}$
NOAA 11261	M6.0	$D1$	≈ 30	$\approx 1.0 \times 10^{21}$
	M6.0	$D2$	≈ 162	$\approx 0.5 \times 10^{21}$
NOAA 11882	M2.7, M4.4	$N1$	≈ 56	$\approx 1.5 \times 10^{21}$
	M2.7, M4.4	$N2$	≈ 123	$\approx 0.2 \times 10^{21}$
NOAA 12222	M6.1	$M1$	≈ 284	$\approx 1.0 \times 10^{21}$
	M6.1	$M2$	≈ 151	$\approx 1.0 \times 10^{21}$
NOAA 12241	M6.9	$Q1$	≈ 192	$\approx 0.3 \times 10^{21}$
	M6.9	$Q2$	≈ 100	$\approx 0.6 \times 10^{21}$
	M6.9	$Q3$	≈ 130	$\approx 0.3 \times 10^{21}$
	M6.9	$Q4$	≈ 166	$\approx 0.2 \times 10^{21}$
	M6.9	$Q5$	≈ 213	$\approx 0.3 \times 10^{21}$
	M6.9	$Q6$	≈ 101	$\approx 0.5 \times 10^{21}$
NOAA 12242	X1.8	$K1$	≈ 114	$\approx 0.1 \times 10^{21}$
	X1.8	$K2$	≈ 156	$\approx 0.4 \times 10^{21}$
NOAA 12297	X2.0	$F1$	≈ 76	$\approx 3.0 \times 10^{21}$
	X2.0	$F2$	≈ 190	$\approx 1.0 \times 10^{21}$
NOAA 12371	C3.9, M6.5	$P1$	≈ 169	$\approx 0.7 \times 10^{21}$
	C3.9, M6.5	$P2$	≈ 123	$\approx 0.3 \times 10^{21}$

3.5 Summary and Conclussions

Our results based on the detailed investigations of seismic emissions accompanying major solar flares in the sunspot away from flaring regions/hard X-rays foot points are presented in Table 3.2. The summary of our analysis, chief findings and interpretation of results are as follows:

To examine the acoustic/seismic enhancements in the sunspots from the power map analysis in the 2.5–4 mHz band for pre- and spanning flare epochs, we utilize photospheric line-of-sight Dopplergrams of the active regions. The selected seismic emission locations (c.f. Table 3.2) are within the sunspots and away from the flaring regions/hard X-ray footpoints. These regions are supposed to be free from any flare-related artefacts in the observational data. We note that the temporal evolution of Doppler velocity in the seismic emission location shows enhancement during the flare and post-flare epochs. We also observe that the temporal evolution of total power corresponding to these seismic emission locations shows enhancement in power accompanying the flare, and it tends to return to normal value after the flare. Additionally, during the flares, the identified seismic emission locations in the sunspots show a significant percentage change in the total acoustic power (c.f. Table 3.2).

In order to better understand the cause of these seismic emissions, we have analyzed magnetic fields (scalar and vector both) in the identified locations. In most cases, the temporal evolution of the magnetic fields corresponding to seismic emission locations shows abrupt and persistent changes of the order of 50–100 Gauss within a duration of 10–20 minutes during the flare and post flare epochs. The plots of the evolution of magnetic fields over the '$B1$' location are shown here (c.f. Figure 3.11), whereas those for the other identified locations are provided in the Appendix.

We have estimated the changes in Lorentz force corresponding to the seismic emission locations. Our analysis shows changes in the Lorentz force of the order of 10^{21} dynes in the seismic emission locations in the sunspots (c.f. Table 3.2). The magnitude of change in Lorentz force in the identified seismic locations as obtained in our analysis is an order lower compared to that estimated by Hudson et al. (2008b) and other previous studies. This is because our locations are away from the centers of the active regions, where the observed magnetic field changes are relatively smaller. On the other hand, those reported in earlier studies (Petrie (2012), Petrie (2014) & Sarkar and Srivastava (2018)) are primarily along the polarity inversion lines (PILs) where the magnetic field vectors become stronger and more horizontal during the flares, and hence the magnetic field changes are more pronounced. The plots of changes in the Lorentz force in '$B1$' location of active region NOAA 11158 and a brief overview of results of the analysis of the NOAA active regions 11261, 11882, 12222, 12241, 12242, 12297 and 12371 are shown in Figures 3.4 to 3.10. The remaining maps and plots of the analysis of these active regions are provided in the Appendix. We observe a good correspondence between the enhancement in acoustic power in the seismic emission locations and the impulsive and other episodic changes of similar size in the Lorentz force in these identified locations. Therefore, our detailed investigation indicates that "magnetic-jerk" is the driving force for seismic emissions in the sunspots away from flare ribbons and hard X-ray foot-point locations observed during the flares.

Further, we estimate the work done by a change in Lorentz force in the seismic emission location '$B1$' in the active region NOAA 11158 and compared this available energy budget with the acoustic emission computed in one of the kernels (5×5 pixels) in the aforementioned seismic location. It is to be noted that Hudson et al. (2008b) have computed the work done by the change in Lorentz force ($\approx 10^{22}$ dyne) as estimated from the results of Sudol and Harvey (2005) and considering the displacement of the photosphere to be $\approx$ 3 km as observed in the amplitude of seismic wave produced during an X2.6 class flare in active region NOAA 7978 (Kosovichev and Zharkova 1998). Thus, they arrived at an energy budget of $\approx 3\times10^{27}$ erg, which was found to be comparable to the energy of acoustic emissions reported in previous studies (Donea et al. 2006; Moradi et al. 2007). Following Hudson et al. (2008b), we have estimated the work done ($W = \delta F.r$) by the change in Lorentz force (δF $\approx 2\times10^{21}$ dyne) as obtained for the seismic emission location '$B1$' in displacing the photospheric plasma by, say, $r \approx 3$ km, which yields $W \approx 6\times10^{26}$ dyne cm. As mentioned earlier, we further compute the excess acoustic energy in the kernel, which could be represented by,

$\delta E = \rho.\delta p.A.d$, where '$\rho$' is the mean density of the solar photosphere ($\approx 2\times10^{-7}$ g cm^{-3}), 'δp' is the change in acoustic power in the identified kernel in the frequency band 2.5–4.0 mHz band ($\approx 5\times10^{6}$ cm^2 s^{-2}), 'A' is the area of the kernel ($\approx 3.2\times10^{16}$ cm^2), and 'd' is the depth of the kernel which could be considered approximately equal to its linear size ($\approx 1.8\times10^{8}$ cm), assuming that as much acoustic energy travels vertically from the source as in each horizontal direction. Thus, we obtain δE $\approx 5.7\times10^{24}$ erg. This is the approximate energy budget of the acoustic emission observed in the identified kernel, which is lower than the magnitude of the work done by the change in Lorentz force in this seismic location. Therefore, our results suggest that the observed seismic emission has been induced by the impulsive changes in Lorentz force in the sunspot region during the flare. We have also tried to investigate a relationship between the change in Lorentz force and percentage change in seismic power; however, we could not find any direct relation between these two parameters. This could be because, in our photospheric Doppler observations, we can observe only the trapped acoustic modes, which is some fraction of the induced seismic emission by "magnetic-jerk". The remaining fraction of these acoustic waves would propagate higher into the solar atmosphere along the magnetic field lines in the form of magnetoacoustic waves, depending on their inclination and interaction with these acoustic waves. Hence, it would be possible to conduct a detailed study of the relation between these two only if we have simultaneous Dopplergrams available for the layers above the photosphere.

These seismic emissions in the sunspots are essential to study because these enhanced locations can provide better information about the deep dynamics in the active regions during the flares. In addition, since these "magnetic-jerk" driven seismic waves can also propagate from the photosphere to higher solar atmospheric layers along the magnetic field lines in the form of magnetoacoustic waves; hence it can contribute to the heating of the solar atmosphere. Thus, considering the importance mentioned above, this study will be further carried out by using the upcoming facility of simultaneous velocity observations of the photosphere and chromosphere from the Multi-Application Solar Telescope (Mathew 2009a; Mathew et al. 2017a; Venkatakrishnan et al. 2017a) operational at the Udaipur Solar Observatory, India.

Chapter 4

Study of the Interaction of Acoustic Waves with the Small Scale Magnetic Fields in the Solar Atmosphere

4.1 Introduction

Acoustic waves are well recognized as an agent of non-thermal energy transfer that couples the lower solar atmospheric layers, primarily through their interactions with and transformations by the highly structured magnetic fields that thread these layers. These waves are generated by turbulent convection within and near the top boundary layers of the convection zone (Lighthill 1952; Stein 1967; Goldreich and Kumar 1990; Bi and Li 1998) and they resonate to form p-modes in the interior of the Sun. Propagation of these waves into the solar atmosphere is determined by the height dependent characteristic cut-off frequency ν_{ac}, which takes the value of ≈ 5.2 mHz for the quiet-Sun photosphere (Bel and Leroy 1977; Jefferies et al. 2006) as estimated from $\omega_{ac} = 2\pi\nu_{ac} = c_s/2H_\rho$, where

c_s and H_ρ are the photospheric sound speed and density scale height, respectively. Height evolution of wave phase in the chromospheric layers at frequencies larger than this cut-off of 5.2 mHz, while evanescent for smaller frequencies, is a well-observed feature in the quiet Sun. However, this condition is altered by the magnetic fields, which affect the propagation of these waves; when plasma β is low (β <1), acoustic cut-off frequency (ν_{ac}) is changed by a factor of $\cos\theta$ (Bel and Leroy 1977; McIntosh and Jefferies 2006; Cally et al. 2016), where θ is the angle between the magnetic field and the direction of gravity (which is normal to the solar surface). This fundamental effect of the inclined magnetic field has been identified as a key mechanism to tap the energetic low-frequency (*p*-mode) acoustic waves to energize the solar atmospheric layers and was termed as "magnetoacoustic portals" (Jefferies et al. 2006). A detailed look at such phenomena, including those due to other possible effects such as non-adiabaticity and magnetohydrodynamic wave modes in structured magnetic fields, has been carried out by Rajaguru et al. (2019). There have also been studies of *p*-mode waves as drivers of impulsive dynamical phenomena that supply mass and energy to the solar atmosphere (De Pontieu et al. 2004, 2005).

Moreover, the interaction of acoustic waves with the background magnetic fields lead to various types of magnetohydrodynamics wave phenomenan like mode conversion, refraction and reflection of waves, formation of high-frequency acoustic halos etc. The observation of high-frequency acoustic halos (above the acoustic cut-off frequency) surrounding the strong magnetic structures such as sunspots, pores, and plages, was first observed at the photosphere (Brown et al. 1992) as well as the chromosphere (Braun et al. 1992; Toner and Labonte 1993) in the frequency range ν = 5.5–7 mHz, in typically weak to intermediate ($B_{LOS} \approx$ 50–300 G) photospheric magnetic field regions. The observational studies of halos (Hindman and Brown 1998; Thomas and Stanchfield 2000; Jain and Haber 2002; Finsterle et al. 2004; Moretti et al. 2007; Nagashima et al. 2007) reveal several features, a summary of which has been presented in Khomenko and Collados (2009). Moreover, there is no single theoretical model which can completely explain all the observed features despite having focused efforts (Kuridze et al. 2008; Hanasoge 2008, 2009; Khomenko and Collados 2009). The majority of the work emphasizes the interaction of acoustic waves with the background magnetic fields from the photospheric to the chromospheric heights, with regards to power halos observed around the sunspots (Khomenko and Collados (2009) and references therein). However, Krijger et al. (2001), McIntosh and Judge (2001), and McIntosh et al. (2003) have investigated the oscillatons in the network and internetwork regions utilizing intensity observations of lower solar atmosphere from Transition Region and Coronal Explorer (TRACE; Handy et al. (1999)). Vecchio et al. (2009), Kontogiannis et al. (2010b), Kontogiannis et al. (2014), and Kontogiannis et al. (2016) have also investigated these oscillations using the velocity observations in the quiet-Sun and the effect of magnetic canopy. The physical characteristics of upward propagating acoustic waves are shaped by the topology of nearby magnetic fields. Numerical modeling done by Rosenthal et al. (2002) and Bogdan et al. (2003) show that the propagation of acoustic waves in the solar atmosphere is affected by the magnetic canopy and plasma $\beta \approx 1$ layer where mode conversion, transmission and reflection take place. Khomenko and Collados (2009) utilizing the numerical simulations of magnetoacoustic wave propagation in a magneto-static sunspot model suggest that halos can be caused by the additional energy injected by the high-frequency fast mode waves, which are refracted in the vicinity of the transformation layer (where Alfven speed is equal to the sound speed) in the higher atmosphere due to rapid increase of the Alfven speed. Schunker and Braun (2011) identified some new properties of acoustic halos in active regions. Rajaguru et al. (2013) further explored different properties of high-frequency acoustic halos around active regions including possible signatures of wave refraction utilizing the photospheric velocities, vector magnetograms and lower atmospheric intensity observations.

In this chapter, we discuss the leakage of low-frequency (2.5–4 mHz) acoustic waves into the higher solar atmospheric layers along small-scale inclined magnetic fields of a quiet magnetic network region exploiting the high-resolution photospheric velocity observations in Fe I 6173 Å line from the HMI/SDO and chromospheric velocity estimated from Ca II 8542 Å line scan observations obtained from the MAST. It is to be noted that *p*-mode oscillations are stochastically excited inside the convection zone beneath the solar photosphere and intermittently interact with the background magnetic fields. Therefore, here we employ wavelet analysis to detect these episodic signals propagating from the photospheric to the chromospheric heights using velocity observations. We also investigate the interaction of acoustic waves with the background magnetic fields resulting in the formation of high-frequency acoustic halos in the velocity power maps of a magnetic network region and their relation with the photospheric vector magnetic fields. In the following sections, we first describe the observational data and analysis. This is followed by the results obtained from the investigation. Finally, we present a summary of our results and conclusions in the Section 4.4.

4.2 Observational Data and Analysis Procedure

We employ two-height velocities observed over a magnetic network region in the solar disk center to investigate the propagation of *p*-mode waves and appearance of high-frequency power halos and their relation with the background magnetic fields. We use photospheric observations in Fe I 6173 Å spectral line obtained from the HMI instrument onboard the SDO spacecraft and chromospheric line-scan observations in Ca II 8542 Å spectral line from the Narrow Band Imager (NBI) with the MAST operational at the Udaipur Solar Observatory, Udaipur, India. The other details of the HMI instrument onboard SDO spacecraft and the NBI instrument with the MAST are presented in the Chapter 2 of this thesis.

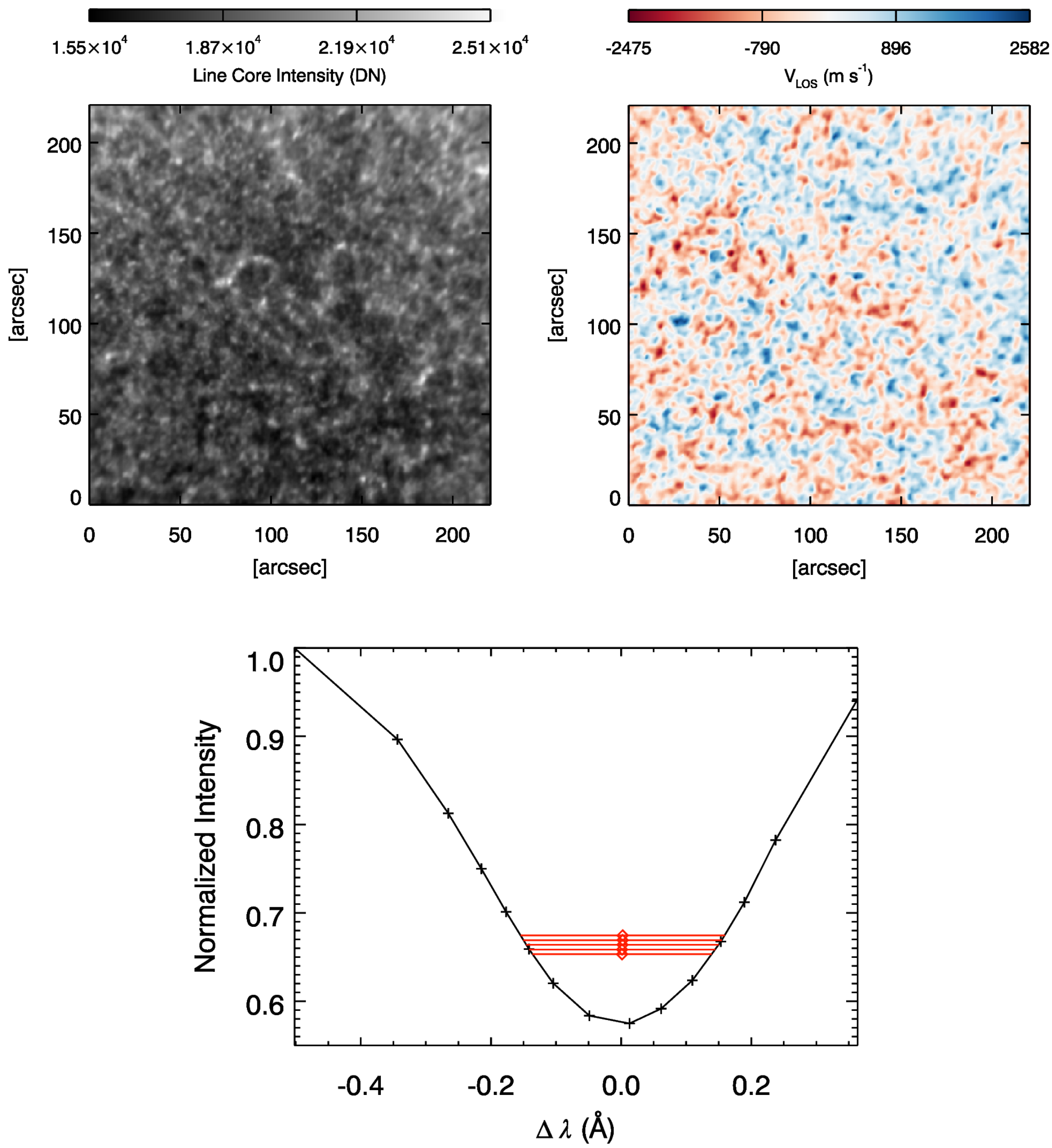

Figure 4.1: Sample maps of chromospheric Ca II 8542 Å near line-core intensity image (*top left panel*), and chromospheric Dopplergram (*top right panel*) of a quiet magnetic network region observed on May 21, 2020 from the MAST. *Bottom panel* shows a sample profile of Ca II 8542 Å spectral line with five bisector points (red diamond) used to derive the chromospheric line-of-sight Doppler velocity. This profile is constructed from the average intensity over the whole field-of-view (FOV) of the MAST (c.f., *top left panel*). The 15 wavelength positions were scanned in about 15 seconds.

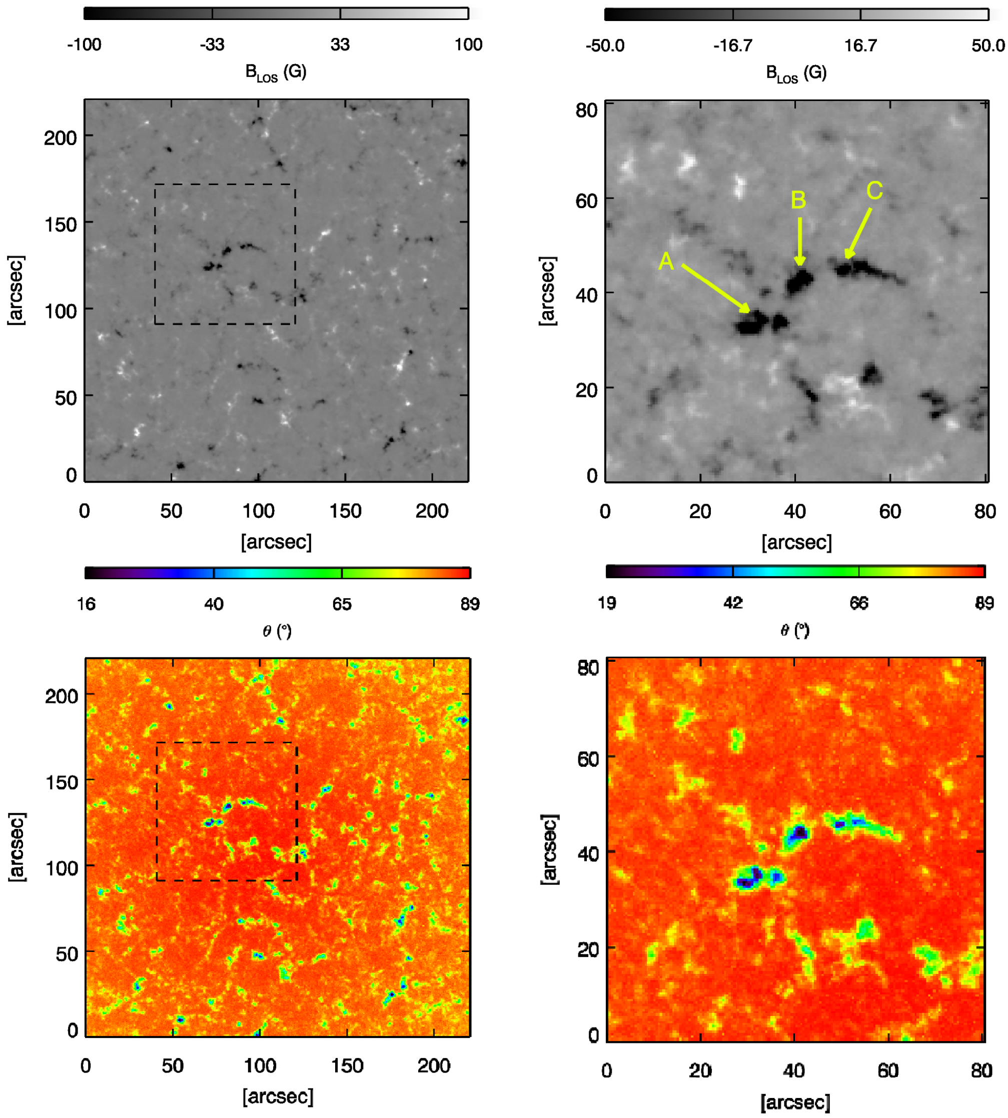

Figure 4.2: Sample maps of average of photospheric line-of-sight magnetograms over 112 minutes duration (*top left panel*), blow up region of a strong magnetic network region (*top right panel*) as denoted by black dashed square box in the top left panel. Line-of-sight magnetogram has been saturated at ±100 G and ± 50 G, respectively, to bring out the small-scale magnetic features. The yellow arrows with labels '*A*', '*B*', and '*C*', show the identified locations for the investigation of leakage of *p*-mode oscillations. *Bottom left panel*: Sample map of θ obtained from the HMI vector magnetograms and integrated over the duration of observations. Blow up region illustrating θ of a selected strong magnetic network location (*bottom right panel*) as denoted by black dashed square box in the left panel.

4.2.1 Estimation of chromospheric line-of-sight velocity from Ca II 8542 Å line scan observations obtained from the MAST

We use chromospheric Ca II 8542 Å line scan observations utilizing the capabilities of the NBI with the MAST. We have observed a magnetic network region in the disk center in the chromosphere of the Sun. The Ca II line profile has been scanned at 15 different wavelength positions starting from 8541.6 Å to 8542.48 Å within 15 s at a spatial sampling of 0.10786 arcsec per pixel on May 21, 2020, from 04:52:42 - 06:45:20 UT. The core of the line profile is scanned with close sampling intervals, whereas wings are sampled at higher wavelength spacing. Moreover, there is a delay of 19 s between two consecutive line scans. We obtained intensity images at different wavelength positions in a FOV of 220×220 arcsec^2. The seeing condition was stable during the observation. The top left panel of Figure 4.1 shows the core intensity image of the Ca II line during the starting time of the observations. We resample the Ca II intensity images to match the coarser HMI spatial scale after dark and flat corrections on the line-scan observations obtained from the NBI with the MAST. We have used the cross_corr.pro routine available in SolarSoftWare (SSW) to co-align each Ca II intensity image with the previous line scan image. The bisector method (Gray 2005) has been used to construct chromospheric Doppler velocity. In order to define the reference wavelength, we have used the bisector method on the line profile constructed from the average intensity over full FOV. The bottom panel of Figure 4.1 shows the Ca II line profile estimated by taking the average over full FOV, with bisector points of five red horizontal lines at different intensity levels in the line core shown by red diamond; the data points marked with plus represent the locations, where the line has been scanned using the NBI with the MAST. According to Cauzzi et al. (2008), the wings of the Ca II spectral line that are 0.5 – 0.7 Å away from the line centre map the middle photosphere around $h = 200 - 300$ km above the $\tau_{500} = 1$ (unity optical depth in the 500 nm continuum) whereas the line core is formed in the height range $h = 1300 - 1500$ km. Here, we have used bisector in between $\pm\, 0.14 - 0.18$ Å from the line center. The contribution in this particular wavelength range comes from a height around $h \approx 900 - 1100$ km (mean height ≈ 1000 km). By taking the average of five bisector points, we obtained a map of $\delta\lambda$, which, after a wavelength shift correction, is then used to estimate the line-of-sight velocity (V_{los}) given by the Doppler shift formula, $V_{los} = (\delta\lambda/\lambda_0)c$, where λ_0 is the rest wavelength, and c is the speed of light. For the wavelength shift corrections, we use a diffuser to take the line-scan observations, which contains only the shift originating from the incident angle (θ) of the light. Again, we utilize bisector method to construct map of $\delta\lambda_{shift}$, which is subtracted from $\delta\lambda$ maps. Following this, by combining the time taken for line-scan and delay time, we obtain chromospheric Doppler velocity at a cadence of 34 s. Further, we linearly interpolate over time to match the lower cadence (45 s) photospheric Dopplergrams from the HMI instrument. The interpolated time series (chromospheric Dopplergrams) are now simultaneous to the photospheric Dopplergrams. The top right panel of Figure 4.1 shows the chromospheric Doppler velocity constructed from the MAST observations. For aligning the photospheric and chromospheric observations, we use 20 min averages of near line core intensity of Ca II spectral line profile and line-of-sight magnetograms and identify similar features for correlation tracking to get sub-pixel accuracy.

4.2.2 Photospheric Observables from the HMI instrument

We use photospheric Dopplergrams obtained from the HMI/SDO instrument, which sample Fe I 6173 Å spectral line. Norton et al. (2006) investigated formation process of Fe I 6173 Å line profile and derive a height range of $h = 20 - 300$ km above the continuum optical depth ($\tau_c = 1$, which corresponds to z = 0) whereas line continuum is formed around $h = 20$ km above z = 0. Fleck et al.

(2011) used 3d time-dependent radiation hydrodynamic simulation to produce Fe I 6173 Å line profile and calculated Doppler velocity to compare with the observations derived with the HMI instrument. They concluded that V_{HMI} forms at a mean height of 150 km. Other photospheric observables used in this study are B_{LOS} and B = [B_x, B_y, B_z] at a cadence of 45 s and 12 min, respectively. The magnetic fields of the quiet Sun rapidly evolve over a short time duration and decay (Bellot Rubio and Orozco Suárez 2019). In order to examine the role of small scale magnetic fields on the leakage of p-mode waves and formation of high-frequency halos, we have taken the average of B_{LOS} over the whole observation duration as shown in the top left panel of Figure 4.2. The average B_{LOS} map shows only the permanent magnetic features. It has been saturated between $\pm$ 100 G to bring out small scale magnetic patches, and a strong network region is selected for final analysis, which is demarcated with a black dashed square box. The top right panel of Figure 4.2 shows the blow-up region of B_{LOS}. From the vector magnetograms, we have B_x, B_y, and B_z components of the magnetic fields. Similar to Rijs et al. (2016) and Rajaguru et al. (2019), we estimate field inclination $\tan(\gamma) = B_z/B_h$, where B_z is the radial component of the magnetic fields, and $B_h = \sqrt{B_x^2 + B_y^2}$ is horizontal magnetic fields. Field inclination with respect to the local vertical direction, θ, in degrees is then simply defined as $\theta = 90. - (180./\pi)|\gamma|$. Map of θ averaged over the whole observation period is shown in the bottom left panel of Figure 4.2, where $\theta = 0$ degrees corresponds to vertical and $\theta = 90$ degrees represents horizontal magnetic fields. It is to be noted that we have averaged B_{LOS} and θ maps over the whole observation period; this may lead to an averaging out of small scale emerging magnetic fields in between the observation period. Finally, we have selected three different locations ('A', 'B', and 'C') with magnetic field strength ($|B_{LOS}|$) greater than 30 G to study the propagation of p-mode waves from the photosphere into the chromosphere as shown with the yellow arrowheads in the blow-up region of B_{LOS} map (c.f. top right panel of Figure 4.2), which is our region of interest (ROI). In our analysis,

Table 4.1: Table represents the values of average line-of-sight magnetic fields ($<|B_{LOS}|>$), inclination ($<\theta>$) and cut-off frequency (ν_{ac}^{B}) over selected locations.

Location	$<|B_{LOS}|>$ (G)	$<\theta>$ (degree)	$\nu_{ac}^{B} = \nu_{ac} cos\theta$ (mHz)
A	42.9	64.2	2.3
B	68.7	58.1	2.7
C	38.5	62.7	2.4

we have considered rasters of 10×10 pixels in the aforementioned identified locations on which the velocity signals are averaged in order to take into account seeing related fluctuations on spatial scales. The values of $<|B_{LOS}|>$, $<\theta>$ and magnetically modified cut-off frequency $\nu_{ac}^{B} = \nu_{ac} cos\theta$ over locations 'A', 'B', and 'C' are listed in the Table 4.1.

4.3 Results

In order to detect the presence of episodic wave propagation signals, from the photosphere to the chromosphere through the intermittent interactions between p-modes and the magnetic fields, we have constructed the wavelet power spectrum of the velocity time series at the identified locations 'A', 'B', and 'C', respectively.

4.3.1 Wavelet analysis of HMI and MAST velocity data

Wavelet analysis is a powerful technique to investigate non-stationary time series or where we expect localized power variations. Thus, to determine the period of episodic signals present in the identified regions, we apply the wavelet technique (Torrence and Compo 1998) on the photospheric and chromospheric velocity time series of locations 'A', 'B', and 'C' obtained from the HMI and the MAST observations. Torrence and Compo (1998) presented a detailed description of the methodology used as the basis for this study. Here, we use the Morlet wavelet, a product of a Gaussian function and a sine wave. In the wavelet power spectrum (WPS), we limit our investigation to a region inside a “cone of influence” corresponding to the periods of less than 25 % of time series length. We have also overplotted the confidence level at 95 % as shown by a solid black line in the WPS. For the different locations on the photospheric velocities, we note the presence of significant power around the 2.5–4 mHz band in the WPS, which is associated with the p-mode oscillations (c.f. left panels of Figures 4.3).

The WPS obtained from chromospheric velocity time series at the identified locations also shows the power around 2.5–4 mHz band and above 5.5 mHz (c.f. right panel of Figures 4.3). Further, the WPS is collapsed over the whole observation time to get the Global Wavelet power spectrum (GWPS). If power is present during the whole length of observation time in WPS, it would also be reflected in the GWPS. The GWPS is similar to the commonly used Fourier power spectrum. In Figures 4.3 GWPS show the peak around 3 mHz above the confidence level in the photospheric and chromospheric locations. Importantly, we note that WPS constructed from the chromospheric velocity time series reveals the presence of significant power around the 3 mHz band at the same time as in the WPS obtained from the photospheric velocity time series (c.f. Figures 4.3). For instance, significant power is present in the WPS constructed from the HMI velocity of location ‘A’ in 0–40 minutes duration in 2.5–4 mHz band (c.f. top left panel of Figure 4.3), and in the same time interval, we notice significant power in WPS obtained from the chromospheric velocity time series (c.f. top right panel of Figure 4.3). We have found similar results in other selected locations (c.f. Figure 4.3). Moreover, the estimated acoustic cut-off frequency (ν_{ac}^{B}) (c.f. Table 4.1) in the locations mentioned above shows that the quiet-Sun photospheric acoustic cut-off frequency (ν_{ac}) is adequately reduced in the presence of inclined magnetic fields. Thus, it indicates that the power present around 2.5–4 mHz band in the chromospheric WPS is possibly associated with the leakage of the photospheric p-mode oscillations into the chromosphere.

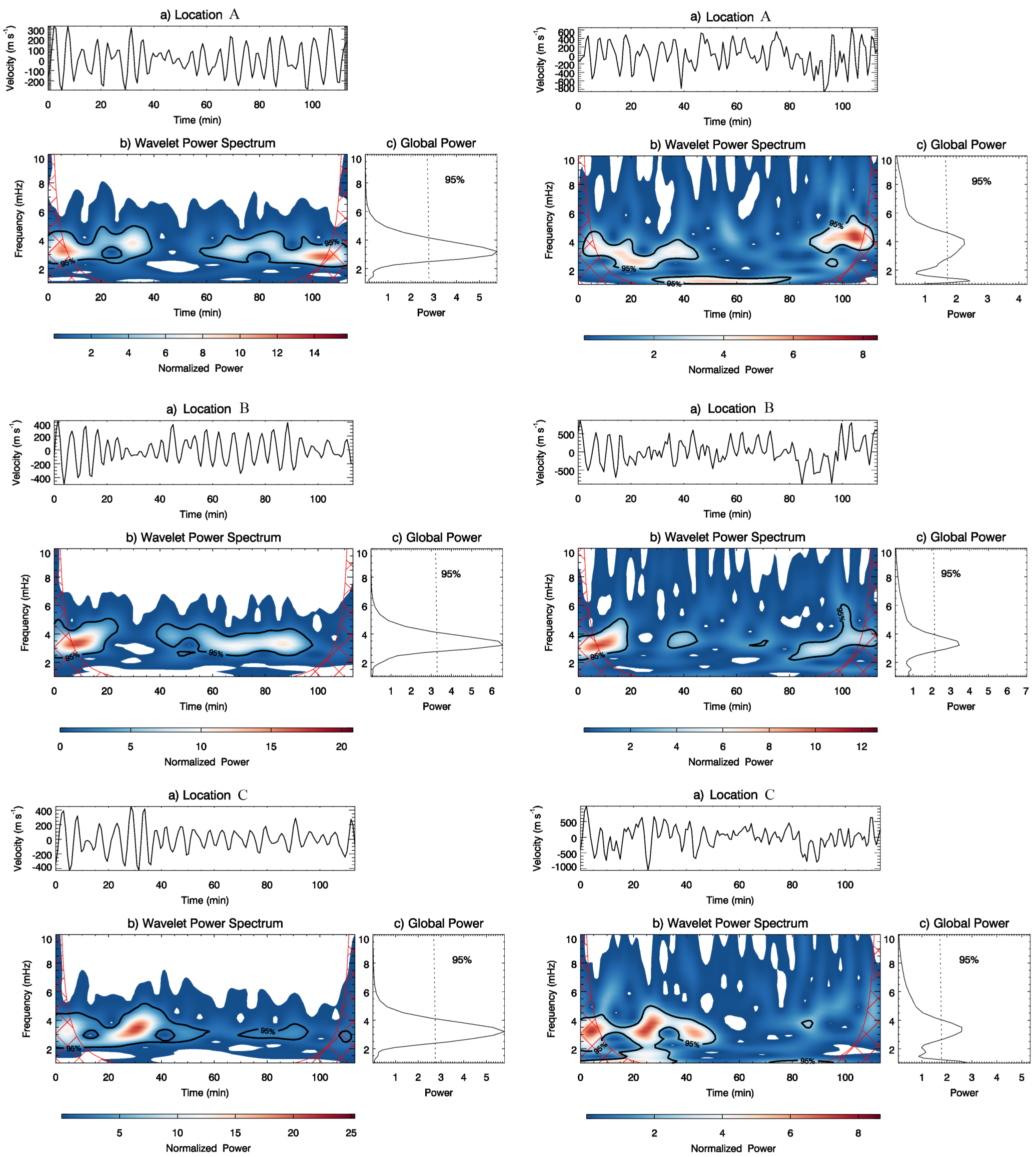

Figure 4.3: *Top left panel*: Upper panel (a) shows the temporal evolution of average velocity signals obtained from the photospheric Dopplergrams for the location 'A'. Bottom panel shows the WPS and the GWPS in (b) and (c), respectively, computed from velocity time series. In the WPS, the solid lines demonstrate regions with the 95% confidence level, and the hatched region indicates the cone of influence. The colour scale represents the wavelet power. The dotted line in GWPS shows a confidence level at 95%. *Top right panel*: Same as *top left panel*, but from chromospheric velocity for location 'A' as estimated from MAST observations. *Middle and bottom panels* are for the locations 'B' and 'C', respectively.

4.3.2 Phase and coherence spectra

Wavelet power spectra of the locations 'A', 'B', and 'C' obtained from the chromospheric Doppler velocities show one-to-one correspondence in the ν = 2.5–4 mHz band with the photospheric 2.5–4 mHz band, suggesting that chromospheric power in 2.5–4 mHz band are related to the leakage of photospheric p-mode oscillations. Hence, we estimate the phase and coherence spectra over the region of interest (ROI) (c.f. right panel of Figure 4.2). We would like to mention here that spatial maps of phase and coherence do not show clear one-to-one correlations. It might be due to the larger height difference between the photospheric and the chromospheric Dopplergrams, and also due to non-achievement of sub-pixel accuracy in the alignment of the HMI and the MAST observations due to seeing fluctuations. Hence, we have not included these maps in our results. Here, we present the average phase and coherence over the ROI. In order to estimate the phase and coherence between two signals at each pixel, we calculate the cross-spectrum of two evenly sample time series (I_1 and I_2) in the following way:

$$X_{12}(\nu) = I_1(\nu) \times I_2^*(\nu), \tag{4.1}$$

where I's are the Fourier transforms, and $*$ denotes the complex conjugate. The phase difference between two-time series is estimated from the phase of complex cross product ($X_{12}(\nu)$), where

$$\delta\phi(\nu) = tan^{-1}(Im(< X_{12}(\nu) >)R(< X_{12}(\nu) >)). \tag{4.2}$$

We are adopting the convention that positive $\delta\phi(\nu)$ means that signal 1 leads 2, i.e., a wave is propagating from lower height to upper height and vice-versa. Further, the magnitude of $X_{12}(\nu)$ is used to estimate the coherence (C), which ranges between 0 and 1, and is given by

$$C(\nu) = sqrt(|< X_{12}(\nu) > |^2/< |I_1|^2 >< |I_2|^2 >), \tag{4.3}$$

where $< . >$ denotes the average. Coherence is a measure of the linear correlation between two signals, 0 indicates no correlation and 1 means perfect correlation. In our case, we have averaged over segments of length 76 data points, which correspond to 57 minutes at a cadence of 45 seconds. We assume that this is the better way to estimate the $\delta\phi(\nu)$ and $C(\nu)$ due to the intermittent nature of the interaction of acoustic waves with the background magnetic fields (Rajaguru et al. 2019).

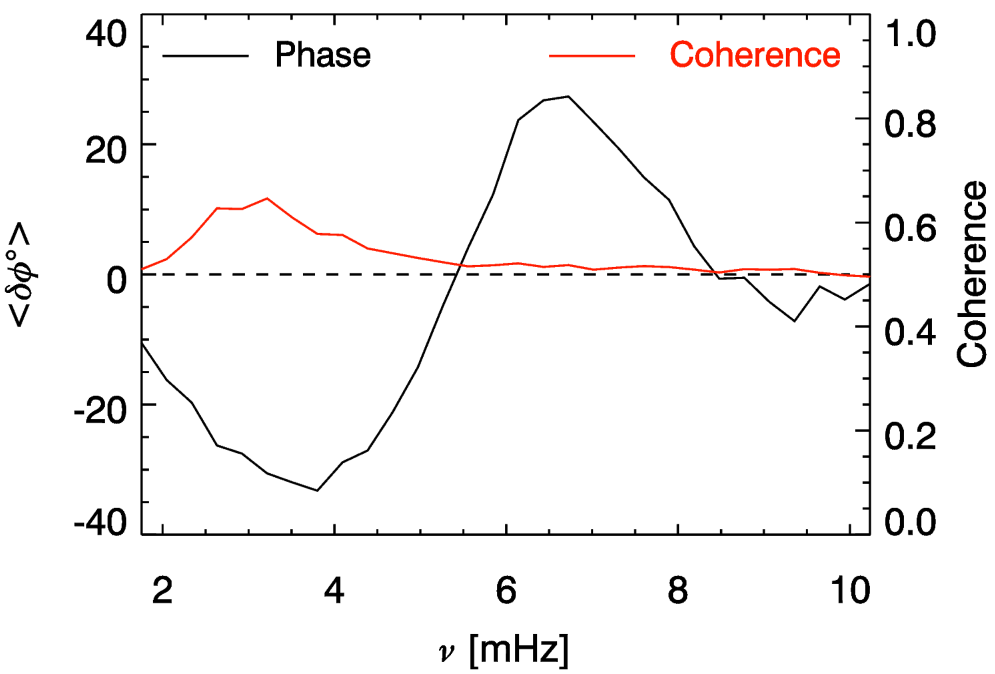

Figure 4.4: Spatially averaged phase and coherence spectra estimated from the photospheric and the chromospheric Doppler velocities over region of interest (ROI) as shown in the right panels of Figure 4.2.

Figure 4.4 shows the average phase (black) and coherence (red) spectra between the photospheric and the chromospheric Doppler velocity observations estimated over the region of interest (ROI) as shown by the black dashed square box on the left panels of Figure 4.2, and blow up region of the same is depicted in the right panels of Figure 4.2. In between the photosphere and the chromosphere, atmospheric gravity waves also contribute to the $\delta\phi$. Gravity waves show the negative phase propagation while transporting energy in the upward direction in the lower frequency band in $k - \omega$ diagram (Straus et al. 2008). In our analysis, we also find the negative $\delta\phi$ in the phase estimation from the photospheric and the chromospheric velocities. This is possibly associated with the contribution of gravity waves. However, we find that $\delta\phi$ starts increasing around $\nu = 3.5$ mHz and continue up to $\nu = 6.5$ mHz after which it decreases. The decline of $\delta\phi$ after 6 mHz is possibly associated with the steepening of the acoustic waves into the shocks. Moreover, the coherence is above 0.5 up to 6 mHz and then slightly decreases. Overall, the estimated average phase and coherence spectra from the photospheric and the chromospheric velocities indicate the propagation of p-mode waves and are qualitatively in agreement with phase travel time estimated by (Rajaguru et al. 2019) utilizing the photospheric and lower chromospheric intensity observations.

4.3.3 Photospheric and chromospheric behaviour of high-frequency acoustic halos

The propagation of acoustic waves into the higher solar atmospheric layers in magnetized regions results into different physical phenomena. One of them is the formation of high-frequency acoustic halos. To gain an insight into the interaction of acoustic waves with the background magnetic fields in the quiet magnetic network region (where the magnetic field strength is typically small), we have constructed power maps in different frequency bands, i.e. $\nu = 6$, 7, 8, and 9 mHz from photospheric and chromospheric velocities over a strong magnetic network region as indicated in the top left panel of Figure 4.2 by the black dashed square box and blow up region of the same is shown here in the top right panel. These maps are integrated over $\pm$ 0.5 mHz frequency band around the center

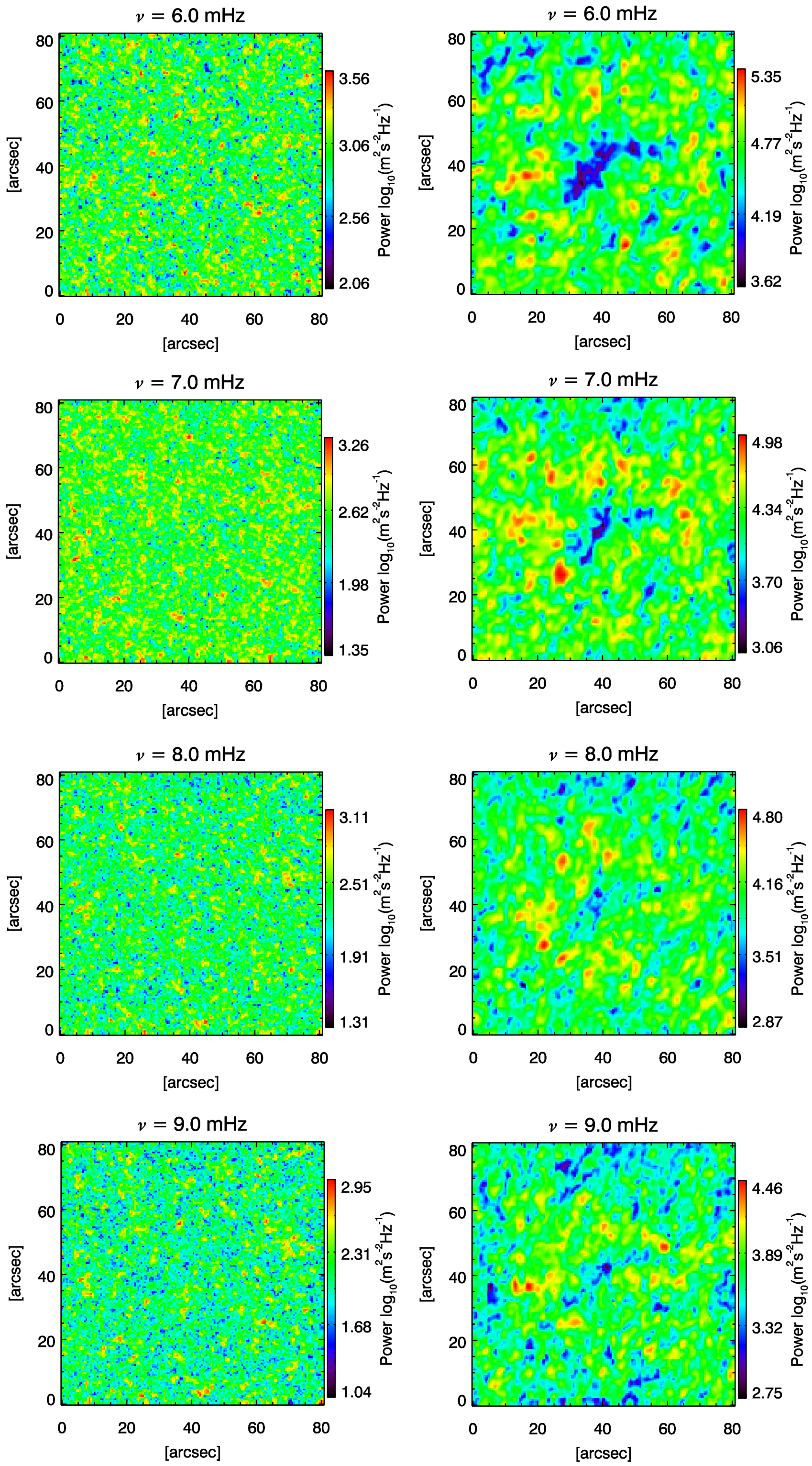

Figure 4.5: *Left panel*: Power maps at different frequencies constructed from photospheric velocity obtained from the HMI instrument over a small strong magnetic network region as shown in the right panels of Figure 4.2. *Right panel*: Same as *left panel* but from the chromospheric velocity estimated from the MAST observations.

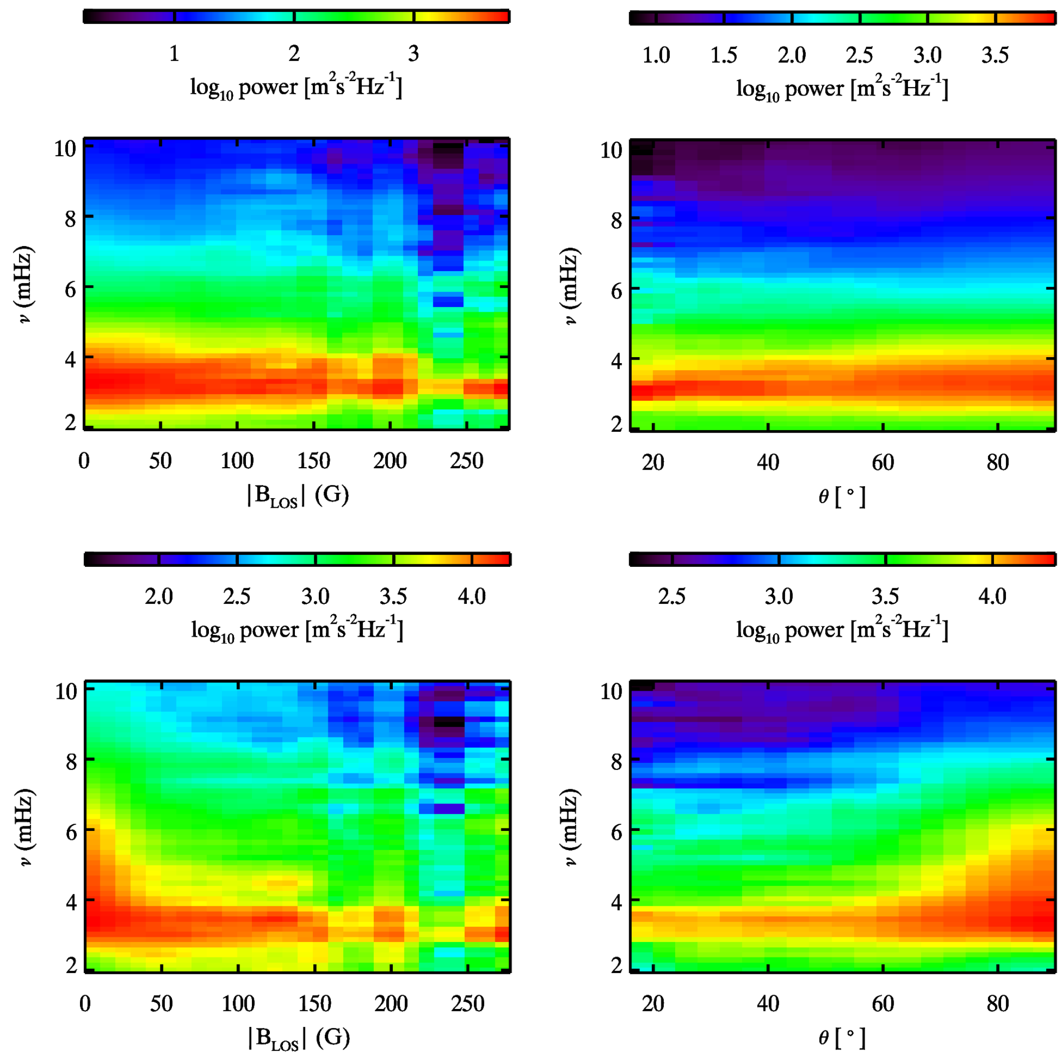

Figure 4.6: *Top panel*: Photospheric power are averaged over photospheric magnetic fields, 10 G bins in $|B_{LOS}|$ (*left hand side*) and 4 degree bins in θ (*right hand side*), respectively, over a magnetic network region as shown in the right panels of Figure 4.2. *Bottom panel*: Same as *top panel*, but estimated from the chromospheric power over the photospheric magnetic fields ($|B_{LOS}|$ and θ), respectively.

as frequency mentioned on the top of each maps (c.f. Figure 4.5). Photospheric and chromospheric power maps are shown in the left and right panels of Figure 4.5, respectively. We do not see high frequency power halos in the photospheric power maps (c.f. left panels of Figure 4.5) surrounding strong network region. However, chromospheric power maps show high frequency acoustic halos around the magnetic network region at ν = 6, 7, 8, and 9 mHz maps as shown in the right panels of Figure 4.5. In the center of strong magnetic network concentrations, chromospheric power is suppressed (c.f. right panels of Figure 4.5).In our analysis, significant enhancement in chromospheric power is observed in areas surrounding the strong magnetic network region in the form of patches. Further, in order to better understand the behaviour of high-frequency acoustic halos with respect to photospheric magnetic fields, we have averaged power over a bin of 10 G in $|B_{LOS}|$ and 4-degree bin in θ. Photospheric and chromospheric power as a function of photospheric $|B_{LOS}|$ and θ (integrated over whole observation period) are shown in the top and bottom panels of Figure 4.6, respectively. It is to be noted that Rajaguru et al. (2013) have estimated power over different ranges of magnetic field strength and inclination from the analysis of different active regions. However, we investigate halos in a quiet magnetic network region, where the magnetic field strengths are much smaller compared to active regions. Photospheric power as a function of $|B_{LOS}|$ shows that more power is present in the 2.5–4.5 mHz band in relatively small magnetic field strengths with more inclined magnetic field regions (c.f. top panels of Figure 4.6). Interestingly, chromospheric power as a function of photospheric $|B_{LOS}|$ and θ shows that excess power in the high-frequency ($\nu > 5$ mHz) band is present in the small magnetic field strength ($|B_{LOS}| < 60$ G) and more inclined magnetic field regions ($\theta > 60$ degree) (c.f. bottom panel of Figure 4.6).

4.4 Summary and Conclusions

Understanding the physics of interactions between acoustic waves and magnetic fields requires identifying and studying the observational signatures of various associated phenomena in the solar atmosphere, viz. mode conversion, refraction and reflection of waves, formation of high-frequency acoustic halos etc. Most of the work in this field emphasizes the propagation of acoustic waves and their interaction within the highly magnetized regions like sunspots and pores. However, it is not well understood as whether we also expect similar behaviour in a quiet magnetic network region. Multi-height observations covering photospheric and chromospheric layers, especially through intensity imaging observations, are widely used towards the above. Simultaneous velocity observations of both photospheric and chromospheric heights are however rare. In this chapter, in order to address some of the above questions, we have observed a quiet-Sun magnetic network region in the chromospheric Ca II 8542 Å line using the NBI/MAST instrument. Using spectral scans of this region, we have derived chromospheric Doppler velocities. Simultaneous photospheric Doppler velocity and vector magnetic field of this region was also extracted from HMI/SDO.

Here, we employ wavelet analysis technique to investigate the episodic changes in the velocity oscillations at the photospheric and the chromospheric heights using the aforementioned observations. Hence, we have estimated wavelet power spectra in the selected locations to investigate the propagation of low-frequency (2.5–4.0 mHz) acoustic waves from the solar photosphere into the chromosphere. These waves are now recognized as a potential candidate to heat the lower solar atmosphere. The investigation of Jefferies et al. (2006) utilizing the velocity observations shows that low-frequency magnetoacoustic waves can propagate into the lower solar chromosphere from the small-scale inclined magnetic field elements. Later on, the detailed investigation done by Rajaguru et al. (2019) provides evidence that a copious amount of energetic low-frequency acoustic waves channel through the small-scale inclined magnetic fields. Usually, acoustic waves of frequency less than photospheric cut-off frequency ($\nu_{ac} \approx 5.2$ mHz) are trapped below the photosphere in the quiet Sun. However, the presence of magnetic fields alters the cut-off frequency, and it is reduced by a factor of cosθ: $\nu_{ac}^{B} = \nu_{ac} cos\theta$ (Bel and Leroy 1977). In our analysis, we have found a significant reduction in the acoustic cut-off frequency, following the above formula, in the presence of inclined magnetic fields. Thus, the presence of low-frequency acoustic waves in the chromospheric wavelet power spectra is clearly associated with the leakage of photospheric oscillations. Moreover, the WPS of both heights show a clear association of chromospheric (5-min) oscillations with the underlying photospheric oscillations as evident from the appearance of low-frequency acoustic waves in chromospheric WPSs approximately at the same time as in the photospheric WPS. The investigation of the average phase over the ROI (80×80 arcsec^2, c.f. right panel of Figure 4.2) also shows the turn-on positive phase around $\nu = 3.5$ mHz and continues upto 6.5 mHz, indicating the channeling of photospheric p-mode oscillations into the chromosphere. Further, the estimated coherence is above 0.5 up to around 8 mHz, and then it decreases. Nevertheless, the bigger height difference between the two observables also reduces the coherence because these waves travel a long distance, hence losing coherency. Our results are consistent with the previous findings related to the leakage of p-mode oscillations into higher solar atmospheric layers along inclined magnetic fields (De Pontieu et al. 2004, 2005; Jefferies et al. 2006; Vecchio et al. 2007; Rajaguru et al. 2019). Moreover, our results add to the previous findings by illustration of a one-to-one correspondence between oscillatory signals present in the WPS of photospheric and the chromospheric velocity observations of a quiet-Sun magnetic network region.

As regards the formation of high frequency acoustic halos surrounding magnetic concentrations, the information gathered from the same is also important to map the thermal and magnetic structure of different heights in the solar atmosphere. The theoretical investigations of Rosenthal et al. (2002), and Bogdan et al. (2003) discussed the effect of magnetic canopy present in the solar atmosphere and plasma $\beta \approx 1$ location. The plasma $\beta \approx 1$ separates two different regions of gas and magnetic pressure dominance. Gary (2001) provided a model of plasma β variation with height in the solar atmosphere over a sunspot and a plage region. Figure 3 of Gary (2001) shows that β is ≈ 1 for plage region at a height of around 1 Mm, while for sunspot it lies below. It is suggested that mode conversion, transmission, and reflection of waves occur at $\beta \approx 1$ (Rosenthal et al. 2002; Bogdan et al. 2003; Khomenko and Collados 2006, 2009; Khomenko and Cally 2012; Nutto et al. 2012). The numerical simulation of Khomenko and Collados (2009) proposes that high-frequency fast mode waves which refract in the higher atmosphere around $\beta \approx 1$ due to rapid increase of the Alfven speed can also cause high-frequency acoustic halos around sunspots. Further, they have added that high-frequency halos should form at a distance where the refraction of fast mode acoustic wave occurs above the line formation layer, i.e., where the Alfven speed is equal to sound speed above the photosphere. Else, it would not be possible to detect these halos in observations. We have found high-frequency acoustic halos around high magnetic concentrations in a quiet magnetic network region in the chromospheric Fourier power maps (c.f. right panels of Figure 4.5). However, halos are not observed in the photospheric power maps. The absence of the acoustic halos in photospheric power maps indicate that formation height of photospheric velocity is far below the mode conversion layer i.e., $\beta \approx 1$, as suggested by Khomenko and Collados (2006) and Rajaguru et al. (2013). Therefore, the presence of halos in the chromospheric power maps is possibly associated with the injection of high frequency fast mode waves, which are refracting from the magnetic canopy and $\beta \approx 1$ layer as proposed by Khomenko and Collados (2009) and Nutto et al. (2012). This fact is also supported by a model of plasma β variation in the solar atmosphere (Gary 2001) suggesting that $\beta \approx 1$ at a height of $\approx$ 1000 km over a plage region. For a quiet magnetic network region like ours, we do expect that $\beta \approx 1$ layer might be above 1000 km. The presence of high-frequency acoustic halos in chromospheric power maps is consistent with the explanation provided by Khomenko and Collados (2006, 2009); Kontogiannis et al. (2010a); Nutto et al. (2012), and Rajaguru et al. (2013). The chromospheric power maps also show the power deficit in the high magnetic concentrations in the quiet magnetic network region. This could be associated with the energy loss due to the multiple mode transformations in a flux tube (Cally and Bogdan 1997). The analysis of chromospheric power dependence on photospheric $|B_{LOS}|$ and θ shows that high-frequency power is also significantly present in the small magnetic field strength and in nearly horizontal magnetic field regions. This finding is qualitatively in agreement with the earlier work (Schunker and Braun 2011), which suggests that the excess power in high-frequency halos is present at the more horizontal and intermediate magnetic field strength region. Our results thus show that small scale magnetic fields also have a significant effect on the propagation of acoustic waves in the solar atmosphere. It is to be noted that we have utilized high resolution photospheric and chromospheric Doppler velocities to investigate the interaction of acoustic waves with the small scale magnetic fields. We intend to follow up with similar analyzes using near-simultaneous multi-height velocity and magnetic field observations from MAST and the newer Daniel K Inouye Solar Telescope (DKIST; Rimmele et al. (2020)) along with HMI and AIA instruments on board SDO spacecraft.

Chapter 5

Investigation of Gravity Waves in the Different Magnetized Regions in the Lower Solar Atmosphere

5.1 Introduction

Waves in a compressible stratified medium in the presence of a gravitational field, like the atmosphere of the Earth or the Sun, can be driven by both compressional and buoyancy forces, resulting in a rich spectrum of acoustic-gravity waves. In the lower solar atmosphere, such waves are well recognized as an agent of non-thermal energy transfer, especially through their interactions with and transformations by the highly structured magnetic fields that thread these layers. These waves are generated by turbulent convection within and near the top boundary layers of the convection zone (Schwarzschild 1948; Lighthill 1952; Stein 1967; Goldreich and Kumar 1990) and the acoustic part of the spectrum resonate to form p-modes in the interior of the Sun. In the solar atmosphere, the behavior of waves becomes more complicated owing to the sharp fall in density and the preferred direction imposed by gravity in the fluid: the propagation characteristics are anisotropic, in general. In addition, the stratification of the atmosphere also imposes height-dependent cutoff frequencies below which gravity modified acoustic waves cannot propagate (Mihalas and Mihalas 1995b) upward of the respective heights. The internal or atmospheric gravity waves (IGWs) are generated by turbulent subsurface convection overshooting or penetrating locally into a stably stratified medium (Lighthill 1967). This is a normal response generated by a gravitationally stratified medium to any perturbations from its equilibrium position, and buoyancy acting as a restoring force. Lighthill (1967) suggested that the oscillations observed in the upper photosphere and lower chromosphere can be interpreted as gravity waves, and also that radiative damping of such gravity waves provides a mechanism of heating of the lower chromosphere. One of the interesting properties of IGWs is that, while transporting energy upward from the photosphere to higher layers, they show a characteristic downward phase propagation (Lighthill 1978). These waves play an important role in the transportation of energy and momentum and mixing the material in the regions that they propagate in. For example, the IGWs in the solar radiative interior and in other stars, despite no clear detection of their signatures at the solar surface, are theorized to play key roles in the mixing and transport of angular momentum. The investigation of Mihalas and Toomre (1981, 1982) revealed that gravity waves can reach a maximum height of 900 - 1600 km in the solar atmosphere depending upon the energy flux carried by these waves, before non-linearities lead to wave breaking. Following the above initial studies, the propagation characteristics of IGWs in the solar atmosphere have been examined utilizing velocity-velocity, intensity-intensity observations or simulations or both by a good number of authors (Deubner and Fleck 1989; Krijger et al. 2001; Rutten and Krijger 2003; Straus et al. 2008; Kneer and Bello González 2011; Nagashima et al. 2014; Vigeesh et al. 2017, 2019; Vigeesh and Roth 2020; Vigeesh et al. 2021). Krijger et al. (2001), utilizing the 1700 Å and 1600 Å intensity observations obtained from the Transition Region and Coronal Explorer (TRACE) instrument of a quiet region observed in the disk center, identified gravity waves in the $k_h - \nu$ phase diagram (c.f. Figure 24, Krijger et al. (2001)). Subsequently, Rutten and Krijger (2003) using the simultaneous UV intensities (1700 Å and 1600 Å intensity images) obtained from the TRACE also detected the gravity waves in $k_h - \nu$ phase diagram (c.f., Figure 3, Rutten and Krijger (2003)). They have also found the signature of gravity waves in the $k_h - \nu$ phase diagram constructed from white light and 1700 Å intensity signal (c.f., Figure 5, Rutten and Krijger (2003)). Using $V - V$ observations along with 3D numerical simulations, Straus et al. (2008) detected the upward propagating atmospheric gravity waves. They also estimated that the energy flux carried by gravity waves was comparable to the radiative losses of the entire chromosphere. Using observations of Fe I 5576 Å and Fe I 5434 Å lines, Kneer and Bello González (2011) studied acoustic and atmospheric gravity waves in the quiet Sun and estimated their energy transport to the chromosphere. They concluded that gravity waves also contribute in the chromospheric heating. Using multi-height velocity extractions from the Fe I 6173 Å line filtergrams provided by the HMI/SDO, Nagashima et al. (2014) also reported the presence of atmospheric gravity waves in the solar atmosphere. More recently, using realistic 3D numerical simulations of the solar atmosphere to investigate the propagation dynamics of acoustic-gravity waves, Vigeesh et al. (2017) conclude that IGWs are absent or partially reflected back into the lower layers in the presence of the magnetic fields. They further argue that the suppression is due to the coupling of IGWs to slow magnetoacoustic waves still within the high plasma-β region of the upper photosphere. Vigeesh et al. (2019) found that the propagation properties of IGWs depend on the average magnetic field strength in the upper photosphere and therefore these waves can be potential candidates for magnetic field diagnostics of these layers.

In this chapter, we present our results from a detailed study of the atmospheric gravity wave dispersion diagrams utilizing intensity observations that cover photospheric to chromospheric heights over regions of different magnetic configurations: quiet-Sun (magnetic network regions), plage, and sunspot. Additionally, we have used two-height velocities estimated within Fe I 6173 Å line over a quiet and a sunspot region. In order to investigate the propagation characteristics, we construct two-height intensity - intensity and velocity - velocity cross-spectra and study the phase and coherence signals in the wavenumber - frequency ($k_h - \nu$) dispersion diagrams and their association with background magnetic fields, utilizing long duration data-sets situated at different locations on the solar disk. We compare the derived signatures of the interaction between the IGWs and magnetic fields with those reported using numerical simulations by Vigeesh et al. (2017, 2019); Vigeesh and Roth (2020). In the following Sections, we first describe the observational data and analysis, which is followed by the results obtained in this investigation. Finally, we present discussions and conclusions in the Section 4 of this chapter.

5.2 Observational Data and Analysis Procedure

We employ two-height cross-spectra of intensities and velocities observed over regions of interest to study the height evolution of wave phases and interaction with the background magnetic fields. Intensity - intensity ($I - I$) cross spectra utilize observations obtained from the HMI instrument onboard the SDO spacecraft for the photosphere using the Fe I 6173 Å line, and from the AIA onboard the SDO for the 1700 Å and 1600 Å UV channels that sample the photosphere - chromosphere. Velocity - Velocity ($V - V$) cross spectra utilize observations obtained using photospheric Fe I 6173 Å line from IBIS instrument installed at the DST at Sacramento Peak, New Mexico, USA. We analyze observations of three large regions, identified as data set 1, 2, and 3, of widely differing magnetic configurations. These regions are also situated on the different locations on the Sun. The data set 1 covers quiet or weak magnetic patches identified by red dashed boxes and labeled as $M1$ and $M2$, a plage and sunspot areas identified by green and white dashed boxes labeled P, S, respectively (c.f., Figure 5.1). This whole region was situated near the disk centre (N16W04) and was observed on August 03, 2010. The observables include photospheric line-of-sight magnetograms (B_{LOS}), continuum intensity (I_c), UV intensities in 1700 (I_{uv1}) and 1600 (I_{uv2}) Å filters, and the data have been tracked and remapped to the same spatial and temporal sampling as the HMI observations for a duration of 14 hours; this data set has previously been used for a study of high-frequency acoustic halos by Rajaguru et al. (2013) and also for a study of the propagation of low-frequency acoustic waves into the chromosphere by Rajaguru et al. (2019). The data set 2 includes a quiet patch identified by red dashed square box labeled as Q, and two further sub-regions near the sunspot demarcated by green square boxes labeled as $R1$ and $R2$ (c.f. Figure 5.2). This large region was away from the disk centre (S20E20) and was observed on October 11, 2014, and the same observables as for data set 1 are tracked and remapped to the same spatial and temporal sampling as the HMI observations for a duration of 12 h 47 minutes. The data set 3 covers a medium size sunspot (NOAA AR10960) and surrounding quiet-Sun situated near the disk center (S07W17) on June 8, 2007, with full Stokes (I,Q,U,V) images scanned over 23 wavelength positions along the Fe I 6173.3 Å line at a spectral resolution of 25 mÅ. The spatial resolution of these observations is 0.33 arcsec (0.165 arcsec per pixel) at a temporal cadence of 47.5 s and total time duration is 3 hours 44 minutes. From these observations, Rajaguru et al. (2010) have estimated 10 bisector line-of-sight Doppler velocities starting from line core (level 0) to line wing (level 9). This IBIS dataset has been previously used for various studies (Rajaguru et al. 2010; Couvidat et al. 2012c; Zhao et al. 2022). Here, we have used two height velocities at 10% (V_{10}) and 80% (V_{80}) intensity levels in our analysis, in which V_{80} corresponds to lower height, whereas V_{10} corresponds to upper height within the Fe I 6173 Å line. The values of average of absolute line-of-sight magnetic fields integrated over whole observation period in the $M1$, $M2$, P, S, Q, $R1$, and $R2$ region are tabulated in Table 5.1.

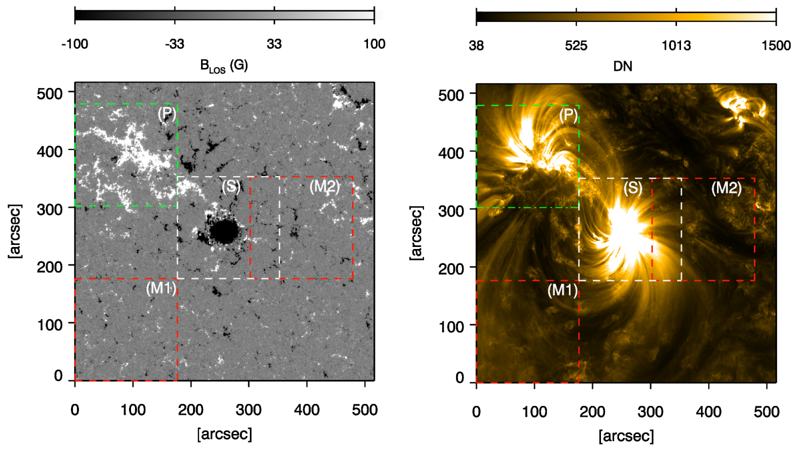

Figure 5.1: *Left panel*: HMI line-of-sight magnetic field of a large region observed on August 3, 2010 corresponding to the start time of data used in this work. The colored dashed regions mark the boundaries of sub-regions studied in this work: regions enclosed in red, white and green colored boxes mark the quiet magnetic network, sunspot and plage regions, and also denoted by $M1$, $M2$, S, P, respectively. The magnetic field grey scale has been saturated at $\pm$ 100 G to view better the small scale magnetic fields. *Right panel*: Same as left panel but from AIA 171 Å channel.

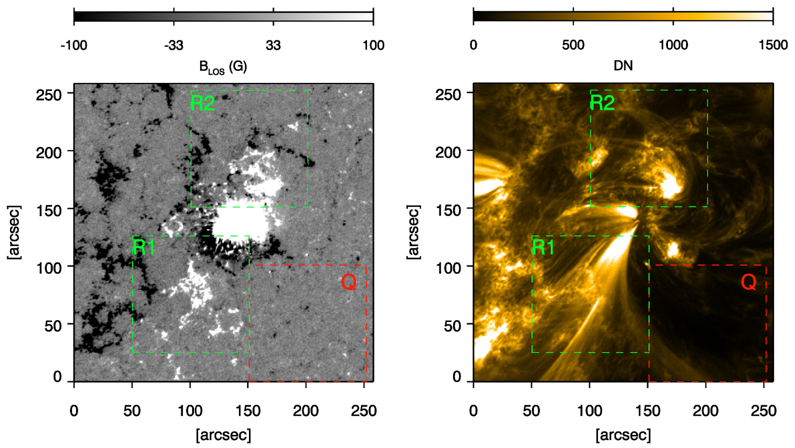

Figure 5.2: *Left panel*: HMI line-of-sight magnetic field of a large region observed on October 11, 2014 corresponding to the start time of data used in this work. The colored dashed regions mark the boundaries of sub-regions studied in this work: regions enclosed in red, and green colored boxes mark the quiet magnetic network, canopy regions, and also denoted by Q, $R1$, and $R2$, respectively. The magnetic field grey scale has been saturated at $\pm$ 100 G to view better the small scale magnetic fields. *Right panel*: Same as left panel but from AIA 171 Å channel.

Table 5.1: Table represents the values of average of absolute line-of-sight magnetic fields over selected locations.

Location	$< \lvert B_{LOS} \rvert >$ (G)
$M1$	3.3
$M2$	5.5
P	37.0
S	53.2
Q	2.7
$R1$	32.2
$R2$	32.8

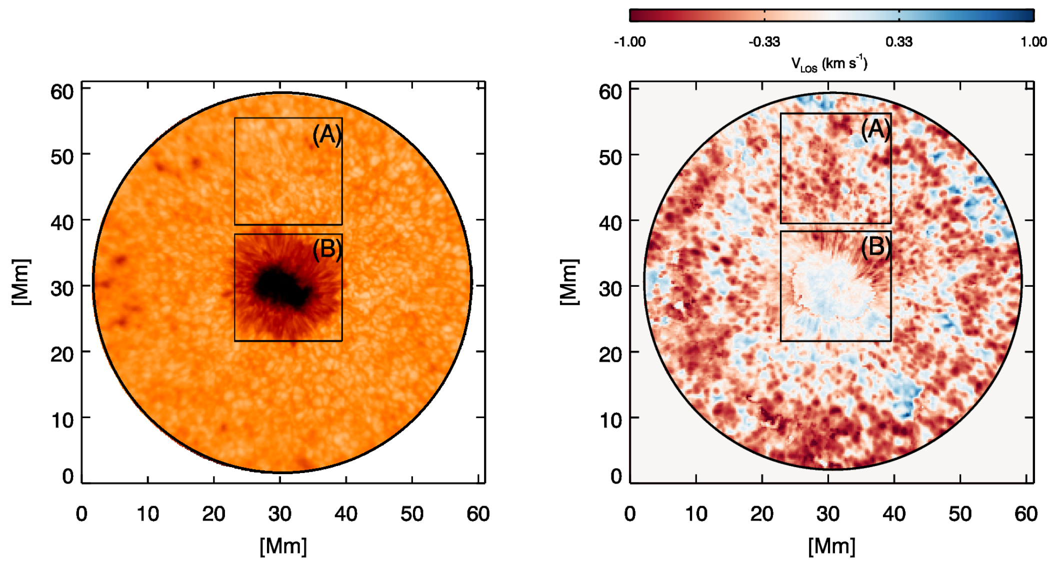

Figure 5.3: *Left panel*: A sample image of continuum intensity showing the field-of-view of the observations obtained from the IBIS/DST with a sunspot at the center. The black square regions mark the boundaries of sub-regions of a quiet and a sunspot regions studied in this work, also denoted by A, and B, respectively. *Right panel*: A sample image of line-of-sight Doppler velocity estimated by bisector method at 10% intensity levels i.e., V_{10} velocity map.

5.2.1 Height coverage of HMI and AIA observations

The HMI and AIA observables, as described above, are chosen to cover the photospheric to mid-chromospheric layers of the solar atmosphere. The formation height of Fe I 6173 Å line in the solar photosphere was investigated by Norton et al. (2006), who derived a height range of $h = 16 - 302$ km above the continuum

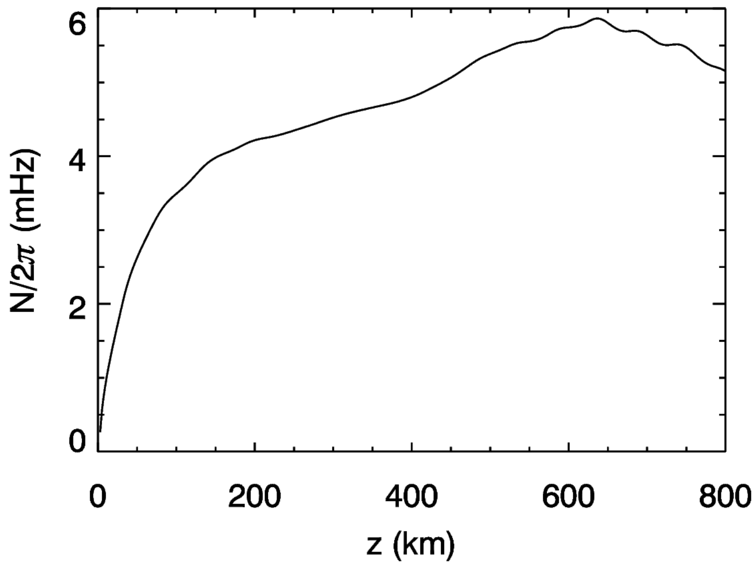

Figure 5.4: Plot shows the height evolution of Brunt-Väisälä frequency (N) for realistic solar atmosphere using the VAL-C model.

optical depth ($\tau_c = 1$, which corresponds to z = 0) in the quiet region. However, the formation height of Fe I 6173 Å line in the magnetized region i.e. umbra is lower compare to quiet region. Norton et al. (2006) utilizing the Maltby-M umbral atmosphere model reported that core of Fe I 6173 Å line form around 270 km, while wings form around 20 km above $\tau_c = 1$ continuum optical depth. Non-LTE radiation hydrodynamic simulations done by Fossum and Carlsson (2005) show that the average formation heights are of 360 and 430 km for the 1700 and 1600 Å passbands, respectively, although the 1600 Å passband has contributions from a wider height-range extending into upper chromosphere. The sub-regions $M1$, $M2$, P and S are of size 176×176 arcsec^2 from data set 1, as shown in the Figure 5.1. The total time duration of data set 1 is 14 hours, spatial sampling and temporal cadence are 0.504 arcsec per pixel and 45 s, respectively. This gives us a frequency resolution ($\Delta\nu$) of 19.8 μHz, wavenumber resolution (Δk_h) of 0.049 rad Mm^{-1} and Nyquist frequency (ν_{Ny}) of 11.11 mHz. The spatial resolution δx = 0.504 arcsec per pixel corresponds to Nyquist wavenumber ($k_{Ny} = \pi/\delta x$) of 8.55 rad Mm^{-1}. The data set 2 comprises of Q, $R1$, and $R2$ regions of 100×100 arcsec^2 as shown in the Figure 5.2. The total time duration of data set 2 is 12 h 47 minutes, spatial sampling and temporal cadence are same as data set 1. Hence, it gives us a wavenumber resolution (Δk_h) of 0.0859 rad Mm^{-1}, and frequency resolution ($\Delta\nu$) of 21.7 μHz, respectively. The data set 3 comprises of a quiet (A) and a sunspot (B) region of 24×24 arcsec^2 and are shown in the continuum intensity image and line-of-sight Doppler velocity map in the Figure 5.3. The total time duration of data set 3 is 3 hours 44 minutes, spatial sampling and temporal cadence are 0.165 arcsec per pixel and 47.5 s, respectively. This gives us a frequency resolution ($\Delta\nu$) of 74.4 μHz, wavenumber resolution (Δk_h) of 0.37 rad Mm^{-1} and Nyquist frequency (ν_{Ny}) of 10.5 mHz. The spatial resolution $\delta z =$ 0.165 arcsec per pixel corresponds to Nyquist wavenumber ($k_{Ny} = \pi/\delta z$) of 26.2 rad Mm^{-1}.

5.2.2 Cross-spectral analysis of wave propagation

We investigate the cross-spectra of IGWs utilizing different observables covering heights from photosphere (20 km) to chromosphere (430 km). We form two-height intensity - intensity ($I - I$) and velocity - velocity ($V - V$) pairs and study their cross-spectra. Cross-spectra of two observables $f_1(x, y, t)$ and $f_2(x, y, t)$ are defined as the complex-valued product of their three dimensional Fourier transforms (Vigeesh et al. 2017),

$$X_{12}(\boldsymbol{k}, \nu) = \boldsymbol{f}_1(\boldsymbol{k}, \nu)\boldsymbol{f}^*{}_2(\boldsymbol{k}, \nu), \tag{5.1}$$

where $\boldsymbol{f}$'s are the Fourier transforms, with a superscript $*$ representing the complex conjugate, $\boldsymbol{k} = \boldsymbol{k}_h = (k_x, k_y)$ is the horizontal wave vector and ν is the cyclic frequency. Here, subscripts 1 and 2 in f_1 and f_2 denote the two heights z_1 and z_2 of the observables. The phase spectrum, $\delta\phi(\boldsymbol{k}, \nu)$, that captures the phase evolution between heights of the two observables is then given by the phase of the complex cross-spectrum $X_{12}(\boldsymbol{k}, \nu)$, where

$$\delta\phi(\boldsymbol{k},\nu) = \tan^{-1}[Im(X_{12}(\boldsymbol{k},\nu))/Re(X_{12}(\boldsymbol{k},\nu))]. \tag{5.2}$$

The normalized magnitude of $X_{12}(\boldsymbol{k},\nu)$ is used to calculate the coherence,

$$C(\boldsymbol{k},\nu) = \frac{|X_{12}(\boldsymbol{k},\nu)|}{\sqrt{|\boldsymbol{f}_1|^2|\boldsymbol{f}_2|^2}}. \tag{5.3}$$

We focus on studying $\delta\phi(k_h,\nu)$ from the different $I-I$ and $V-V$ cross-spectra that trace photopsheric - chromospheric height ranges, viz. the HMI continuum I_c, AIA UV intensities I_{uv1} (1700 Å) and I_{uv2} (1600 Å) offer pairs of heights from among 20, 360, and 430 km, respectively, and two height velocities estimated within Fe I 6173 Å line formation region i.e. V_{80} and V_{10} are corresponding to within 16 – 300 km height range above $\tau = 1$. In all our analyzes, we azimuthally average the three-dimensional spectra in the $k_x - k_y$ plane to derive $k_h - \nu$ diagrams of $\delta\phi(k_h,\nu)$ and $C(k_h,\nu)$, where $k_h = \sqrt{k_x^2 + k_y^2}$.

In order to guide the analysis, we employ the well known dispersion relation, derived under the Cowling approximation that neglects perturbations in the gravitational potential for adiabatic acoustic-gravity waves in the solar interior and atmosphere (Leibacher and Stein 1981),

$$k_z^2 = \frac{(\omega^2 - \omega_{ac}^2)}{c_s^2} - \frac{(\omega^2 - N^2)}{\omega^2} k_h^2, \tag{5.4}$$

where $\omega = 2\pi\nu$ is the angular frequency, ω_{ac} is the acoustic cut-off frequency and N is the Brunt-Väisälä frequency. In a $k_h - \nu$ diagram, regions where $k_z^2 > 0$ demarcates vertically propagating acoustic-gravity waves from the evanescent ($k_z^2 < 0$) ones. In all our two-height $\delta\phi(k_h,\nu)$ that we derive from observations, we mark such propagation boundaries by evaluating the $k_z^2 = 0$ condition using the dispersion relation given by Eqn. 5.4 for the upper height using the VAL-C model of the solar chromosphere (Vernazza et al. 1981). The expressions for ω_{ac} and N applicable for a gravitationally stratified atmospheres are,

$$\omega_{ac}^2 = \frac{c_s^2}{4H_\rho^2}(1 - 2\frac{dH_\rho}{dz}), \tag{5.5}$$

and

$$N^2 = \frac{g}{H_\rho} - \frac{g^2}{c_s^2}. \tag{5.6}$$

We have two solutions for $k_z^2 = 0$, and hence two propagation boundaries separating vertically propagating waves from the evanescent ones in the $k_h - \nu$ diagram: the higher frequency boundary corresponds to the cut-off frequency for acoustic waves while the lower frequency one, typically falling lower than the f-mode frequencies, is that for the internal or atmospheric gravity waves. The locations of these boundaries in the $k_h - \nu$ plane depends on height in the atmosphere, and we typically overplot these boundaries for upper heights (solid black line) involved in each pair of variables for which the cross-spectral phases, ($\delta\phi$), coherences, (C) are derived. We also overplot the dispersion curve of the surface gravity mode (f-mode) and that of acoustic Lamb mode in each diagrams.

5.3 Results

The IGWs in the solar atmosphere have their sources in the photospheric granular convection, which overshoots into the stable layers above. As alluded to earlier, the IGWs have the characteristics of transporting energy upward while their phases propagate downward, hence exhibit negative phase in the gravity wave regime of $k_h - \nu$ cross-spectral phase diagram. We first present and analyze the phase and coherence signals in the $I - I$ cross-spectra that we obtain for the two large regions covering different magnetic configurations, viz. quiet magnetic network, plage, and sunspots, which are shown in Figures 5.1 and 5.2. Next, we analyze the phase and coherence diagrams constructed from $V - V$ pair over a quiet and a sunspot region. The wave propagation boundary corresponding to k_z^2

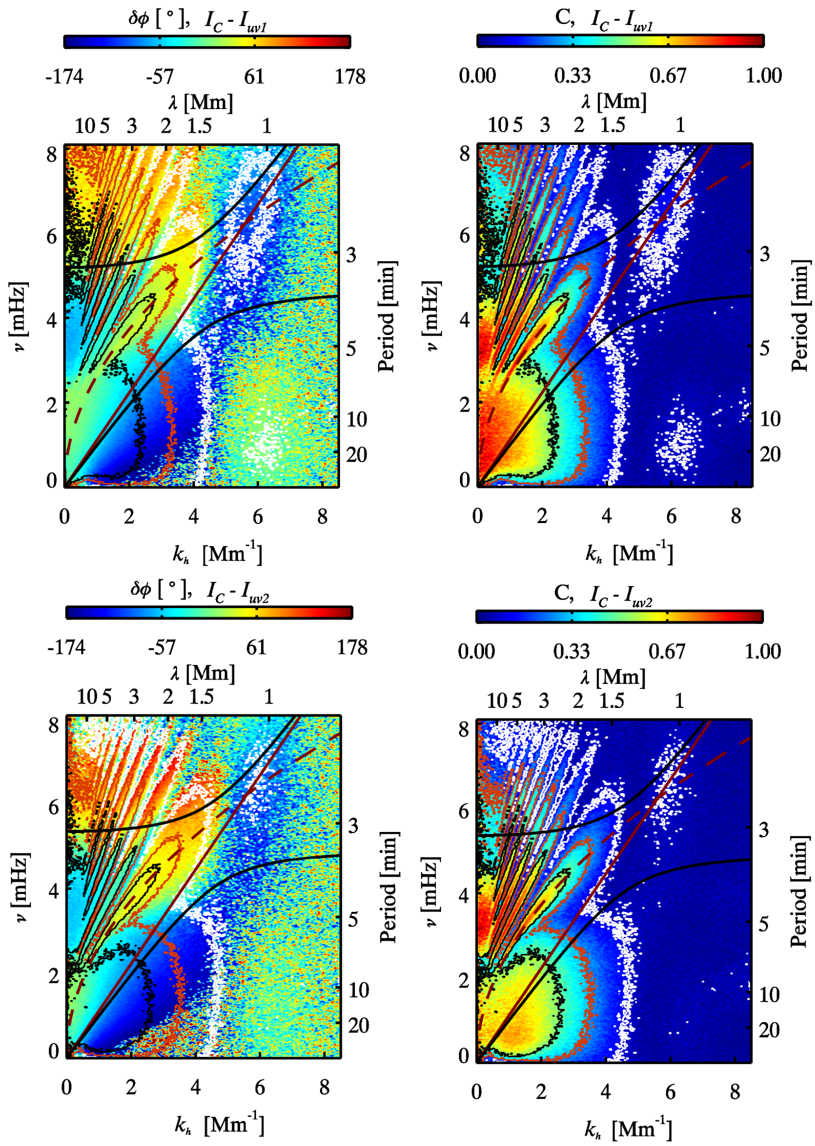

Figure 5.5: *Top panel*: Cross-spectral phase difference, $\delta\phi(k_h, \nu)$ (*top left panel*), and coherence, $\mathrm{C}(k_h, \nu)$ (*top right panel*), diagrams of $M1$ region constructed from $I_c - I_{uv1}$ pair of photospheric continuum intensity (HMI) and UV 1700 Å channel of AIA, which correspond to 20 – 360 km above z = 0 in the solar atmosphere. *Bottom panel*: same as *top panel*, but from $I_c - I_{uv2}$ pair of photospheric continuum intensity (HMI) and UV 1600 Å channel of AIA, which correspond to 20 – 430 km above z = 0 in the solar atmosphere. The solid black lines separate vertically propagating waves ($k_z^2 > 0$) from the evanescent ones ($k_z^2 < 0$) at upper height. The dashed red line is the f-mode dispersion curve and solid red line is the Lamb mode. The overplotted black, red and white contours represent the coherence at 0.5, 0.3 and 0.1 levels, respectively.

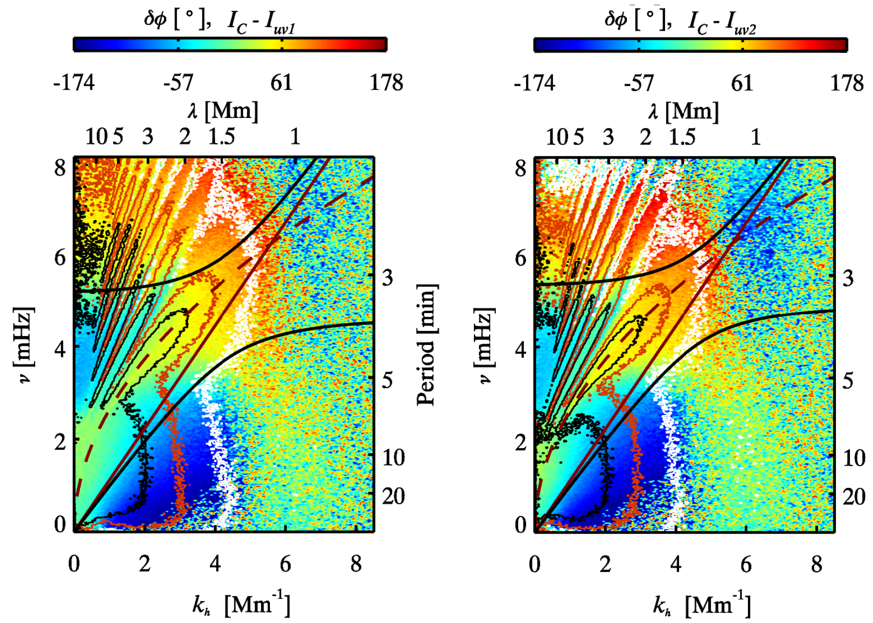

Figure 5.6: Cross-spectral phase difference, $\delta\phi(k_h, \nu)$ diagrams of $M2$ region as indicated by $M2$ in Figure 5.1 constructed from $I_c - I_{uv1}$, and $I_c - I_{uv2}$ intensity pairs, respectively. The overplotted black, red and white contours represent the coherence at 0.5, 0.3 and 0.1 levels, respectively.

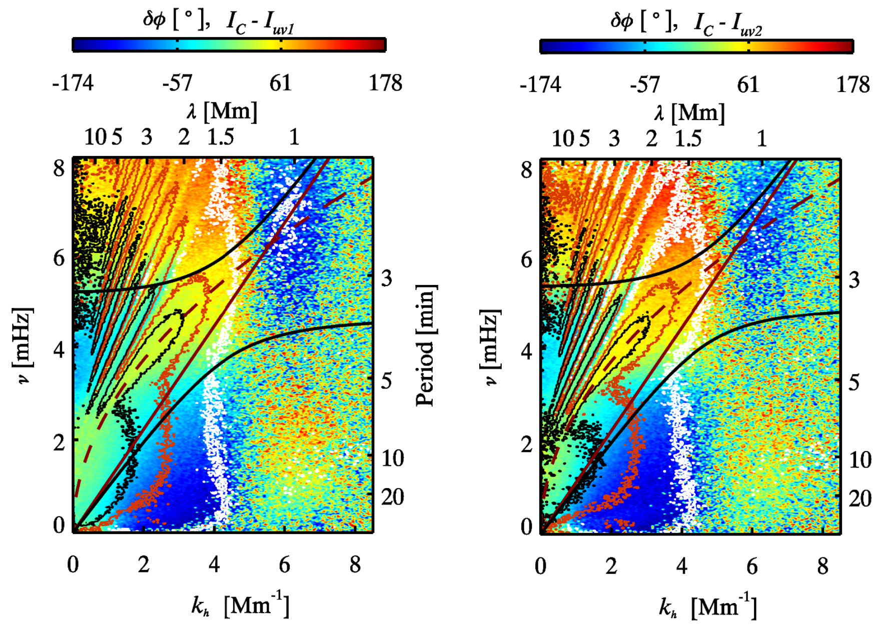

Figure 5.7: Same as Figure 5.6, but for plage region as indicated by P in Figure 5.1.

= 0 for the IGWs is set by the Brunt-Väisälä frequency, N, which is a function of height in the solar atmosphere and is given by Equation 5.6. Using the VAL-C model (Vernazza et al. 1981), we have calculated the N and plotted in Figure 5.4 as a function of height in the solar atmosphere. The $I - I$ pairs, $I_c - I_{uv1}$ and $I_c - I_{uv2}$, that we employ sample the photosphere – chromosphere region, with their mean heights in the range of 20 – 360 km, and 20 – 430 km (Fossum and Carlsson 2005). The $V - V$ pair ($V_{80} - V_{10}$), which we use in our analysis sample the formation height of Fe I 6173 Å line i.e. 16 – 300 km. Figure 5.4 shows that N increases upto a height of $\approx$ 600 km and then it starts decreasing. For the mean height of formation of intensity I_{uv2}, N approaches $\approx$ 5 mHz.

As the primary objective of this work is to study the effect of magnetic fields on the propagation of IGWs, we first discuss the phase spectra of gravity waves in the quiet magnetic network regions followed by those obtained for strongly magnetized regions and a comparison between them.

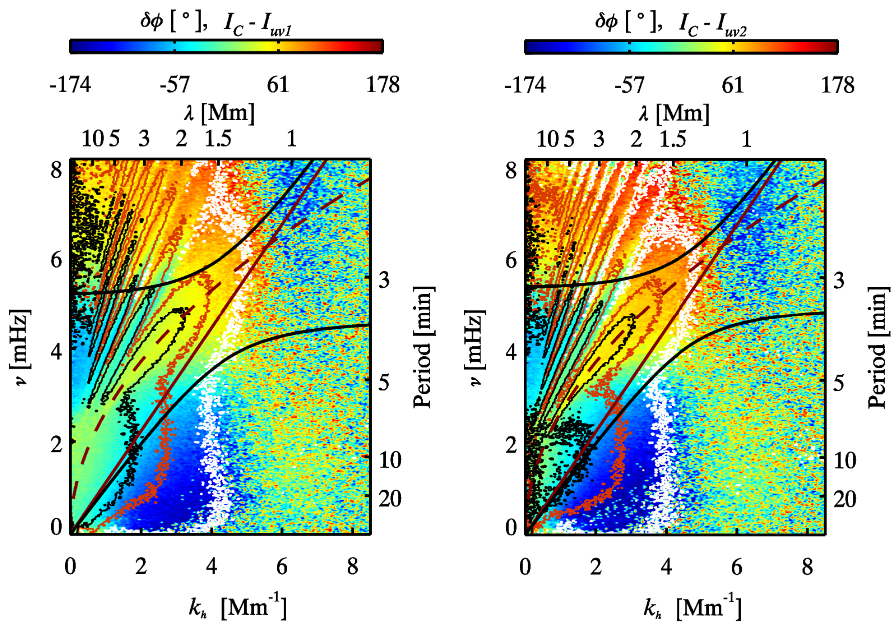

Figure 5.8: Same as Figure 5.6 but for sunspot region as indicated by symbol S in the Figure 5.1.

5.3.1 Phase spectra of IGWs in quiet-Sun regions

The region labeled as $M1$ in Figure 5.1 has the average absolute line-of-sight magnetic field of ≈ 3 G (integrated over whole observation period) and is chosen to represent the quiet-Sun. The cross-spectral phase difference, $\delta\phi$, and coherence, C, diagrams obtained for this region (from data set 1) are shown in Figure 5.5: top panels are for the $I_c - I_{uv1}$ pair, corresponding to heights of 20 – 360 km, and bottom panels are for the $I_c - I_{uv2}$ pair, corresponding to heights of 20 – 430 km. The propagation boundaries separating vertically propagating waves from the evanescent ones for the upper height of each pair are overplotted in the panels (solid black line), and these are estimated as described in the previous Section. We have also overplotted f-mode and the Lamb mode dispersion relations as red dashed and solid lines in the diagnostic diagrams, respectively. Further, we also overplot the contours of coherence at 0.5, 0.3 and 0.1 on all the phase and coherence diagrams as shown with black, red and white colors, respectively.

We mainly focus on the effect of magnetic fields on the gravity waves, and hence are not discussing the acoustic wave regimes. In the gravity wave region of the diagnostic diagrams (c.f. Figure 5.5), we observe the well known negative phase as expected for IGWs, whose phase and group velocities have opposite signs. In general, in all our $\delta\phi(k_h, \nu)$ diagrams, we observe noisy phase signals with very low coherence C for $k_h > 5.5$ Mm^{-1} and also even at lower k_h when $\nu < 0.5$ mHz. We avoid such regions in (k_h, ν) and focus only on IGWs that have $\nu \geq 0.5$ mHz and $k_h < 5.5$ Mm^{-1}. The magnitudes and wavenumber-extents of IGWs depend on the height separation in the solar atmosphere, and also vary significantly from region to region or location even in the quiet-Sun. For the quiet-Sun region $M1$, interestingly, the negative $\delta\phi(k_h, \nu)$ (c.f. left panel of Figure 5.5) corresponding to IGWs extend over, along a curved band, to the evanescent region and beyond into higher frequency domain, over the $k_h = 4.1$ – 6.8 Mm^{-1} and over ν beyond 4 mHz. This seems to indicate that there are IGW-like waves extending beyond the classical gravity wave boundary expected from the simple dispersion relation given by Equation 5.4. Interestingly, exactly such a behaviour is seen in the numerical simulations of IGWs performed by Vigeesh and Roth (2020) and as seen in their Figure 5(b), where they also synthesized spectral lines and derived $\delta\phi(k_h, \nu)$ from line core intensities of Fe 5576 Å and Fe 5434 Å lines. However, the coherence $C(k_h, \nu)$ (c.f. right panel of Figure 5.5) is less than 0.1 in $k_h = 4.1 - 5.5$ Mm^{-1} & $\nu > 3.5$ mHz, corresponding to the negative phase observed in the evanescent wave regimes of $\delta\phi$ diagrams. Hence the reality of these seemingly high frequency IGWs, in the evanescent region and beyond, is doubtful despite their resemblance to the simulation results of Vigeesh and Roth (2020). Nevertheless, there are several factors which can affect the coherence; for example, results of Vigeesh and Roth (2020) from synthetic observations show that coherence decreases as height separation increases, and we also see such behaviour for the $I_c - I_{uv2}$ intensity pair, which corresponds to higher height (h = 20 – 430 km). Additionally, they suggested that the angle of wave propagation with respect to normal for a given wave of a given frequency can also influence the coherence, which is governed by the local Brunt-Väisälä frequency (N). A wave launched at a particular frequency, without any non-linear interaction, will eventually follow a curved trajectory if the local N changes with height. Therefore, the coherency of the waves propagating between two heights for a given Fourier frequency may locally change over the field of view (Vigeesh and Roth 2020).

We show the $\delta\phi$, and C diagrams constructed from another quiet-Sun subregion labeled as Q within a larger region including a small sunspot and neighbouring plage region (c.f. data set 2 shown in Figure 5.2) in Figure 5.9. Here, we see the negative $\delta\phi(k_h, \nu)$ in the gravity wave region extending upto $k_h = 6.2$ Mm^{-1} and also exhibiting 180 deg. wrapping of phase at low frequencies (less than 0.8 mHz), especially for the higher height pair $I_c - I_{uv2}$ (c.f. bottom left panel of Figure 5.9). Comparing the two quiet-Sun regions Q and $M1$ in left panels of Figures 5.9 and 5.5, respectively, also reveals significant differences, especially in regard to the curved band of negative $\delta\phi(k_h, \nu)$ that extends through the evanescent region to higher frequencies in the $M1$ region – it is absent in the Q region. Furthermore, the $\delta\phi(k_h, \nu)$ and $C(k_h, \nu)$ diagrams of $M1$ region shows reduced extent of negative phase and coherence over k_h and ν corresponding to Q region. In the $M1$ region, negative $\delta\phi$ and contour of coherence at $C = 0.1$ is extended only upto $k_h = 4.1$ Mm^{-1} whereas Q region occupy bigger extent than $M1$, upto $k_h = 6.2$ Mm^{-1}. This is possibly associated with the fact that gravity waves propagate horizontally in the atmosphere. Thus, as we are going away from the disk center, we are detecting more and more gravity wave signal compared to that of disk center location. In addition to that, the phase and coherence diagrams constructed from $V - V$ pair i.e. $V_{80} - V_{10}$ over a quiet region (A) as depicted in the Figure 5.3 are shown in the Figure 5.12. The over plotted black and red contours represent the coherence at 0.5 and 0.3, respectively. The gravity wave regime shows the well known negative phase extending upto $k_h = 6$ Mm^{-1} with a very high coherence (c.f. Figure 5.12).

5.3.2 Phase spectra of IGWs in magnetic regions and comparisons with quiet regions

From the data of three large regions (data set 1, 2, and 3), we have several strongly magnetized regions of different configurations, P, S, $R1$, $R2$, and B and the $\delta\phi(k_h, \nu)$ and $C(k_h, \nu)$ diagrams of these regions are shown in Figures 5.7, 5.8, 5.10, 5.11, and 5.13 respectively. The region $M2$ is close to the sunspot in data set 1 and has one side of the sunspot canopy field covered within it, and it is clear from the left panels of Figure 5.6 that the extent of gravity wave regime in the $M2$ region is reduced over ν and k_h as compared to that seen in the quiet network region (c.f. Figure 5.5): while it occupies $\nu = 0 - 4$ mHz range extending up to about $k_h = 5.5$ Mm^{-1} in $M1$, the negative phases taper off and become

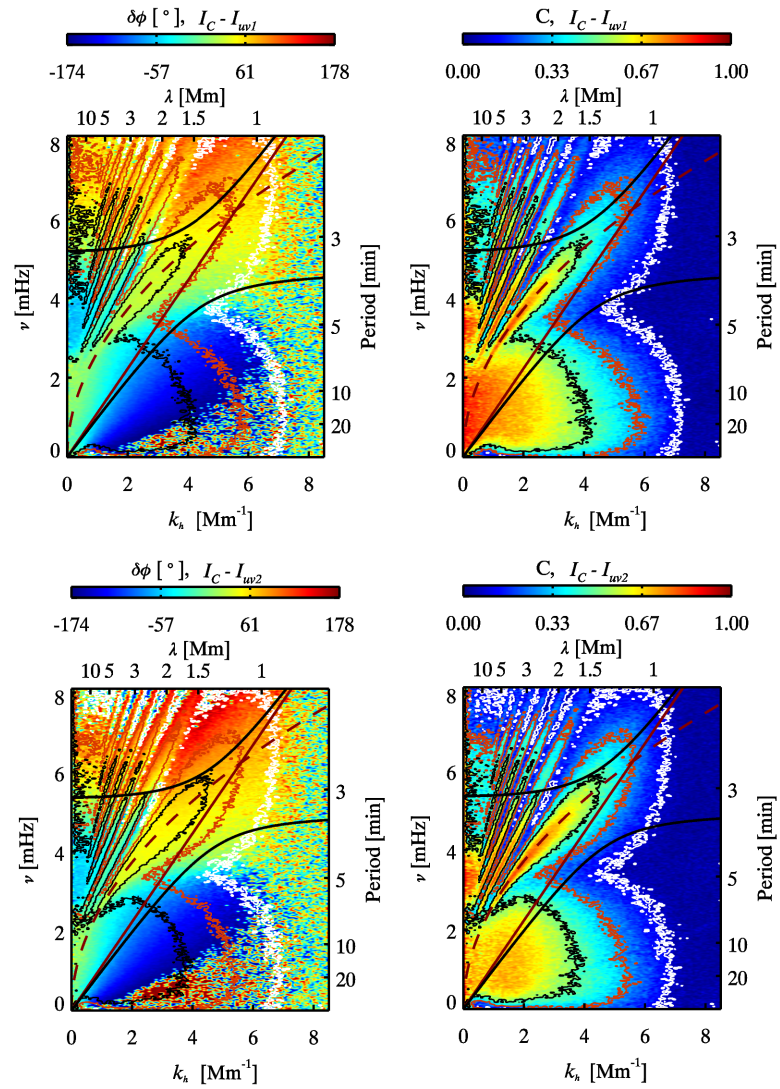

Figure 5.9: *Top panel*: Cross-spectral phase difference, $\delta\phi(k_h, \nu)$ (*top left panel*), and coherence, $\mathrm{C}(k_h, \nu)$ (*top right panel*), diagrams of Q region constructed from $I_c - I_{uv1}$ pair of photospheric continuum intensity (HMI) and UV 1700 Å channel of AIA, which correspond to 20 – 360 km above z = 0 in the solar atmosphere. *Bottom panel*: same as *top panel*, but from $I_c - I_{uv2}$ pair of photospheric continuum intensity (HMI) and UV 1600 Å channel of AIA, which correspond to 20 – 430 km above z = 0 in the solar atmosphere. The black solid lines separate vertically propagating waves ($k_z^2 > 0$) from the evanescent ones ($k_z^2 < 0$) at upper height. The dashed red line is the f-mode dispersion curve and solid red line is the Lamb mode. The over plotted black, red and white contours represent the coherence at 0.5, 0.3 and 0.1 levels, respectively.

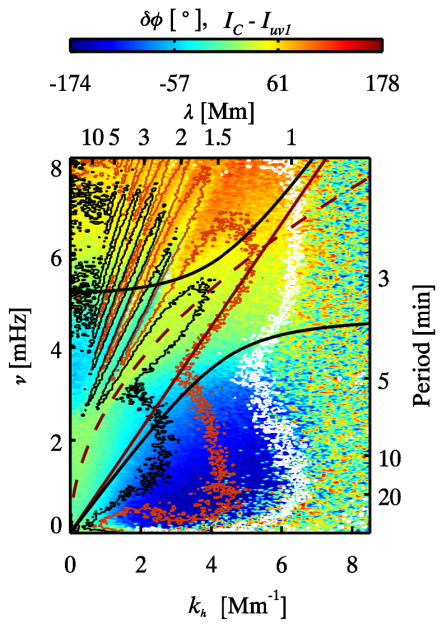

Figure 5.10: Cross-spectral phase difference, $\delta\phi(k_h, \nu)$ diagrams of $R1$ region as indicated in the Figure 5.2 constructed from $I_c - I_{uv1}$, and $I_c - I_{uv2}$ intensity pairs, respectively. The over plotted black, red and white contours represent the coherence at 0.5, 0.3 and 0.1 levels, respectively.

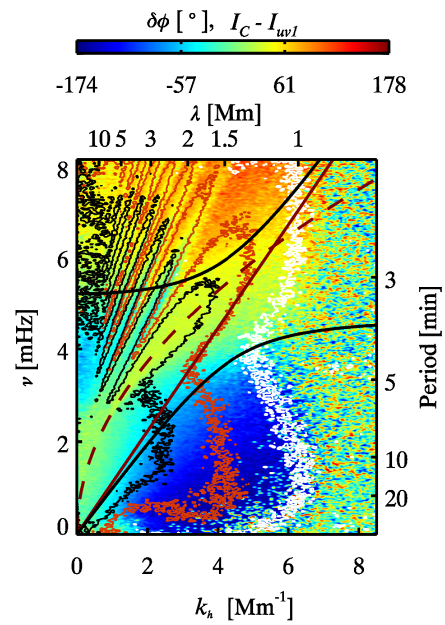

Figure 5.11: Same as Figure 5.10, but for $R2$ region as indicated in the Figure 5.2

.

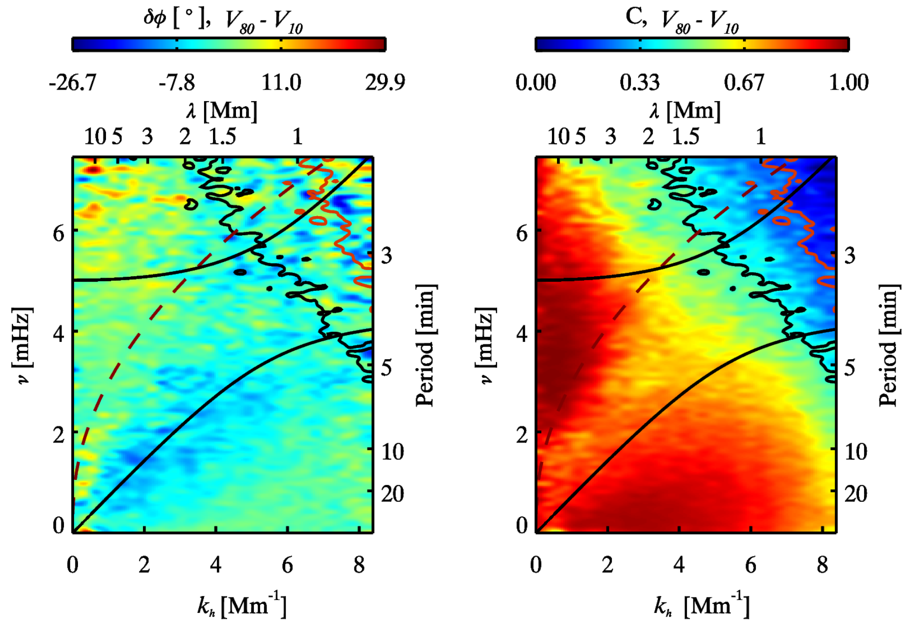

Figure 5.12: Cross-spectral phase difference, $\delta\phi(k_h, \nu)$ (*left panel*), and coherence, C(k_h, ν) (*right panel*), diagrams of A region constructed from $V_{80} - V_{10}$ velocity pair of photospheric Fe I 6173 Å line observations obtained from the IBIS instrument, which correspond to different heights within 16 – 302 km above z = 0 in the solar atmosphere. The black solid lines separate vertically propagating waves ($k_z^2 > 0$) from the evanescent ones ($k_z^2 < 0$) at upper height. The dashed red line is the f-mode dispersion curve. The overplotted black, red and white contours represent the coherence at 0.5, 0.3 and 0.1 levels, respectively.

positive over $\nu > 3$ mHz and $k_h > 4.41$ Mm^{-1}. In their synthetic observations based on numerical simulations, Vigeesh and Roth (2020) have shown that the magnitude and wavenumber-extent of negative phase reduces as the magnetic field strength increases. We observe a similar trend in the $\delta\phi$ diagrams obtained from magnetized regions. In the phase diagrams of $M2$, P and S regions negative $\delta\phi$ tapers off at approximately $\nu = 2.5$ mHz and at $k_h = 4.82$ Mm^{-1}. Similarly, the phase diagrams of $R1$, and $R2$ regions of data set 2 indicate that negative phase is extended upto only $\nu = 3.0$ mHz, and $k_h = 5.8$ Mm^{-1} (c.f. Figures 5.10, and 5.11); these two regions also exhibit reduced coherence as compared to that in the Q region. The above general reducing extents of negative $\delta\phi$ of IGWs in magnetic regions have to be compared with those observed in the quiet-Sun re-

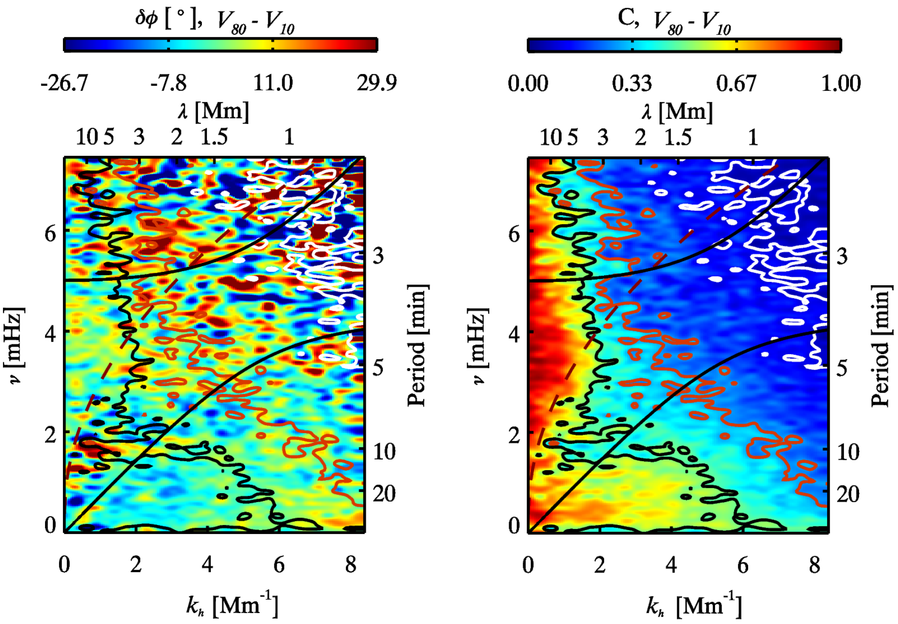

Figure 5.13: Same as Figure 5.12, but for B region as indicated in the Figure 5.3.

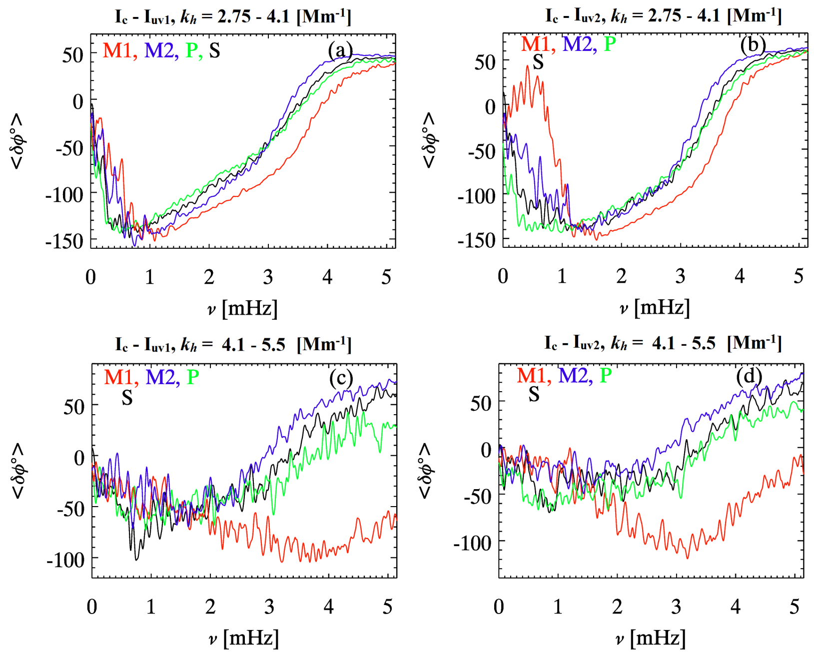

Figure 5.14: Plots indicate average phase over k_h = 2.75 – 4.1, and 4.1 – 5.5 Mm^{-1}, estimated from $I_c - I_{uv1}$, and $I_c - I_{uv2}$ intensity pairs, over $M1$, $M2$, P, and S regions, respectively, as indicated in Figure 5.1.

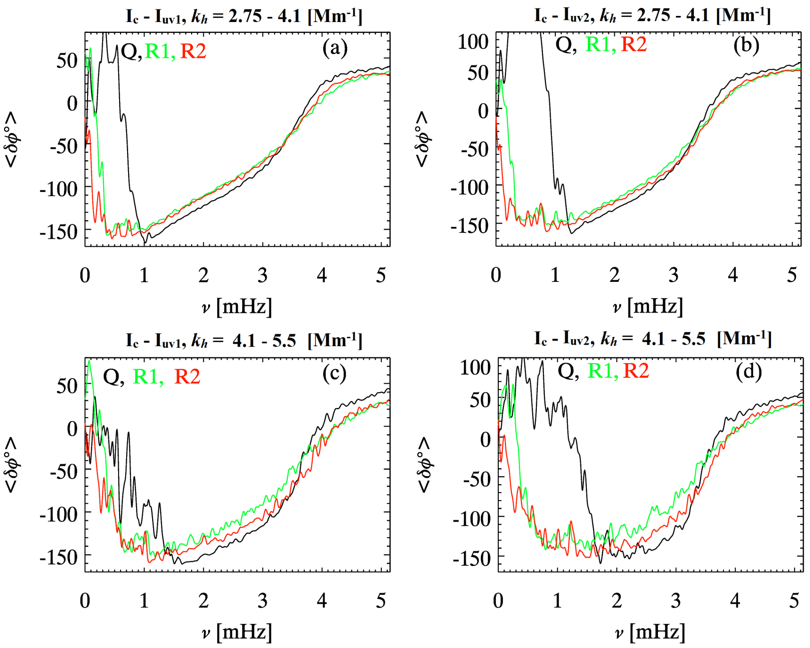

Figure 5.15: Plots indicate average phase over k_h = 2.75 – 4.1, and 4.1 – 5.5 Mm^{-1}, estimated from $I_c - I_{uv1}$, and $I_c - I_{uv2}$ intensity pairs, over Q, $R1$, and $R2$ regions, respectively, as indicated in Figure 5.2

.

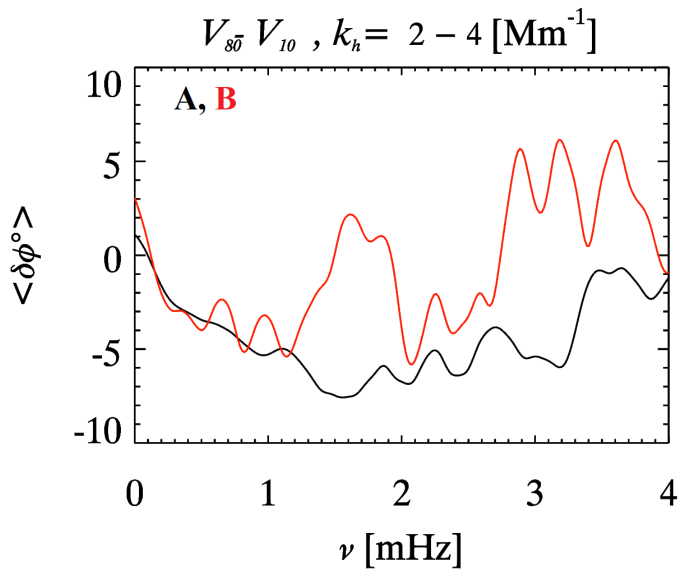

Figure 5.16: Plots indicate average phase over k_h = 2.0 – 4.0 Mm^{-1}, estimated from $V_{80} - V_{10}$ velocity-velocity pairs, over A, and B regions, respectively, as indicated in Figure 5.3.

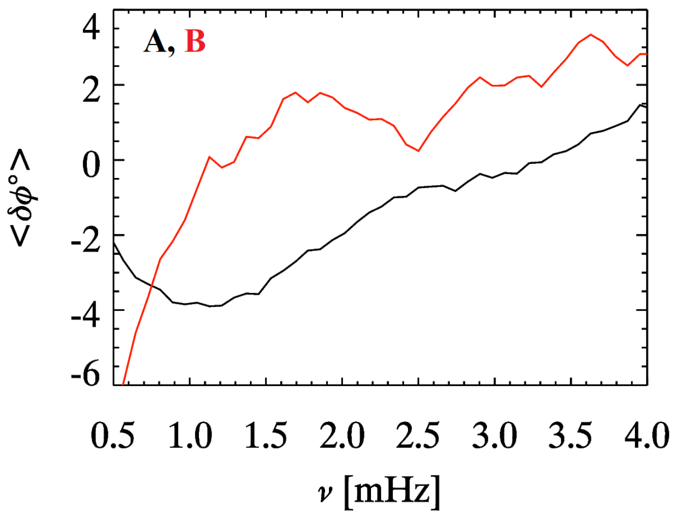

Figure 5.17: Plots indicate average phase estimated over A and B regions from $V_{80} - V_{10}$ pairs from pixel-by-pixel calculation, after removing the acoustic wave regime part above the f-mode region in the $k_h - \nu$ diagram.

gions $M1$ (c.f. Figure 5.5) and Q (c.f. Figure 5.9), where they extend upto about $\nu = 4$ mHz, and $k_h = 6.2$ Mm^{-1}. Moreover, the phase and coherence diagrams constructed from $V_{80} - V_{10}$ velocity pair from a high magnetic concentrations over a sunspot (B) are shown in the Figure 5.13. The over plotted black, red, and white contours demonstrate the regions of coherence equal to 0.5, 0.3 and 0.1, respectively. The $\delta\phi(k_h, \nu)$ and $C(k_h, \nu)$ diagrams (c.f. Figure 5.13) over B region show that phase and coherence both are reduced in the sunspot over k_h and ν extent, compared to quiet (A) region as shown in the Figure 5.12. It is very clear that, the coherence diagrams of P, S, and B regions as shown in the right panels of Figures 5.7, 5.8, and 5.13 indicate that magnetic fields also affect coherence apart from other factors as suggested by Vigeesh and Roth (2020).

In order to better understand the effect of magnetic fields on the IGWs, we have averaged $\delta\phi$ over $k_h = 2.75 - 4.1$, and $4.1 - 5.5$ Mm^{-1} in $M1$, $M2$, P, and S regions of data set 1 and have plotted them in Figure 5.14. The left panels [(a), and (c)] correspond to intensity $I_c - I_{uv1}$ pair, while right panels [(b), and (d)] are from higher height intensity $I_c - I_{uv2}$ pair. We have smoothed $< \delta\phi >$ by taking a smoothing window of 13 points to reduce the noise. In our analysis, the IGWs mostly lie up to $k_h = 7.0$ Mm^{-1}, and ν up to about 3.5 mHz. The panels (a) and (b) of Figure 5.14, in the $k_h = 2.75 - 4.1$ Mm^{-1} demonstrate that there is a change in the phase of the order of 30 – 40 and 20 – 30 degrees in the $\nu = 2.5$ – 3 mHz band estimated over $M2$, P, and S regions, respectively, corresponding to $M1$ region. Additionally, panels (c) and (d) of Figure 5.14 indicate that there is a change in the phase of the order of 30 – 70, and 80 – 100 degrees in 2.5 – 3.0 mHz as estimated for the $k_h = 4.1 - 5.5$ Mm^{-1} wavenumber over $M2$, P, and S regions with respect to $M1$ region. Interestingly, we find that the phase is reduced in large amount in the higher wavenumber (k_h = 4.1 - 5.5 Mm^{-1}) in magnetized regions compared to quiet region, almost changing from negative to positive sign as shown in the panel (c) and (d) of Figure 5.14. We also notice that the $< \delta\phi >$ estimated from $M2$ region, which is very close to the sunspot is notably affected in $k_h = 2.75 - 4.1$, and 4.1 – 5.5 Mm^{-1} (c.f. Figure 5.14) compared to $M1$ region. Similarly, the $< \delta\phi >$ vs ν plots over $k_h = 2.75 - 4.1$, and 4.1 – 5.5 Mm^{-1} for Q, $R1$, and $R2$ regions of data set 2 as shown in the Figure 5.15 also demonstrate the reduction in phase over $R1$, and $R2$ regions upto $\nu = 4.0$ mHz band. The panels (a) and (b) of Figure 5.15 for $k_h = 2.75 - 4.1$ Mm^{-1} indicate the change in $< \delta\phi >$ over $\nu = 2.5 - 3$ mHz band of the order of 10 – 20 degrees, while for panels (c) and (d) for $k_h = 4.1 - 5.5$ Mm^{-1} show the change in $< \delta\phi >$ of the order of 25 – 50 degree in 2.5 – 3 mHz band (c.f. figure 5.15) compared to Q region. The bottom panel [(c), and (d)] of Figure 5.15 also shows that phase of gravity waves are reduced in larger amount in the higher wavenumber $k_h = 4.1$ – 5.5 Mm^{-1} as compared to quiet region (Q). Further, it is to be noted that $M2$, and $R1$ regions cover a large amount of looping magnetic fields, hence they are largely horizontal, as can be seen in the AIA 171 Å passband (c.f. right panel of Figures 5.1 and 5.2), respectively. We also find that suppression of phase is more in these regions ($M2$, and $R1$) as compared to others.

Additionally, we also estimate and plot $< \delta\phi >$ over quiet (A) and sunspot (B) region over k_h = 2 – 4 Mm^{-1} from $V_{80} - V_{10}$ velocity pair as shown in the Figure 5.16. It indicates that $< \delta\phi >$ is positive in the sunspot (B) region, while it is negative over the quiet (A) region around ν = 1.5 mHz. Further, we also estimate $< \delta\phi >$ over A and B region from pixel by pixel calculation after removing the acoustic wave regime part from $k_h - \nu$ diagram i.e., above the f-mode in the diagnostic diagram utilizing a 3D FFT filter. The $< \delta\phi >$ over A and B regions are shown in the Figure 5.17, which shows that there is a change in sign of the $< \delta\phi >$ estimated over sunspot (B) region compared to the quiet (A) region. It is to be noted that we have used velocity V_{80} and V_{10} estimated within the Fe I 6173 Å line at two heights. The formation height of Fe I 6173 Å line is different in the quiet and the magnetized region i.e., sunspot. In the quiet region, Fe I line forms within h = 16 – 300 km, whereas in umbra it is around h = 20 – 270 km above the τ = 1. Hence, we estimate the percentage change in the formation heights of quiet and sunspot regions. There is an approximately 12% change in the formation height of Fe I line in a sunspot with respect to a quiet region. However, the percentage change in the $< \delta\phi >$ in the sunspot as estimated from Figure 5.17 at ν = 1.5 mHz is found to be of the order of 114.3% as compared to the quiet region. Nevertheless, the $< \delta\phi >$ estimated over a quiet (A) and a sunspot (B) region from Figure 5.16 in ν = 1.5–3.5 mHz and k_h = 2–4 Mm^{-1} are of the order of -5.35 degree and 0.255 degree, respectively. Thus, such a change in $< \delta\phi >$ and change in sign is not possibly due to the lowering in the formation height of Fe I 6173 Å line in sunspot, indicating that it is due to the suppression or reflection of gravity waves in the magnetized regions. The formation height of I_{uv1} and I_{uv2} might be decreased in the magnetized regions. However, the observed percentage change in phase over the highly magnetized regions are more than 50%–100% at ν = 2.0 – 2.5 mHz, and change in sign between quiet and magnetic regions near 3 mHz (c.f. Figure 5.14) and their similarities with the phase analysis of $V - V$ spectrum indicate that it is not due to change in formation heights of observables used but due to the direct effect of magnetic fields on their propagation. This is because a sign change in phase shifts between quiet and magnetic regions cannot come from the formation height differences, however big they are.

5.4 Summary and Conclusions

The IGWs in the solar atmosphere, which are thought to be generated by the turbulent convection penetrating locally into a stably stratified medium are believed to dissipate their energy by radiative damping just above the solar surface (Lighthill 1967). Earlier studies (Mihalas and Toomre 1981, 1982) suggest that IGWs can reach upto the middle chromosphere, before breaking of these waves due to nonlinearities resulting in a complete dissipation. Recent simulations (Vigeesh et al. 2017, 2019; Vigeesh and Roth 2020) have shown that these waves are still present in the higher atmosphere, where the radiative damping time scale is high, and that magnetic fields suppress or scatter IGWs in the solar atmosphere.

Our investigations of $k_h - \nu$ phases and coherences of IGWs within the photosphere and from photospheric to lower chromospheric height ranges over a varied levels of background magnetic fields and their configurations have brought out clear signatures of reduced extent of negative phase and a change of sign in phases in the gravity wave regime due to the magnetic fields as compared to quiet regions – as demonstrated in Figures 5.5, 5.6, 5.7, 5.8, 5.9, 5.10, 5.11. The above findings from the intensity observations are also strengthened from the phase and coherence diagrams estimated from velocity - velocity cross-spectral pairs observed over a quiet (A) and a sunspot (B) region (c.f. Figure 5.12, and 5.13). Further, from the comparison of average phase in $k_h = 2.75 - 4.1$, and $4.1 - 5.5$ Mm^{-1} over quiet and magnetic regions from data set 1 and 2 as shown in the Figures 5.14, and

5.15, we find that the phase of IGWs are much reduced in the magnetized regions. Moreover, this effect is more prominent in the higher wavenumber regions i.e., for the waves of lower wavelength ($\lambda = 2.175 - 2.75$ Mm) suggesting that these gravity waves are scattered by the background magnetic fields or partially reflecting from the upper atmospheric layers leading to positive phase in the gravity wave regime. The average phase estimated from $V - V$ pair in $k_h = 2 - 4$ Mm^{-1} (c.f. Figure 5.16) also indicates change in sign at $\nu = 1.5$ mHz in sunspot (B) compare to quiet (A) region. Moreover, the average phase estimated from $V - V$ pair from pixel-by-pixel analysis over quiet (A) and sunspot (B) regions also demonstrate the change in sign of the phase. Furthermore, the observed percentage change in phase in the sunspot (B) compared to quiet (A) region is much higher than percentage change in the formation height of Fe I line in sunspot as compared to quiet region, strongly favoring the suppression or reflection of gravity waves in the high magnetized region i.e., sunspot (c.f. Figur 5.17). Importantly, we also find the reduction in coherence in the presence of background magnetic fields. Previously, Straus et al. (2008) showed that the *rms* wave velocity fluctuations due to IGWs were suppressed at locations of magnetic flux. Here, we have provided further observational evidences in the $k_h - \nu$ diagrams for the suppression or scattering or partial reflection of gravity waves in the magnetized regions of the solar atmosphere.

In general, the above nature of IGWs in magnetized regions are broadly consistent with the simulation results of Vigeesh et al. (2017) and Vigeesh et al. (2019); Vigeesh and Roth (2020) suggesting the suppression of gravity waves in magnetized regions. This led to identifying our reported differences between quiet and magnetic regions as observational evidences for such influences of magnetic fields. We anticipate that several of our analyzes and findings reported here will be examined in more detail in the near future containing bigger FOV, involving coordinated simultaneous multi-height observations of photosphere and chromosphere utilizing Dopplergrams data from the newer Daniel K Inouye Solar Telescope (DKIST; Rimmele et al. (2020)) (National Solar Observatory USA) facility along with MAST (Mathew 2009b; Venkatakrishnan et al. 2017b) and HMI, AIA onboard SDO spacecraft.

Chapter 6

Summary and Future Plan

In this chapter, we summarize the work and results obtained from our analysis in this thesis. We also outline the scope of future work. In this thesis, we investigate the evolution of velocity and magnetic fields in the solar atmosphere in different magnetic structures with an emphasis on understanding the propagation of waves in the lower solar atmosphere in the quiet phase as well as during the dynamical activities like solar flares. Understanding the evolution of velocity and magnetic fields is essential to analyze various physical mechanisms associated with the wave dynamics in the solar atmosphere. To accomplish the objective of the thesis, we have extensively used observational data acquired from multiple ground- and space-based instruments. In the following, we summarize the work presented in each chapter, the results obtained and then discussions on the future work.

6.1 Summary

Chapter 1- In this chapter, we begin with a brief introduction to the Sun and its various dynamical activities and then present some of the basic concepts necessary to form the ground to describe the work carried out in this thesis. Towards the end, we discuss the motivation and organization of the thesis.

Chapter 2- In this chapter, we describe various data sources utilized to achieve the scientific objectives of this thesis with a brief description of NBI with the MAST. In order to obtain the chromospheric line-of-sight Doppler velocity over a quiet and a sunspot region, we have scanned the Ca II 8542 Å line profile at various wavelength positions with the NBI/MAST. In this connection, we present various necessary data reduction steps, which we have used for the MAST observations. We have also acquired data from other ground-based instruments, viz. IBIS/DST and GONG, and hence a brief discussion of them is also presented. Further, we describe space-based instruments like HMI and AIA aboard SDO spacecraft, along with RHESSI and GOES satellites.

Chapter 3- In this chapter, we discuss the analysis of seismic emissions in the sunspots accompanying major solar flares. For this purpose, we utilize photospheric Dopplergrams and line-of-sight magnetograms at a cadence of 45 s and vector magnetograms at a cadence of 135 s acquired from the HMI instrument onboard the SDO spacecraft. We have also used H_α chromospheric intensity images obtained from GONG network and RHESSI hard X-rays observations in 12–25 keV band for flare ribbon and hard X-ray footpoints information. The X-ray observations from GOES satellite have been used for information related to temporal evolution of flares. Further, we have constructed photospheric acoustic power maps in the pre-, spanning and post-flare epochs in 2.5–4 mHz band to identify the seismic emission locations in the sunspots away from flaring kernels. We have selected only those seismic emission locations, which are away from the flaring regions because these locations are considered to be free from any flare-related contamination in the observational data. We find that there is a step-like change in the photospheric magnetic fields of the order of 50–100 Gauss within a time of 10–20 minutes in the seismic emission locations accompanying the solar flares. In addition, change in Lorentz force of the order of 10^{21} dyne in these locations is found to be sufficient to enhance these seismic emissions during solar flares. Investigation of these seismic emissions in the sunspots is important for the understanding of the propagation of magnetoacoustic waves in the solar atmosphere during dynamic activities like solar flares. Nevertheless, these seismic locations are also important to understand the dynamics beneath the active regions because these regions have better strength of velocity signals as compared to the other areas in the sunspots.

Chapter 4- In this chapter, we discuss the interaction of acoustic waves with the background magnetic fields of a magnetic network region, resulting in various magnetohydrodynamic waves and their associated different wave phenomena in the solar atmosphere. Here, we also present leakage of trapped low-frequency (2.5–4 mHz) acoustic waves along the inclined magnetic fields of a magnetic network region due to a reduction in the acoustic cut-off frequency. These acoustic waves are stochastically excited beneath the photosphere and intermittently interact with the background magnetic fields. Therefore, we use wavelet analysis to detect these episodic signals in the photospheric and chromospheric Dopplergrams obtained from the HMI instrument onboard SDO spacecraft and MAST observations, respectively. We also use photospheric scalar and vector magnetograms to get information on high magnetic concentration regions and magnetically modified acoustic cut-off frequency. We find a one-to-one correspondence between photospheric and chromospheric wavelet power spectra. The velocity power maps show the presence of high-frequency power halos in the chromospheric power maps. The observed power halos in the chromospheric power maps manifest the injection of fast magnetoacoustic waves refracting from the magnetic canopy in the solar atmosphere.

Chapter 5- In this chapter, we present a detailed analysis of the propagation of gravity waves in the lower solar atmosphere in various magnetic configurations. To carry out this work, we have utilized photospheric to lower chromospheric intensity observations (I_c, I_{uv1}, and I_{uv2}) obtained from the HMI and AIA instrument onboard SDO spacecraft. We have also used two height photospheric velocities estimated within Fe I 6173 Å line observations obtained from the IBIS/DST instrument over a sunspot surrounded by a quiet region. We have constructed I-I and V-V phase and coherence $k_h - \omega$ diagrams over different magnetized structures. The comparison of the average phase estimated over quiet and magnetized regions shows that gravity waves are scattered/suppressed or refracted back to the photosphere in the presence of background magnetic fields. These findings are also strengthened by the analysis of the average phase from pixel-by-pixel estimation after removing the acoustic wave regime part from the $k_h - \omega$ diagram, which shows the positive phase in the sunspot region compared to the quiet region. In general, our findings are qualitatively in agreement with the recent simulations performed by Vigeesh et al. (2017, 2019); Vigeesh and Roth (2020) suggesting the suppression/scattering or refraction of gravity waves in the magnetized regions.

6.2 Future Work

In order to better understand the evolution of velocity and magnetic fields in the solar atmosphere with an emphasis to understand the propagation of mechanical waves in the lower solar atmosphere and their interaction with the background magnetic fields resulting in the different wave dynamics, it is crucial to have multi-height velocity, intensity and magnetic field observations ranging from the photosphere to the chromosphere. It is possible if we obtain near-simultaneous observations in multiple magnetically sensitive spectral lines forming from the photospheric to chromospheric height range. However, it is difficult to have such observations due to several constraints. Moreover, we can also estimate multi-height velocity and magnetic fields from a single line scan observations if that line covers a broader height range in the solar atmosphere. The Ca II 8542 Å line scan observations are suitable for this purpose. Figure 6.1 shows the Ca II

8542 Å line (black line) profile and contribution function estimated from FALC model atmosphere (Fontenla et al. 1993). The Ca II 8542 Å line covers a broader height range in the solar atmosphere. The core of Ca II line sample around h = 1200–1600 km height above optical depth $\tau_{500} = 1$, whereas Ca II filtergrams at -0.6 Å from the line core sample photosphere around h = 200 km (Ortiz et al. 2014). Therefore, scanning the Ca II line profile with appropriate spectral and temporal resolution becomes essential. The Narrow Band Imager with the Multi-Application Solar Telescope operational at Udaipur Solar Observatory, Udaipur, India, is one of the suitable telescopes in the solar observers community, which is capable of scanning Ca II 8542 Å line profile within a wavelength range of ± 1.38 Å from the centre of Ca II 8542 Å line (Mathew et al. 2017b).

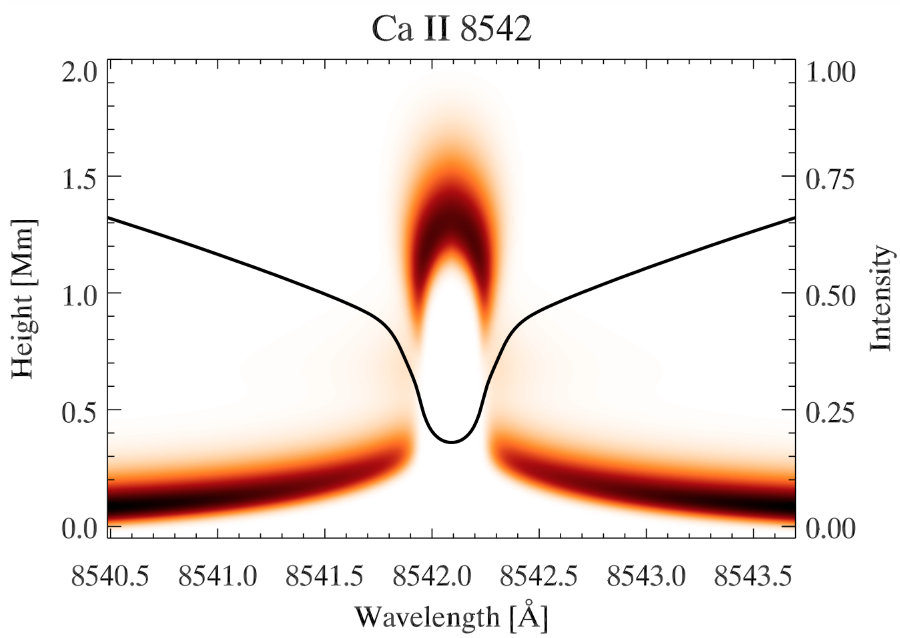

Figure 6.1: Contributation function (dark red colour) of Ca II 8542 Å line (black colour) estimated from FALC model atmosphere (Source: Ortiz et al. (2014)) .

In the near future, we plan to address the following research problems with the multi-height velocity and magnetic fields obtained from the ground- and space-based instruments such as the Multi-Application Solar Telescope (MAST), Swedish Solar Telescope (SST: Scharmer et al. (2003)), Daniel K Inouye Solar

Telescope (DKIST), Helioseismic and Magnetic Imager (HMI) instrument on-board SDO spacecraft, and Interface Region Imaging Spectrograph (IRIS: De Pontieu et al. (2014)) .

- We plan to study the propagation of acoustic waves and their interaction with the background magnetic fields utilizing near-simultaneous multi-height velocity and magnetic field observations acquired from ground- and space based instruments covering from photosphere to the corona over magnetic networks, pores, and sunspots regions.

- We plan to investigate the refraction of gravity waves in magnetic network regions utilizing near-simultaneous multi-height velocity observations from the photosphere to the chromosphere.

- We also have plans to verify the effects of magnetic fields on the propagation of gravity waves in the magnetized regions like sunspots and pores compared to the quiet region utilizing near-simultaneous multi-height photospheric to chromospheric velocity observations.

Appendix

These results are related to the Chapter 3 of the thesis.

[1] Active region NOAA 11261

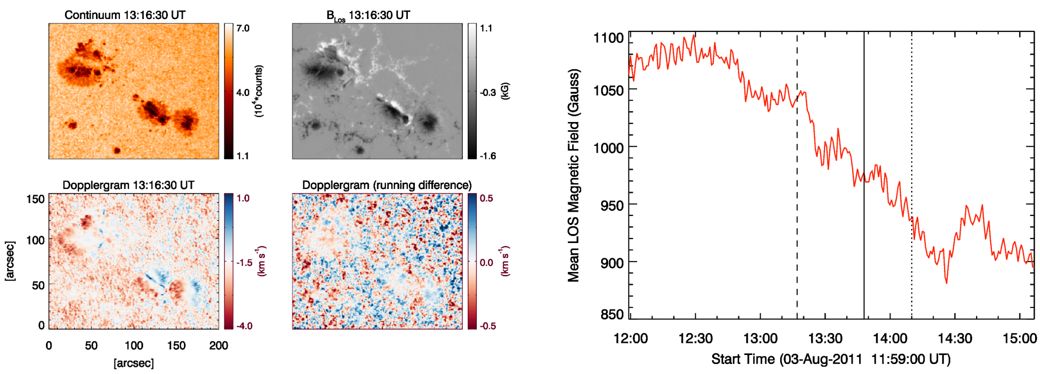

Figure 6.2: *Left panel*: Sample images of the active region NOAA 11261 showing continuum intensity (top left panel), photospheric line-of-sight magnetic fields (top right panel), Dopplergram (bottom left panel) and running difference of Doppler images (bottom right panel) acquired from HMI instrument aboard the *SDO* spacecraft on 2011 August 03. *Right panel*: Plot shows the temporal evolution of line-of-sight magnetic fields in the '*D*2' location of active region NOAA 11261. The dashed, solid and dotted vertical lines represent onset, peak and decay time of the flare.

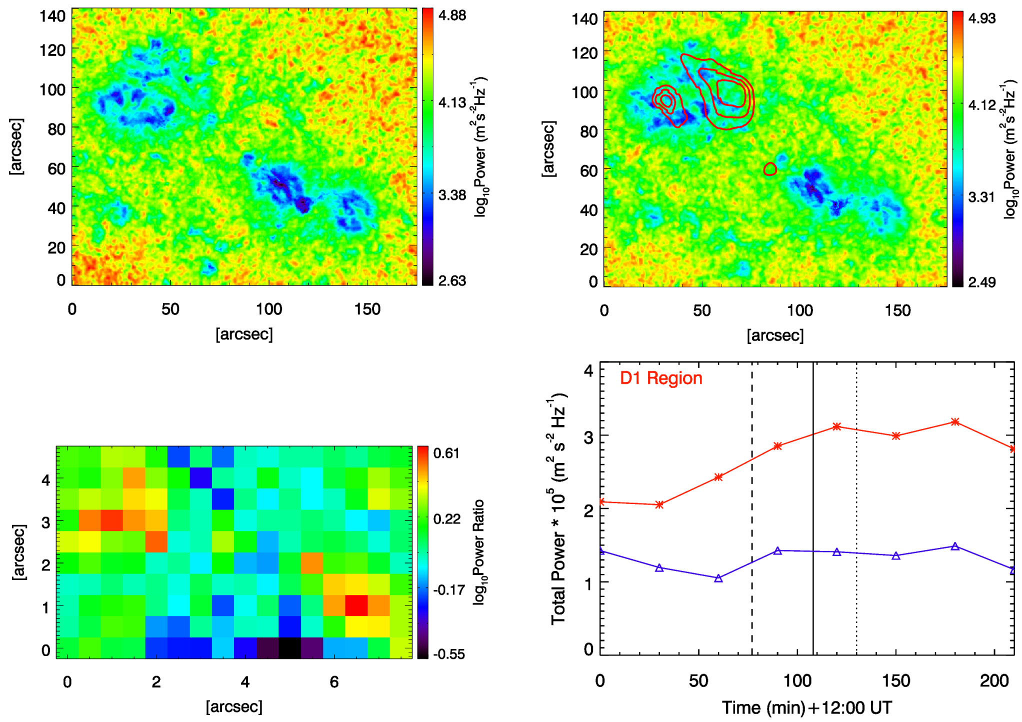

Figure 6.3: *Top panel* shows the pre and spanning flare power maps in 2.5–4 mHz band of the active region NOAA 11261, respectively. Here, red contours represent flare-ribbon locations from Hα chromospheric intensity observations at 70, 80 and 90 % of its maximum value as observed by the GONG instrument. *Bottom left panel* illustrates the blow-up region of '$D1$' enhanced location in the sunspot as indicated in the power map ratio in Figure 3.6 of Chapter 3. *Bottom right panel*: Plot shows the temporal evolution of integrated acoustic power over the '$D1$' location (red colour with asterisks) whereas that shown in blue colour with triangles represents evolution of total acoustic power in an unaffected region in the same sunspot. It is to be noted that there is a time offset of about $\pm$ 30-minutes between the acoustic power variation and the GOES flare-time.

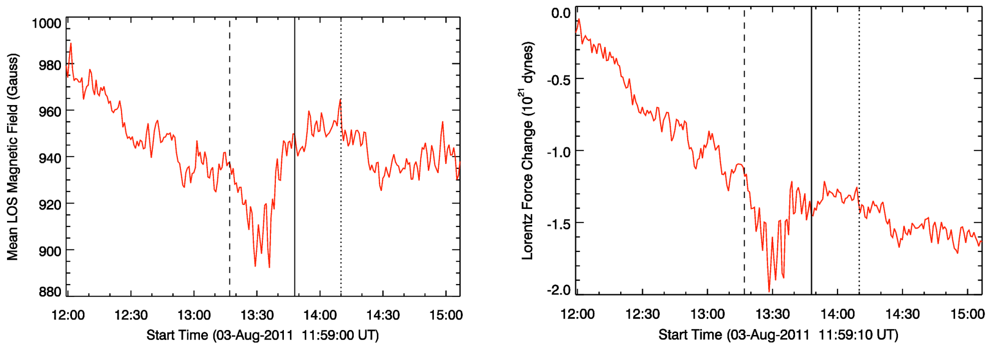

Figure 6.4: *Left panel*: Plot showing the temporal evolution of line-of-sight magnetic fields in the '$D1$' location of active region NOAA 11261. *Right panel*: Plot showing the temporal evolution of change in radial component of Lorentz force in the '$D1$' location. The dashed, solid and dotted vertical lines represent onset, peak and decay time of the flare.

[2] Active region NOAA 11882

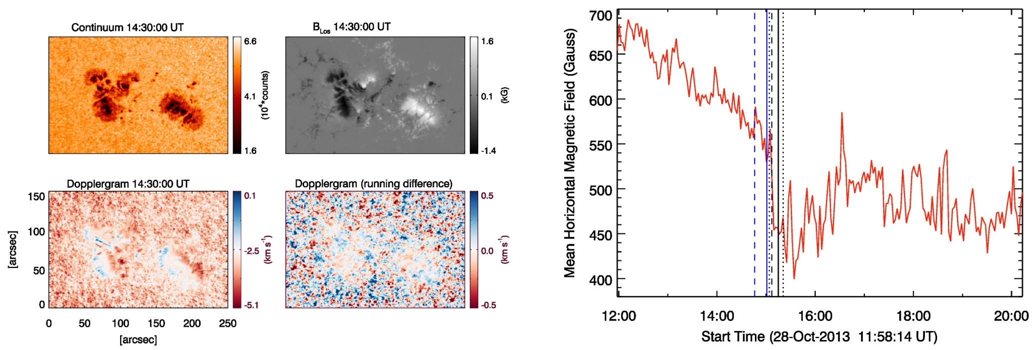

Figure 6.5: *Left panel*: Sample images of the active region NOAA 11882 showing continuum intensity (top left panel), photospheric line-of-sight magnetic fields (top right panel), Dopplergram (bottom left panel) and running difference of Doppler images (bottom right panel) acquired from HMI instrument aboard the *SDO* spacecraft on 2013 October 28. *Right panel*: Plot shows the temporal evolution of horizontal magnetic fields in the '$N1$' location of active region NOAA 11882. The dashed, solid and dotted vertical blue colour and black colour lines represent the onset, peak and decay time of M2.7 & M4.4 class flares, respectively.

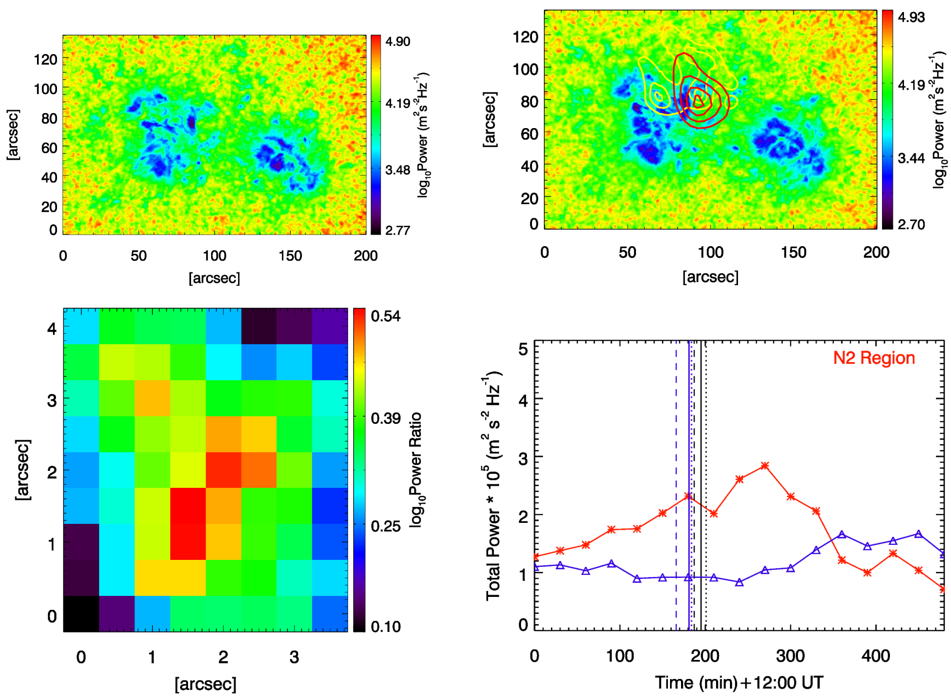

Figure 6.6: *Top panel* shows the post and spanning flare power maps in 2.5–4 mHz band of the active region NOAA 11882, respectively. Here, yellow contours represent flare-ribbon locations from Hα chromospheric intensity observations at 60, 80 and 95 % of its maximum value as observed by the GONG instrument whereas red contours represent hard X-rays foot points at 40, 60, 80 and 95% of its maximuum as observed in 12–25 KeV band from RHESSI spacecraft, respectively. *Bottom left panel*: Illustrates the blow-up region of '$N2$' enhanced location, as indicated in the power map ratio in Chapter 3. *Bottom right panel*: Plot showing the temporal evolution of integrated acoustic power over the '$N2$' location (red colour with asterisks) whereas that shown in blue colour with triangles represents evolution of total acoustic power in an unaffected region in the same sunspot. It is to be noted that there is a time offset of about $\pm$ 30-minutes between the acoustic power variation and the GOES flare-time. The dashed, solid and dotted vertical blue colour and black colour lines represent the onset, peak and decay time of M2.7 & M4.4 class flares, respectively.

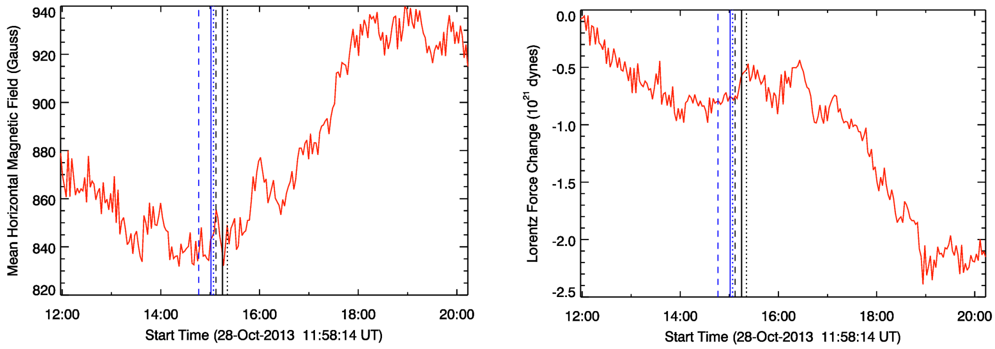

Figure 6.7: *Left panel*: Plot showing the temporal evolution of horizontal magnetic fields in the '$N2$' location of active region NOAA 11882. *Right Panel*: Plot showing the temporal evolution of change in radial component of Lorentz force in the '$N2$' location. The dashed, solid and dotted vertical blue colour and black colour lines represent the onset, peak and decay time of M2.7 & M4.4 class flares, respectively.

[3] Active region NOAA 12222

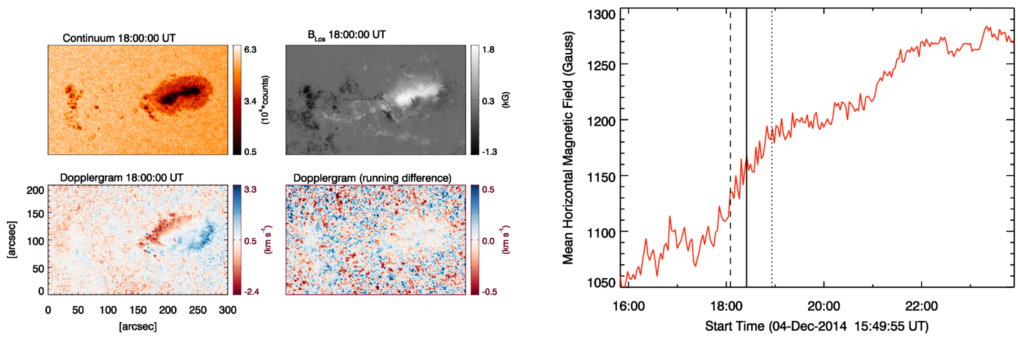

Figure 6.8: *Left panel*: Sample images of the active region NOAA 12222 showing continuum intensity (top left panel), photospheric line-of-sight magnetic fields (top right panel), Dopplergram (bottom left panel) and running difference of Doppler images (bottom right panel) acquired from HMI instrument aboard the *SDO* spacecraft on 2014 December 04. *Right panel*: Plot shows the temporal evolution of horizontal magnetic fields in the '$M1$' location of active region NOAA 12222. The dashed, solid and dotted vertical lines represent the onset, peak and decay time of the flare.

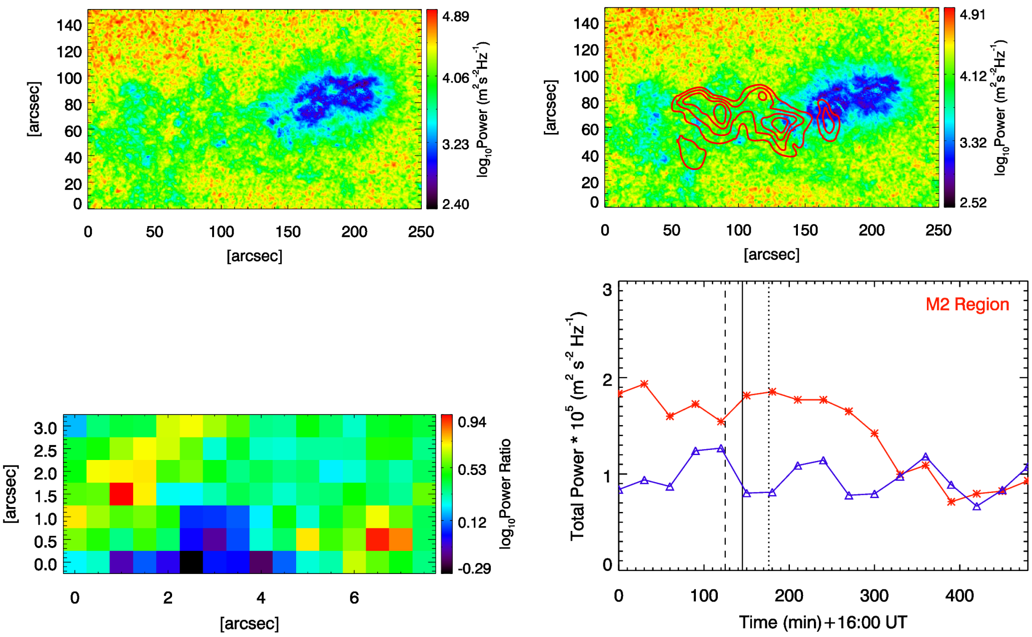

Figure 6.9: *Top panel* shows the post and spanning flare power maps in 2.5–4 mHz band of the active region NOAA 12222, respectively. Here, red contours represent flare-ribbon locations from Hα chromospheric intensity observations at 60, 70, 80 and 90 % of its maximum value as observed by the GONG instrument. *Bottom left panel*: Illustrates the blow-up region of '$M2$' enhanced location of active region 12222, as indicated in the power map ratio in Chapter 3. *Right panel*: Plot showing the temporal evolution of integrated power over the '$M2$' location (red colour with asterisks) whereas that shown in blue colour with triangles represents evolution of total power in an unaffected region in the same sunspot. It is to be noted that there is a time offset of about $\pm$ 30-minutes between the acoustic power variation and the GOES flare-time.

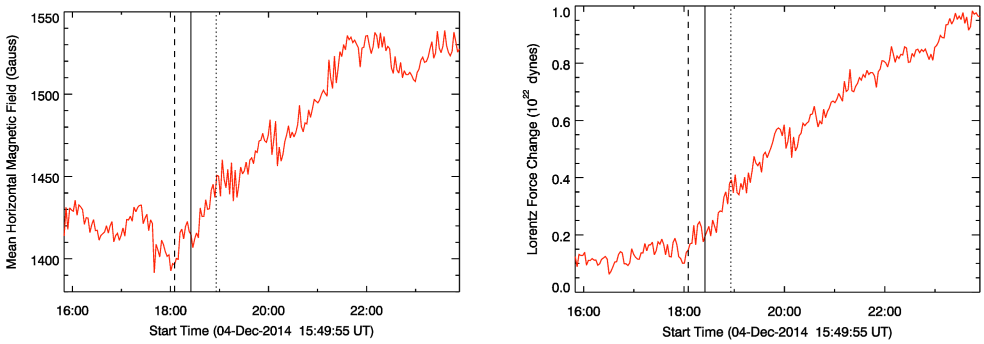

Figure 6.10: *Left panel*: Plot showing the temporal evolution of horizontal magnetic fields in the '$M2$' location of active region NOAA 12222. *Right panel*: Plot showing the temporal evolution of change in horizontal component of Lorentz force in the '$M2$' location. The dashed, solid and dotted vertical lines represent the onset, peak and decay time of the flare.

[4] Active region NOAA 12241

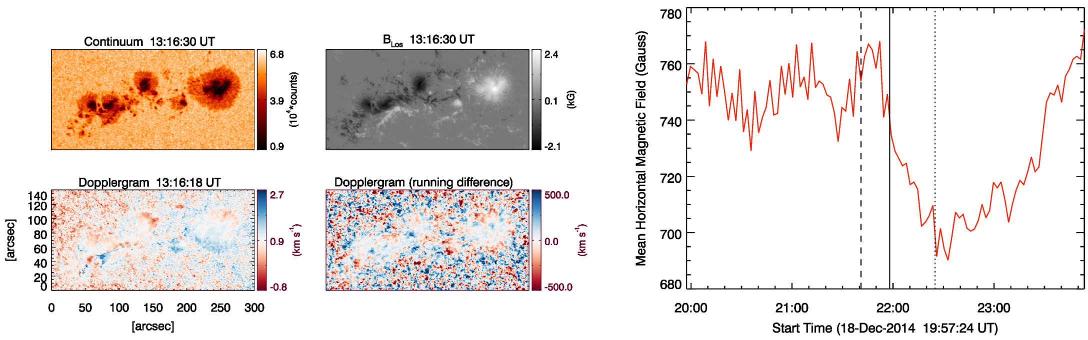

Figure 6.11: *Left panel*: Sample images of the active region NOAA 12241 showing continuum intensity (top left panel), photospheric line-of-sight magnetic fields (top right panel), Dopplergram (bottom left panel) and running difference of Doppler images (bottom right panel) acquired from HMI instrument aboard the *SDO* spacecraft on 2014 December 18. *Right panel*: Plot shows the temporal evolution of horizontal magnetic fields in the 'Q1' location of the active region NOAA 12241.

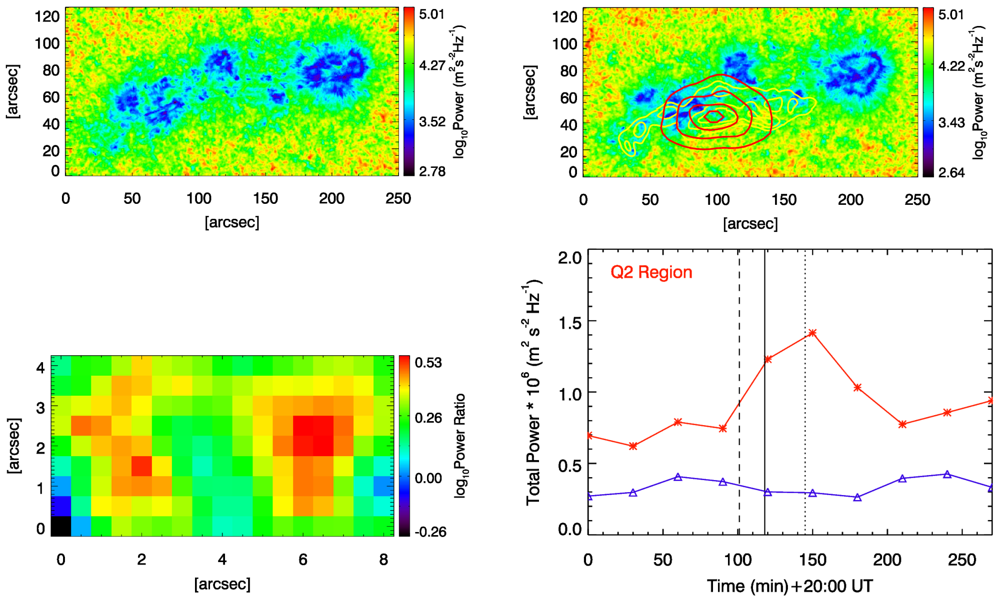

Figure 6.12: *Top panel* shows the pre and spanning flare power maps in 2.5–4 mHz band of the active region NOAA 12241, respectively. Here, yellow contours represent flare-ribbon locations from Hα chromospheric intensity observations at 70, 80 and 90 % of its maximum value as observed by the GONG instrument whereas red contours represent hard X-rays foot points at 40, 60, 80 and 95% of its maximum as observed in 12–25 KeV band from RHESSI spacecraft, respectively. *Bottom left panel:* Illustrates the blow-up region of '$Q2$' enhanced location of active region NOAA 12241, as indicated in the power map ratio in Chapter 3. *Right panel*: Plot showing the temporal evolution of integrated power over the '$Q2$' location (red colour with asterisks) whereas that shown in blue colour with triangles represents evolution of total power in an unaffected region in the same sunspot. It is to be noted that there is a time offset of about ± 30-minutes between the acoustic power variation and the GOES flare-time.

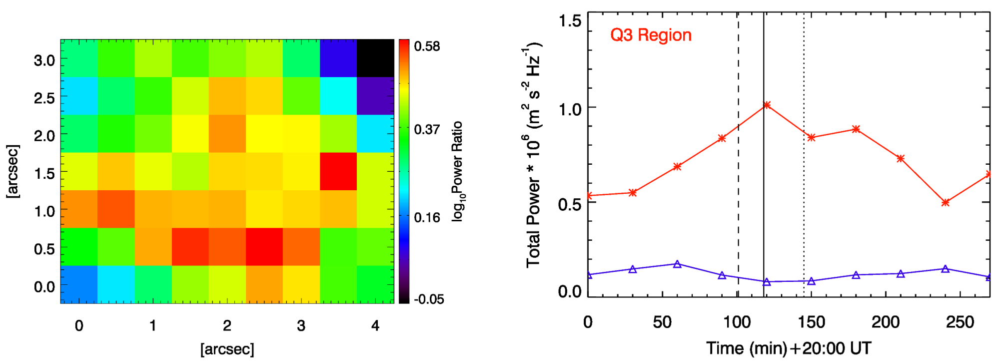

Figure 6.13: Same as Figure 11, but for '$Q3$' location.

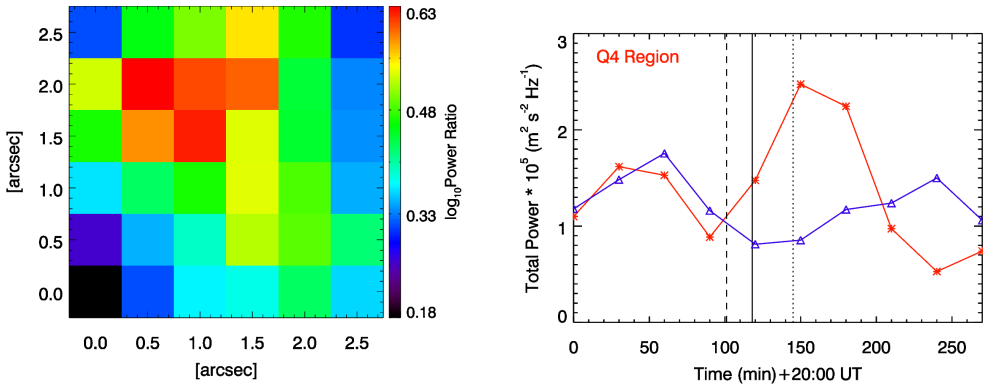

Figure 6.14: Same as Figure 11, but for '$Q4$' location.

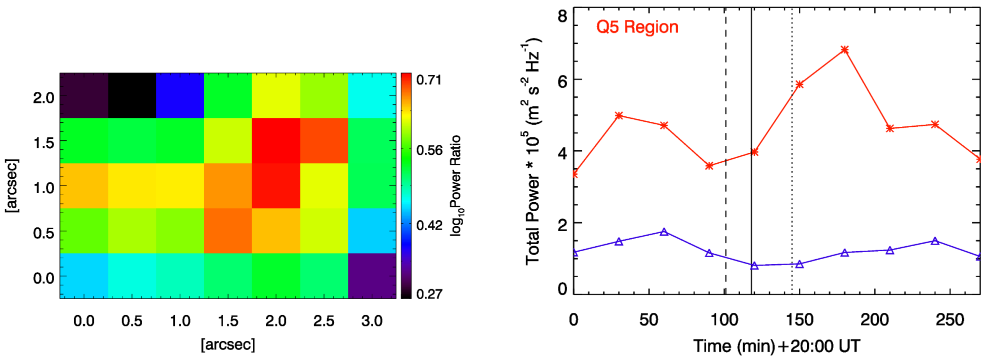

Figure 6.15: Same as Figure 11, but for '$Q5$' location.

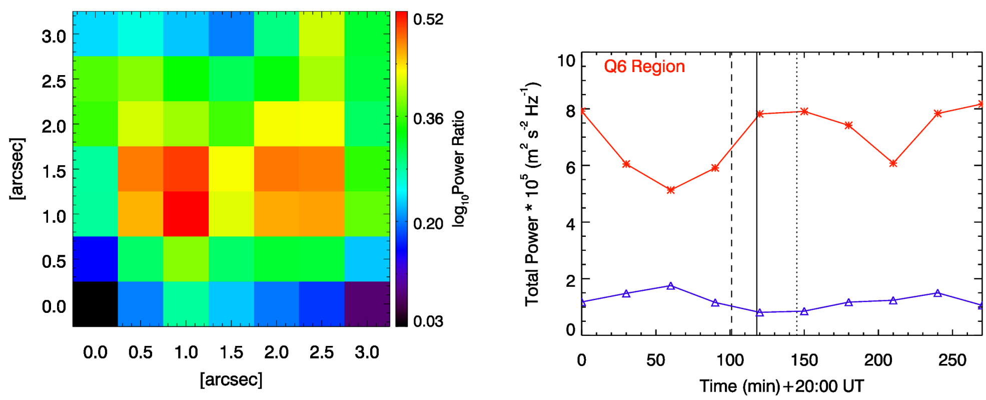

Figure 6.16: Same as Figure 11, but for '$Q6$' location.

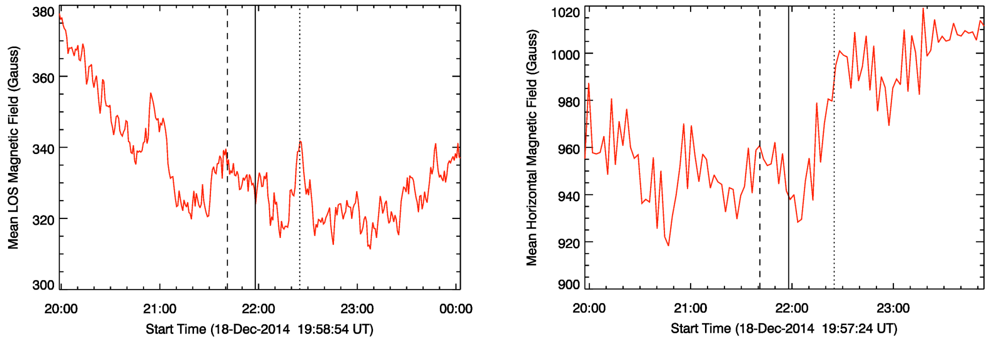

Figure 6.17: Plot showing the temporal evolution of line-of-sight magnetic fields (left panel) and horizontal magnetic fields (right panel) of '$Q3$' and '$Q4$' locations, respectively.

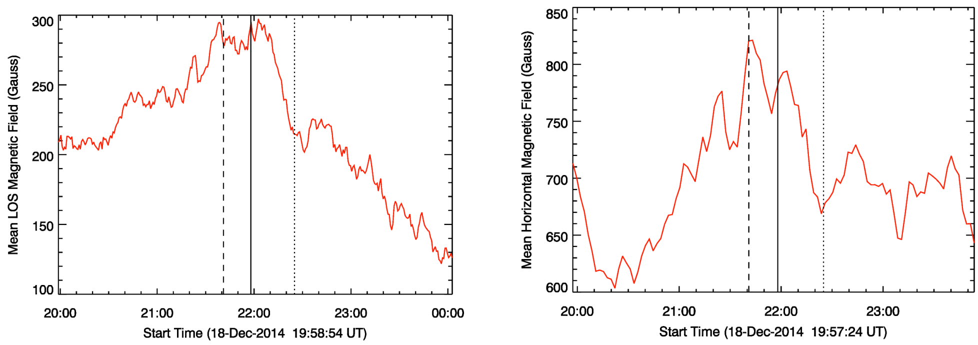

Figure 6.18: Plot showing the temporal evolution of line-of-sight magnetic fields (left panel) and horizontal magnetic fields (right panel) of '$Q5$' and '$Q6$' locations, respectively.

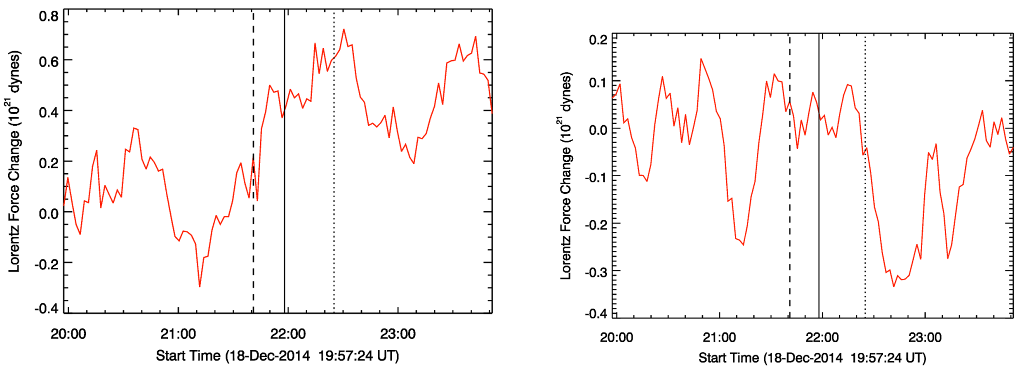

Figure 6.19: *Left panel*: Plot showing the temporal evolution of change in radial component of Lorentz force in the '$Q2$' location of active region NOAA 12241. *Right panel*: Same as shown in the left panel but for '$Q3$' location. The dashed, solid and dotted vertical lines represent the onset, peak and decay time of the flare.

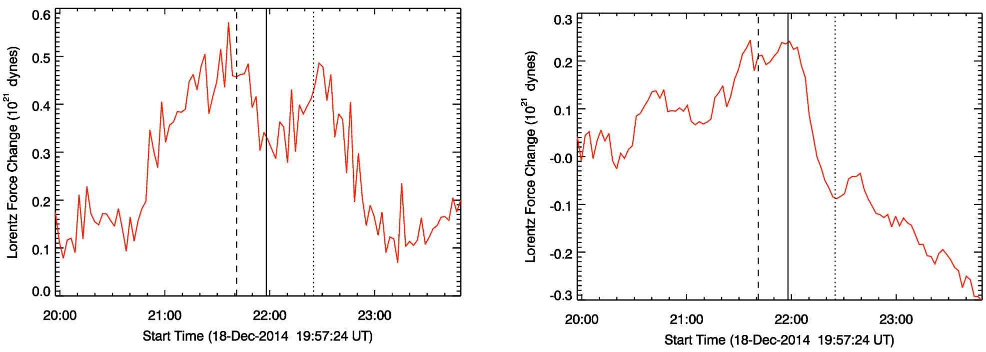

Figure 6.20: *Left panel*: Plot showing the temporal evolution of change in horizontal component of Lorentz force in the '$Q4$' location of active region NOAA 12241. *Right panel*: Same as shown in the left panel but for '$Q5$' location. The dashed, solid and dotted vertical lines represent onset, peak and decay time of the flare.

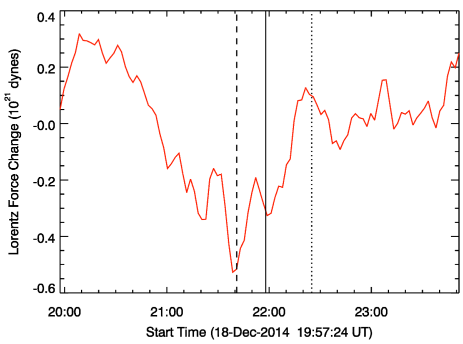

Figure 6.21: Plot showing the temporal evolution of change in radial component of Lorentz force in the '$Q6$' location of active region NOAA 12241. The dashed, solid and dotted vertical lines represent onset, peak and decay time of the flare.

[5] Active region NOAA 12242

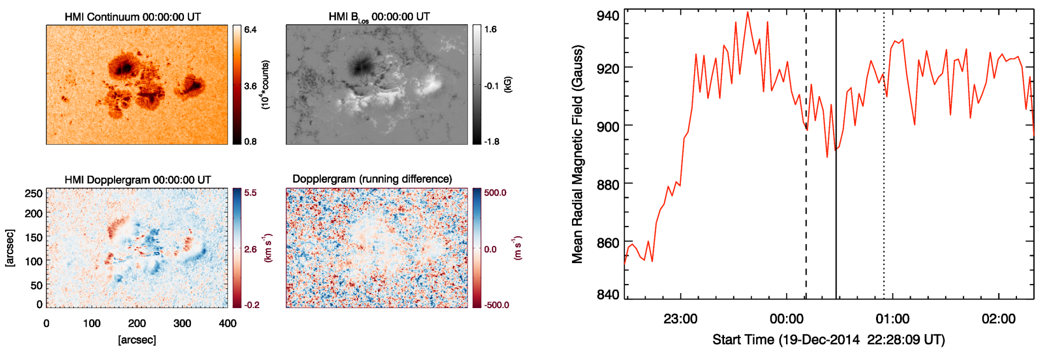

Figure 6.22: *Left panel*: Sample images of the active region NOAA 12242 showing continuum intensity (top left panel), photospheric line-of-sight magnetic fields (top right panel), Dopplergram (bottom left panel) and running difference of Doppler images (bottom right panel) acquired from HMI instrument aboard the *SDO* spacecraft on 2014 December 20. *Right panel*: Plot shows the temporal evolution of radial magnetic fields in the 'K1' location of active region NOAA 12242. The dashed, solid and dotted vertical lines represent the onset, peak and decay time of the flare.

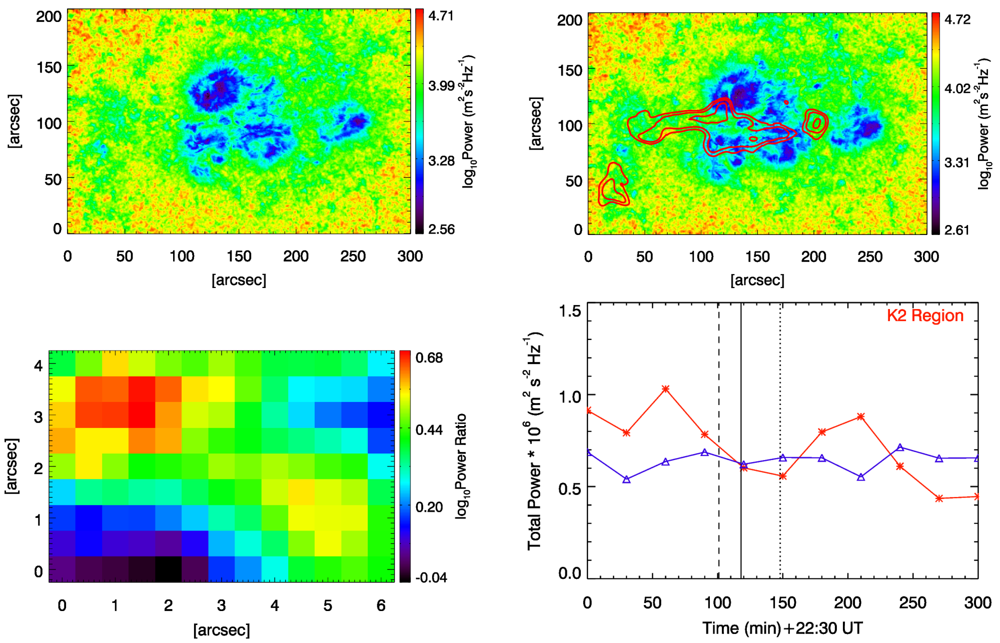

Figure 6.23: *Top panel* shows the post and spanning flare power maps in 2.5–4 mHz band of the active region NOAA 12242, respectively. Here, red contours represent flare-ribbon locations from Hα chromospheric intensity observations at 60, 70 and 90 % of its maximum value as observed by the GONG instrument. *Bottom left panel*: Illustrates the blow-up region of '$K2$' enhanced location as indicated in the power map ratio in Chapter 3. *Right panel*: Plot showing the temporal evolution of integrated acoustic power over the $'K2$' location (red colour with asterisks) whereas that shown in blue colour with triangles represents evolution of total acoustic power in an unaffected region in the same sunspot. It is to be noted that there is a time offset of about $\pm$ 30-minutes between the acoustic power variation and the GOES flare-time.

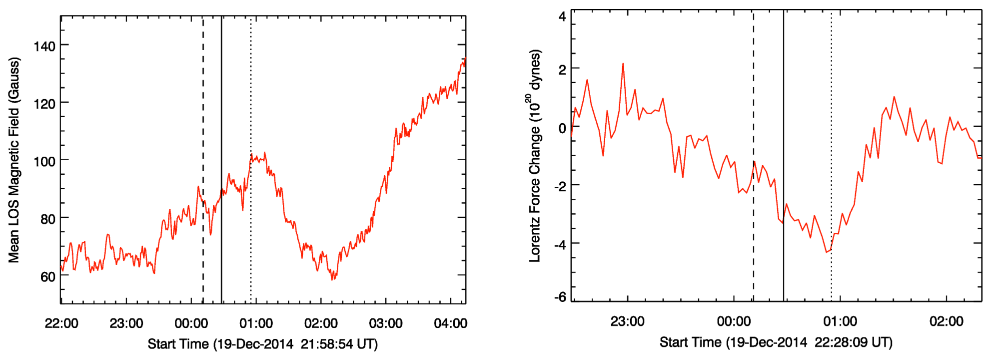

Figure 6.24: *Left panel*: Plot shows the temporal evolution of line-of-sight magnetic fields in the '$K2$' location of active region NOAA 12242. *Right panel*: Plot shows the temporal evolution of change in radial component of Lorentz force in the '$K2$' location. The dashed, solid and dotted vertical lines represent the onset, peak and decay time of the flare.

[6] Active region NOAA 12297

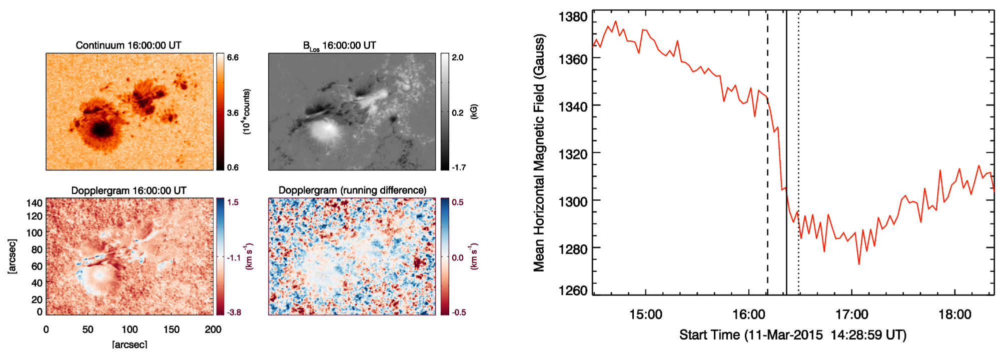

Figure 6.25: *Left panel*: Sample images of the active region NOAA 12297 showing continuum intensity (top left panel), photospheric line-of-sight magnetic fields (top right panel), Dopplergram (bottom left panel) and running difference of Doppler images (bottom right panel) acquired from HMI instrument aboard the *SDO* spacecraft on 2015 March 11. *Right panel*: Plot shows the temporal evolution of horizontal magnetic fields in the 'F2' location of active region NOAA 12297. The dashed, solid and dotted vertical lines represent the onset, peak and decay time of the flare.

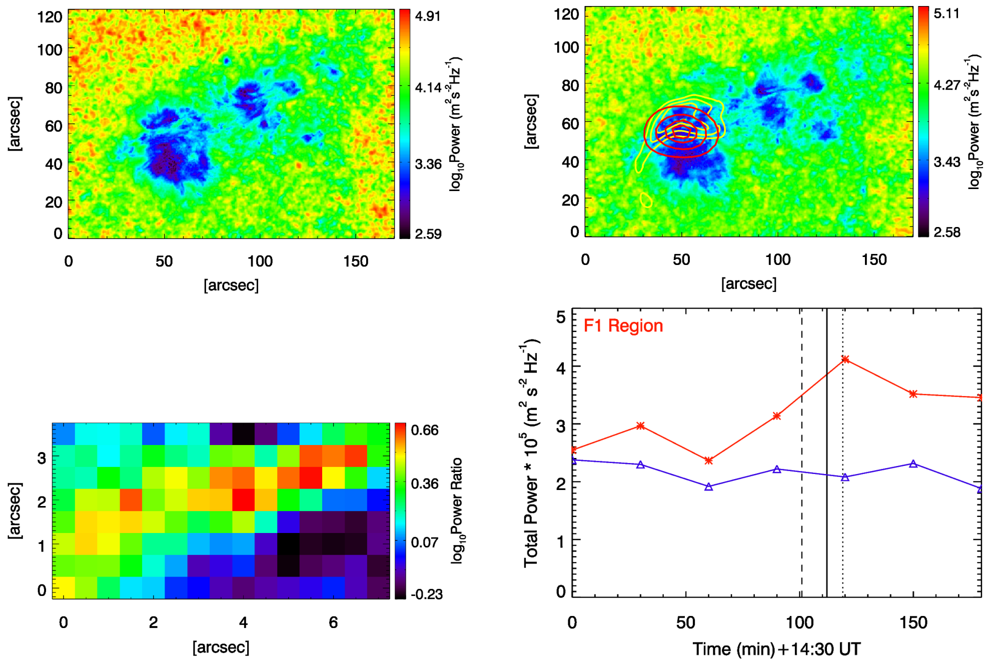

Figure 6.26: *Top panel* shows the pre and spanning flare power maps in 2.5–4 mHz band of the active region NOAA 12297, respectively. Here, yellow contours represent flare-ribbon locations from Hα chromospheric intensity observations at 70, 80 and 90 % of its maximum value as observed by the GONG instrument whereas red contours represent hard X-rays foot points at 25, 50, 75 and 90% of its maximuum as observed in 12–25 KeV band from RHESSI spacecraft, respectively. *Bottom left panel*: Illustrates the blow-up region of '$F1$' location as indicated in the power map ratio in Chapter 3. *Right panel*: Plot showing the temporal evolution of integrated acoustic power over the '$F1$' location (red colour with asterisks) whereas that shown in blue colour with triangles represents evolution of total power in an unaffected region in the same sunspot. It is to be noted that there is a time offset of about $\pm$ 30-minutes between the acoustic power variation and the GOES flare-time.

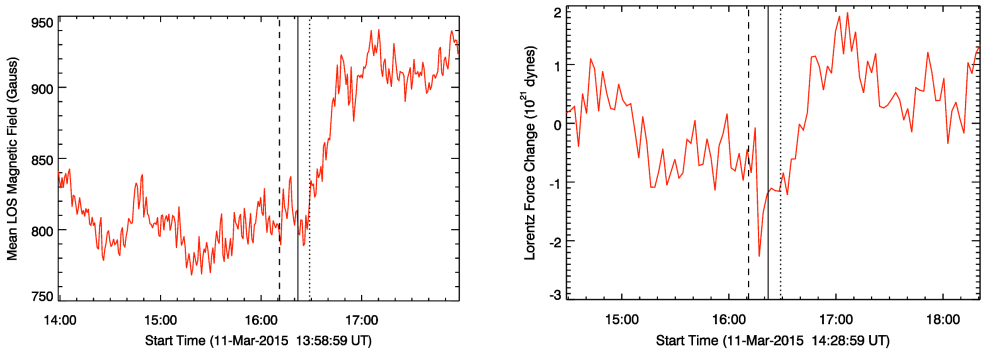

Figure 6.27: *Left panel*: Plot shows the temporal evolution of line-of-sight magnetic field in the '$F1$' location of active region NOAA 12297. *Right panel*: Plot shows the temporal evolution of change in radial component of Lorentz force in the '$F1$' location. The dashed, solid and dotted vertical lines represent onset, peak and decay time of the flare.

[7] Active region NOAA 12371

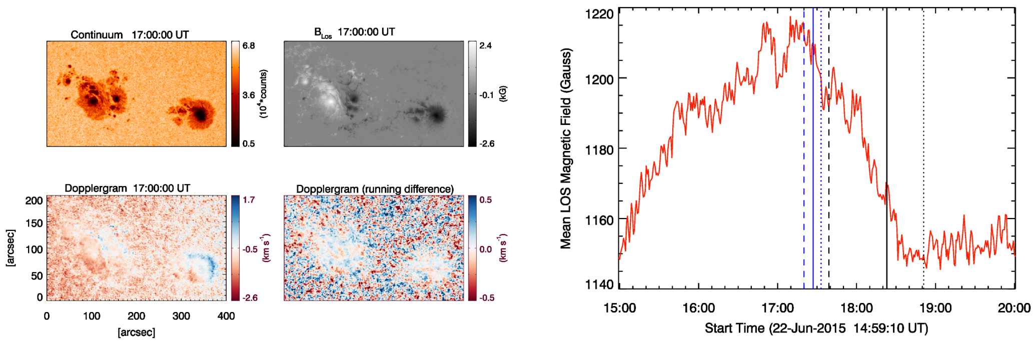

Figure 6.28: *Left panel*: Sample images of the active region NOAA 12371 showing continuum intensity (top left panel), photospheric line-of-sight magnetic fields (top right panel), Dopplergram (bottom left panel) and running difference of Doppler images (bottom right panel) acquired from HMI instrument aboard the *SDO* spacecraft on 2015 June 22. *Right panel*: Plot shows the temporal evolution of line-of-sight magnetic fields in the 'P1' location. The dashed, solid and dotted vertical lines represent the onset, peak and decay time of the flare.

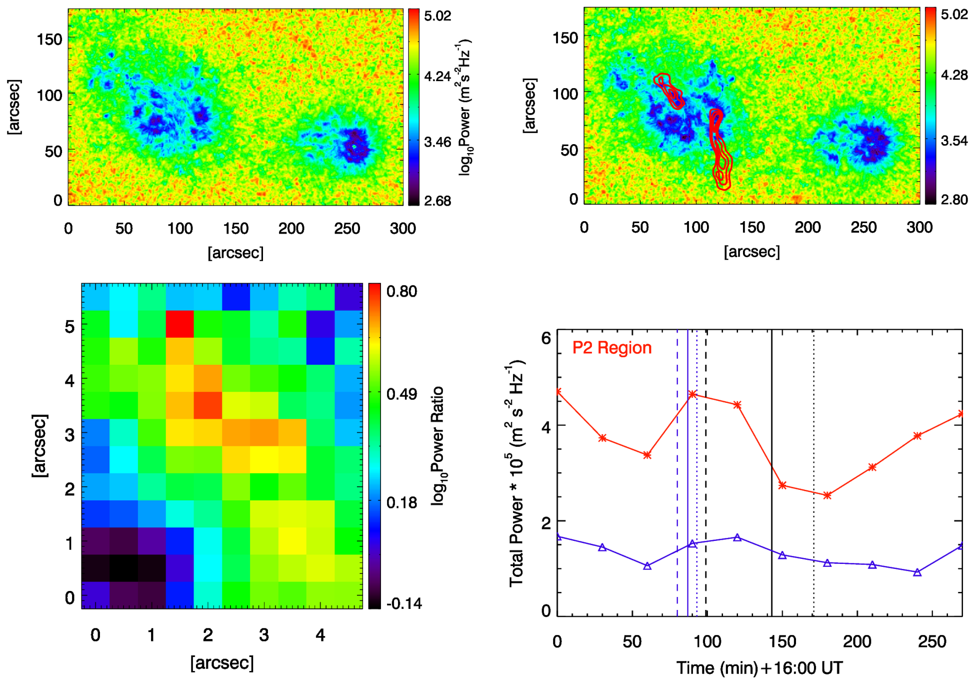

Figure 6.29: *Top panel* shows the pre and spanning flare power maps in 2.5–4 mHz band of the active region NOAA 12371, respectively. Here, yellow contours represent flare-ribbon locations from Hα chromospheric intensity observations at 70, 80 and 90 % of its maximum value as observed by the GONG instrument. *Bottom left panel*: Illustrates the blow-up region of '$P2$' enhanced location as indicated in the power map ratio in Chapter 3. *Right panel*: Plot showing the temporal evolution of integrated acoustic power over the '$P2$' location (red colour with asterisks) whereas that shown in blue colour with triangles represents evolution of total power in an unaffected region in the same sunspot. It is to be noted that there is a time offset of about $\pm$ 30-minutes between the acoustic power variation and the GOES flare-time.

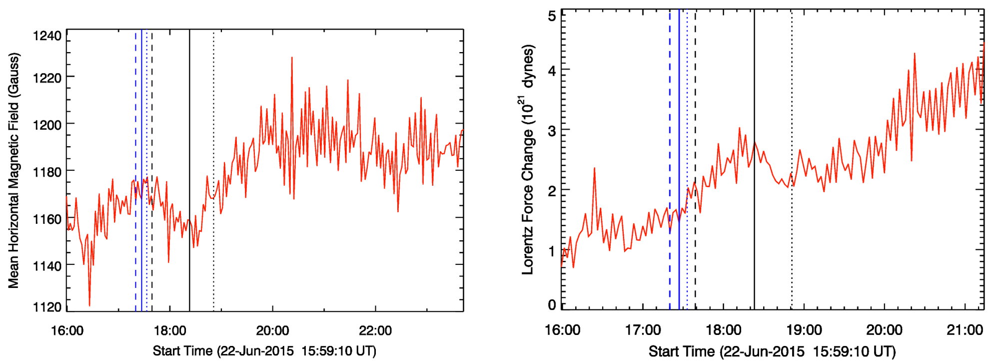

Figure 6.30: *Left panel*: Plot showing the temporal evolution of horizontal magnetic fields in the '$P2$' location of active region NOAA 12371. *Right panel*: Plot showing the temporal evolution of change in horizontal component of Lorentz force in the '$P2$' location. The dashed, solid and dotted vertical lines represent the onset, peak and decay time of the flare.

References

Abramenko, V. I. and Baranovsky, E. A.: 2004, *Solar Phys.* **220(1)**, 81

Alfvén, H.: 1947, *Mon. Not. Roy. Astron. Soc.* **107**, 211

Bahcall, J. N., Huebner, W. F., Lubow, S. H., Parker, P. D., and Ulrich, R. K.: 1982, *Reviews of Modern Physics* **54(3)**, 767

Bahcall, J. N., Pinsonneault, M. H., and Basu, S.: 2001, *Astrophys. J.* **555(2)**, 990

Bel, N. and Leroy, B.: 1977, *Astron. Astrophys.* **55**, 239

Bellot Rubio, L. and Orozco Suárez, D.: 2019, *Living Reviews in Solar Physics* **16(1)**, 1

Bi, S. and Li, R.: 1998, *Astron. Astrophys.* **335**, 673

Bogdan, T. J., Carlsson, M., Hansteen, V. H., McMurry, A., Rosenthal, C. S., Johnson, M., Petty-Powell, S., Zita, E. J., Stein, R. F., McIntosh, S. W., and Nordlund, Å.: 2003, *Astrophys. J.* **599(1)**, 626

Born, M. and Wolf, E.: 1999, *Principles of Optics*, Cambridge University Press, 7 edition

Borrero, J. M., Tomczyk, S., Kubo, M., Socas-Navarro, H., Schou, J., Couvidat, S., and Bogart, R.: 2011, *Solar Phys.* **273**, 267

Braun, D. C., Lindsey, C., Fan, Y., and Jefferies, S. M.: 1992, *Astrophys. J.* **392**, 739

Brown, J. C.: 1971, *Solar Phys.* **18(3)**, 489

Brown, T. M., Bogdan, T. J., Lites, B. W., and Thomas, J. H.: 1992, *Astrophys. J. Lett.* **394**, L65

Cally, P. S. and Bogdan, T. J.: 1997, *Astrophys. J. Lett.* **486(1)**, L67

Cally, P. S., Moradi, H., and Rajaguru, S. P.: 2016, *Washington DC American Geophysical Union Geophysical Monograph Series* **216**, 489

Cauzzi, G., Reardon, K. P., Uitenbroek, H., Cavallini, F., Falchi, A., Falciani, R., Janssen, K., Rimmele, T., Vecchio, A., and Wöger, F.: 2008, *Astron. Astrophys.* **480(2)**, 515

Cavallini, F.: 2006, *Solar Phys.* **236(2)**, 415

Couvidat, S., Rajaguru, S. P., Wachter, R., Sankarasubramanian, K., Schou, J., and Scherrer, P. H.: 2012a, *Solar Phys.* **278(1)**, 217

Couvidat, S., Rajaguru, S. P., Wachter, R., Sankarasubramanian, K., Schou, J., and Scherrer, P. H.: 2012b, *Solar Phys.* **278(1)**, 217

Couvidat, S., Rajaguru, S. P., Wachter, R., Sankarasubramanian, K., Schou, J., and Scherrer, P. H.: 2012c, *Solar Phys.* **278(1)**, 217

Couvidat, S., Schou, J., Shine, R. A., Bush, R. I., Miles, J. W., Scherrer, P. H., and Rairden, R. L.: 2012d, *Solar Phys.* **275(1-2)**, 285

De Pontieu, B., Erdélyi, R., and De Moortel, I.: 2005, *Astrophys. J. Lett.* **624(1)**, L61

De Pontieu, B., Erdélyi, R., and James, S. P.: 2004, *Nature* **430(6999)**, 536

De Pontieu, B., Title, A. M., Lemen, J. R., Kushner, G. D., Akin, D. J., Allard, B., Berger, T., Boerner, P., Cheung, M., Chou, C., Drake, J. F., Duncan, D. W., Freeland, S., Heyman, G. F., Hoffman, C., Hurlburt, N. E., Lindgren, R. W., Mathur, D., Rehse, R., Sabolish, D., Seguin, R., Schrijver, C. J., Tarbell, T. D., Wülser, J. P., Wolfson, C. J., Yanari, C., Mudge, J., Nguyen-Phuc, N., Timmons, R., van Bezooijen, R., Weingrod, I., Brookner, R., Butcher, G., Dougherty, B., Eder, J., Knagenhjelm, V., Larsen, S., Mansir, D., Phan, L., Boyle, P., Cheimets, P. N., DeLuca, E. E., Golub, L., Gates, R., Hertz, E., McKillop, S., Park, S., Perry, T., Podgorski, W. A., Reeves, K., Saar, S., Testa, P., Tian, H., Weber, M., Dunn, C., Eccles, S., Jaeggli, S. A., Kankelborg, C. C., Mashburn, K., Pust, N., Springer, L., Carvalho, R., Kleint, L., Marmie, J., Mazmanian, E., Pereira, T. M. D., Sawyer, S., Strong, J., Worden, S. P., Carlsson, M., Hansteen, V. H., Leenaarts, J., Wiesmann, M., Aloise, J., Chu, K. C., Bush, R. I., Scherrer, P. H., Brekke, P., Martinez-Sykora, J., Lites, B. W., McIntosh, S. W., Uitenbroek, H., Okamoto, T. J., Gummin, M. A., Auker, G., Jerram, P., Pool, P., and Waltham, N.: 2014, *Solar Phys.* **289(7)**, 2733

Deubner, F. L.: 1975, *Astron. Astrophys.* **44(2)**, 371

Deubner, F. L. and Fleck, B.: 1989, *Astron. Astrophys.* **213(1-2)**, 423

Deubner, F.-L. and Gough, D.: 1984, *Ann. rev. Astron. Astrophys.* **22**, 593

Domingo, V., Fleck, B., and Poland, A. I.: 1995, *Solar Phys.* **162(1-2)**, 1

Donea, A. C., Besliu-Ionescu, D., Cally, P. S., Lindsey, C., and Zharkova, V. V.: 2006, *Solar Phys.* **239(1-2)**, 113

Donea, A. C. and Lindsey, C.: 2005, *Astrophys. J.* **630(2)**, 1168

Edlén, B.: 1943, *Zeitschrift fr Astrophysik* **22**, 30

Evans, J. W. and Michard, R.: 1962, *Astrophys. J.* **135**, 812

Finsterle, W., Jefferies, S. M., Cacciani, A., Rapex, P., and McIntosh, S. W.: 2004, *Astrophys. J. Lett.* **613(2)**, L185

Fisher, G. H.: 1989, *Astrophys. J.* **346**, 1019

Fisher, G. H., Bercik, D. J., Welsch, B. T., and Hudson, H. S.: 2012, *Solar Phys.* **277(1)**, 59

Fisher, G. H., Canfield, R. C., and McClymont, A. N.: 1985, *Astrophys. J.* **289**, 425

Fleck, B., Couvidat, S., and Straus, T.: 2011, *Solar Phys.* **271(1-2)**, 27

Fletcher, L., Dennis, B. R., Hudson, H. S., Krucker, S., Phillips, K., Veronig, A., Battaglia, M., Bone, L., Caspi, A., Chen, Q., Gallagher, P., Grigis, P. T., Ji, H., Liu, W., Milligan, R. O., and Temmer, M.: 2011, *Space Sci. Rev.* **159(1-4)**, 19

Fontenla, J. M., Avrett, E. H., and Loeser, R.: 1993, *Astrophys. J.* **406**, 319

Fossum, A. and Carlsson, M.: 2005, *Astrophys. J.* **625(1)**, 556

Foukal, P. V.: 2004, *Solar Astrophysics*, WILEY-VCH, 3 edition

Gary, F. D.: 2005, *The Observation and Analysis of Stellar Photosphere*, Cambridge University Press, 3 edition

Gary, G. A.: 2001, *Solar Phys.* **203(1)**, 71

Gary, G. A. and Hagyard, M. J.: 1990, *Solar Phys.* **126**, 21

Goldreich, P. and Kumar, P.: 1990, *Astrophys. J.* **363**, 694

Gonczi, G. and Roddier, F.: 1969, *Solar Phys.* **8(2)**, 255

Gray, D. F.: 2005, *The Observation and analysis of Stellar Photospheres*, Cambridge University Press, 3 edition

Grotrian, W.: 1939, *Naturwissenschaften* **27(13)**, 214

Hale, G. E.: 1908, *Astrophys. J.* **28**, 315

Hanasoge, S.: 2015, *Introduction*, pp 1–19, Springer International Publishing, Cham

Hanasoge, S. M.: 2008, *Astrophys. J.* **680(2)**, 1457

Hanasoge, S. M.: 2009, *Astron. Astrophys.* **503(2)**, 595

Handy, B. N., Acton, L. W., Kankelborg, C. C., Wolfson, C. J., Akin, D. J., Bruner, M. E., Caravalho, R., Catura, R. C., Chevalier, R., Duncan, D. W., Edwards, C. G., Feinstein, C. N., Freeland, S. L., Friedlaender, F. M., Hoffmann, C. H., Hurlburt, N. E., Jurcevich, B. K., Katz, N. L., Kelly, G. A., Lemen, J. R., Levay, M., Lindgren, R. W., Mathur, D. P., Meyer, S. B., Morrison, S. J., Morrison, M. D., Nightingale, R. W., Pope, T. P., Rehse, R. A., Schrijver, C. J., Shine, R. A., Shing, L., Strong, K. T., Tarbell, T. D., Title, A. M., Torgerson, D. D., Golub, L., Bookbinder, J. A., Caldwell, D., Cheimets, P. N., Davis, W. N., Deluca, E. E., McMullen, R. A., Warren, H. P., Amato, D., Fisher, R., Maldonado, H., and Parkinson, C.: 1999, *Solar Phys.* **187(2)**, 229

Harvey, J., Tucker, R., and Britanik, L.: 1998, in S. Korzennik (ed.), *Structure and Dynamics of the Interior of the Sun and Sun-like Stars*, Vol. 418 of *ESA Special Publication*, p. 209

Harvey, J. W., Bolding, J., Clark, R., Hauth, D., Hill, F., Kroll, R., Luis, G., Mills, N., Purdy, T., Henney, C., Holland, D., and Winter, J.: 2011, in *AAS/Solar Physics Division Abstracts #42*, Vol. 42 of *AAS/Solar Physics Division Meeting*, p. 17.45

Harvey, J. W., Hill, F., Kennedy, J. R., Leibacher, J. W., and Livingston, W. C.: 1988, *Advances in Space Research* **8(11)**, 117

Hindman, B. W. and Brown, T. M.: 1998, *Astrophys. J.* **504(2)**, 1029

Hudson, H. S.: 2000, *Astrophys. J. Lett.* **531(1)**, L75

Hudson, H. S., Fisher, G. H., and Welsch, B. T.: 2008a, in R. Howe, R. W. Komm, K. S. Balasubramaniam, and G. J. D. Petrie (eds.), *Subsurface and Atmospheric Influences on Solar Activity*, Vol. 383 of *Astronomical Society of the Pacific Conference Series*, p. 221

Hudson, H. S., Fisher, G. H., and Welsch, B. T.: 2008b, in R. Howe, R. W. Komm, K. S. Balasubramaniam, and G. J. D. Petrie (eds.), *Subsurface and Atmospheric Influences on Solar Activity*, Vol. 383 of *Astronomical Society of the Pacific Conference Series*, p. 221

Hudson, H. S. and Ohki, K.: 1972, *Solar Phys.* **23(1)**, 155

Hurford, G. J., Schmahl, E. J., Schwartz, R. A., Conway, A. J., Aschwanden, M. J., Csillaghy, A., Dennis, B. R., Johns-Krull, C., Krucker, S., Lin, R. P., McTiernan, J., Metcalf, T. R., Sato, J., and Smith, D. M.: 2002, *Solar Phys.* **210(1)**, 61

Jain, R. and Haber, D.: 2002, *Astron. Astrophys.* **387**, 1092

Jefferies, S. M., McIntosh, S. W., Armstrong, J. D., Bogdan, T. J., Cacciani, A., and Fleck, B.: 2006, *Astrophys. J. Lett.* **648(2)**, L151

Jess, D. B., Morton, R. J., Verth, G., Fedun, V., Grant, S. D. T., and Giagkiozis, I.: 2015, *Space Sci. Rev.* **190(1-4)**, 103

Khomenko, E. and Cally, P. S.: 2012, *Astrophys. J.* **746(1)**, 68

Khomenko, E. and Collados, M.: 2006, *Astrophys. J.* **653(1)**, 739

Khomenko, E. and Collados, M.: 2009, *Astron. Astrophys.* **506(2)**, L5

Kneer, F. and Bello González, N.: 2011, *Astron. Astrophys.* **532**, A111

Kontogiannis, I., Tsiropoula, G., and Tziotziou, K.: 2010a, *Astron. Astrophys.* **510**, A41

Kontogiannis, I., Tsiropoula, G., and Tziotziou, K.: 2014, *Astron. Astrophys.* **567**, A62

Kontogiannis, I., Tsiropoula, G., and Tziotziou, K.: 2016, *Astron. Astrophys.* **585**, A110

Kontogiannis, I., Tsiropoula, G., Tziotziou, K., and Georgoulis, M. K.: 2010b, *Astron. Astrophys.* **524**, A12

Kosovichev, A. G.: 2015, in *Extraterrestrial Seismology*, pp 306–322

Kosovichev, A. G. and Zharkova, V. V.: 1998, *Nature* **393(6683)**, 317

Krijger, J. M., Rutten, R. J., Lites, B. W., Straus, T., Shine, R. A., and Tarbell, T. D.: 2001, *Astron. Astrophys.* **379**, 1052

Kumar, B., Raja Bayanna, A., Venkatakrishnan, P., and Kuchandy Mathew, S.: 2016a, *Research in Astronomy and Astrophysics* **16(8)**, 129

Kumar, B., Raja Bayanna, A., Venkatakrishnan, P., and Kuchandy Mathew, S.: 2016b, *Research in Astronomy and Astrophysics* **16(8)**, 129

Kumar, B. and Ravindra, B.: 2006, *Journal of Astrophysics and Astronomy* **27**, 425

Kumar, P., Duvall, T. L., J., Harvey, J. W., Jefferies, S. M., Pomerantz, M. A., and Thompson, M. J.: 1990, in Y. Osaki and H. Shibahashi (eds.), *Progress of Seismology of the Sun and Stars*, Vol. 367, p. 87

Kumar, P. and Lu, E.: 1991, *Astrophys. J. Lett.* **375**, L35

Kuridze, D., Zaqarashvili, T. V., Shergelashvili, B. M., and Poedts, S.: 2008, *Annales Geophysicae* **26(10)**, 2983

Landolfi, M. and Landi Degl'Innocenti, E.: 1982, *Solar Phys.* **78(2)**, 355

Lang, K. R.: 2008, *The sun from Space*, Springer, 2 edition

Leibacher, J. W., Noyes, R. W., Toomre, J., and Ulrich, R. K.: 1985, *Scientific American* **253**, 48

Leibacher, J. W. and Stein, R. F.: 1971, *Astrophysical Letters* **7**, 191

Leibacher, J. W. and Stein, R. F.: 1981, in S. Jordan (ed.), *NASA Special Publication*, Vol. 450, pp 263–287

Leighton, R. B., Noyes, R. W., and Simon, G. W.: 1962, *Astrophys. J.* **135**, 474

Leka, K. D., Barnes, G., Crouch, A. D., Metcalf, T. R., Gary, G. A., Jing, J., and Liu, Y.: 2009, *Solar Phys.* **260(1)**, 83

Lemen, J. R., Title, A. M., Akin, D. J., Boerner, P. F., Chou, C., Drake, J. F., Duncan, D. W., Edwards, C. G., Friedlaender, F. M., Heyman, G. F., Hurlburt, N. E., Katz, N. L., Kushner, G. D., Levay, M., Lindgren, R. W., Mathur, D. P., McFeaters, E. L., Mitchell, S., Rehse, R. A., Schrijver, C. J., Springer, L. A., Stern, R. A., Tarbell, T. D., Wuelser, J.-P., Wolfson, C. J., Yanari, C., Bookbinder, J. A., Cheimets, P. N., Caldwell, D., Deluca, E. E., Gates, R., Golub, L., Park, S., Podgorski, W. A., Bush, R. I., Scherrer, P. H., Gummin, M. A., Smith, P., Auker, G., Jerram, P., Pool, P., Soufli, R., Windt, D. L., Beardsley, S., Clapp, M., Lang, J., and Waltham, N.: 2012, *Solar Phys.* **275(1-2)**, 17

Libbrecht, K. G.: 1988, *Astrophys. J.* **334**, 510

Lighthill, J.: 1978, *Waves in Fluids*, Cambridge University Press, Cambridge

Lighthill, M. J.: 1952, *Proceedings of the Royal Society of London Series A* **211(1107)**, 564

Lighthill, M. J.: 1967, in R. N. Thomas (ed.), *Aerodynamic Phenomena in Stellar Atmospheres*, Vol. 28, p. 429

Lin, R. P., Dennis, B. R., Hurford, G. J., Smith, D. M., Zehnder, A., Harvey, P. R., Curtis, D. W., Pankow, D., Turin, P., Bester, M., Csillaghy, A., Lewis, M., Madden, N., van Beek, H. F., Appleby, M., Raudorf, T., McTiernan, J., Ramaty, R., Schmahl, E., Schwartz, R., Krucker, S., Abiad, R., Quinn, T., Berg, P., Hashii, M., Sterling, R., Jackson, R., Pratt, R., Campbell, R. D., Malone, D., Landis, D., Barrington-Leigh, C. P., Slassi-Sennou, S., Cork, C., Clark, D., Amato, D., Orwig, L., Boyle, R., Banks, I. S., Shirey, K., Tolbert, A. K., Zarro, D., Snow, F., Thomsen, K., Henneck, R., McHedlishvili, A., Ming, P., Fivian, M., Jordan, J., Wanner, R., Crubb, J., Preble, J., Matranga, M., Benz, A., Hudson, H., Canfield, R. C., Holman, G. D., Crannell, C., Kosugi, T., Emslie, A. G., Vilmer, N., Brown, J. C., Johns-Krull, C., Aschwanden, M., Metcalf, T., and Conway, A.: 2002, *Solar Phys.* **210(1)**, 3

Lindsey, C. and Donea, A. C.: 2008, *Solar Phys.* **251(1-2)**, 627

Mathew, S. K.: 2009a, in S. V. Berdyugina, K. N. Nagendra, and R. Ramelli (eds.), *Solar Polarization 5: In Honor of Jan Stenflo*, Vol. 405 of *Astronomical Society of the Pacific Conference Series*, p. 461

Mathew, S. K.: 2009b, in S. V. Berdyugina, K. N. Nagendra, and R. Ramelli (eds.), *Solar Polarization 5: In Honor of Jan Stenflo*, Vol. 405 of *Astronomical Society of the Pacific Conference Series*, p. 461

Mathew, S. K., Bayanna, A. R., Tiwary, A. R., Bireddy, R., and Venkatakrishnan, P.: 2017a, *Solar Phys.* **292(8)**, 106

Mathew, S. K., Bayanna, A. R., Tiwary, A. R., Bireddy, R., and Venkatakrishnan, P.: 2017b, *Solar Phys.* **292(8)**, 106

Maurya, R. A. and Ambastha, A.: 2009, *Solar Phys.* **258(1)**, 31

Maurya, R. A., Vemareddy, P., and Ambastha, A.: 2012, *Astrophys. J.* **747(2)**, 134

McIntosh, S. W., Fleck, B., and Judge, P. G.: 2003, *Astron. Astrophys.* **405**, 769

McIntosh, S. W. and Jefferies, S. M.: 2006, *Astrophys. J. Lett.* **647(1)**, L77

McIntosh, S. W. and Judge, P. G.: 2001, *Astrophys. J.* **561(1)**, 420

Metcalf, T. R.: 1994, *Solar Phys.* **155(2)**, 235

Mihalas, B. W. and Toomre, J.: 1981, *Astrophys. J.* **249**, 349

Mihalas, B. W. and Toomre, J.: 1982, *Astrophys. J.* **263**, 386

Mihalas, D. and Mihalas, B. W.: 1995a, *Foundations of Radiation Hydrodynamics*, Oxford University Press, 1 edition

Mihalas, D. and Mihalas, B. W.: 1995b, *Foundations of Radiation Hydrodynamics*, Oxford University Press

Mitalas, R. and Sills, K. R.: 1992, *Astrophys. J.* **401**, 759

Moradi, H., Donea, A. C., Lindsey, C., Besliu-Ionescu, D., and Cally, P. S.: 2007, *Mon. Not. Roy. Astron. Soc.* **374(3)**, 1155

Moretti, P. F., Jefferies, S. M., Armstrong, J. D., and McIntosh, S. W.: 2007, *Astron. Astrophys.* **471(3)**, 961

Nagashima, K., Löptien, B., Gizon, L., Birch, A. C., Cameron, R., Couvidat, S., Danilovic, S., Fleck, B., and Stein, R.: 2014, *Solar Phys.* **289(9)**, 3457

Nagashima, K., Sekii, T., Kosovichev, A. G., Shibahashi, H., Tsuneta, S., Ichimoto, K., Katsukawa, Y., Lites, B., Nagata, S., Shimizu, T., Shine, R. A., Suematsu, Y., Tarbell, T. D., and Title, A. M.: 2007, *Pub. Astron. Soc. Japan* **59**, S631

Norton, A. A., Graham, J. P., Ulrich, R. K., Schou, J., Tomczyk, S., Liu, Y., Lites, B. W., López Ariste, A., Bush, R. I., Socas-Navarro, H., and Scherrer, P. H.: 2006, *Solar Phys.* **239(1-2)**, 69

Noyes, R. W. and Leighton, R. B.: 1963, *Astrophys. J.* **138**, 631

Nutto, C., Steiner, O., Schaffenberger, W., and Roth, M.: 2012, *Astron. Astrophys.* **538**, A79

Orrall, F. Q.: 1965, *Astrophys. J.* **141**, 1131

Ortiz, A., Bellot Rubio, L. R., Hansteen, V. H., de la Cruz Rodríguez, J., and Rouppe van der Voort, L.: 2014, *Astrophys. J.* **781(2)**, 126

Parker, E. N.: 1955, *Astrophys. J.* **121**, 491

Patterson, A.: 1984, *Astrophys. J.* **280**, 884

Patterson, A. and Zirin, H.: 1981, *Astrophys. J. Lett.* **243**, L99

Pesnell, W. D., Thompson, B. J., and Chamberlin, P. C.: 2012, *Solar Phys.* **275**, 3

Petrie, G. J. D.: 2012, *Astrophys. J.* **759(1)**, 50

Petrie, G. J. D.: 2014, *Solar Phys.* **289(10)**, 3663

Petrie, G. J. D. and Sudol, J. J.: 2010, *Astrophys. J.* **724(2)**, 1218

Priest, E.: 2014, *Magnetohydrodynamics of the Sun*, Cambridge University Press, 3 edition

Priest, E. R.: 1984, *Solar magneto-hydrodynamics*

Qiu, J. and Gary, D. E.: 2003, *Astrophys. J.* **599(1)**, 615

Raja Bayanna, A., Kumar, B., Venkatakrishnan, P., Kunchandy Mathew, S., Ravindra, B., Mathur, S., and Garcia, R. A.: 2014a, *Research in Astronomy and Astrophysics* **14(2)**, 207

Raja Bayanna, A., Mathew, S. K., Venkatakrishnan, P., and Srivastava, N.: 2014b, *Solar Phys.* **289**, 4007

Rajaguru, S. P., Couvidat, S., Sun, X., Hayashi, K., and Schunker, H.: 2013, *Solar Phys.* **287(1-2)**, 107

Rajaguru, S. P., Sangeetha, C. R., and Tripathi, D.: 2019, *Astrophys. J.* **871(2)**, 155

Rajaguru, S. P., Wachter, R., Sankarasubramanian, K., and Couvidat, S.: 2010, *Astrophys. J. Lett.* **721(2)**, L86

Reardon, K. P. and Cavallini, F.: 2008, *Astron. Astrophys.* **481(3)**, 897

Rijs, C., Rajaguru, S. P., Przybylski, D., Moradi, H., Cally, P. S., and Shelyag, S.: 2016, *Astrophys. J.* **817(1)**, 45

Rimmele, T. R., Warner, M., Keil, S. L., Goode, P. R., Knölker, M., Kuhn, J. R., Rosner, R. R., McMullin, J. P., Casini, R., Lin, H., Wöger, F., von der Lühe, O., Tritschler, A., Davey, A., de Wijn, A., Elmore, D. F., Fehlmann, A., Harrington, D. M., Jaeggli, S. A., Rast, M. P., Schad, T. A., Schmidt, W., Mathioudakis, M., Mickey, D. L., Anan, T., Beck, C., Marshall, H. K., Jeffers, P. F., Oschmann, J. M., Beard, A., Berst, D. C., Cowan, B. A., Craig, S. C., Cross, E., Cummings, B. K., Donnelly, C., de Vanssay, J.-B., Eigenbrot, A. D., Ferayorni, A., Foster, C., Galapon, C. A., Gedrites, C., Gonzales, K., Goodrich, B. D., Gregory, B. S., Guzman, S. S., Guzzo, S., Hegwer, S., Hubbard, R. P., Hubbard, J. R., Johansson, E. M., Johnson, L. C., Liang, C., Liang, M., McQuillen, I., Mayer, C., Newman, K., Onodera, B., Phelps, L., Puentes, M. M., Richards, C., Rimmele, L. M., Sekulic, P., Shimko, S. R., Simison, B. E., Smith, B., Starman, E., Sueoka, S. R., Summers, R. T., Szabo, A., Szabo, L., Wampler, S. B., Williams, T. R., and White, C.: 2020, *Solar Phys.* **295(12)**, 172

Rosenthal, C. S., Bogdan, T. J., Carlsson, M., Dorch, S. B. F., Hansteen, V., McIntosh, S. W., McMurry, A., Nordlund, Å., and Stein, R. F.: 2002, *Astrophys. J.* **564(1)**, 508

Rutten, R. J. and Krijger, J. M.: 2003, *Astron. Astrophys.* **407**, 735

Sarkar, R. and Srivastava, N.: 2018, *Solar Phys.* **293(2)**, 16

Scharmer, G. B., Bjelksjo, K., Korhonen, T. K., Lindberg, B., and Petterson, B.: 2003, in S. L. Keil and S. V. Avakyan (eds.), *Innovative Telescopes and Instrumentation for Solar Astrophysics*, Vol. 4853 of *Society of Photo-Optical Instrumentation Engineers (SPIE) Conference Series*, pp 341–350

Scherrer, P. H., Bogart, R. S., Bush, R. I., Hoeksema, J. T., Kosovichev, A. G., Schou, J., Rosenberg, W., Springer, L., Tarbell, T. D., Title, A., Wolfson, C. J., Zayer, I., and MDI Engineering Team: 1995, *Solar Phys.* **162(1-2)**, 129

Scherrer, P. H., Schou, J., Bush, R. I., Kosovichev, A. G., Bogart, R. S., Hoeksema, J. T., Liu, Y., Duvall, T. L., Zhao, J., Title, A. M., Schrijver, C. J., Tarbell, T. D., and Tomczyk, S.: 2012, *Solar Phys.* **275**, 207

Schunker, H. and Braun, D. C.: 2011, *Solar Phys.* **268(2)**, 349

Schwabe, H.: 1844, *Astronomische Nachrichten* **21(15)**, 233

Schwarzschild, M.: 1948, *Astrophys. J.* **107**, 1

Simon, G. W. and Leighton, R. B.: 1964, *Astrophys. J.* **140**, 1120

Solanki, S. K., Inhester, B., and Schüssler, M.: 2006, *Reports on Progress in Physics* **69(3)**, 563

Stein, R. F.: 1967, *Solar Phys.* **2(4)**, 385

Stix, M.: 2004, *The Sun*, Springer-verlag Gmbh, 2 edition

Straus, T., Fleck, B., Jefferies, S. M., Cauzzi, G., McIntosh, S. W., Reardon, K., Severino, G., and Steffen, M.: 2008, *Astrophys. J. Lett.* **681(2)**, L125

Sudol, J. J. and Harvey, J. W.: 2005, *Astrophys. J.* **635(1)**, 647

Thomas, J. H. and Stanchfield, Donald C. H., I.: 2000, *Astrophys. J.* **537(2)**, 1086

Thomas, J. H. and Weiss, N. O.: 2004, *Ann. rev. Astron. Astrophys.* **42(1)**, 517

Toner, C. G. and Labonte, B. J.: 1993, *Astrophys. J.* **415**, 847

Torrence, C. and Compo, G. P.: 1998, *Bulletin of the American Meteorological Society* **79(1)**, 61

Ulrich, R. K.: 1970, *Astrophys. J.* **162**, 993

Vecchio, A., Cauzzi, G., and Reardon, K. P.: 2009, *Astron. Astrophys.* **494(1)**, 269

Vecchio, A., Cauzzi, G., Reardon, K. P., Janssen, K., and Rimmele, T.: 2007, *Astron. Astrophys.* **461(1)**, L1

Venkatakrishnan, P., Kumar, B., and Uddin, W.: 2008, *Mon. Not. Roy. Astron. Soc.* **387(1)**, L69

Venkatakrishnan, P., Mathew, S. K., Srivastava, N., Bayanna, A. R., Kumar, B., Ramya, B., Jain, N., and Saradava, M.: 2017a, *Current Science* **113(4)**, 686

Venkatakrishnan, P., Mathew, S. K., Srivastava, N., Bayanna, A. R., Kumar, B., Ramya, B., Jain, N., and Saradava, M.: 2017b, *Current Science* **113(4)**, 686

Vernazza, J. E., Avrett, E. H., and Loeser, R.: 1981, *Astro Phys. Suppl. Series* **45**, 635

Vigeesh, G., Jackiewicz, J., and Steiner, O.: 2017, *Astrophys. J.* **835(2)**, 148

Vigeesh, G. and Roth, M.: 2020, *Astron. Astrophys.* **633**, A140

Vigeesh, G., Roth, M., Steiner, O., and Fleck, B.: 2021, *Philosophical Transactions of the Royal Society of London Series A* **379(2190)**, 20200177

Vigeesh, G., Roth, M., Steiner, O., and Jackiewicz, J.: 2019, *Astrophys. J.* **872(2)**, 166

Wang, H.: 1992, *Solar Phys.* **140(1)**, 85

Wang, H., Ewell, M. W., J., Zirin, H., and Ai, G.: 1994, *Astrophys. J.* **424**, 436

Wang, H., Spirock, T. J., Qiu, J., Ji, H., Yurchyshyn, V., Moon, Y.-J., Denker, C., and Goode, P. R.: 2002, *Astrophys. J.* **576(1)**, 497

Whitney, C. A.: 1958, *Smithsonian Contributions to Astrophysics* **2**, 365

Wiegelmann, T., Thalmann, J. K., and Solanki, S. K.: 2014, *Astron. Astrophys. Rev.* **22**, 78

Wolff, C. L.: 1972a, *Astrophys. J.* **176**, 833

Wolff, C. L.: 1972b, *Astrophys. J.* **176**, 833

Woods, T. N., Eparvier, F. G., Hock, R., Jones, A. R., Woodraska, D., Judge, D., Didkovsky, L., Lean, J., Mariska, J., Warren, H., McMullin, D., Chamberlin, P., Berthiaume, G., Bailey, S., Fuller-Rowell, T., Sojka, J., Tobiska, W. K., and Viereck, R.: 2012, *Solar Phys.* **275(1-2)**, 115

Zhao, J., Rajaguru, S. P., and Chen, R.: 2022, *Astrophys. J.* **933(1)**, 109

Zharkova, V. V. and Zharkov, S. I.: 2007, *Astrophys. J.* **664(1)**, 573

Zwaan, C.: 1978, *Solar Phys.* **60(2)**, 213

Zwaan, C.: 1987, *Ann. rev. Astron. Astrophys.* **25**, 83

List of Publications

Publications in Journals

1. **Kumar, H.**, and Kumar, B., 2020 *"On the seismic emission in sunspots associated with Lorentz force changes accompanying major solar flares"*, Monthly Notices of the Royal Astronomical Society, Volume 497, Pages 976-987, https://doi.org/10.1093/mnras/staa1974.

2. **Kumar, H.**, Kumar, B., Rajaguru S. P., Mathew S. K., and Bayanna, A. R., 2022 *"A study of the propagation of acoustic waves in small-scale magnetic fields using solar photospheric and chromospheric Dopplergrams: HMI/SDO and MAST observations"*, J. Atmos. Sol. Terr. Phys. (2023) https://doi.org/10.1016/j.jastp.2023.106071.

3. **Kumar, H.**, Kumar, B., and Rajaguru S. P., 2022 *"On the propagation of gravity waves in the lower solar atmosphere in different magnetic configurations"*, Advances in Space Research (2023), https://doi.org/10.1016/j.asr.2023.04.054.

Publications attached with thesis

1. **Kumar, H.**, and Kumar, B., 2020 *"On the seismic emission in sunspots associated with Lorentz force changes accompanying major solar flares"*, Monthly Notices of the Royal Astronomical Society, Volume 497, Pages 976-987, https://doi.org/10.1093/mnras/staa1974.

2. **Kumar, H.**, Kumar, B., Rajaguru S. P., Mathew S. K., and Bayanna, A. R., 2022 *"A study of the propagation of acoustic waves in small-scale magnetic fields using solar photospheric and chromospheric Dopplergrams: HMI/SDO and MAST observations"*, J. Atmos. Sol. Terr. Phys. (2023) https://doi.org/10.1016/j.jastp.2023.106071.

3. **Kumar, H.**, Kumar, B., and Rajaguru S. P., 2022 *"On the propagation of gravity waves in the lower solar atmosphere in different magnetic configurations"*, Advances in Space Research (2023), https://doi.org/10.1016/j.asr.2023.04.054.

Monthly Notices of the ROYAL ASTRONOMICAL SOCIETY

MNRAS **497,** 976–987 (2020)
Advance Access publication 2020 July 8

doi:10.1093/mnras/staa1974

On the seismic emission in sunspots associated with Lorentz force changes accompanying major solar flares

Hirdesh Kumar[1,2]★ and Brajesh Kumar[1]★

[1]*Udaipur Solar Observatory, Physical Research Laboratory, Dewali, Badi Road, Udaipur 313004 Rajasthan, India*
[2]*Department of Physics, Indian Institute of Technology Gandhinagar, Gandhinagar 382 355 Gujarat, India*

Accepted 2020 July 1. Received 2020 July 1; in original form 2020 May 15

ABSTRACT

Solar flares are known to generate seismic waves in the Sun. We present a detailed analysis of seismic emission in sunspots accompanying M- and X-class solar flares. For this purpose, we have used high-resolution Dopplergrams and line-of-sight magnetograms at a cadence of 45 s, along with vector magnetograms at a cadence of 135 s obtained from Helioseismic and Magnetic Imager instrument aboard the *Solar Dynamics Observatory* space mission. In order to identify the location of flare ribbons and hard X-ray footpoints, we have also used Hα chromospheric intensity observations obtained from Global Oscillation Network Group instruments and hard X-ray images in 12–25 keV band from the *Reuvan Ramaty High Energy Solar Spectroscopic Imager* spacecraft. The fast Fourier transform technique is applied to construct the acoustic velocity power map in 2.5–4 mHz band for pre-flare, spanning flare, and post-flare epochs for the identification of seismic emission locations in the sunspots. In the power maps, we have selected only those locations which are away from the flare ribbons and hard X-ray footpoints. These regions are believed to be free from any flare related artefacts in the observational data. We have identified concentrated locations of acoustic power enhancements in sunspots accompanying major flares. Our investigation provides evidence that abrupt changes in the magnetic fields and associated impulsive changes in the Lorentz force could be the driving source for these seismic emissions in the sunspots during solar flares.

Key words: Sun: flares – Sun: magnetic fields – Sun: oscillations – Sun: photosphere – sunspots.

1 INTRODUCTION

Solar flares are the magnetized events in the solar atmosphere, in which previously stored magnetic energy of the order of 10^{27}–10^{32} erg are released into the solar atmosphere in the form of thermal radiation, mass motion, and accelerated charged particles within few minutes to an hour. During solar flares, the back bombarded charged particles gyrate along the magnetic fields lines and generate gyrosynchrotron emissions (Hudson & Ohki 1972). The bremsstrahlung radiation generated by deacceleration of charged particles while striking the chromospheric plasma produces hard X-rays (Brown 1971). It was suggested by Wolff (1972) that large solar flares could also stimulate free global oscillations in the Sun. Much later, Fisher, Canfield & McClymont (1985) proposed that during the course of solar flares, the bombardment of charged particles on the chromospheric layers heats the chromospheric plasma and, as result of that, chromospheric evaporation into the corona takes place. Further, the downward settlement of the condensed material can launch a shock on the photosphere thereby delivering large momentum to the photospheric layers (Fisher 1989) and this high amount of energy can excite the acoustic waves inside the Sun. Kosovichev & Zharkova (1998) found the first instance of flare-induced seismic emission in the Sun during a moderate X-class solar flare, which occurred on 1996 July 09, using the data from Michelson Doppler Imager (MDI; Scherrer et al. 1995) instrument aboard the *Solar and Heliospheric Observatory* (*SOHO*; Domingo, Fleck & Poland 1995) space mission. They identified this phenomenon as 'sunquake'. Later on, there are several others cases reported by Donea & Lindsey (2005), Donea et al. (2006), Moradi et al. (2007), and Kumar & Ravindra (2006), in which they have found acoustic emissions accompanying different classes of solar flares. Zharkova & Zharkov (2007) found acoustic emissions in a proton-rich solar flare and they explained these enhancements as due to the backreaction of the shock driven by high energetic charged particles impinging on the solar photosphere during the flare. Following this, Venkatakrishnan, Kumar & Uddin (2008) observationally found that these high energetic charged particles can reach up to the photosphere from the chromosphere in a time span of about 1 min and thus could be responsible for enhancing the velocity oscillations. Hudson, Fisher & Welsch (2008) proposed an another mechanism, known as 'magnetic jerk', which could be responsible for the generation of seismic waves in sunspots, apart from the high energetic charged particles and backreaction of shock at the solar photosphere.

It is well established that during solar flares, magnetic fields of the corona change and the signatures of those appear in the form of the temporal evolution of the magnetic fields at the photosphere. The changes in the magnetic fields take place within short time-scales before the flare, during the flare, and the post-flare epochs. Patterson & Zirin (1981) were the first to report the rapid short-term changes (transient changes) in the magnetic fields during solar flares. Further, Patterson (1984) illustrated that these observed transient

★ E-mail: hirdesh@prl.res.in (HK); brajesh@prl.res.in (BK)

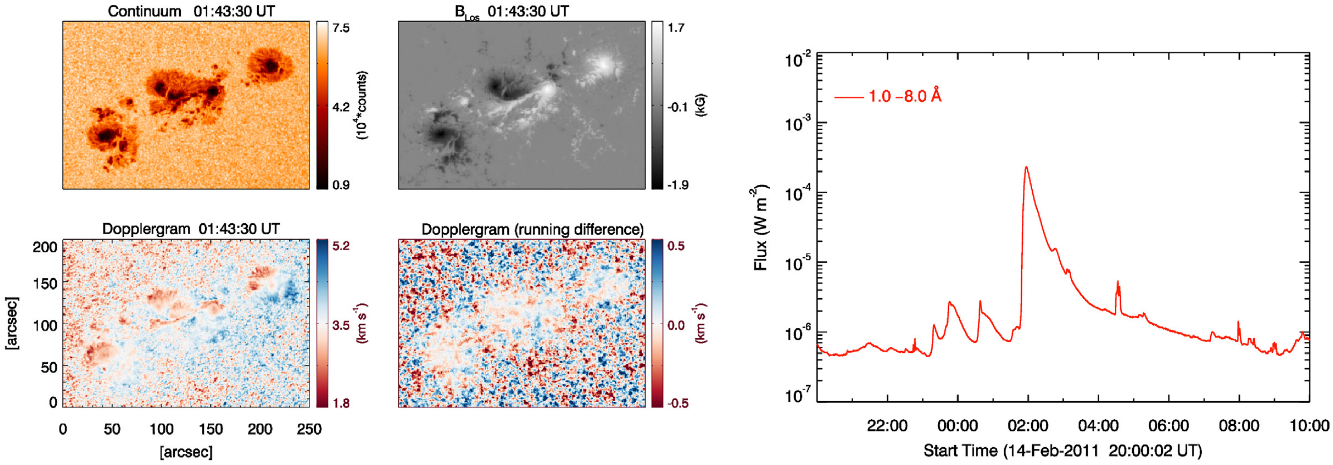

Figure 1. Left-hand panel: sample images of the active region NOAA 11158 showing continuum intensity image (top left panel), photospheric line-of-sight (i.e. longitudinal and scalar) magnetic fields (top right panel), Dopplergram (bottom left panel), and running difference of Doppler images (bottom right panel) acquired from HMI instrument aboard *SDO* spacecraft on 2011 February 15. Right-hand panel: plot shows the temporal evolution of disc-integrated solar flux in 1–8 Å band during an X2.2 class flare on 2011 February 15, obtained from *GOES* satellite.

Table 1. Details of the active regions used in our analysis and information related to the flare evolution as seen in GOES soft X-ray (1–8 Å band).

Active region	Location on the disc	Flare class	Date	Start time	Peak time	Decay time
NOAA 11158	S28W17	X2.2	2011 February 15	01:44 UT	01:56 UT	02:06 UT
NOAA 11261	N15W35	M6.0	2011 August 03	13:17 UT	13:48 UT	14:10 UT
NOAA 11882	S06E28	M2.7	2013 October 28	14:46 UT	15:01 UT	15:04 UT
NOAA 11882	S06E28	M4.4	2013 October 28	15:07 UT	15:15 UT	15:21 UT
NOAA 12222	S20W31	M6.1	2014 December 04	18:05 UT	18:25 UT	18:56 UT
NOAA 12241	S09W09	M6.9	2014 December 18	21:41 UT	21:58 UT	22:25 UT
NOAA 12242	S21W24	X1.8	2014 December 20	00:11 UT	00:28 UT	00:58 UT
NOAA 12297	S16E13	X2.0	2015 March 11	16:11 UT	16:22 UT	16:29 UT
NOAA 12371	N13W06	C3.9	2015 June 22	17:20 UT	17:27 UT	17:33 UT
NOAA 12371	N13W06	M6.5	2015 June 22	17:39 UT	18:23 UT	18:23 UT

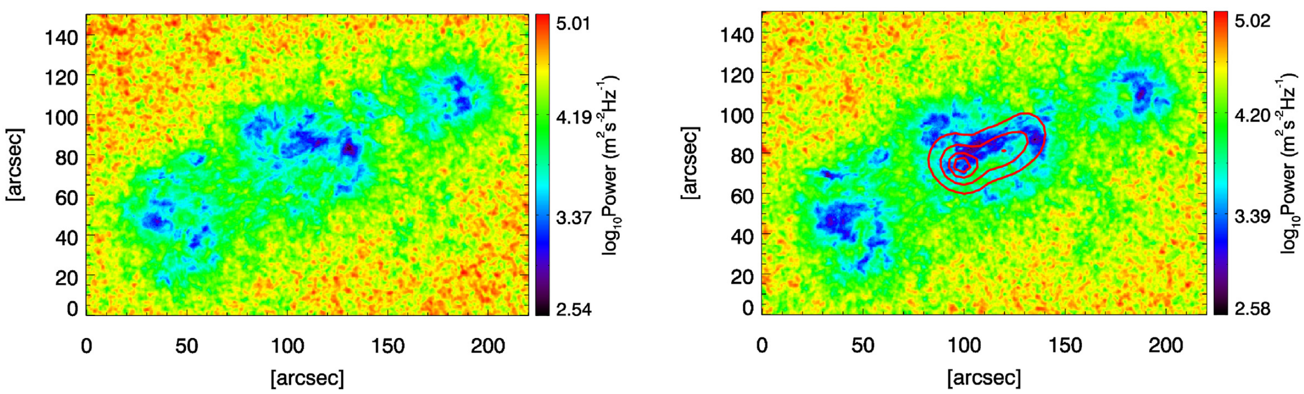

Figure 2. Left-hand panel: acoustic power map of active region NOAA 11158 in 2.5–4 mHz band estimated over 2 h duration for pre-flare epoch. Right-hand panel: same as shown in the left-hand panel but for spanning the flare. Here, red contours represent hard X-ray footpoints at 25, 50, 75, and 90 per cent of its maximum as observed in 12–25 keV band from *RHESSI* spacecraft.

changes in the magnetic fields could be due to emission in the core of the spectral line, which is used to derive the information of the magnetic fields. In addition, Qiu & Gary (2003) discussed the possibility of change in line profiles during a transient polarity reversal observed in the photospheric magnetic field measurements obtained from the MDI instrument aboard *SOHO* space mission. Wang (1992) and Wang et al. (1994, 2002) reported abrupt and permanent changes in the evolution of magnetic fields in the flaring region during the different class of solar flares using the data from Big Bear Solar Observatory. Later on, extensive analysis done by Sudol & Harvey (2005) and Petrie & Sudol (2010) of X- and M-class solar flares using the line-of-sight (i.e. longitudinal) magnetic fields obtained from Global Oscillation Network Group (GONG; Harvey et al. 1996) instruments, showed abrupt and permanent changes in the

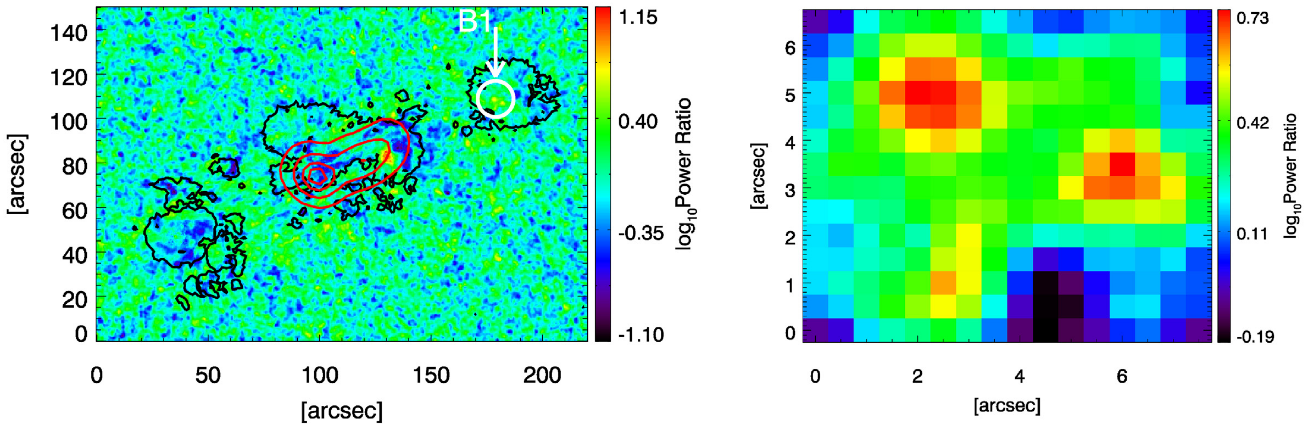

Figure 3. Left-hand panel: this illustrates the ratio of acoustic power maps estimated for spanning flare and pre-flare epochs in the 2.5–4 mHz band. Here, black contours represent the outer boundary of the sunspot penumbra obtained from continuum intensity image, whereas the red contours represent hard X-ray footpoints from *RHESSI* spacecraft in 12–25 keV band. Right-hand panel: illustrates the blow-up region of ‘B1’ enhanced location in the sunspot as indicated in the power map ratio.

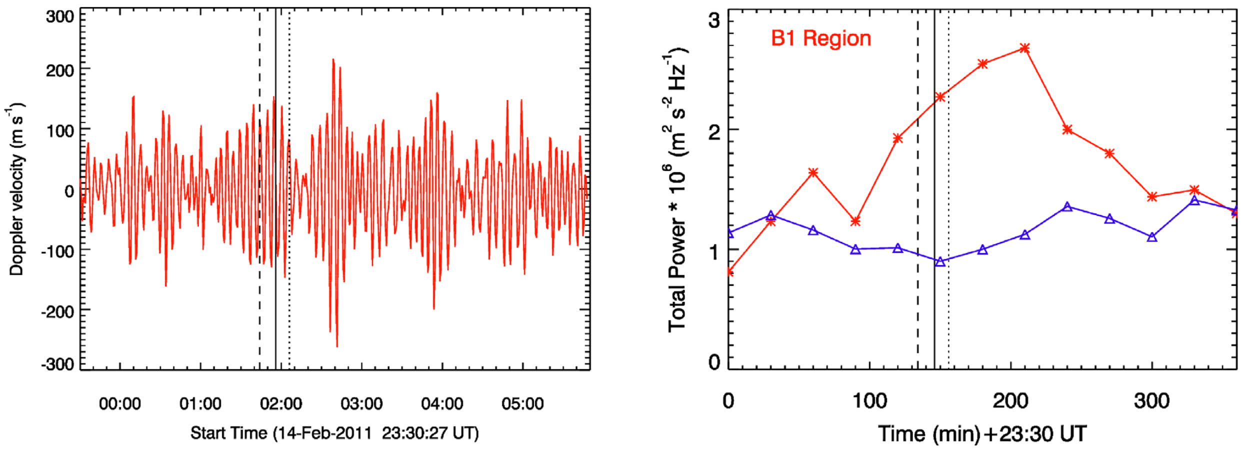

Figure 4. Left-hand panel: plot in red colour shows the temporal evolution of Doppler velocity at a cadence of 45 s in the ‘B1’ location of active region NOAA 11158. The dashed, solid, and dotted vertical lines represent onset, peak, and decay time of the flare. Right-hand panel: plot showing the temporal evolution of integrated acoustic power over the ‘B1’ location (red colour with asterisks) whereas that shown in blue colour with triangles represents evolution of total power in an unaffected region in the same sunspot. It is to be noted that there is a time offset of about ± 30 min between the acoustic power variation and the *GOES* flare time.

magnetic fields in the flaring locations within 10-min duration with a median magnitude of 100 G. In addition, Kumar et al. (2016) also found abrupt and persistent changes in line-of-sight magnetic fields at different locations in active region during an M6.5 class solar flare using the data from Helioseismic and Magnetic Imager (HMI; Schou et al. 2012) instrument aboard the *Solar Dynamics Observatory* (*SDO*; Pesnell, Thompson & Chamberlin 2012) space mission.

Hudson et al. (2008) and Fisher et al. (2012) proposed that abrupt changes in the magnetic fields can lead to an impulsive change in Lorentz force, which is also known as ‘magnetic-jerk’, and this can induce seismic emission in the sunspots. However, Raja Bayanna et al. (2014) observed distortions in the two circular polarization states of light, the left (LCP) and the right circular polarization (RCP) observations in the flaring locations which showed transient changes in Doppler velocity and line-of-sight magnetic fields during an X-class flare, using the line profile observations from HMI instrument aboard the *SDO* space mission. They showed that observed transient changes in Doppler velocity and line-of-sight magnetic fields in flaring locations are prone to artefacts in the measurements.

Therefore, in this paper, we present a detailed analysis of seismic emission in the sunspots, which are away from the flare ribbons and hard X-ray footpoints accompanying large solar flares. Such acoustic enhancements are supposed to be free from any flare related problems in the observational data.

In the following sections, we first describe the observational data and selection criteria for choosing the active regions aimed for our analysis. This is followed by methods of analysis and the results obtained. We finally conclude with discussions concerning our results.

2 THE OBSERVATIONAL DATA

We have extensively used observations from the HMI instrument aboard the *SDO* spacecraft, which is a solar space mission of the National Aeronautics and Space Administration (NASA). The HMI instrument observes the photosphere of the Sun in Fe I 6173 Å absorption spectral line at six different wavelengths positions in ± 172 mÅ wavelength window in two different cameras. One of the cameras is

Table 2. Details of the active regions and flare produced, identified seismic emission locations in the sunspots, observed changes in the total power and estimated changes in Lorentz force corresponding to the seismic emission locations accompanying the flares.

Active region	Flare class	Seismic emission locations	Change in power (per cent)	Change in Lorentz force (dyne)
NOAA 11158	X2.2	B1	≈ 113	$\approx 2.0 \times 10^{21}$
NOAA 11261	M6.0	D1	≈ 30	$\approx 1.0 \times 10^{21}$
	M6.0	D2	≈ 162	$\approx 0.5 \times 10^{21}$
NOAA 11882	M2.7, M4.4	N1	≈ 56	$\approx 1.5 \times 10^{21}$
	M2.7, M4.4	N2	≈ 123	$\approx 0.2 \times 10^{21}$
NOAA 12222	M6.1	M1	≈ 284	$\approx 1.0 \times 10^{21}$
	M6.1	M2	≈ 151	$\approx 1.0 \times 10^{21}$
NOAA 12241	M6.9	Q1	≈ 192	$\approx 0.3 \times 10^{21}$
	M6.9	Q2	≈ 100	$\approx 0.6 \times 10^{21}$
	M6.9	Q3	≈ 130	$\approx 0.3 \times 10^{21}$
	M6.9	Q4	≈ 166	$\approx 0.2 \times 10^{21}$
	M6.9	Q5	≈ 213	$\approx 0.3 \times 10^{21}$
	M6.9	Q6	≈ 101	$\approx 0.5 \times 10^{21}$
NOAA 12242	X1.8	K1	≈ 114	$\approx 0.1 \times 10^{21}$
	X1.8	K2	≈ 156	$\approx 0.4 \times 10^{21}$
NOAA 12297	X2.0	F1	≈ 76	$\approx 3.0 \times 10^{21}$
	X2.0	F2	≈ 190	$\approx 1.0 \times 10^{21}$
NOAA 12371	C3.9, M6.5	P1	≈ 169	$\approx 0.7 \times 10^{21}$
	C3.9, M6.5	P2	≈ 123	$\approx 0.3 \times 10^{21}$

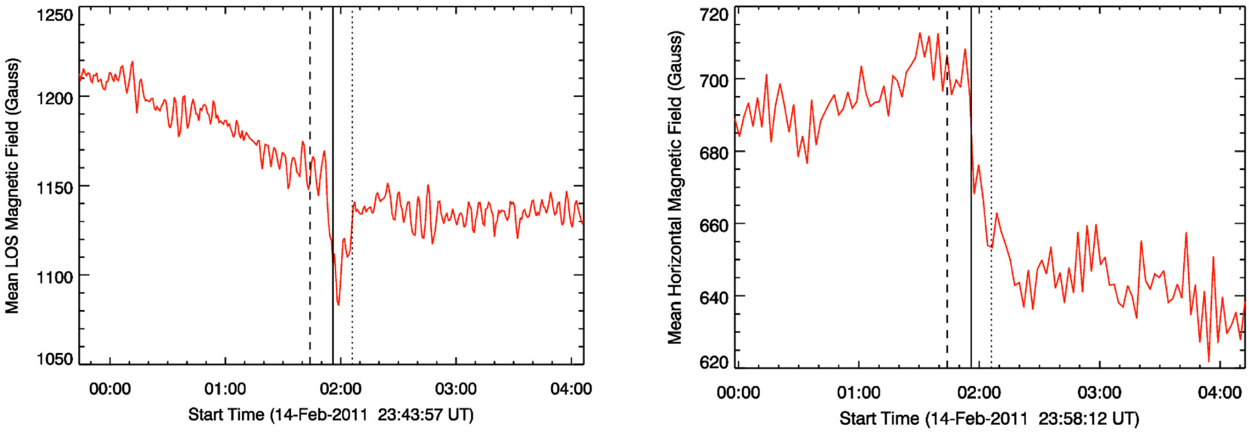

Figure 5. Left-hand panel: plot in red colour shows the temporal evolution of line-of-sight (i.e. longitudinal and scalar) magnetic fields at a cadence of 45 s in the 'B1' location of active region NOAA 11158. Right-hand panel: plot in red colour shows the temporal evolution of horizontal (i.e. transverse) component of vector magnetic fields at a cadence of 135 s in the 'B1' location. The dashed, solid, and dotted vertical lines represent the onset, peak, and decay time of the flare.

mainly dedicated to the 45 s cadence observations, which provides full-disc Dopplergrams, line-of-sight (i.e. longitudinal and scalar) magnetograms and continuum intensity images at spatial sampling of 0.5 arcsec pixel^{-1}. The second camera provides vector magnetic field observations of the solar photosphere with the same spatial sampling. The Stokes parameters (I, Q, U, V) are observed at six different wavelength positions from the centre of Fe I 6173 Å absorption line, which requires 135 s to complete the line profiles (Sun et al. 2017). Then, to extract the vector magnetic field components from these Stokes parameters, Very Fast Inversion of the Stokes algorithm code (Borrero et al. 2011) is used to derive vector magnetic field components at the photosphere. The remaining 180° disambiguity in the azimuthal field component is resolved using the minimum-energy method (Metcalf 1994; Leka et al. 2009). A coordinate transformation for remapping the vector fields on to the Lambert cylindrical equal-area projection is carried out, and finally, the vector fields are transformed into heliocentric spherical coordinates (B_r, B_θ, B_ϕ). These coordinates are approximated to (B_z, -B_y, B_x) in heliographic Cartesian coordinates for ready use in various parameter studies (Gary & Hagyard 1990). Thus, we have used the tracked photospheric continuum intensity (hmi.Ic_45s), Dopplergrams (hmi.V_45s), and line-of-sight magnetograms (hmi.M_45s) at a cadence of 45 s and high cadence vector magnetograms (hmi.B_135s) at a cadence of 135 s, acquired from the HMI instrument aboard the *SDO* spacecraft for our motivated analysis. The left-hand panel of Fig. 1 shows the sample images of the National Oceanic and Atmospheric Administration (NOAA) solar active region 11158 from the HMI instrument, which produced an X2.2 class solar flare on 2011 February 15. In the continuum intensity image, we can see the complex structure of this active region while the morphology of the magnetic fields is seen in the line-of-sight magnetogram. The Dopplergram shows the Doppler velocity flows in the active region while the running difference image of Dopplergrams shows the suppression of velocity oscillations in the sunspots in contrast with the dominant velocity

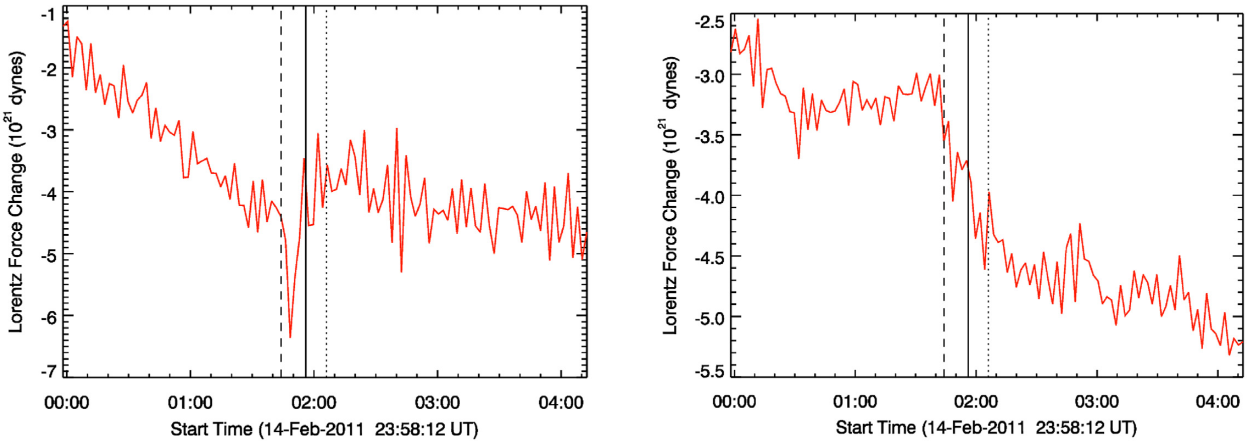

Figure 6. Left-hand panel: plot in red colour shows the temporal evolution of change in radial (i.e. upward) component of Lorentz force in the 'B1' location of the active region NOAA 11158. Right-hand panel: same as shown in the left-hand panel but for change in horizontal (i.e. transverse) component of Lorentz force in the aforementioned location. The dashed, solid, and dotted vertical lines represent the onset, peak, and decay time of the flare.

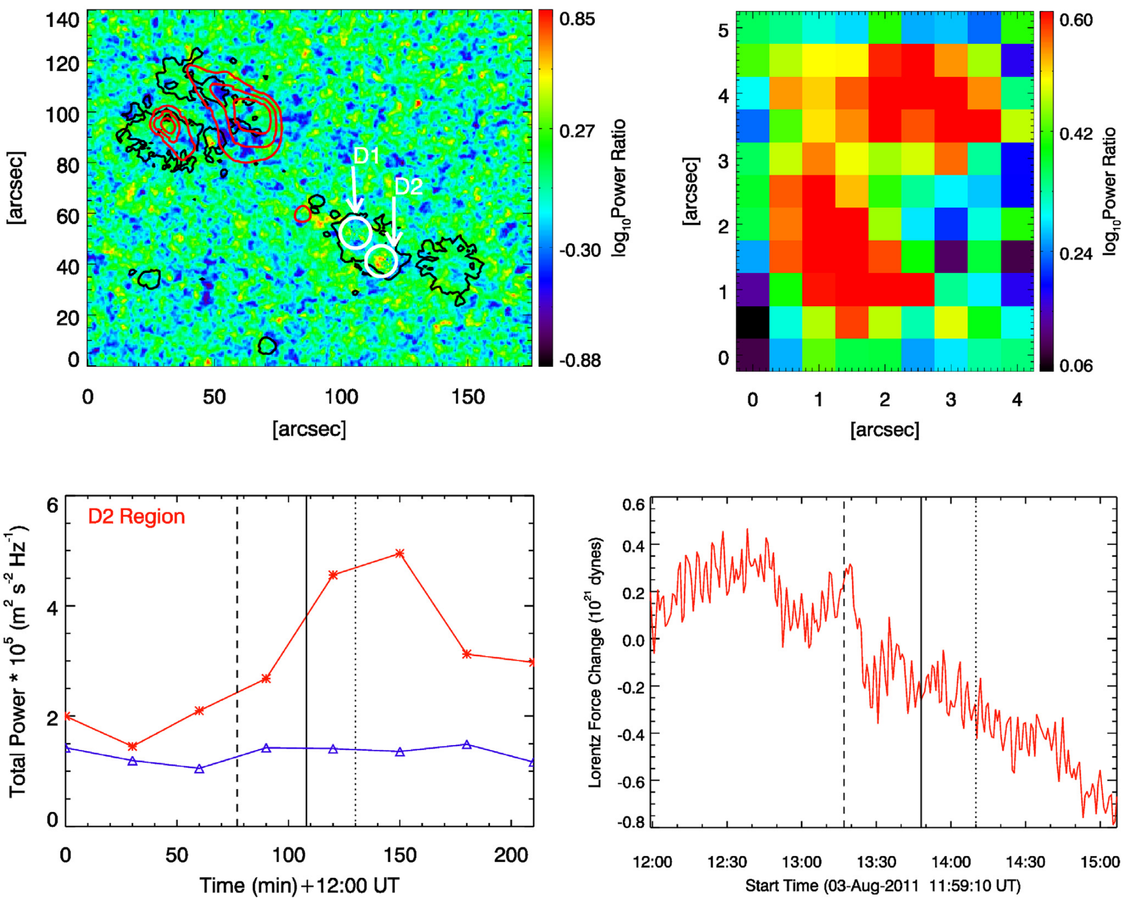

Figure 7. A brief illustration of important results obtained for the active region NOAA 11261. Top left panel: this illustrates the ratio of acoustic power maps estimated for spanning flare and pre-flare epochs in the 2.5–4 mHz band. Here, black contours represent the outer boundary of the sunspot penumbra obtained from continuum intensity image, whereas the red contours represent flare-ribbon locations from Hα chromospheric intensity observations at 70, 80, and 90 per cent of its maximum value as observed by the GONG instrument. Top right panel: illustrates the blow-up region of 'D2' enhanced location in the sunspot as indicated in the power map ratio. Bottom left panel: plots showing the temporal evolution of integrated acoustic power over the 'D2' location (red colour with asterisks) whereas that shown in blue colour with triangles represents evolution of total power in an unaffected region in the same sunspot. It is to be noted that there is a time offset of about ± 30 min between the acoustic power variation and the *GOES* flare time. Bottom right panel: plot in red colour shows the temporal evolution of change in radial (i.e. upward) component of Lorentz force in the 'D2' location. The dashed, solid, and dotted vertical lines represent the onset, peak, and decay time of the flare. The remaining maps and plots have been provided in the online Supporting Information.

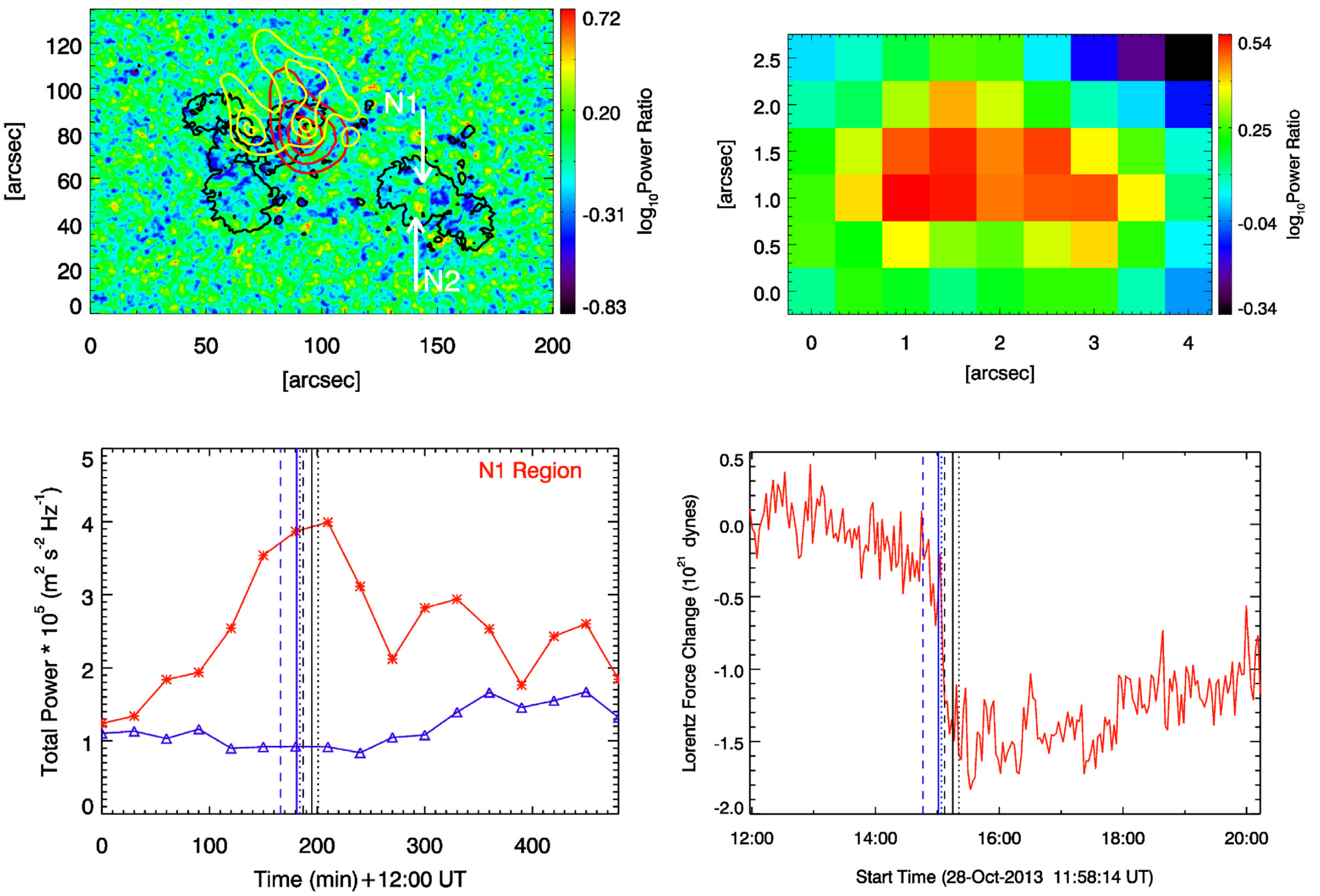

Figure 8. Same as Fig. 7, but for 'N1' location of active region NOAA 11882. It is to be noted that there is a time offset of about ± 30 min between the acoustic power variation and the *GOES* flare time in the bottom left panel. The bottom right panel illustrates the change in horizontal (i.e. transverse) component of Lorentz force in the aforementioned location. The dashed, solid, and dotted blue and black vertical lines represent the onset, peak, and decay time of M2.7 and M4.4 class flares, respectively. The remaining maps and plots have been provided in the online Supporting Information.

oscillations in the quiet regions. For flare-ribbon information at the chromospheric layer of the Sun, we have used Hα chromospheric intensity observations obtained from GONG instruments at 60 s cadence having a spatial sampling of 1.05 arcsec pixel^{-1} (in full-disc mode). In order to identify hard X-ray footpoint locations during the flare evolution, we have used hard X-ray images from the *Reuven Ramaty High Energy Solar Spectroscopic Imager* (*RHESSI*; Hurford et al. 2002) spacecraft in 12–25 keV energy band. We have also used disc-integrated soft X-ray solar flux in 1–8 Å range from the *Geostationary Orbital Environmental Satellite* (*GOES*; Garcia 1994) for having information on the temporal evolution of the flare and flare-class. The right-hand panel of Fig. 1 demonstrates the temporal evolution of soft X-rays (1–8 Å) from *GOES* satellite, which shows enhancement in flux around 01:44 UT and further provides information on the peak and decay time of an X2.2 class flare on 2011 February 15.

We have adopted selection criteria to choose NOAA active regions for our analysis, which are as follows:

(1) We have selected only those active regions which are within 40° latitude and longitude of the solar disc since *p*-mode oscillations are dominant near the disc centre and as we go away from the disc centre, these signals suffer from projection effects. Therefore, we restricted ourselves to within the ± 40° of the disc centre.

(2) We have analysed only those active regions which have produced M- and X-class flares.

(3) We have restricted our analysis to only those active regions in which magnetic field strength does not exceed 3000 G and the Doppler velocity is less then ± 6 km s^{-1}, including the orbital velocity of the spacecraft. It is to be noted that in the active regions where the magnetic field strength is more than ± 3800 G or the total Doppler velocity exceeds ± 8.5 km s^{-1}, the Fe I 6173 Å spectral line can go outside the observing window in HMI instrument thereby causing saturation problem in the observational data (Couvidat et al. 2012).

On applying the aforementioned selections criteria, we have selected eight active regions for our analysis, the details of which are as shown in Table 1.

3 ANALYSIS AND RESULTS

The main objective of this work is to identify the seismic emissions in the sunspots, accompanying major solar flares and to further investigate the changes in magnetic fields in those affected locations. We also aim to estimate the corresponding changes in Lorentz force in the aforementioned locations.

In the following sections, we describe the analysis procedure of the Dopplergrams, line-of-sight magnetograms and the vector

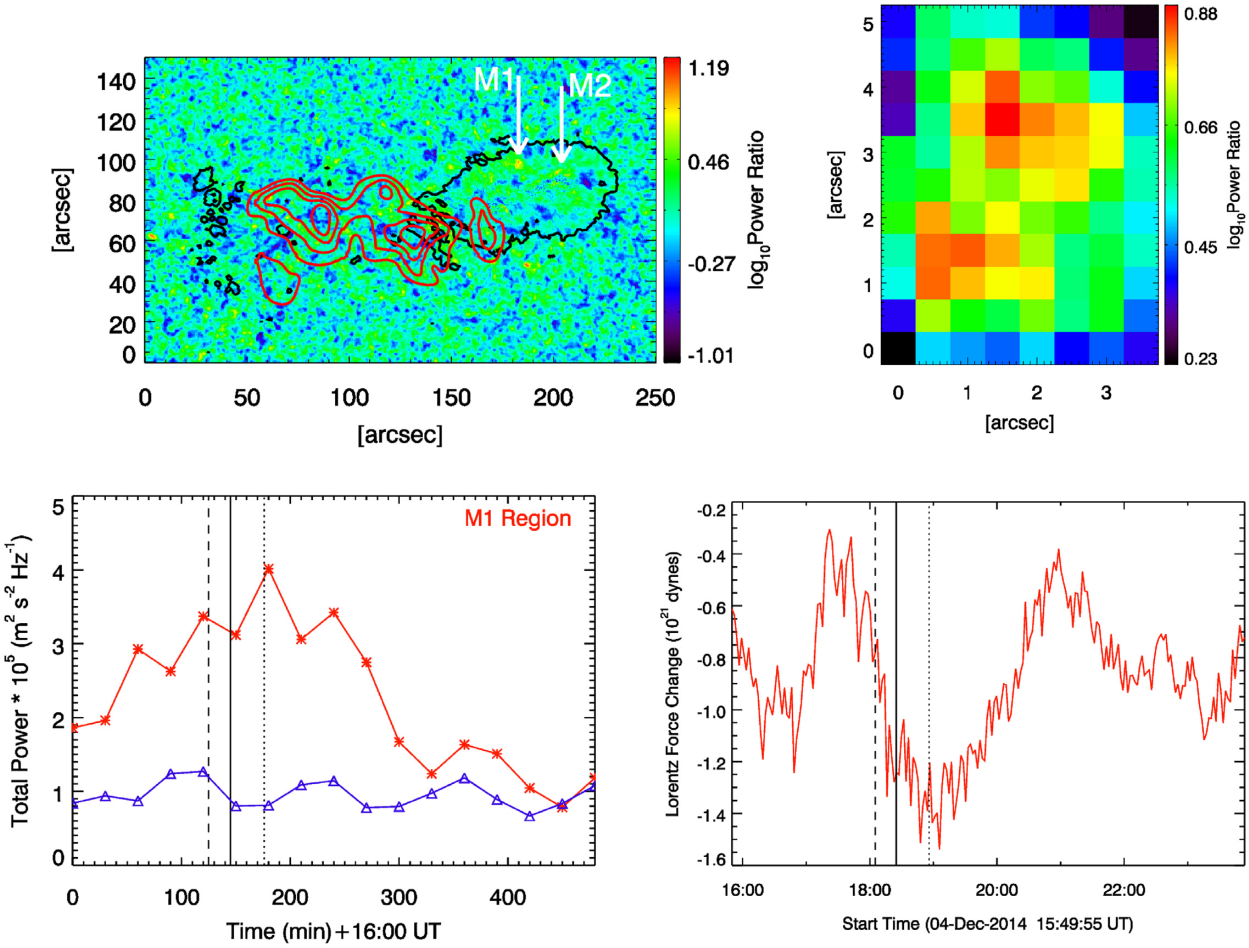

Figure 9. Same as Fig. 7, but for 'M1' location of active region NOAA 12222. It is to be noted that there is a time offset of about ± 30 min between the acoustic power variation and the *GOES* flare-time in the bottom left panel. The bottom right panel illustrates the change in radial (i.e. upward) component of Lorentz force in the aforementioned location. The remaining maps and plots have been provided in the online Supporting Information.

magnetograms obtained from HMI instrument aboard the *SDO* spacecraft.

3.1 Analysis of Dopplergram data

We have analysed the Dopplergrams to identify any seismic emissions in the sunspots. For this purpose, we have analysed several active regions as listed in Table 1. Here, we present in detail the analysis procedure and results of the active region NOAA 11158, however a brief overview of important results concerning other active regions are also presented. The remaining results are being provided in the online Supporting Information.

The active region NOAA 11158 produced several flares during its passage on the solar disc. This was the first active region of the Solar Cycle 24, which produced an X2.2 class flare on 2011 February 15 around 01:44 UT (cf. right-hand panel of Fig. 1). We have used the tracked Dopplergrams (hmi.V_45s) at a cadence of 45 s (cf. left-hand panel of Fig. 1) obtained from HMI instrument aboard the *SDO* spacecraft. In order to study the *p*-mode oscillations, we have applied a two-point backward difference filter which removes the slowly varying features from the Dopplergrams. Those filtered Dopplergrams are then subjected to fast Fourier transform for estimating power spectrum at each pixel. Following this, we construct power maps in the frequency range 2.5–4 mHz band (*p*-mode oscillations) for pre-flare and spanning flare epochs (cf. Fig. 2). Further, we have overplotted the hard X-ray contours from *RHESSI* instrument in 12–25 keV energy band on the spanning flare power map (cf. right-hand panel of Fig. 2) in order to know the hard X-ray footpoint locations. These acoustic power maps (cf. Fig. 2), demonstrate that there is a suppression of *p*-mode power in the sunspot region, while it is dominant in the quiet region. In the right-hand panel of Fig. 2 (spanning flare power map), red contours represent hard X-rays from *RHESSI* instrument in 12–25 keV band at 25, 50, 75, and 90 per cent of its maximum level. It is believed that corresponding to the hard X-ray footpoints, high energetic charged particles can reach up to the photosphere and they can induce photospheric *p*-mode oscillations. However, in the flaring region/hard X-ray footpoint locations, it has been demonstrated that there could be distortions in the line profiles during the flares due to the change in the local thermodynamic conditions (Raja Bayanna et al. 2014). Therefore, we have looked for only those acoustically enhanced locations in the sunspots which are away from hard X-ray footpoints and flare ribbons.

Although, by visualization of these two power maps (cf. Fig. 2), it is difficult to infer any adequate changes in the acoustic power in the sunspot regions during the flare. Hence, we have taken the ratio of these two power maps (spanning flare to pre-flare) as shown in the left-hand panel of Fig. 3. Again, we have overplotted hard X-ray footpoint contours (red colour) from *RHESSI* instrument in

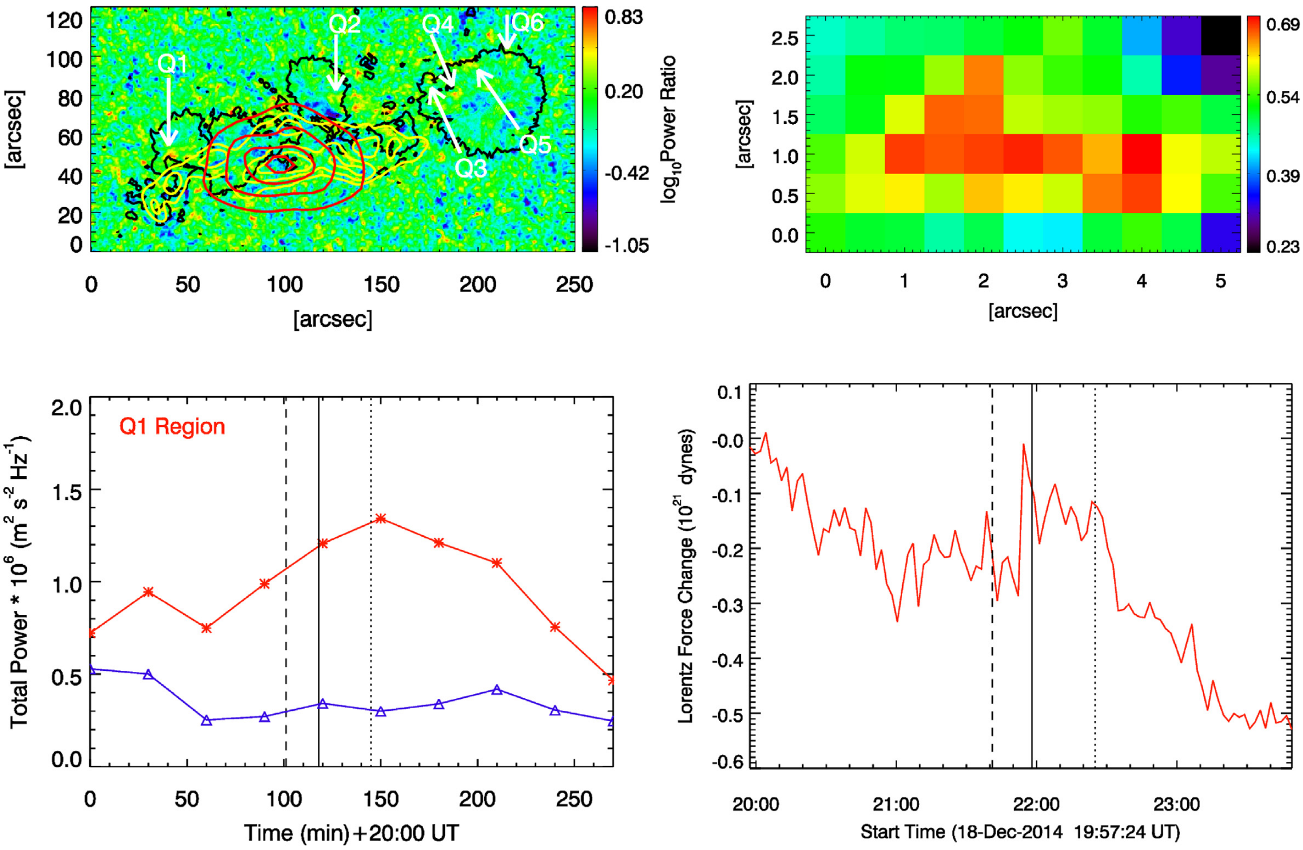

Figure 10. Same as Fig. 7, but for 'Q1' location of active region NOAA 12241. It is to be noted that there is a time offset of about ± 30 min between the acoustic power variation and the *GOES* flare-time in the bottom left panel. The bottom right panel illustrates the change in horizontal (i.e. transverse) component of Lorentz force in the aforementioned location. The remaining maps and plots have been provided in the online Supporting Information.

12–25 keV band on this power map ratio. In addition, we have also overplotted contours of the outer boundary of the sunspot penumbra (black colour) from HMI continuum intensity image on the power map ratio. Thus, we selected the acoustically enhanced 'B1' location in the sunspot, which is away from the flaring regions. The blow-up region of the 'B1' location shows enhancement in power ratio in patches (right-hand panel of Fig. 3). The temporal evolution of Doppler velocity in 'B1' location shows enhancement in *p*-mode velocity oscillations after the solar flare (cf. left-hand panel of Fig. 4). We have also examined the temporal evolution of total power integrated over 'B1' region as shown in red colour with asterisks in the left-hand panel of Fig. 4. This is done by estimating the power spectrum for 1-h duration and then shifting it for every 30-min during the observation period. Thus, it will have a time offset of about ± 30 min with respect to onset, peak and decay time of the flare. The temporal evolution of total power over 'B1' location demonstrates significant enhancement spanning the flare. On the other hand, the plot shown in blue colour with triangles representing the evolution of total power for an unaffected region in the same sunspot shows normal evolution over the whole duration. We have also calculated the percentage change in total power of the regions showing acoustic enhancement in sunspots in power map ratios of the other active regions considered in our analysis. All the seismic emission regions and corresponding percentage changes in total power spanning the flare are listed in Table 2, which demonstrate significant values. We further examined the cause of these seismic emissions in the sunspot regions, which are away from flaring sites. For this purpose, we have analysed the scalar and vector magnetograms acquired from HMI instrument aboard the *SDO* spacecraft. In Section 3.2, we describe the analysis procedure of the magnetogram data.

3.2 Analysis of magnetogram data

We have analysed sequences of tracked line-of-sight (i.e. longitudinal and scalar) magnetograms (hmi.M_45s) at a cadence of 45 s and vector magnetograms (hmi.B_135s) at a cadence of 135 s obtained from HMI instrument aboard the *SDO* spacecraft, in order to examine the evolution of magnetic fields corresponding to the seismic emission regions in the sunspots accompanying the flares. The left-hand panel of Fig. 5 represents the temporal evolution of line-of-sight magnetic fields over the 'B1' location. Here, we find that before the flare the magnetic field is evolving normally, while there is an abrupt change in the magnetic field of the order of 80–90 G within the time-scale of 10–20 min spanning the flare and again there is a normal evolution after the flare. Further, in order to have the complete information on the evolution of magnetic fields in the seismic emission locations, we also examined the vector magnetogram data. The right-hand panel of Fig. 5 shows the temporal evolution of horizontal (i.e. transverse) component of vector magnetic fields over 'B1' location. Here, we observe that there is a step-like change in the horizontal magnetic fields of the order of 60–70 G within 10–20 min during the flare. We have done similar analysis of magnetogram data for the seismic emission

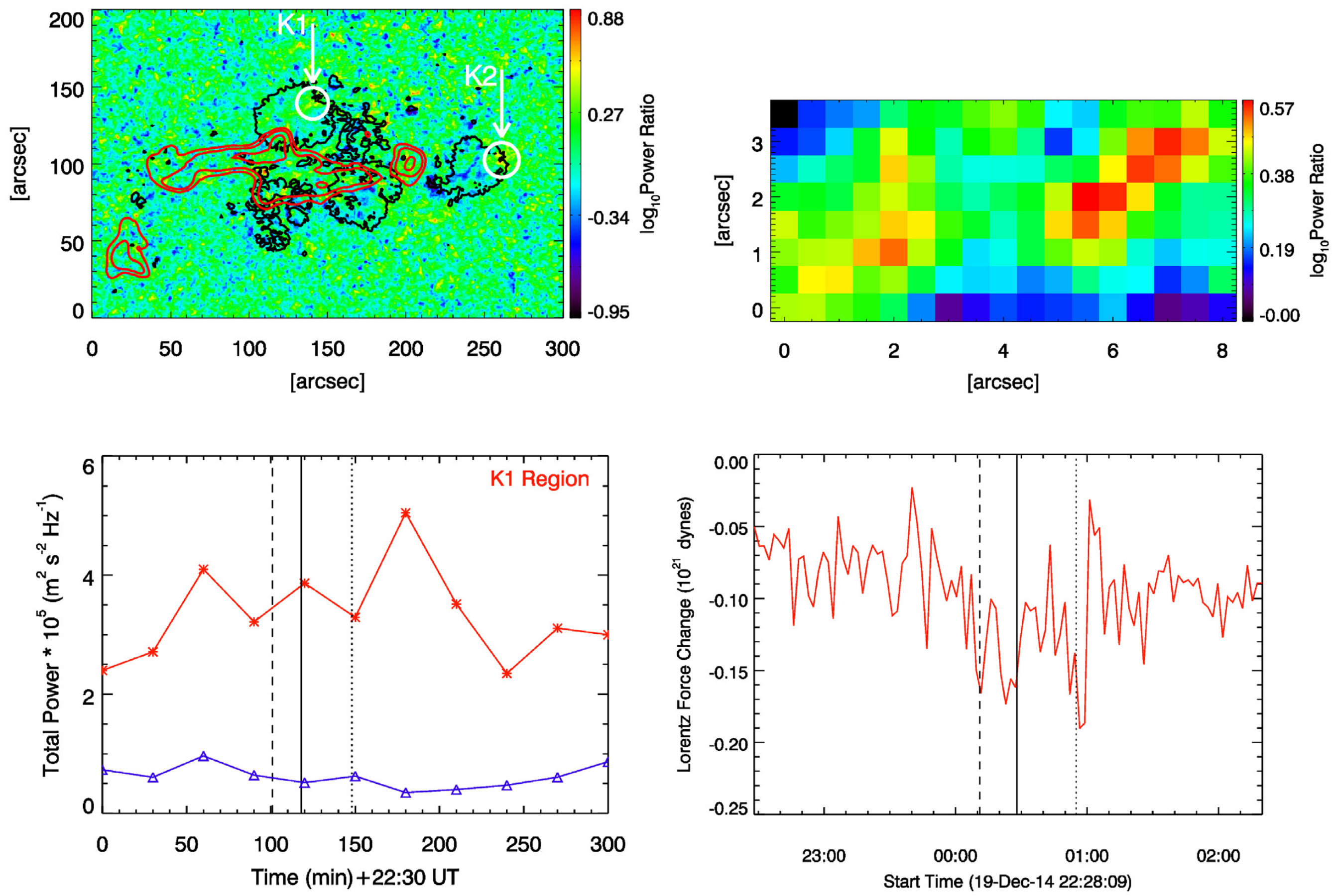

Figure 11. Same as Fig. 7, but for 'K1' location of active region NOAA 12242. It is to be noted that there is a time offset of about ± 30 min between the acoustic power variation and the *GOES* flare time in the bottom left panel. The bottom right panel illustrates the change in horizontal (i.e. transverse) component of Lorentz force in the aforementioned location. The remaining maps and plots have been provided in the online Supporting Information.

locations for others active regions, which are mentioned in Table 1. The temporal evolution of magnetic fields corresponding to seismic emission locations in all active regions shows similar changes in the magnetic fields. These results have been provided in the online Supporting Information.

Hudson et al. (2008) and Fisher et al. (2012) proposed that abrupt changes in the magnetic fields can lead to an impulsive change in the Lorentz force (known as 'magnetic-jerk') of the order of 10^{22} dyne, which can excite seismic emission in the sunspots accompanying flares. Hence, we have estimated the change in Lorentz force from the available photospheric vector magnetograms at a cadence of 135 s corresponding to the identified seismic emission locations as shown in Table 2.

To calculate the change in Lorentz force acting on the solar photosphere, we have used the equations (17) and (18) introduced by Fisher et al. (2012), which are as follows:

$$\delta F_{r,\mathrm{interior}} = \frac{1}{8\pi}\int_{A_{\mathrm{ph}}} \mathrm{d}A(\delta B_r^2 - \delta B_h^2) \quad (1)$$

$$\delta F_{h,\mathrm{interior}} = \frac{1}{4\pi}\int_{A_{\mathrm{ph}}} \mathrm{d}A\,\delta(B_r B_h) \quad (2)$$

Where, B_r and B_h are the radial (i.e. upward) and horizontal (i.e. transverse) components of vector magnetic fields, respectively, δF_r and δF_h are the changes in radial and horizontal components of Lorentz force acting on the solar interior, dA is the elementary surface area over the photosphere, and A_{ph} represents the area of the photospheric domain containing the active region.

It is to be noted that Petrie (2014) further discussed the application of formulation introduced by Fisher et al. (2012) within a subdomain of active region. Petrie (2014) concluded that these expressions could be used in a subdomain of active region at photosphere if the horizontal length scale of the structure is much more than 300 km and magnetic field strength is greater than 630 G at the height of the observations. In our analysis, the horizontal length scale and magnetic field strength are more than the aforementioned thresholds in all the seismic emission locations.

By using equations (1) and (2), we have calculated changes in both the components of Lorentz force. Fig. 6 shows the temporal evolution of changes in radial and horizontal components of Lorentz force over 'B1' location. These plots demonstrate that there is an abrupt change in radial component of Lorentz force and step-like change in horizontal component of Lorentz force of the order of 10^{21} dyne within 10–20 min duration spanning the flare. We have found similar changes in the Lorentz force corresponding to the analysis of other active regions (cf. Table 2), which are in close approximation to the estimates of Hudson et al. (2008) and Fisher et al. (2012). The plots of change in Lorentz force for the other active regions are shown in Figs 7–13 and also have been provided in the online Supporting Information.

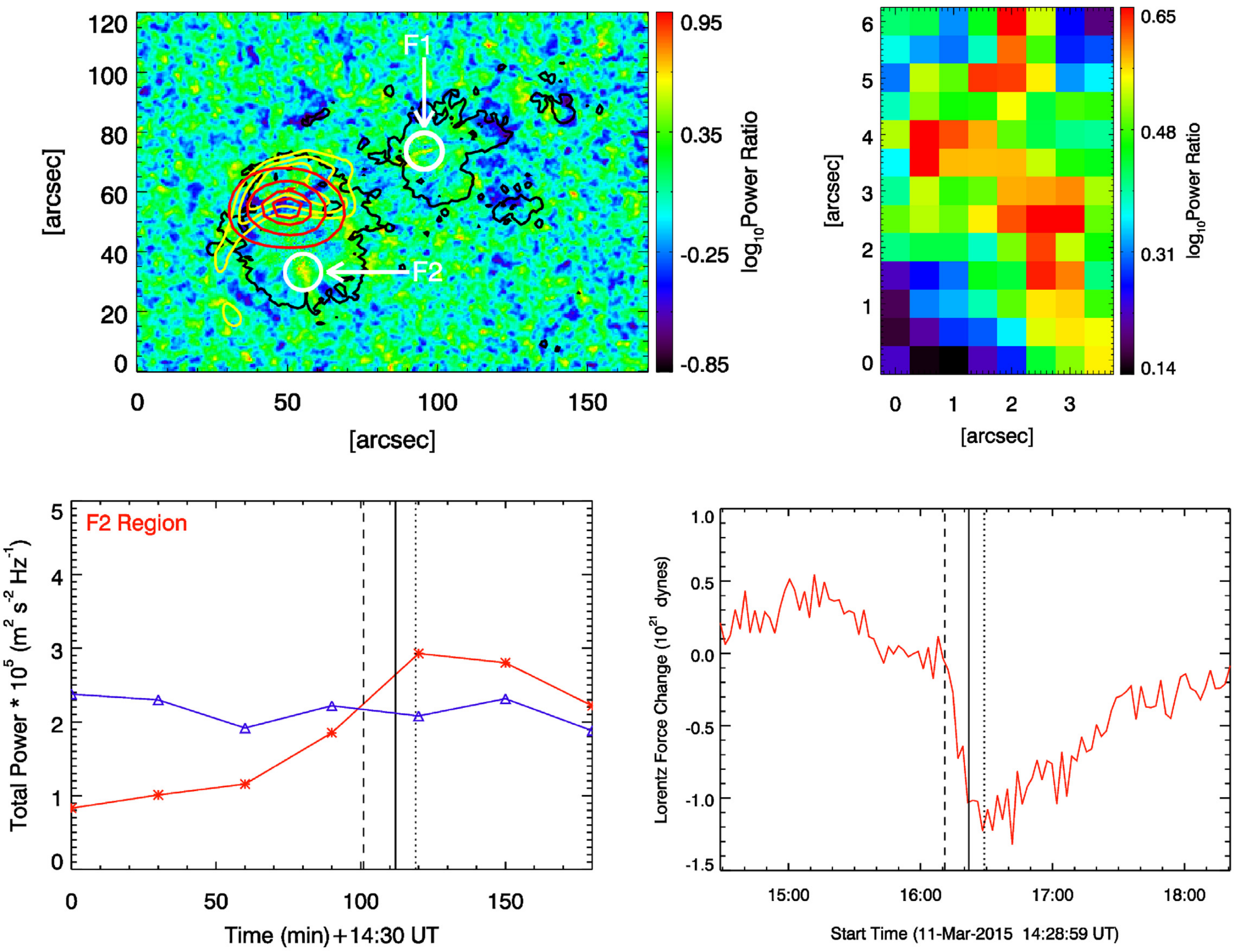

Figure 12. Same as Fig. 7, but for 'F2' location of active region NOAA 12297. It is to be noted that there is a time offset of about ± 30-minutes between the acoustic power variation and the *GOES* flare time in the bottom left panel. The bottom right panel illustrates the change in horizontal (i.e. transverse) component of Lorentz force in the aforementioned location. The remaining maps and plots have been provided in the online Supporting Information.

4 DISCUSSION AND CONCLUSIONS

We have studied seismic emission in the sunspots accompanying large solar flares for several active regions as referred in Table 1 using the high-resolution observations from HMI instrument aboard the *SDO* space mission. The summary of our analysis, chief findings, and interpretation of results are as follows:

(1) We have analysed the Dopplergrams of the active regions at a cadence of 45 s to examine acoustic enhancements in sunspots using power maps in 2.5–4 mHz band for the pre-flare and spanning flare epochs. We have selected only those locations for our study (cf. Table 2), which are within the sunspots and away from the flare ribbons and hard X-ray footpoints, since these are supposed to be free from any flare related artefacts in the observational data. The temporal evolution of total power corresponding to these seismic emission locations shows enhancement in power accompanying the flare and it tends to return to normal value after the flare. We also note that the temporal evolution of Doppler velocity in the seismic emission location shows enhancement during the flare and post-flare epochs. Additionally, the identified seismic emission locations in the sunspots show significant quantity of percentage change in total acoustic power (cf. Table 2) during the flares. Thus, we believe that these seismic emissions in the sunspots during the flare are solar in nature.

(2) In order to understand the cause of these seismic emissions, we have analysed line-of-sight (i.e. longitudinal) magnetic fields at a cadence of 45 s as well as high cadence (135 s) vector magnetograms in these identified locations. In most of the cases, the temporal evolution of these magnetic fields corresponding to seismic emission locations shows abrupt and persistent changes of the order of 50–100 G within a duration of 10–20 min during the flare and post-flare epochs. The plots of the evolution of magnetic fields in 'B1' location are shown here (cf. Fig. 5) whereas those for the other identified locations are provided in the online Supporting Information. These results are consistent with the earlier flare related magnetic field changes reported by Sudol & Harvey (2005) and Petrie & Sudol (2010).

(3) We have estimated the changes in Lorentz force corresponding to the seismic emission locations. Our analysis shows changes in the Lorentz force of the order of 10^{21} dyne in the seismic emission locations in the sunspots (cf. Table 2). The magnitude of change in Lorentz force in the identified seismic locations as obtained in our analysis is an order lower as compared to that estimated by Hudson et al. (2008) and other previous studies. Apparently, this is because our locations are away from the centres of the active regions where the observed magnetic field changes are relatively smaller. On the other hand, those reported in earlier studies (Petrie 2012, 2014; Sarkar & Srivastava 2018) are mostly along the polarity inversion lines where the magnetic field vectors become stronger and more horizontal

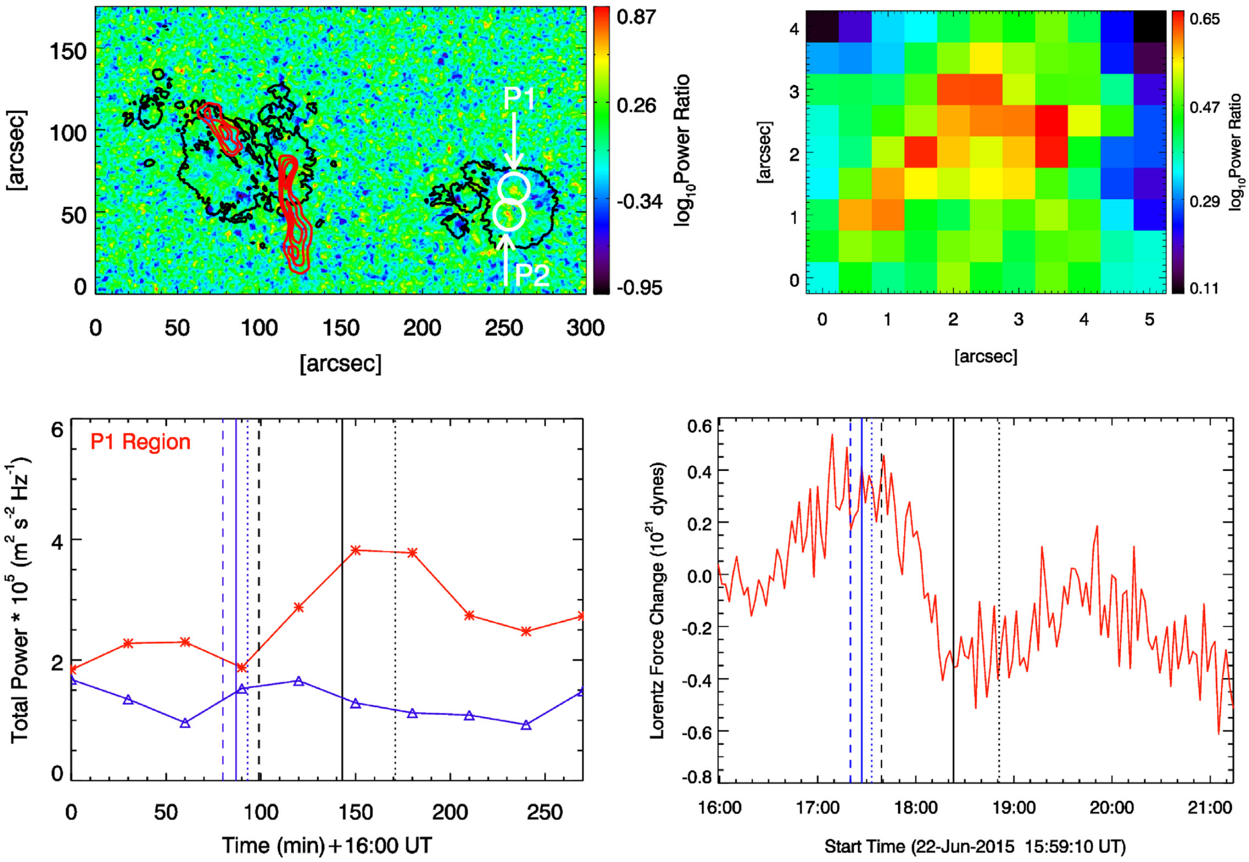

Figure 13. Same as Fig. 7, but for 'P1' location of active region NOAA 12371. It is to be noted that there is a time offset of about ± 30 min between the acoustic power variation and the *GOES* flare time in the bottom left panel. The bottom right panel illustrates the change in radial (i.e. upward) component of Lorentz force in the aforementioned location. The dashed, solid, and dotted blue and black vertical lines denote onset, peak, and decay time of C3.9 and M6.5 class flares, respectively. The remaining maps and plots have been provided in the online Supporting Information.

during the flares and hence the magnetic field changes are more pronounced. The plots of changes in the Lorentz force in 'B1' location of active region NOAA 11158 and brief overview of results of the analysis of the NOAA active regions 11261, 11882, 12222, 12241, 12242, 12297, and 12371 are shown in Figs 6–13. The remaining maps and plots of the analysis of these active regions are provided in the online Supporting Information. We observe a good correspondence between the enhancement in acoustic power in the seismic emission locations and the impulsive and other episodic changes of similar size in the Lorentz force in these identified locations. Therefore, our investigation indicates that 'magnetic-jerk' is the driving force for seismic emissions in the sunspots away from flare ribbons and hard X-ray footpoint locations observed during the flares.

(4) We have also estimated the work done by change in Lorentz force in the seismic emission location 'B1' in the active region NOAA 11158 and compared this available energy budget with the acoustic emission computed in one of the kernels (5 × 5 pixels) in the aforementioned seismic location. It is to be noted that Hudson et al. (2008) have computed the work done by the change in Lorentz force ($\approx 10^{22}$ dyne) as estimated from the results of Sudol & Harvey (2005) and considering the displacement of the photosphere to be ≈ 3 km as observed in the amplitude of seismic wave produced during an X2.6 class flare in active region NOAA 7978 (Kosovichev & Zharkova 1998). Thus, they arrived at an energy budget of $\approx 3 \times 10^{27}$ erg, which was found to be comparable to the energy of acoustic emissions reported in previous studies (Donea et al. 2006; Moradi et al. 2007). Following Hudson et al. (2008), we have estimated the work done ($W = \delta F.r$) by the change in Lorentz force ($\delta F \approx 2 \times 10^{21}$ dyne) as obtained for the seismic emission location 'B1' in displacing the photoshperic plasma by, say, $r \approx 3$ km, which yields $W \approx 6 \times 10^{26}$ dyne cm. We further compute the excess acoustic energy in the aforementioned kernel, which could be represented by, $\delta E = \rho.\delta p.A.d$, where '$\rho$' is the mean density of the solar photosphere ($\approx 2 \times 10^{-7}$ g cm^{-3}), 'δp' is the change in acoustic power in the identified kernel in the frequency band 2.5–4.0 mHz band ($\approx 5 \times 10^6$ cm^2 s^{-2}), 'A' is the area of the kernel ($\approx 3.2 \times 10^{16}$ cm^2), and 'd' is the depth of the kernel which could be considered approximately equal to its linear size ($\approx 1.8 \times 10^8$ cm), assuming that as much acoustic energy travels vertically from the source as in each horizontal direction. Thus, we obtain $\delta E \approx 5.7 \times 10^{24}$ erg. This is the approximate energy budget of the acoustic emission observed in the identified kernel, which is lower than the magnitude of the work done by the change in Lorentz force in this seismic location. Thus, our results suggest that the observed seismic emission has been induced by the impulsive changes in Lorentz force in the sunspot region during the flare.

(5) We have also tried to investigate a relationship between the change in Lorentz force and percentage change in seismic power, however we could not find any explicit relation between these two parameters. This could be due to the reason that in our photospheric Doppler observations, we are able to observe only the trapped acoustic modes, which is some fraction of the

induced seismic emission by 'magnetic-jerk'. The remaining fraction of these acoustic waves would propagate higher into the solar atmosphere along the magnetic field lines in the form of magnetoacoustic waves depending on their inclination and interaction with these acoustic waves. Hence, it would be possible to conduct a detailed study of the relation between these two, only if we have simultaneous Dopplergrams available for the layers above the photosphere.

(6) These seismic emissions in the sunspots are essential to study because these enhanced locations can give better information about the deep dynamics in the active regions during the flares. In addition, since these 'magnetic-jerk' driven seismic waves can also propagate from the photosphere to higher solar atmospheric layers along the magnetic field lines in the form of magnetoacoustic waves, hence it can contribute to the heating of the solar atmosphere. Thus, considering its aforementioned importance this study will be further carried out by using the upcoming facility of simultaneous velocity observations of the photosphere and chromosphere from the Multi Application Solar Telescope (Mathew 2009; Mathew et al. 2017; Venkatakrishnan et. al. 2017) operational at the Udaipur Solar Observatory, India.

ACKNOWLEDGEMENTS

We acknowledge the use of data from HMI instrument aboard the *SDO* spacecraft. Our sincere thanks goes to HMI team for providing high cadence (135 s) vector magnetogram data for our analysis. We acknowledge the use of Hα data from Global Oscillations Network Group. We also acknowledge the use of soft X-ray data from *GOES-15* satellite and hard X-ray data from *RHESSI* spacecraft. We are thankful for the support being provided by Udaipur Solar Observatory/Physical Research Laboratory. Thanks to Paul Rajaguru and Shibu K. Mathew for useful discussions related to this work. Finally, we are very much thankful to the anonymous referee for the constructive and fruitful comments and suggestions that improved the presentation of results and inclusion of relevant discussions in this paper.

DATA AVAILABILITY

The data underlying this article are available in HMI aboard the *SDO* data archive at http://jsoc.stanford.edu/ajax/lookdata.html, GONG data archive at https://gong2.nso.edu/archive/patch.pl?menutype = a and *RHESSI* data archive at http://hesperia.gsfc.nasa.gov/hessidata/.

REFERENCES

Borrero J. M., Tomczyk S., Kubo M., Socas-Navarro H., Schou J., Couvidat S., Bogart R., 2011, Sol. Phys., 273, 267
Brown J. C., 1971, Sol. Phys., 18, 489
Couvidat S., Rajaguru S. P., Wachter R., Sankarasubramanian K., Schou J., Scherrer P. H., 2012, Sol. Phys., 278, 217
Domingo V., Fleck B., Poland A. I., 1995, Sol. Phys., 162, 1
Donea A.-C., Lindsey C., 2005, ApJ, 630, 1168
Donea A.-C., Besliu-Ionescu D., Cally P. S., Lindsey C., Zharkova V. V., 2006, Sol. Phys., 239, 113
Fisher G. H., 1989, ApJ, 346, 1019
Fisher G. H., Canfield R. C., McClymont A. N., 1985, ApJ, 289, 425
Fisher G. H., Bercik D. J., Welsch B. T., Hudson H. S., 2012, Sol. Phys., 277, 59
Garcia H. A., 1994, Sol. Phys., 154, 275
Gary G. A., Hagyard M. J., 1990, Sol. Phys., 126, 21
Harvey J. W. et al., 1996, Science, 272, 1284
Hudson H. S., Ohki K., 1972, Sol. Phys., 23, 155
Hudson H. S., Fisher G. H., Welsch B. T., 2008, in Howe R., Komm R. W., Balasubramaniam K. S., Petrie G. J. D., eds, ASP Conf., Vol. 383. Astronomical Society of the Pacific, San Francisco, p. 221
Hurford G. J. et al., 2002, Sol. Phys., 210, 61
Kosovichev A. G., Zharkova V. V., 1998, Nature, 393, 317
Kumar B., Ravindra B., 2006, J. Astrophys. Astron., 27, 425
Kumar B., Raja Bayanna A., Venkatakrishnan P., Kuchandy Mathew S., 2016, Res. Astron. Astrophys., 16, 129
Leka K. D., Barnes G., Crouch A. D., Metcalf T. R., Gary G. A., Jing J., Liu Y., 2009, Sol. Phys., 260, 83
Mathew S. K., 2009, in Berdyugina S. V., Nagendra K. N., Ramelli R., eds, ASP Conf. Ser., Vol. 405. Astronomical Society of the Pacific, San Francisco, p. 461
Mathew S. K., Bayanna A. R., Tiwary A. R., Bireddy R., Venkatakrishnan P., 2017, Sol. Phys., 292, 106
Metcalf T. R., 1994, Sol. Phys., 155, 235
Moradi H., Donea A.-C., Lindsey C., Besliu-Ionescu D., Cally P. S., 2007, MNRAS, 374, 1155
Patterson A., 1984, ApJ, 280, 884
Patterson A., Zirin H., 1981, ApJ, 243, L99
Pesnell W. D., Thompson B. J., Chamberlin P. C., 2012, Sol. Phys., 275, 3
Petrie G. J. D., 2012, ApJ, 759, 50
Petrie G. J. D., 2014, Sol. Phys., 289, 3663
Petrie G. J. D., Sudol J. J., 2010, ApJ, 724, 1218
Qiu J., Gary D. E., 2003, ApJ, 599, 615
Raja Bayanna A., Kumar B., Venkatakrishnan P., Kunchandy Mathew S., Ravindra B., Mathur S., Garcia R. A., 2014, Res. Astron. Astrophys., 14, 207
Sarkar R., Srivastava N., 2018, Sol. Phys., 293, 16
Scherrer P. H. et al., 1995, Sol. Phys., 162, 129
Schou J. et al., 2012, Sol. Phys., 275, 229
Sudol J. J., Harvey J. W., 2005, ApJ, 635, 647
Sun X., Hoeksema J. T., Liu Y., Kazachenko M., Chen R., 2017, ApJ, 839, 67
Venkatakrishnan P. et al., 2017, Curr. Sci., 113, 686
Venkatakrishnan P., Kumar B., Uddin W., 2008, MNRAS, 387, L69
Wang H. et al., 2002, ApJ, 576, 497
Wang H., 1992, Sol. Phys., 140, 85
Wang H., Ewell M. W., Zirin H., Ai G., 1994, ApJ, 424, 436
Wolff C. L., 1972, ApJ, 176, 833
Zharkova V. V., Zharkov S. I., 2007, ApJ, 664, 573

SUPPORTING INFORMATION

Supplementary data are available at *MNRAS* online.

supplementry_material_final_Hirdesh_Kumar.pdf

Please note: Oxford University Press is not responsible for the content or functionality of any supporting materials supplied by the authors. Any queries (other than missing material) should be directed to the corresponding author for the article.

This paper has been typeset from a TEX/LATEX file prepared by the author.

Journal of Atmospheric and Solar–Terrestrial Physics 247 (2023) 106071

Contents lists available at ScienceDirect

Journal of Atmospheric and Solar–Terrestrial Physics

journal homepage: www.elsevier.com/locate/jastp

Research paper

A study of the propagation of magnetoacoustic waves in small-scale magnetic fields using solar photospheric and chromospheric Dopplergrams: HMI/SDO and MAST observations

Hirdesh Kumar [a,b,*], Brajesh Kumar [a], S.P. Rajaguru [c,d], Shibu K. Mathew [a], Ankala Raja Bayanna [a]

[a] Udaipur Solar Observatory, Physical Research Laboratory, Dewali, Badi Road, Udaipur, 313001, Rajasthan, India
[b] Department of physics, Indian Institute of Technology Gandhinagar, Gandhinagar, 382355, Gujarat, India
[c] Indian Institute of Astrophysics, Bangalore, 560034, India
[d] Solar Observatories Group, Department of Physics and W.W. Hansen Experimental Physics Lab, Stanford University, Stanford CA, 94305-4085, USA

ARTICLE INFO

Keywords:
Sun: Photosphere
Sun: Chromosphere
Sun: Quiet-Sun
Sun: Magnetic fields
Sun: Acoustic waves
Sun: Oscillations

ABSTRACT

In this work, we present a study of the propagation of low-frequency magneto-acoustic waves into the solar chromosphere within small-scale inclined magnetic fields over a quiet-magnetic network region utilizing near-simultaneous photospheric and chromospheric Dopplergrams obtained from the HMI instrument onboard SDO spacecraft and the Multi-Application Solar Telescope (MAST) operational at the Udaipur Solar Observatory, respectively. Acoustic waves are stochastically excited inside the convection zone of the Sun and intermittently interact with the background magnetic fields resulting into episodic signals. In order to detect these episodic signals, we apply the wavelet transform technique to the photospheric and chromospheric velocity oscillations in magnetic network regions. The wavelet power spectrum over photospheric and chromospheric velocity signals show a one-to-one correspondence between the presence of power in the 2.5–4 mHz band. Further, we notice that power in the 2.5–4 mHz band is not consistently present in the chromospheric wavelet power spectrum despite its presence in the photospheric wavelet power spectrum. This indicates that leakage of photospheric oscillations (2.5–4 mHz band) into the higher atmosphere is not a continuous process. The average phase and coherence spectra estimated from these photospheric and chromospheric velocity oscillations illustrate the propagation of photospheric oscillations (2.5–4 mHz) into the solar chromosphere along the inclined magnetic fields. Additionally, chromospheric power maps estimated from the MAST Dopplergrams also show the presence of high-frequency acoustic halos around relatively high magnetic concentrations, depicting the refraction of high-frequency fast mode waves around $v_A \approx v_s$ layer in the solar atmosphere.

1. Introduction

Acoustic waves are well recognized as an agent of non-thermal energy transfer that couples the lower solar atmospheric layers, primarily through their interactions with and transformations by the highly structured magnetic fields that thread these layers. These waves are generated by turbulent convection within and near the top boundary layers of the convection zone (Lighthill, 1952; Stein, 1967; Goldreich and Kumar, 1990; Bi and Li, 1998) and they resonate to form p-modes in the interior of the Sun. Propagation of these waves into the solar atmosphere is determined by the height dependent characteristic cut-off frequency ν_{ac}, which takes the value of ≈ 5.2 mHz for the quiet-Sun photosphere (Bel and Leroy, 1977; Jefferies et al., 2006) as estimated from $\omega_{ac} = 2\pi\nu_{ac} = c_s/2H_\rho$, where c_s and H_ρ are the photospheric sound speed and density scale height, respectively. Height evolution of wave phase in the chromospheric layers at frequencies larger than this cut-off of 5.2 mHz, while evanescent for smaller frequencies, is a well-observed feature in the quiet Sun. However, this condition is altered by the magnetic fields, which affect the propagation of these waves; when plasma β is low (β <1), acoustic cut-off frequency (ν_{ac}) is changed by a factor of $\cos\theta$ (Bel and Leroy, 1977; McIntosh and Jefferies, 2006; Cally et al., 2016), where θ is the angle between the magnetic field and the direction of gravity (which is normal to the solar surface). This fundamental effect of the inclined magnetic field has been identified as a key mechanism to tap the energetic low-frequency (p-mode) acoustic waves to energize the solar atmospheric layers and was termed as "magnetoacoustic portals" (Jefferies et al., 2006). Sobotka et al. (2013, 2016), Rajaguru et al. (2019), Abbasvand et al. (2020a), and Abbasvand et al. (2020b) have also investigated

* Corresponding author at: Udaipur Solar Observatory, Physical Research Laboratory, Dewali, Badi Road, Udaipur, 313001, Rajasthan, India.
E-mail address: hirdesh@prl.res.in (H. Kumar).

https://doi.org/10.1016/j.jastp.2023.106071
Received 15 December 2022; Received in revised form 21 March 2023; Accepted 11 April 2023
Available online 17 April 2023
1364-6826/

the propagation of acoustic and magnetoacoustic waves in different magnetic configurations in the lower solar atmosphere. There have also been studies of p-mode waves as drivers of impulsive dynamical phenomena that supply mass and energy to the solar atmosphere (De Pontieu et al., 2004, 2005).

In addition to that, we also observe high-frequency power enhancement (above the acoustic cut-off frequency) surrounding the strong magnetic structures such as sunspots, pores, and plages. These excess power enhancements are known as "acoustic halos". This was first observed at the photosphere (Brown et al., 1992) as well as chromosphere (Braun et al., 1992; Toner and Labonte, 1993) in the frequency range ν = 5.5–7 mHz, in typically weak to intermediate ($B_{LOS} \approx$ 50–300 G) photospheric magnetic field regions. The observational studies of halos (Hindman and Brown, 1998; Thomas and Stanchfield, 2000; Jain and Haber, 2002; Finsterle et al., 2004; Moretti et al., 2007; Nagashima et al., 2007) reveal several features, a summary of which has been presented in Khomenko and Collados (2009). Moreover, there is no single theoretical model which can completely explain all the observed features despite having focused efforts (Kuridze et al., 2008; Hanasoge, 2008, 2009; Khomenko and Collados, 2009). The majority of the work emphasizes the interaction of acoustic waves with the background magnetic fields from the photospheric to the chromospheric heights, with regards to power halos observed around the sunspots (Khomenko and Collados (2009) and references therein). However, Krijger et al. (2001), McIntosh and Judge (2001), and McIntosh et al. (2003) have investigated the oscillations in the network and internetwork regions utilizing observations of lower solar atmosphere from Transition Region and Coronal Explorer (TRACE; (Handy et al., 1999)). The physical characteristics of upward propagating acoustic waves are shaped by the topology of nearby magnetic fields. Numerical modelling done by Rosenthal et al. (2002) and Bogdan et al. (2003) show that the propagation of acoustic waves in the solar atmosphere is affected by the magnetic canopy and plasma $\beta \approx 1$ layer where mode conversion, transmission and reflection take place. Khomenko and Collados (2009) utilizing the numerical simulations of magnetoacoustic wave propagation in a magneto-static sunspot model suggest that halos can be caused by the additional energy injected by the high-frequency fast mode waves, which are refracted in the vicinity of the transformation layer (where Alfven speed is equal to the sound speed) in the higher atmosphere due to rapid increase of the Alfven speed. Schunker and Braun (2011) identified some new properties of acoustic halos in active regions. Rajaguru et al. (2013) further explored different properties of high-frequency acoustic halos around active regions including possible signatures of wave refraction utilizing the photospheric velocities, vector magnetograms and lower atmospheric intensity observations.

In this article, we present an analysis of leakage of low-frequency (2.5–4 mHz) acoustic waves into the higher solar atmospheric layers along small-scale inclined magnetic fields of a quiet magnetic network region in the form of magnetoacoustic waves exploiting the high-resolution photospheric velocity observations in Fe I 6173 Å line from Helioseismic and Magnetic Imager (HMI; Schou et al. (2012)) instrument onboard the *Solar Dynamics Observatory* (SDO; Pesnell et al. (2012)) spacecraft and chromospheric velocity estimated from Ca II 8542 Å line scan observations obtained from the Multi-Application Solar Telescope (MAST; Mathew (2009), Venkatakrishnan et al. (2017)). It is to be noted that p-mode oscillations are stochastically excited inside the convection zone beneath the solar photosphere and intermittently interact with the background magnetic fields, resulting in episodic signals. Hence, here we employ wavelet analysis to detect these episodic signals propagating from the photospheric to the chromospheric heights using velocity observations. We also investigate the interaction of acoustic waves with the background magnetic fields resulting in the formation of high-frequency acoustic halos in the velocity power maps of a magnetic network region and their relation with the photospheric vector magnetic fields. Our analysis aims to provide insight into the interaction of acoustic waves with small-scale magnetic fields of a quiet network region, depicting different physical phenomena. In the following, Section 2 provides a detailed account of the observational data used in this article, Section 3 discusses the analysis procedure and results obtained from the investigation, and Section 4 provides a further discussion and summary of our results.

2. The observational data

We employ two-height velocities observed over a magnetic network region in the disk centre to investigate the propagation of p-mode waves and appearance of high-frequency power halos and their relation with the background magnetic fields. We use photospheric observations in Fe I 6173 Å spectral line obtained from the HMI instrument onboard the *SDO* spacecraft and chromospheric line-scan observations in Ca II 8542 Å spectral line from the MAST operational at the Udaipur Solar Observatory, Udaipur, India. The following sub-Sections provide brief descriptions of the instruments and data reduction done for the above observations.

2.1. Chromospheric observations in Ca II 8542 Å line from the MAST

The MAST is a 50 cm off-axis Gregorian solar telescope situated at the Island observatory in the middle of Fatehsagar lake at the Udaipur Solar Observatory, Udaipur, India. It is capable of providing observations of the photosphere and chromosphere of the Sun. In order to obtain these observations, an imager optimized with two or more wavelengths is integrated with this telescope. For this purpose, two voltage-tunable lithium niobate Fabry–Perot etalons along with a set of interference blocking filters have been used for developing the Narrow Band Imager (NBI: Raja Bayanna et al. (2014); Mathew et al. (2017)). These two etalons are used in tandem for photospheric observation in Fe I 6173 Å spectral line. However, only one of the etalons is used for the chromospheric observation in Ca II 8542 Å (hereafter Ca II) spectral line. The maximum circular field-of-view (FOV) of the MAST is 6 arcmins, and diffraction-limited resolution is 0.310 arcsec at Fe I 6173 Å wavelength. Utilizing the capabilities of NBI with the MAST, we have observed a magnetic network region in the disk centre in the chromosphere of the Sun. The Ca II line profile has been scanned at 15 different wavelength positions starting from 8541.6 Å to 8542.48 Å within 15 s at a spatial sampling of 0.10786 arcsec per pixel on May 21, 2020, from 04:52:42–06:45:20 UT. The core of the line profile is scanned with close sampling intervals, whereas wings are sampled at higher wavelength spacing. Moreover, there is a delay of 19 s between two consecutive line scans. We obtained intensity images at different wavelength positions in a FOV of 220 × 220 arcsec^2. The seeing condition was stable during the observation. The top left panel of Fig. 1 shows the near-core intensity image of the Ca II line during the starting time of the observations. The bottom panel of Fig. 1 shows the Ca II line profile estimated from the average intensity over the full FOV, where plus symbols on the line profile represent the wavelength positions where the line profile has been scanned with the NBI. The centre points of red horizontal lines in the core of the Ca II spectral profile denote the bisector points, which we have used to estimate the line-of-sight velocity. We have explained the estimation of chromospheric velocity from these observations in Section 3 of this paper.

2.2. Photospheric observations in Fe I 6173 Å line from HMI/SDO

The HMI instrument onboard the *SDO* spacecraft observes the photosphere of the Sun in Fe I 6173 Å absorption line at six different wavelength positions within ±172 mÅ window from the centre of Fe I 6173 Å line. It uses two 4096 × 4096 pixels CCD cameras. One of the cameras, also known as a scalar camera, provides full disk line depth, Dopplergrams, continuum intensity, and line-of-sight magnetic fields at a spatial sampling of 0.504 arcsec per pixel and a temporal cadence

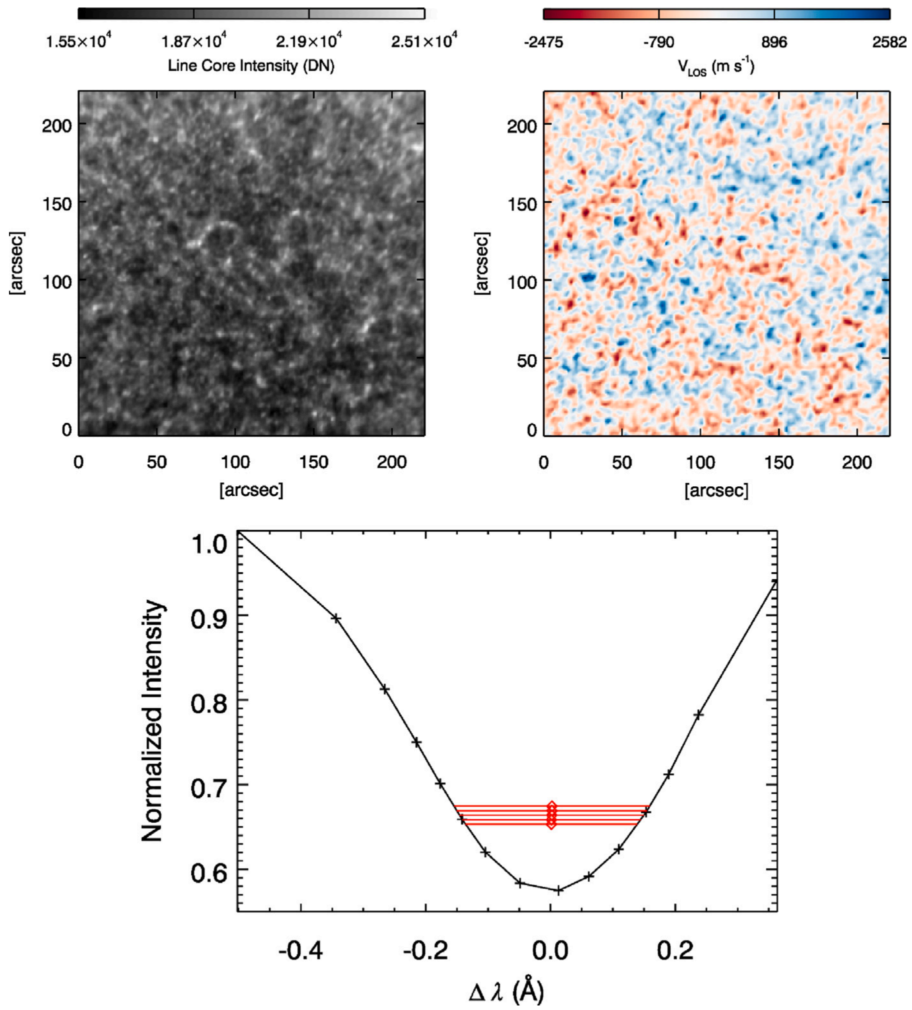

Fig. 1. Sample maps of chromospheric Ca II 8542 Å near line-core intensity image (*top left panel*), and chromospheric Dopplergram (*top right panel*) of a quiet magnetic network region observed on May 21, 2020 from the MAST. *Bottom panel* shows a sample profile of Ca II 8542 Å spectral line with five bisector points (red diamond) used to derive the chromospheric line-of-sight Doppler velocity. This profile is constructed from the average intensity over the whole field-of-view (FOV) of the MAST (c.f., *top left panel*). The 15 wavelength locations were scanned in about 15 s.

of 45 s. The second camera, i.e. vector camera, is dedicated to the measurement of vector magnetic fields of the photosphere of the Sun at the same spatial sampling as scalar camera. It provides full-disk vector magnetograms at a lower cadence (12 min) as a standard product, although it can also be obtained at a cadence of 135 s (Hoeksema et al., 2014). To obtain the vector magnetic field observations, Stokes parameters (I, Q, U, V) are observed at six different wavelength positions from the centre of Fe I 6173 Å absorption spectral line profile. Further, to get the information of vector magnetograms of the photosphere from these Stokes parameters, the HMI team utilize Very Fast Inversion of the Stokes algorithm code (VFSIV; Borrero et al. (2011)) to invert the Stokes profiles. The remaining 180 deg. ambiguity in the azimuthal field component is resolved using the minimum-energy method as described by Metcalf (1994), and Leka et al. (2009). Thereafter, these heliocentric spherical coordinates (B_r, B_θ, B_ϕ) are approximated to (B_z, $-B_y$, B_x) in heliographic cartesian coordinates for ready use in various parameter studies (Gary and Hagyard, 1990). We have photospheric Dopplergrams, line-of-sight magnetograms at 45 s and vector magnetic fields at 12 min cadence. The top left panel of Fig. 2 shows the average line-of-sight magnetic field image of the photosphere over the whole observation period as mentioned in Section 2.1 of this paper. We have tracked all these photospheric observables and also removed the differential rotation velocity signals using the Snodgrass formula (Snodgrass, 1984) and the spacecraft velocity from the HMI Dopplergrams.

3. Analysis and results

In the following, we discuss the analysis procedure of velocities, and magnetic fields over a magnetic network region and results obtained from the investigation.

3.1. Estimation of line-of-sight velocity from Ca II 8542 Å line scan observations from MAST

We resample the Ca II intensity images to match the coarser HMI spatial scale after dark and flat corrections on the line-scan observations obtained from NBI with the MAST. We have used the cross_corr.pro routine available in SolarSoftWare (SSW) to co-align each Ca II intensity image with the previous line scan image. The bisector method (Gray, 2005) has been used to construct chromospheric Doppler velocity. In order to define the reference wavelength, we have used the bisector method on the line profile constructed from the average intensity over full FOV. The bottom panel of Fig. 1 shows the Ca II line profile estimated by taking the average over full FOV, with bisector points of five red horizontal lines at different intensity levels in the line core shown by red diamond; the data points marked with plus represent the locations, where the line has been scanned using NBI with the MAST. According to Cauzzi et al. (2008), the wings of the Ca II spectral line that are 0.5–0.7 Å away from the line centre map the middle photosphere around h = 200–300 km above the $\tau_{500} = 1$ (unity optical depth

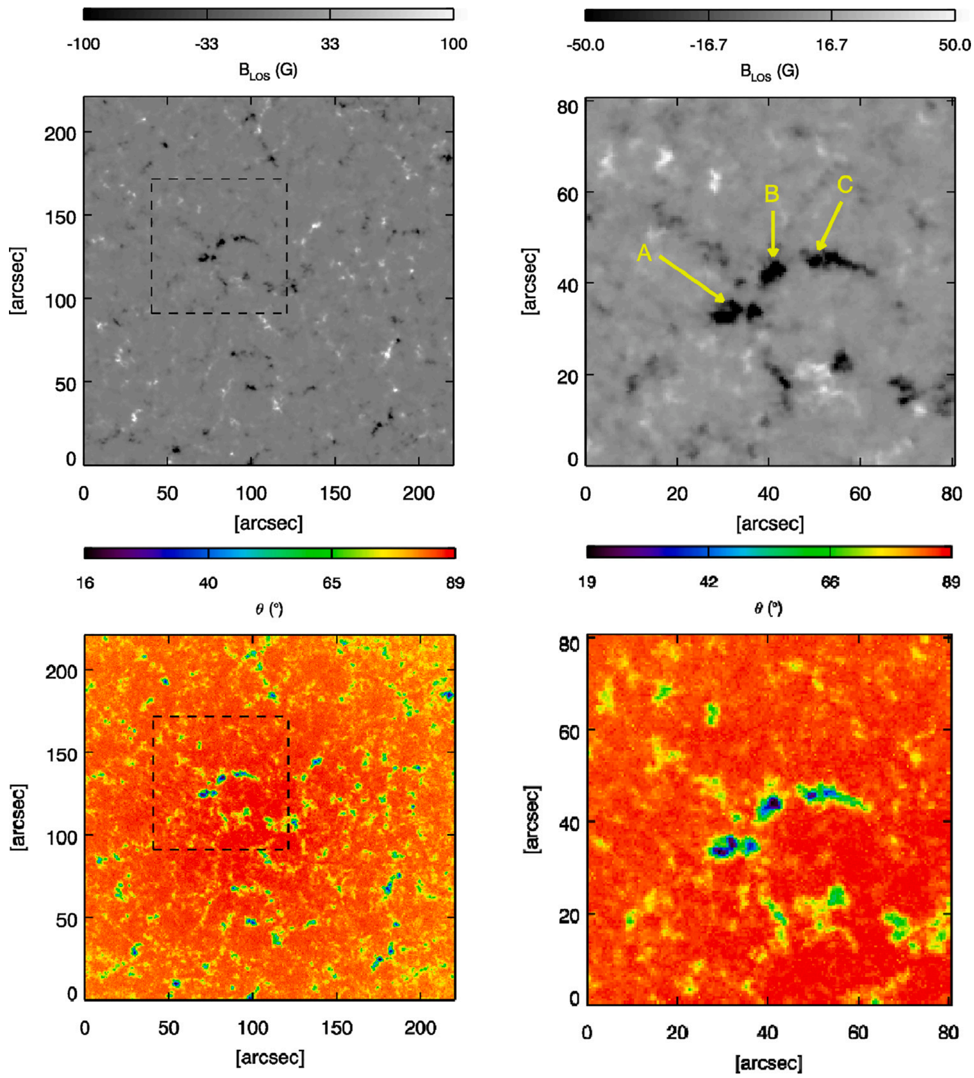

Fig. 2. Sample maps of average of photospheric line-of-sight magnetogram over 112 min duration (*top left panel*), blow up region of a strong magnetic network region (*top right panel*) as denoted by black dashed square box in the top left panel. Line-of-sight (LOS) magnetogram has been saturated at ±100 G and ± 50 G, respectively, to bring out the small-scale magnetic features. The yellow arrows with labels 'A'', 'B'', and 'C'', show the identified locations for the investigation of leakage of *p*-mode oscillations. *Bottom left panel*: Sample map of θ obtained from the HMI vector magnetograms and integrated over the duration of observations. Blow up region illustrating θ of a selected strong magnetic network location (*bottom right panel*) as denoted by black dashed square box in the left panel.

in the 500 nm continuum) whereas the line core is formed in the height range h = 1300–1500 km. Here, we have used bisector in between ±0.14–0.18 Å from the line centre. The contribution in this particular wavelength range comes from a height around $h \approx$ 900–1100 km (mean height ≈ 1000 km). By taking the average of five bisector points, we obtained a map of $\delta\lambda$, which, after a wavelength shift correction, is then used to estimate the line-of-sight velocity (V_{los}) given by the Doppler shift formula, $V_{los} = (\delta\lambda/\lambda_0)c$, where λ_0 is the rest wavelength, and c is the speed of light. For the wavelength shift corrections, we use a diffuser to take the line-scan observations, which contains only the shift originating from the incident angle (θ) of light. Further, we utilize bisector method to construct map of $\delta\lambda_{shift}$, which is subtracted from $\delta\lambda$ maps. Following this, by combining the time taken for line-scan and delay time, we obtain chromospheric Doppler velocity at a cadence of 34 s. Further, we linearly interpolate over time to match the lower cadence (45 s) photospheric Dopplergrams from the HMI instrument. The interpolated time series (chromospheric Dopplergrams) are now simultaneous to the photospheric Dopplergrams. The top right panel of Fig. 1 shows the chromospheric Doppler velocity constructed from MAST observations. For aligning the photospheric and chromospheric observations, we use 20 min averages of line core intensity of Ca II spectral profile and line-of-sight magnetograms and identify similar features for correlation tracking to get sub-pixel accuracy.

3.2. Photospheric observables from HMI instrument

We use photospheric Dopplergrams obtained from the HMI instrument, which sample Fe I 6173 Å spectral line. Norton et al. (2006) investigated formation process of Fe I 6173 Å line profile and derive a height range of h = 20–300 km above the continuum optical depth (τ_c = 1, which corresponds to z = 0) whereas line continuum is formed around h = 20 km above z = 0. Fleck et al. (2011) used 3d time-dependent radiation hydrodynamic simulation to produce Fe I 6173 Å line profile and calculated Doppler velocity to compare with the observations derived with the HMI instrument. They concluded that V_{HMI} forms at a mean height of 150 km. Other photospheric observables used in this study are B_{LOS} and B = [B_x, B_y, B_z] at a cadence of 45 s and 12 min, respectively. The magnetic fields of the quiet Sun rapidly evolve over a short time duration and decay (Bellot Rubio and Orozco Suárez, 2019). To examine the role of small scale magnetic fields on the leakage of p-mode waves and formation of high-frequency halos, we have taken the average of B_{LOS} over the whole observation

Table 1
Table represents the values of average line-of-sight magnetic fields ($< |B_{LOS}| >$), inclination ($< \theta >$) and cut-off frequency (ν_{ac}^{B}) over selected locations.

Location	$< \|B_{LOS}\| >$ (G)	$< \theta >$ (degree)	$\nu_{ac}^{B} = \nu_{ac} cos\theta$ (mHz)
A	42.9	64.2	2.3
B	68.7	58.1	2.7
C	38.5	62.7	2.4

duration as shown in the top left panel of Fig. 2. The average B_{LOS} map shows only the permanent magnetic features. It has been saturated between ±100 G to bring out small scale magnetic patches, and a strong network region is selected for final analysis, which is demarcated with a black dashed square box. The top right panel of Fig. 2 shows the blow-up region of B_{LOS}. From the vector magnetograms, we have B_x, B_y, and B_z components of the magnetic fields. Similar to Rijs et al. (2016) and Rajaguru et al. (2019), we estimate field inclination $\theta = 90. - (180./\pi)|\tan^{-1}(B_z/B_h)|$, where B_z is the radial component of the magnetic fields, and $B_h = \sqrt{B_x^2 + B_y^2}$ is horizontal magnetic fields. Map of θ averaged over the whole observation period is shown in the bottom left panel of Fig. 2, where $\theta = 0$ degrees corresponds to vertical and $\theta = 90$ degrees represents horizontal magnetic fields. It is to be noted that we have averaged B_{LOS} and θ maps over the whole observation period; this may lead to an averaging out of small scale emerging magnetic fields in between the observation period. Finally, we have selected three different locations ('*A*', '*B*', and '*C*') with magnetic field strength ($|B_{LOS}|$) greater than 30 G to study the propagation of *p*-mode waves from the photosphere into the chromosphere as shown with the yellow arrowheads in the blow-up region of B_{LOS} map (c.f. top right panel of Fig. 2), which is our region of interest (ROI). In our analysis, we have considered rasters of 10 × 10 pixels in the aforementioned identified locations on which the velocity signals are averaged in order to take into account seeing related fluctuations on spatial scales. The values of $< |B_{LOS}| >$, $< \theta >$ and magnetically modified cut-off frequency $\nu_{ac}^{B} = \nu_{ac} cos\theta$ over locations '*A*', '*B*', and '*C*' are listed in Table 1.

3.3. Wavelet analysis of HMI and MAST velocity data

In order to detect the presence of episodic wave propagation signals, from the photosphere to the chromosphere through the intermittent interactions between *p*-modes and the magnetic fields, we have constructed the wavelet power spectrum of the velocity oscillations at the identified locations '*A*', '*B*', and '*C*'.

Wavelet analysis is a powerful technique to investigate non-stationary time series or where we expect localized power variations. Thus, to determine the period of episodic signals present in the identified regions, we apply the wavelet technique (Torrence and Compo, 1998) on the photospheric and chromospheric velocity time series of locations '*A*', '*B*', and '*C*' obtained from HMI and MAST observations. Torrence and Compo (1998) presented a detailed description of the methodology used as the basis for this study. Here, we use the Morlet wavelet, a product of a Gaussian function and a sine wave. In the wavelet power spectrum (WPS), we limit our investigation to a region inside a "cone of influence" corresponding to the periods of less than 25% of time series length. We have also overplotted the confidence level at 95% as shown by a solid black line in WPS. For the different locations on the photospheric velocities, we note the presence of significant power around the 2.5–4 mHz band in WPS, which is associated with the *p*-mode oscillations (c.f. left panels of Figs. 3). The WPS obtained from chromospheric velocities at identified locations also shows the power around 2.5–4 mHz band and above 5.5 mHz (c.f. right panel of Figs. 3). Further, the WPS is collapsed over the whole observation time to get the Global Wavelet power spectrum (GWPS). If power is present during the whole length of observation time in WPS, it would also be reflected in the GWPS. The GWPS is similar to the commonly used Fourier power spectrum. In Figs. 3 GWPS show the peak around 3 mHz above the confidence level in photospheric and chromospheric locations. Importantly, we note that WPS constructed from the chromospheric velocity time series reveals the presence of significant power around the 3 mHz band at the same time as in the WPS obtained from the photospheric velocity time series (c.f. Figs. 3). For instance, significant power is present in the WPS constructed from HMI velocity of location '*A*' in 0–40 min duration in 2.5–4 mHz band (c.f. top left panel of Fig. 3), and in the same time interval, we notice significant power in WPS obtained from the chromospheric velocity time series (c.f. top right panel of Fig. 3). We have found similar results in other selected locations (c.f. Fig. 3). We also notice that despite the presence of significant power in photospheric WPS, we do not see the power in chromospheric WPS. For example prominent power is present in the location '*B′*' in 40–100 min time duration in photospheric WPS (c.f. middle left panel of Fig. 3), whereas feeble power is observed in the chromospheric WPS (c.f. middle right panel of Fig. 3), pointing that low-frequency acoustic waves intermittently interact with background magnetic fields. We also plot frequency versus height (c.f. Fig. 4) of the oscillations observed in the photospheric and chromospheric wavelet power spectrum obtained at two different heights in the solar atmosphere. In the photospheric WPS, we see the presence of dominant 5-min (3.3 mHz) oscillations, however chromospheric WPS indicate the presence of 1.5, 3.3, and 5.0 mHz oscillations. The presence of 3.3 mHz oscillations in the chromosphere is associated with underlying photospheric oscillations, whereas 1.5 and 5.0 mHz oscillations are chromospheric in nature. These findings are consistent with earlier numerical simulations done by Kraśkiewicz et al. (2019), and Kraśkiewicz et al. (2023), where they have derived the cutoff frequency of upward propagating magnetoacoustic waves. Moreover, the estimated acoustic cut-off frequency (ν_{ac}^{B}) (c.f. Table 1) in the locations mentioned above shows that the quiet-Sun photospheric acoustic cut-off frequency (ν_{ac}) is adequately reduced in the presence of inclined magnetic fields. Thus, it indicates that the power present around 2.5–4 mHz band in the chromospheric WPS is possibly associated with the leakage of the photospheric *p*-mode oscillations into the chromosphere.

3.4. Phase and coherence spectra

Wavelet power spectrums of locations '*A*', '*B*', and '*C*' of chromospheric Doppler velocities show one-to-one correspondence in the ν = 2.5–4 mHz band with the photospheric 2.5–4 mHz band, suggesting that chromospheric power in 2.5–4 mHz band are related to the leakage of photospheric *p*-mode oscillations. Hence, we estimate the phase and coherence spectra over the region of interest (ROI) (c.f. right panel of Fig. 2). We would like to mention here that, spatial maps of phase and coherence do not show clear one-to-one correlations. It might be due to the larger height difference between the photospheric and the chromospheric Dopplergrams, and also due to non-achievement of sub-pixel accuracy in the alignment of the HMI and the MAST observations due to seeing fluctuations. Hence, we have not included these maps in our results. Here, we present the average phase and coherence over the ROI. In order to estimate the phase and coherence between two signals at each pixel, we calculate the cross-spectrum of two evenly sample time series (I_1 and I_2) in the following way:

$$X_{12}(\nu) = I_1(\nu) \times I_2^*(\nu) \quad (1)$$

Where I's are the Fourier transforms, and $*$ denotes the complex conjugate. The phase difference between two-time series is estimated from the phase of complex cross product ($X_{12}(\nu)$)

$$\delta\phi(\nu) = tan^{-1}(Im(< X_{12}(\nu) >)R(< X_{12}(\nu) >)) \quad (2)$$

We are adopting the convention that positive $\delta\phi(\nu)$ means that signal 1 leads 2, i.e., a wave is propagating from lower height to

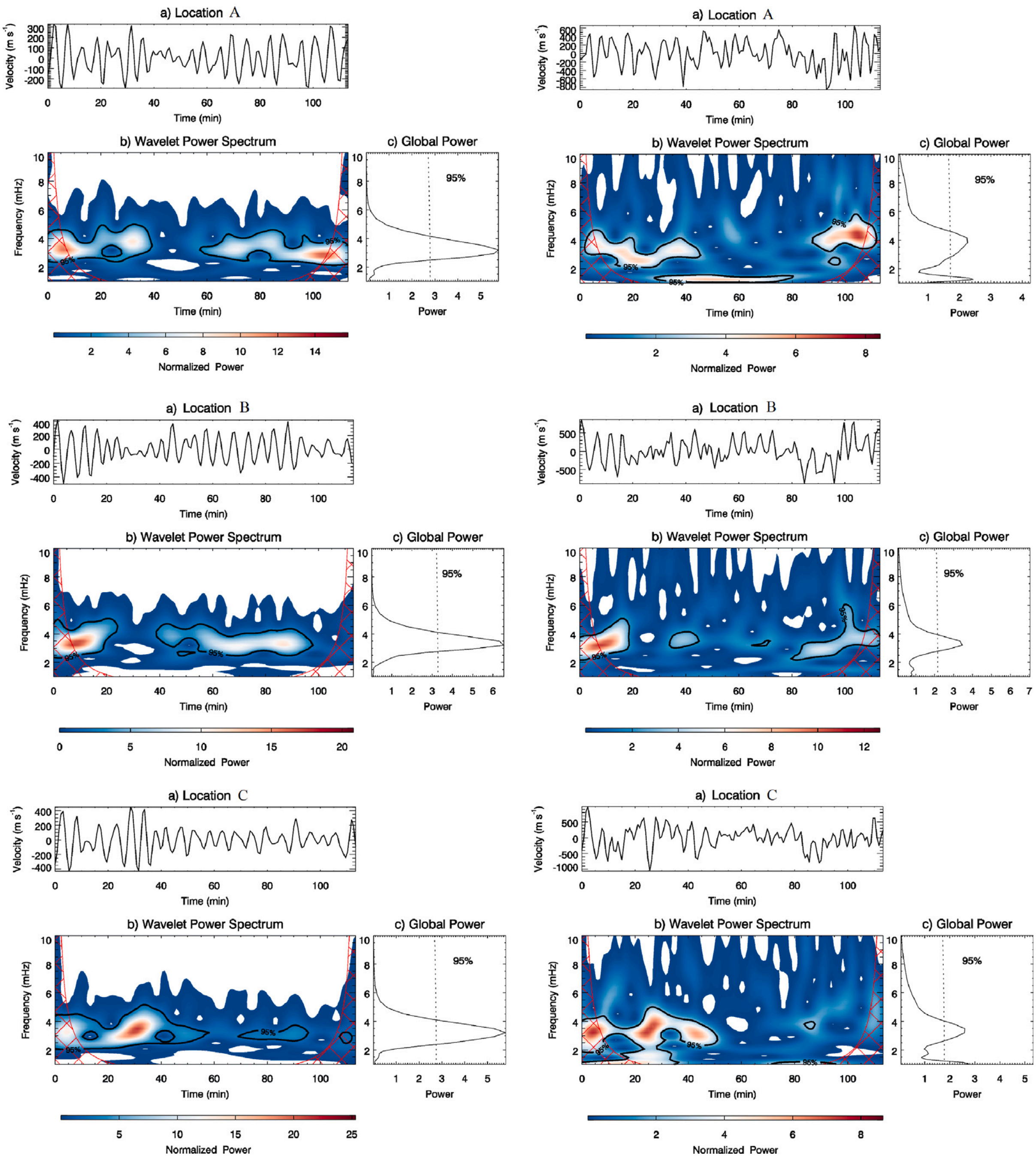

Fig. 3. *Top left panel*: Upper panel (a) shows the temporal evolution of average velocity signals obtained from the photospheric Dopplergrams for the location '*A*'. Bottom panel shows the WPS and the GWPS in (b) and (c), respectively, computed from velocity time series. In the WPS, the solid lines demonstrate regions with the 95% confidence level, and the hatched region indicates the cone of influence. The colour scale represents the wavelet power. The dotted line in GWPS shows a confidence level at 95%. *Top right panel*: Same as *top left panel*, but from chromospheric velocity for location '*A*' as estimated from MAST observations. *Middle and bottom panels* are for the locations '*B*' and '*C*', respectively.

upper height and vice-versa. Further, the magnitude of $X_{12}(\nu)$ is used to estimate the coherence (C), which ranges between 0 to 1.

$$C(\nu) = sqrt(|<X_{12}(\nu)>|^2/<|I_1|^2><|I_2|^2>) \quad (3)$$

Where < . > denotes the average. Coherence is a measure of the linear correlation between two signals, 0 indicates no correlation and 1 means perfect correlation. In our case, we have averaged over segments of length 76 data points, which correspond to 57 min at a cadence of 45 s. We assume that this is the better way to estimate the $\delta\phi(\nu)$ and $C(\nu)$ due to the intermittent nature of the interaction of acoustic waves with the background magnetic fields (Rajaguru et al., 2019).

Fig. 5 shows the average phase (black) and coherence (red) spectra between photospheric and chromospheric Doppler velocity observations estimated over the region of interest (ROI) as shown by the black dashed square box on the left panels of Fig. 2, and blow up region of the same is depicted in the right panels of Fig. 2. In between the photosphere and the chromosphere, atmospheric gravity waves also contribute to the $\delta\phi$. Gravity waves show the negative phase propagation while transporting energy in the upward direction in the lower frequency band in $k-\omega$ diagram (Straus et al., 2008). In our analysis, we also found the negative $\delta\phi$ in the phase estimation from the photospheric and the chromospheric velocities. This is possibly

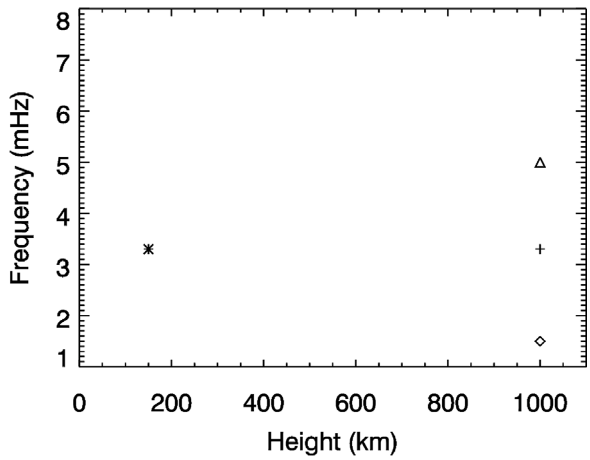

Fig. 4. Plot shows the frequency versus height of the oscillations observed in the photospheric and chromospheric wavelet power spectrum. In this plot, the asterisk shows the dominant photospheric frequency observed at 3.3 mHz, whereas the diamond, plus, and triangle represent the chromospheric frequencies observed at 1.5, 3.3, and 5.0 mHz, respectively. The presence of 3.3 mHz oscillations in the chromosphere is associated with the leakage of underlying photospheric oscillations along the inclined background magnetic fields.

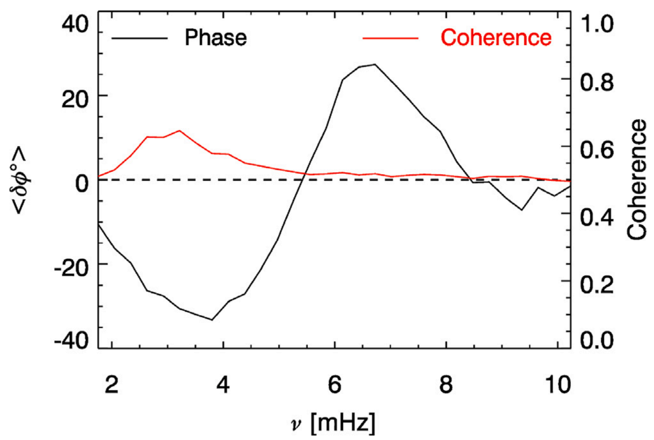

Fig. 5. Spatially averaged phase and coherence spectra estimated from photospheric and chromosphere Doppler velocities over region of interest (ROI) as shown in the right panels of Fig. 2.

associated with the contribution of gravity waves. However, we found that $\delta\phi$ started increasing around ν = 3.5 mHz and continue up to ν = 6.5 mHz after which it decreases. The decline of $\delta\phi$ after 6 mHz is possibly associated with steepening of acoustic waves into the shocks. Moreover, the coherence is above 0.5 up to 6 mHz and then slightly decreases. Overall, the estimated average phase and coherence spectra from photospheric and chromospheric velocities indicate the propagation of p-mode waves and are qualitatively in agreement with phase travel time estimated by Rajaguru et al. (2019) utilizing the photospheric and lower chromospheric intensity observations.

3.5. Photospheric and chromospheric behaviour of high-frequency acoustic halos

The propagation of acoustic waves into the higher solar atmospheric layers in magnetized regions results into different physical phenomena. One of them is the formation of high-frequency acoustic halos. To gain an insight into the interaction of acoustic waves with the background magnetic fields in the quiet magnetic network region (where the magnetic field strength is typically small), we have constructed power maps in different frequency bands, i.e. ν = 6, 7, 8, and 9 mHz from photospheric and chromospheric velocities over a strong magnetic network region as indicated in the top left panel of Fig. 2 by the black dashed square box and blow up region of the same is shown here in the top right panel. These maps are integrated over ±0.5 mHz frequency band around the centre as frequency mentioned on the top of each maps (c.f. Fig. 6). Photospheric and chromospheric power maps are shown in the left and right panels of Fig. 6, respectively. We do not see high frequency power halos in the photospheric power maps (c.f. left panels of Fig. 6) surrounding strong network region. However, chromospheric power maps show high frequency acoustic halos around the magnetic network region at ν = 6, 7, 8, and 9 mHz maps as shown in the right panels of Fig. 6. In the centre of strong magnetic network concentrations, chromospheric power is suppressed (c.f. right panels of Fig. 6). It is to be noted that the magnetic fields of network region spread and diverge at chromospheric height and become significantly inclined in higher atmosphere and changing the height of $\beta = 1$ layer. In our analysis, significant enhancement in chromospheric power is observed in areas surrounding the strong magnetic network region in the form of patches. Further, to better understand the behaviour of high-frequency acoustic halos with respect to photospheric magnetic fields, we have averaged power over a bin of 10 G in $|B_{LOS}|$ and 4-degree bin in θ. Photospheric and chromospheric power as a function of photospheric $|B_{LOS}|$ and θ (integrated over whole observation period) are shown in the top and bottom panels of Fig. 7, respectively. It is to be noted that Rajaguru et al. (2013) have estimated power over different ranges of magnetic field strength and inclination from the analysis of different active regions. However, we investigate halos in a quiet magnetic network region, where the magnetic field strengths are much smaller compared to active regions. Photospheric power as a function of $|B_{LOS}|$ shows that more power is present in the 2.5–4.5 mHz band in relatively small magnetic field strengths with more inclined magnetic field regions (c.f. top panels of Fig. 7). Interestingly, chromospheric power as a function of photospheric $|B_{LOS}|$ and θ shows that excess power in the high-frequency (ν > 5 mHz) band is present in the small magnetic field strength ($|B_{LOS}|$ < 60 G) and more inclined magnetic field regions (θ > 60 degree) (c.f. bottom panel of Fig. 7).

4. Discussion and conclusion

Understanding the physics of interactions between acoustic waves and magnetic fields requires identifying and studying the observational signatures of various associated phenomena in the solar atmosphere, viz. mode conversion, refraction and reflection of waves, formation of high-frequency acoustic halos etc. Most of the work in this field emphasizes the propagation of acoustic waves and their interaction within the highly magnetized regions like sunspots and pores. However, it is not well understood as whether we also expect similar behaviour in a quiet magnetic network region. Multi-height observations covering photospheric and chromospheric layers, especially through intensity imaging observations, are widely used towards the above. Simultaneous velocity observations of both photospheric and chromospheric heights are however rare. In this work, in order to address some of the above questions, we have observed a quiet-Sun magnetic network region in the chromospheric Ca II 8542 Å line using the NBI instrument now operational at MAST/USO. Using spectral scans of this region, we have derived chromospheric Doppler velocities. Simultaneous photospheric Doppler velocity and vector magnetic field of this region was also extracted from SDO/HMI data.

We employ wavelet analysis technique to investigate the intermittent interaction of low-frequency (2.5–4.0 mHz) acoustic waves with background magnetic fields in the velocity oscillations at the photospheric and the chromospheric heights using the aforementioned observations. Therefore, we have estimated wavelet power spectra in the selected locations to investigate the propagation of low-frequency acoustic waves from the solar photosphere into the chromosphere as

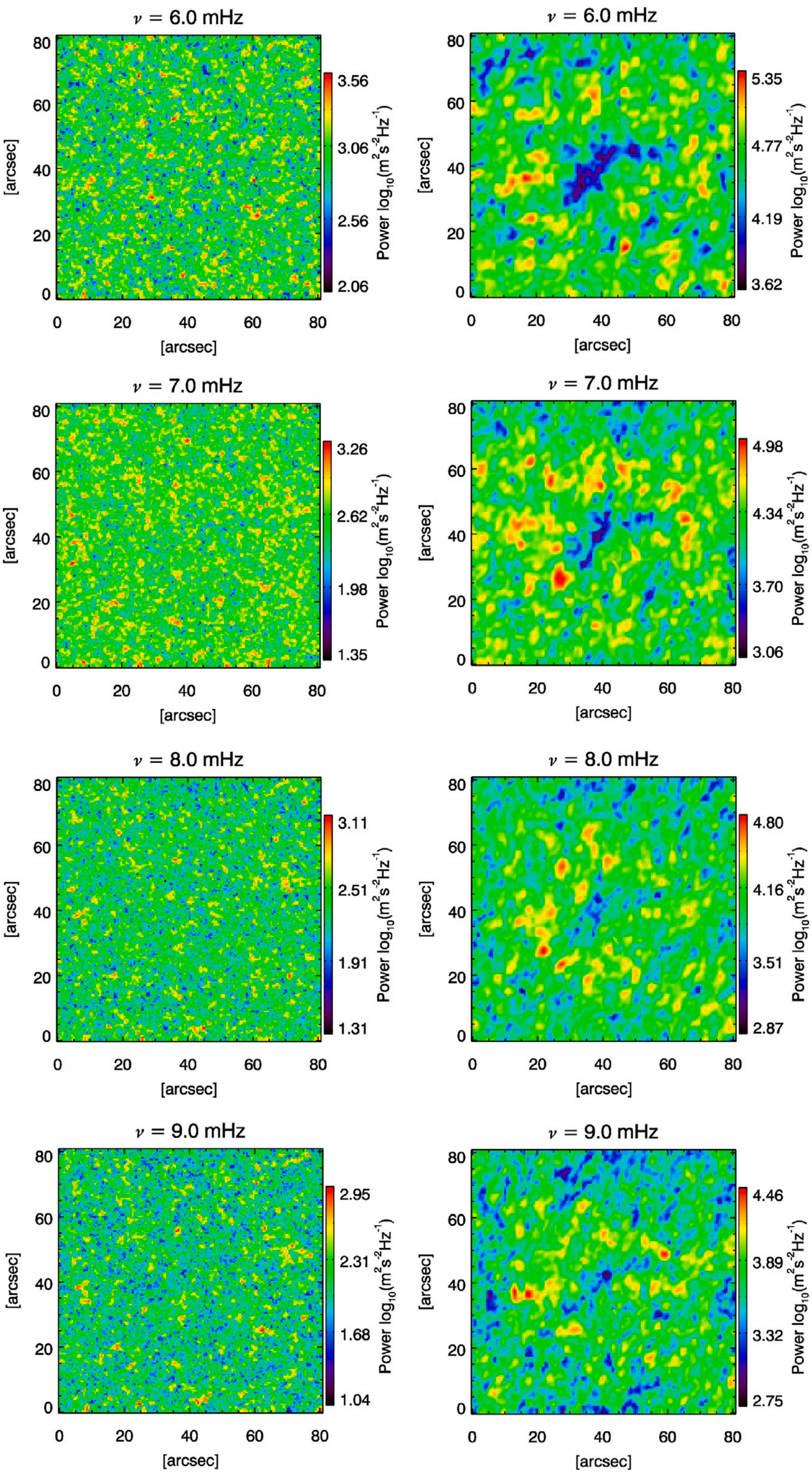

Fig. 6. *Left panel*: Power maps at different frequencies constructed from photospheric velocity obtained from HMI instrument over a small strong magnetic network region as shown in the right panels of Fig. 2. *Right panel*: Same as *left panel* but from chromospheric velocity estimated from MAST observations.

magnetoacoustic waves. These waves are now recognized as a potential candidate to heat the lower solar atmosphere. The investigation of Jefferies et al. (2006) utilizing the velocity observations shows that low-frequency magnetoacoustic waves can propagate into the lower solar chromosphere from the small-scale inclined magnetic field elements. Later on, the detailed investigation done by Rajaguru et al. (2019) provides evidence that a copious amount of energetic low-frequency acoustic waves channel through the small-scale inclined magnetic fields. Usually, acoustic waves of frequency less than photospheric cut-off frequency ($\nu_{ac} \approx 5.2$ mHz) are trapped below the photosphere in the quiet Sun. However, the presence of magnetic fields alters the cut-off frequency, and it is reduced by a factor of $\cos\theta$:

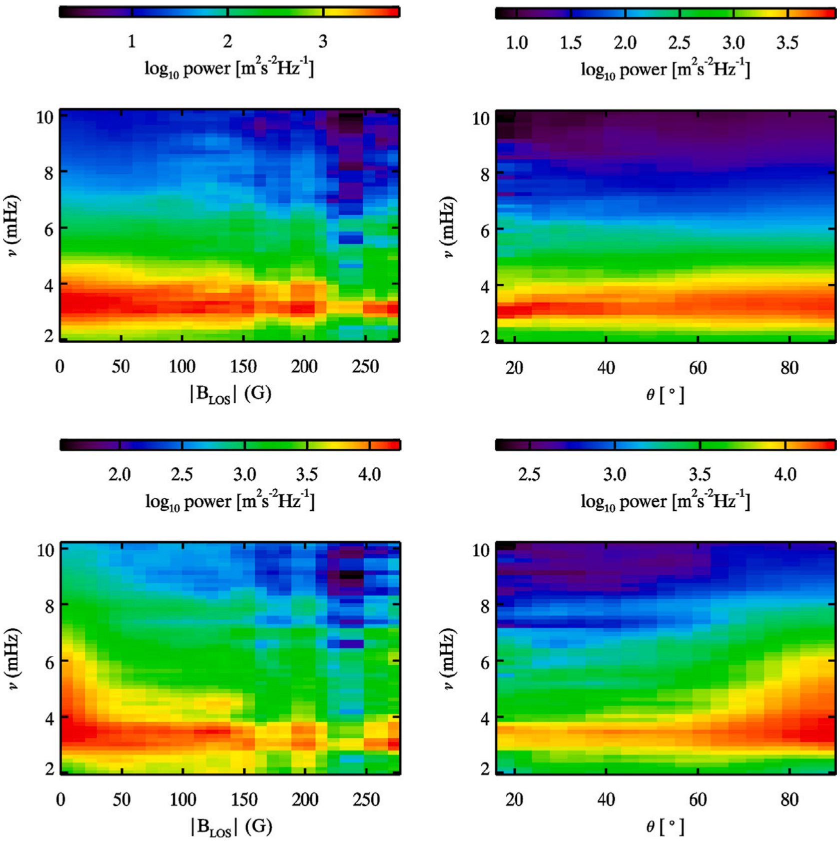

Fig. 7. *Top panel*: Photospheric power are averaged over photospheric magnetic fields, 10 G bins in $|B_{LOS}|$ (*left hand side*) and 4 degree bins in θ (*right hand side*), respectively, over a magnetic network region as shown in the right panels of Fig. 2. *Bottom panel*: Same as *top panel*, but estimated from chromospheric power over photospheric magnetic fields ($|B_{LOS}|$ and θ), respectively.

$v_{ac}^{B} = v_{ac} cos\theta$ (Bel and Leroy, 1977). In our analysis, we have found a significant reduction in the acoustic cut-off frequency, following the above formula, in the presence of inclined magnetic fields. Thus, the presence of low-frequency acoustic waves in the chromospheric wavelet power spectra is clearly associated with the leakage of photospheric oscillations. Moreover, the WPS of both heights show a clear association of chromospheric (5-min) oscillations with the underlying photospheric oscillations as evident from the appearance of low-frequency acoustic waves in chromospheric WPSs approximately at the same time as in the photospheric WPS. The investigation of the average phase over the ROI (80 × 80 arcsec^2, c.f. right panel of Fig. 2) also shows the turn-on positive phase around $\nu = 3.5$ mHz and continues upto 6.5 mHz, indicating the channelling of photospheric p-mode oscillations into the chromosphere. Additionally, the estimated coherence is above 0.5 up to around 8 mHz, and then it decreases. Nevertheless, the bigger height difference between the two observables also reduces the coherence because these waves travel a long distance, hence losing coherency. Our results are consistent with the previous findings related to the leakage of p-mode oscillations into higher solar atmospheric layers along inclined magnetic fields (De Pontieu et al., 2004, 2005; Jefferies et al., 2006; Vecchio et al., 2007; Rajaguru et al., 2019). However, our results add to the previous findings by illustration of a one-to-one correspondence between oscillatory signals present in the WPS of photospheric and the chromospheric velocity observations of a quiet-Sun magnetic network region. Nevertheless, we also note that leakage of low-frequency acoustic waves along the inclined magnetic fields is not a continuous process, indicating that energy flux estimated from short duration observations could be underestimated or overestimated.

As regards the formation of high frequency acoustic halos surrounding magnetic concentrations, the information gathered from the same is also important to map the thermal and magnetic structure of different heights in the solar atmosphere. The theoretical investigations of Rosenthal et al. (2002), and Bogdan et al. (2003) discussed the effect of magnetic canopy present in the solar atmosphere and plasma $\beta \approx 1$ location. The plasma $\beta \approx 1$ separates two different regions of gas and magnetic pressure dominance. Gary (2001) provided a model of plasma β variation with height in the solar atmosphere over a sunspot and a plage region. Figure 3 of Gary (2001) shows that β is ≈ 1 for plage region at a height of around 1 Mm, while for sunspot it lies below. It is suggested that mode conversion, transmission, and reflection of waves occur at $\beta \approx 1$ (Rosenthal et al., 2002; Bogdan et al., 2003; Khomenko and Collados, 2006, 2009; Khomenko and Cally, 2012; Nutto et al., 2012). The numerical simulation of Khomenko and Collados (2009) proposes that high-frequency fast mode waves which refract in the higher atmosphere around $\beta \approx 1$ due to rapid increase of the Alfven speed can also cause high-frequency acoustic halos around sunspots. Further, they have added that high-frequency halos should form at a distance where the refraction of fast mode acoustic wave occurs above the line formation layer, i.e., where the Alfven speed is equal to sound speed above the photosphere. Else, it would not be possible to detect these halos in observations. We have found high-frequency acoustic halos around a high magnetic concentrations in quiet magnetic network region in the chromospheric Fourier power maps (c.f. right panels of Fig. 6). However, halos are not observed in the photospheric power maps. The absence of the acoustic halos in photospheric power maps indicate that formation height of photospheric velocity is far below the mode conversion layer i.e., $\beta \approx 1$, as suggested by Khomenko and Collados (2006) and Rajaguru et al. (2013). Therefore, the presence of halos in the chromospheric power maps is possibly associated with the injection of high frequency fast mode waves, which are refracting from the magnetic canopy and $\beta \approx 1$ layer as proposed by Khomenko and Collados (2009) and Nutto et al.

(2012). This fact is also supported by a model of plasma β variation in the solar atmosphere (Gary, 2001) suggesting that $\beta \approx 1$ at a height of ≈ 1000 km over a plage region. For a quiet magnetic network region like ours, we do expect that $\beta \approx 1$ layer might be above 1000 km. The presence of high-frequency acoustic halos in chromospheric power maps is consistent with the explanation provided by Khomenko and Collados (2006, 2009), Kontogiannis et al. (2010), Nutto et al. (2012), and Rajaguru et al. (2013). The chromospheric power maps also show the power deficit in the high magnetic concentrations in the quiet magnetic network region. This could be associated with the energy loss due to the multiple mode transformations in a flux tube (Cally and Bogdan, 1997). The analysis of chromospheric power dependence on photospheric $|B_{LOS}|$ and θ shows that high-frequency power is also significantly present in the small magnetic field strength and in nearly horizontal magnetic field regions. This finding is qualitatively in agreement with the earlier work (Schunker and Braun, 2011), which suggests that the excess power in high-frequency halos is present at the more horizontal and intermediate magnetic field strength region. Our results thus show that small scale magnetic fields also have a significant effect on the propagation of acoustic waves in the solar atmosphere. It is to be noted that we have utilized high resolution photospheric and chromospheric Doppler velocities to investigate the interaction of acoustic waves with the small scale magnetic fields. We intend to follow up with similar analyses using near-simultaneous multi-height velocity and magnetic field observations from MAST and the newer Daniel K Inouye Solar Telescope (DKIST; (Rimmele et al., 2020)) along with HMI and AIA instruments on board SDO spacecraft.

Declaration of competing interest

The authors declare that they have no known competing financial interests or personal relationships that could have appeared to influence the work reported in this paper.

Data availability

Data will be made available on request.

Acknowledgements

We acknowledge the use of data from HMI instrument onboard the *Solar Dynamics Observatory* spacecraft of NASA. This work utilizes data obtained from the Multi-Application Solar Telescope (MAST) operated by the Udaipur Solar Observatory, Physical Research Laboratory, Dept. of Space, Govt. of India. We are thankful to the MAST team for providing the data used in this work. We are also thankful for the support being provided by Udaipur Solar Observatory/Physical Research Laboratory, Udaipur, India. S.P.R. acknowledges support from the Science and Engineering Research Board (SERB, Govt. of India) grant CRG/2019/003786. All authors approved the version of the manuscript to be published. Finally, we are thankful to the reviewers for fruitful comments and suggestions, which improved the presentation of the results.

References

Abbasvand, V., Sobotka, M., Heinzel, P., Švanda, M., Jurčák, J., del Moro, D., Berrilli, F., 2020a. Chromospheric heating by acoustic waves compared to radiative cooling. II. Revised grid of models. Astrophys. J. 890 (1), 22. http://dx.doi.org/10.3847/1538-4357/ab665f, arXiv:2001.03413.

Abbasvand, V., Sobotka, M., Švanda, M., Heinzel, P., García-Rivas, M., Denker, C., Balthasar, H., Verma, M., Kontogiannis, I., Koza, J., Korda, D., Kuckein, C., 2020b. Observational study of chromospheric heating by acoustic waves. Astron. Astrophys. 642, A52. http://dx.doi.org/10.1051/0004-6361/202038559, arXiv:2008.02688.

Bel, N., Leroy, B., 1977. Analytical study of magnetoacoustic gravity waves. Astron. Astrophys. 55, 239.

Bellot Rubio, L., Orozco Suárez, D., 2019. Quiet Sun magnetic fields: an observational view. Living Rev. Sol. Phys. 16 (1), 1. http://dx.doi.org/10.1007/s41116-018-0017-1.

Bi, S., Li, R., 1998. Excitation of the solar p-modes by turbulent stress. Astron. Astrophys. 335, 673–678.

Bogdan, T.J., Carlsson, M., Hansteen, V.H., McMurry, A., Rosenthal, C.S., Johnson, M., Petty-Powell, S., Zita, E.J., Stein, R.F., McIntosh, S.W., Nordlund, Å., 2003. Waves in the magnetized solar atmosphere. II. Waves from localized sources in magnetic flux concentrations. Astrophys. J. 599 (1), 626–660. http://dx.doi.org/10.1086/378512.

Borrero, J.M., Tomczyk, S., Kubo, M., Socas-Navarro, H., Schou, J., Couvidat, S., Bogart, R., 2011. VFISV: Very fast inversion of the Stokes vector for the helioseismic and magnetic imager. Sol. Phys. 273 (1), 267–293. http://dx.doi.org/10.1007/s11207-010-9515-6, arXiv:0901.2702.

Braun, D.C., Lindsey, C., Fan, Y., Jefferies, S.M., 1992. Local acoustic diagnostics of the solar interior. Astrophys. J. 392, 739. http://dx.doi.org/10.1086/171477.

Brown, T.M., Bogdan, T.J., Lites, B.W., Thomas, J.H., 1992. Localized sources of propagating acoustic waves in the solar photosphere. Astrophys. J. Lett. 394, L65. http://dx.doi.org/10.1086/186473.

Cally, P.S., Bogdan, T.J., 1997. Simulation of f- and p-mode interactions with a stratified magnetic field concentration. Astrophys. J. Lett. 486 (1), L67–L70. http://dx.doi.org/10.1086/310833.

Cally, P.S., Moradi, H., Rajaguru, S.P., 2016. p-Mode interaction with sunspots. In: Washington DC American Geophysical Union Geophysical Monograph Series. Vol. 216. pp. 489–502. http://dx.doi.org/10.1002/9781119055006.ch28.

Cauzzi, G., Reardon, K.P., Uitenbroek, H., Cavallini, F., Falchi, A., Falciani, R., Janssen, K., Rimmele, T., Vecchio, A., Wöger, F., 2008. The solar chromosphere at high resolution with IBIS. I. New insights from the Ca II 854.2 nm line. Astron. Astrophys. 480 (2), 515–526. http://dx.doi.org/10.1051/0004-6361:20078642, arXiv:0709.2417.

De Pontieu, B., Erdélyi, R., De Moortel, I., 2005. How to channel photospheric oscillations into the corona. Astrophys. J. Lett. 624 (1), L61–L64. http://dx.doi.org/10.1086/430345.

De Pontieu, B., Erdélyi, R., James, S.P., 2004. Solar chromospheric spicules from the leakage of photospheric oscillations and flows. Nature 430 (6999), 536–539. http://dx.doi.org/10.1038/nature02749.

Finsterle, W., Jefferies, S.M., Cacciani, A., Rapex, P., McIntosh, S.W., 2004. Helioseismic mapping of the magnetic canopy in the solar chromosphere. Astrophys. J. Lett. 613 (2), L185–L188. http://dx.doi.org/10.1086/424996.

Fleck, B., Couvidat, S., Straus, T., 2011. On the formation height of the SDO/HMI Fe 6173 Å Doppler signal. Sol. Phys. 271 (1–2), 27–40. http://dx.doi.org/10.1007/s11207-011-9783-9, arXiv:1104.5166.

Gary, G.A., 2001. Plasma beta above a Solar Active Region: Rethinking the paradigm. Sol. Phys. 203 (1), 71–86. http://dx.doi.org/10.1023/A:1012722021820.

Gary, G.A., Hagyard, M.J., 1990. Transformation of vector magnetograms and the problems associated with the effects of perspective and the azimuthal ambiguity. Sol. Phys. 126, 21–36. http://dx.doi.org/10.1007/BF00158295.

Goldreich, P., Kumar, P., 1990. Wave generation by turbulent convection. Astrophys. J. 363, 694. http://dx.doi.org/10.1086/169376.

Gray, D.F., 2005. The Observation and Analysis of Stellar Photospheres, third ed. Cambridge University Press.

Hanasoge, S.M., 2008. Seismic Halos around active regions: A magnetohydrodynamic theory. Astrophys. J. 680 (2), 1457–1466. http://dx.doi.org/10.1086/587934, arXiv:0712.3578.

Hanasoge, S.M., 2009. A wave scattering theory of solar seismic power haloes. Astron. Astrophys. 503 (2), 595–599. http://dx.doi.org/10.1051/0004-6361/200912449, arXiv:0906.4671.

Handy, B.N., Acton, L.W., Kankelborg, C.C., Wolfson, C.J., Akin, D.J., Bruner, M.E., Caravalho, R., Catura, R.C., Chevalier, R., Duncan, D.W., Edwards, C.G., Feinstein, C.N., Freeland, S.L., Friedlaender, F.M., Hoffmann, C.H., Hurlburt, N.E., Jurcevich, B.K., Katz, N.L., Kelly, G.A., Lemen, J.R., Levay, M., Lindgren, R.W., Mathur, D.P., Meyer, S.B., Morrison, S.J., Morrison, M.D., Nightingale, R.W., Pope, T.P., Rehse, R.A., Schrijver, C.J., Shine, R.A., Shing, L., Strong, K.T., Tarbell, T.D., Title, A.M., Torgerson, D.D., Golub, L., Bookbinder, J.A., Caldwell, D., Cheimets, P.N., Davis, W.N., Deluca, E.E., McMullen, R.A., Warren, H.P., Amato, D., Fisher, R., Maldonado, H., Parkinson, C., 1999. The transition region and coronal explorer. Sol. Phys. 187 (2), 229–260. http://dx.doi.org/10.1023/A:1005166902804.

Hindman, B.W., Brown, T.M., 1998. Acoustic power maps of Solar Active Regions. Astrophys. J. 504 (2), 1029–1034. http://dx.doi.org/10.1086/306128.

Hoeksema, J.T., Liu, Y., Hayashi, K., Sun, X., Schou, J., Couvidat, S., Norton, A., Bobra, M., Centeno, R., Leka, K.D., Barnes, G., Turmon, M., 2014. The helioseismic and magnetic imager (HMI) vector magnetic field pipeline: Overview and performance. Sol. Phys. 289 (9), 3483–3530. http://dx.doi.org/10.1007/s11207-014-0516-8, arXiv:1404.1881.

Jain, R., Haber, D., 2002. Solar p-modes and surface magnetic fields: Is there an acoustic emission?. MDI/SOHO observations. Astron. Astrophys. 387, 1092–1099. http://dx.doi.org/10.1051/0004-6361:20020310.

Jefferies, S.M., McIntosh, S.W., Armstrong, J.D., Bogdan, T.J., Cacciani, A., Fleck, B., 2006. Magnetoacoustic portals and the basal heating of the solar chromosphere. Astrophys. J. Lett. 648 (2), L151–L155. http://dx.doi.org/10.1086/508165.

Khomenko, E., Cally, P.S., 2012. Numerical simulations of conversion to Alfvén waves in sunspots. Astrophys. J. 746 (1), 68. http://dx.doi.org/10.1088/0004-637X/746/1/68, arXiv:1111.2851.

Khomenko, E., Collados, M., 2006. Numerical modeling of magnetohydrodynamic wave propagation and refraction in sunspots. Astrophys. J. 653 (1), 739–755. http://dx.doi.org/10.1086/507760.

Khomenko, E., Collados, M., 2009. Sunspot seismic halos generated by fast MHD wave refraction. Astron. Astrophys. 506 (2), L5–L8. http://dx.doi.org/10.1051/0004-6361/200913030, arXiv:0905.3060.

Kontogiannis, I., Tsiropoula, G., Tziotziou, K., 2010. Power halo and magnetic shadow in a solar quiet region observed in the Hα line. Astron. Astrophys. 510, A41. http://dx.doi.org/10.1051/0004-6361/200912841.

Kraśkiewicz, J., Murawski, K., Musielak, Z.E., 2019. Cutoff periods of magnetoacoustic waves in the solar atmosphere. Astron. Astrophys. 623, A62. http://dx.doi.org/10.1051/0004-6361/201833186.

Kraśkiewicz, J., Murawski, K., Musielak, Z.E., 2023. Numerical simulations of two-fluid magnetoacoustic waves in the solar atmosphere. Mon. Not. R. Astron. Soc. 518 (4), 4991–5000. http://dx.doi.org/10.1093/mnras/stac2987, arXiv:2211.16463.

Krijger, J.M., Rutten, R.J., Lites, B.W., Straus, T., Shine, R.A., Tarbell, T.D., 2001. Dynamics of the solar chromosphere. III. Ultraviolet brightness oscillations from TRACE. Astron. Astrophys. 379, 1052–1082. http://dx.doi.org/10.1051/0004-6361:20011320.

Kuridze, D., Zaqarashvili, T.V., Shergelashvili, B.M., Poedts, S., 2008. Acoustic oscillations in a field-free cavity under solar small-scale bipolar magnetic canopy. Ann. Geophys. 26 (10), 2983–2989. http://dx.doi.org/10.5194/angeo-26-2983-2008, arXiv:0801.2877.

Leka, K.D., Barnes, G., Crouch, A.D., Metcalf, T.R., Gary, G.A., Jing, J., Liu, Y., 2009. Resolving the 180° ambiguity in solar vector magnetic field data: Evaluating the effects of noise, spatial resolution, and method assumptions. Sol. Phys. 260 (1), 83–108. http://dx.doi.org/10.1007/s11207-009-9440-8.

Lighthill, M.J., 1952. On sound generated aerodynamically. I. General theory. Proc. R. Soc. Lond. Ser. A 211 (1107), 564–587. http://dx.doi.org/10.1098/rspa.1952.0060.

Mathew, S.K., 2009. A new 0.5 m telescope (MAST) for solar imaging and polarimetry. In: Berdyugina, S.V., Nagendra, K.N., Ramelli, R. (Eds.), Solar Polarization 5: In Honor of Jan Stenflo. In: Astronomical Society of the Pacific Conference Series, vol. 405, p. 461.

Mathew, S.K., Bayanna, A.R., Tiwary, A.R., Bireddy, R., Venkatakrishnan, P., 2017. First observations from the multi-application solar telescope (MAST) narrow-band imager. Sol. Phys. 292 (8), 106. http://dx.doi.org/10.1007/s11207-017-1127-y.

McIntosh, S.W., Fleck, B., Judge, P.G., 2003. Investigating the role of plasma topography on chromospheric oscillations observed by TRACE. Astron. Astrophys. 405, 769–777. http://dx.doi.org/10.1051/0004-6361:20030627.

McIntosh, S.W., Jefferies, S.M., 2006. Observing the modification of the acoustic cutoff frequency by field inclination angle. Astrophys. J. Lett. 647 (1), L77–L81. http://dx.doi.org/10.1086/507425.

McIntosh, S.W., Judge, P.G., 2001. On the nature of magnetic shadows in the solar chromosphere. Astrophys. J. 561 (1), 420–426. http://dx.doi.org/10.1086/323068.

Metcalf, T.R., 1994. Resolving the 180-degree ambiguity in vector magnetic field measurements: The 'minimum' energy solution. Sol. Phys. 155 (2), 235–242. http://dx.doi.org/10.1007/BF00680593.

Moretti, P.F., Jefferies, S.M., Armstrong, J.D., McIntosh, S.W., 2007. Observational signatures of the interaction between acoustic waves and the solar magnetic canopy. Astron. Astrophys. 471 (3), 961–965. http://dx.doi.org/10.1051/0004-6361:20077247.

Nagashima, K., Sekii, T., Kosovichev, A.G., Shibahashi, H., Tsuneta, S., Ichimoto, K., Katsukawa, Y., Lites, B., Nagata, S., Shimizu, T., Shine, R.A., Suematsu, Y., Tarbell, T.D., Title, A.M., 2007. Observations of sunspot oscillations in G band and CaII H line with solar optical telescope on hinode. Pub. Astron. Soc. Jpn. 59, S631. http://dx.doi.org/10.1093/pasj/59.sp3.S631, arXiv:0709.0569.

Norton, A.A., Graham, J.P., Ulrich, R.K., Schou, J., Tomczyk, S., Liu, Y., Lites, B.W., López Ariste, A., Bush, R.I., Socas-Navarro, H., Scherrer, P.H., 2006. Spectral line selection for HMI: A comparison of Fe I 6173 Å and Ni I 6768 Å. Sol. Phys. 239 (1–2), 69–91. http://dx.doi.org/10.1007/s11207-006-0279-y, arXiv:astro-ph/0608124.

Nutto, C., Steiner, O., Schaffenberger, W., Roth, M., 2012. Modification of wave propagation and wave travel-time by the presence of magnetic fields in the solar network atmosphere. Astron. Astrophys. 538, A79. http://dx.doi.org/10.1051/0004-6361/201016083.

Pesnell, W.D., Thompson, B.J., Chamberlin, P.C., 2012. The solar dynamics observatory (SDO). Sol. Phys. 275 (1–2), 3–15. http://dx.doi.org/10.1007/s11207-011-9841-3.

Raja Bayanna, A., Mathew, S.K., Venkatakrishnan, P., Srivastava, N., 2014. Narrow-band imaging system for the multi-application solar telescope at udaipur solar observatory: Characterization of lithium Niobate Etalons. Sol. Phys. 289 (10), 4007–4019. http://dx.doi.org/10.1007/s11207-014-0557-z, arXiv:1407.7627.

Rajaguru, S.P., Couvidat, S., Sun, X., Hayashi, K., Schunker, H., 2013. Properties of high-frequency wave power halos Around Active Regions: An analysis of multi-height data from HMI and AIA onboard SDO. Sol. Phys. 287 (1–2), 107–127. http://dx.doi.org/10.1007/s11207-012-0180-9, arXiv:1206.5874.

Rajaguru, S.P., Sangeetha, C.R., Tripathi, D., 2019. Magnetic fields and the supply of low-frequency acoustic wave energy to the solar chromosphere. Astrophys. J. 871 (2), 155. http://dx.doi.org/10.3847/1538-4357/aaf883.

Rijs, C., Rajaguru, S.P., Przybylski, D., Moradi, H., Cally, P.S., Shelyag, S., 2016. 3D simulations of realistic power halos in magnetohydrostatic sunspot atmospheres: Linking theory and observation. Astrophys. J. 817 (1), 45. http://dx.doi.org/10.3847/0004-637X/817/1/45, arXiv:1512.01297.

Rimmele, T.R., Warner, M., Keil, S.L., Goode, P.R., Knölker, M., Kuhn, J.R., Rosner, R.R., McMullin, J.P., Casini, R., Lin, H., Wöger, F., von der Lühe, O., Tritschler, A., Davey, A., de Wijn, A., Elmore, D.F., Fehlmann, A., Harrington, D.M., Jaeggli, S.A., Rast, M.P., Schad, T.A., Schmidt, W., Mathioudakis, M., Mickey, D.L., Anan, T., Beck, C., Marshall, H.K., Jeffers, P.F., Oschmann, J.M., Beard, A., Berst, D.C., Cowan, B.A., Craig, S.C., Cross, E., Cummings, B.K., Donnelly, C., de Vanssay, J.-B., Eigenbrot, A.D., Ferayorni, A., Foster, C., Galapon, C.A., Gedrites, C., Gonzales, K., Goodrich, B.D., Gregory, B.S., Guzman, S.S., Guzzo, S., Hegwer, S., Hubbard, R.P., Hubbard, J.R., Johansson, E.M., Johnson, L.C., Liang, C., Liang, M., McQuillen, I., Mayer, C., Newman, K., Onodera, B., Phelps, L., Puentes, M.M., Richards, C., Rimmele, L.M., Sekulic, P., Shimko, S.R., Simison, B.E., Smith, B., Starman, E., Sueoka, S.R., Summers, R.T., Szabo, A., Szabo, L., Wampler, S.B., Williams, T.R., White, C., 2020. The Daniel K. Inouye solar telescope - Observatory overview. Sol. Phys. 295 (12), 172. http://dx.doi.org/10.1007/s11207-020-01736-7.

Rosenthal, C.S., Bogdan, T.J., Carlsson, M., Dorch, S.B.F., Hansteen, V., McIntosh, S.W., McMurry, A., Nordlund, Å., Stein, R.F., 2002. Waves in the magnetized solar atmosphere. I. Basic processes and internetwork oscillations. Astrophys. J. 564 (1), 508–524. http://dx.doi.org/10.1086/324214.

Schou, J., Scherrer, P.H., Bush, R.I., Wachter, R., Couvidat, S., Rabello-Soares, M.C., Bogart, R.S., Hoeksema, J.T., Liu, Y., Duvall, T.L., Akin, D.J., Allard, B.A., Miles, J.W., Rairden, R., Shine, R.A., Tarbell, T.D., Title, A.M., Wolfson, C.J., Elmore, D.F., Norton, A.A., Tomczyk, S., 2012. Design and ground calibration of the helioseismic and magnetic imager (HMI) instrument on the solar dynamics observatory (SDO). Sol. Phys. 275 (1–2), 229–259. http://dx.doi.org/10.1007/s11207-011-9842-2.

Schunker, H., Braun, D.C., 2011. Newly identified properties of surface acoustic power. Sol. Phys. 268 (2), 349–362. http://dx.doi.org/10.1007/s11207-010-9550-3, arXiv:0911.3042.

Snodgrass, H.B., 1984. Separation of large-scale photospheric Doppler patterns. Sol. Phys. 94 (1), 13–31. http://dx.doi.org/10.1007/BF00154804.

Sobotka, M., Heinzel, P., Švanda, M., Jurčák, J., del Moro, D., Berrilli, F., 2016. Chromospheric heating by acoustic waves compared to radiative cooling. Astrophys. J. 826 (1), 49. http://dx.doi.org/10.3847/0004-637X/826/1/49, arXiv:1605.04794.

Sobotka, M., Švanda, M., Jurčák, J., Heinzel, P., Del Moro, D., Berrilli, F., 2013. Dynamics of the solar atmosphere above a pore with a light bridge. Astron. Astrophys. 560, A84. http://dx.doi.org/10.1051/0004-6361/201322148, arXiv:1309.7790.

Stein, R.F., 1967. Generation of acoustic and gravity waves by turbulence in an isothermal stratified atmosphere. Sol. Phys. 2 (4), 385–432. http://dx.doi.org/10.1007/BF00146490.

Straus, T., Fleck, B., Jefferies, S.M., Cauzzi, G., McIntosh, S.W., Reardon, K., Severino, G., Steffen, M., 2008. The energy flux of internal gravity waves in the lower solar atmosphere. Astrophys. J. Lett. 681 (2), L125. http://dx.doi.org/10.1086/590495.

Thomas, J.H., Stanchfield, I., 2000. Fine-scale magnetic effects on P-modes and higher frequency acoustic waves in a Solar Active Region. Astrophys. J. 537 (2), 1086–1093. http://dx.doi.org/10.1086/309046.

Toner, C.G., Labonte, B.J., 1993. Direct mapping of solar acoustic power. Astrophys. J. 415, 847. http://dx.doi.org/10.1086/173206.

Torrence, C., Compo, G.P., 1998. A practical guide to wavelet analysis. Bull. Am. Meteorol. Soc. 79 (1), 61–78. http://dx.doi.org/10.1175/1520-0477(1998)079.

Vecchio, A., Cauzzi, G., Reardon, K.P., Janssen, K., Rimmele, T., 2007. Solar atmospheric oscillations and the chromospheric magnetic topology. Astron. Astrophys. 461 (1), L1–L4. http://dx.doi.org/10.1051/0004-6361:20066415, arXiv:astro-ph/0611206.

Venkatakrishnan, P., Mathew, S.K., Srivastava, N., Bayanna, A.R., Kumar, B., Ramya, B., Jain, N., Saradava, M., 2017. The multi application solar telescope. Current Sci. 113 (4), 686. http://dx.doi.org/10.18520/cs/v113/i04/686-690.

Available online at www.sciencedirect.com

ScienceDirect

Advances in Space Research xx (2023) xxx-xxx

ADVANCES IN SPACE RESEARCH
(a COSPAR publication)

www.elsevier.com/locate/asr

On the propagation of gravity waves in the lower solar atmosphere in different magnetic configurations

Hirdesh Kumar[a,b,*], Brajesh Kumar[a], S. P. Rajaguru[c,d]

[a] Udaipur Solar Observatory, Physical Research Laboratory, Dewali, Badi Road, Udaipur 313004 Rajasthan, India
[b] Department of Physics, Indian Institute of Technology Gandhinagar, Gandhinagar 382 355 Gujarat, India
[c] Indian Institute of Astrophysics, Bangalore 560034, India
[d] Solar Observatories Group, Department of Physics and W.W. Hansen Experimental Physics Lab, Stanford University, Stanford CA, 94305-4085 USA.

Abstract

Gravity waves are generated by turbulent subsurface convection overshooting or penetrating locally into a stably stratified medium. While propagating energy upwards, their characteristic negative phase shift over height is a well-recognized observational signature. Since their first detailed observational detection and estimates of energy content, a number of studies have explored their propagation characteristics and interaction with magnetic fields and other waves modes in the solar atmosphere. Here, we present a study of the atmospheric gravity wave dispersion diagrams utilizing intensity observations that cover photospheric to chromospheric heights over different magnetic configurations of quiet-Sun (magnetic network regions), a plage, and a sunspot as well as velocity observations within the photospheric layer over a quiet and a sunspot region. In order to investigate the propagation characteristics, we construct two-height intensity - intensity and velocity- velocity cross-spectra and study phase and coherence signals in the wavenumber - frequency dispersion diagrams and their association with background magnetic fields. We find signatures of association between magnetic fields and much reduced coherence and phase shifts over height from intensity-intensity and velocity-velocity phase and coherence diagrams, both indicating suppression/scattering of gravity waves by the magnetic fields. Our results are consistent with the earlier numerical simulations, which indicate that gravity waves are suppressed or scattered and reflected back into the lower solar atmosphere in the presence of magnetic fields.

Keywords: Sun: photosphere – Sun: chromosphere – Sun: magnetic fields – Sun: oscillations – Sun: sunspots

1. Introduction

Waves in a compressible stratified medium in the presence of a gravitational field, like the atmosphere of the Earth or the Sun, can be driven by both compressional and buoyancy forces, resulting in a rich spectrum of acoustic-gravity waves. In the lower solar atmosphere, such waves are well recognised as an agent of non-thermal energy transfer, especially through their interactions with and transformations by the highly structured magnetic fields that thread these layers. These waves are generated by turbulent convection within and near the top boundary layers of the convection zone (Schwarzschild, 1948; Lighthill, 1952; Stein, 1967; Goldreich & Kumar, 1990) and the acoustic part of the spectrum resonate to form p-modes in the interior of the Sun. In the solar atmosphere, the behaviour of waves become more complicated owing to the sharp fall in density and the preferred direction imposed by gravity in the fluid: the propagation characteristics are anisotropic, in general. In addition, the stratification of the atmosphere also imposes height-dependent cutoff frequencies below which gravity modified acoustic waves cannot propagate (Mihalas & Mihalas, 1995) upward of the respective heights. The internal or atmospheric gravity waves (IGWs) are generated by turbulent subsurface convection overshooting or penetrating locally into a stably stratified medium (Lighthill, 1967). This is a normal response generated by a gravitationally stratified medium to any

*Corresponding author: Email: hirdesh@prl.res.in

https://dx.doi.org/10.1016/j.jasr.xxxx.xx.xxx

perturbations from its equilibrium position, and buoyancy acting as a restoring force. Lighthill (1967) suggested that the oscillations observed in the upper photosphere and lower chromosphere can be interpreted as gravity waves, and also that radiative damping of such gravity waves provides a mechanism of heating of the lower chromosphere. One of the interesting properties of IGWs is that, while transporting energy upward from the photosphere to higher layers, they show a characteristic downward phase propagation (Lighthill, 1978). These waves play an important role in the transportation of energy and momentum and mixing the material in the regions that they propagate in. For example, the IGWs in the solar radiative interior and in other stars, despite no clear detection of their signatures at the solar surface, are theorized to play key roles in the mixing and transport of angular momentum. The investigation of Mihalas & Toomre (1981, 1982) revealed that gravity waves can reach a maximum height of 900 - 1600 km in the solar atmosphere depending upon the energy flux carried by these waves, before nonlinearities lead to wave breaking. Following the above initial studies, the propagation characteristics of IGWs in the solar atmosphere have been examined utilizing velocity-velocity, intensity-intensity observations or simulations or both by a good number of authors (Deubner & Fleck, 1989; Krijger et al., 2001; Rutten & Krijger, 2003; Straus et al., 2008; Kneer & Bello González, 2011; Nagashima et al., 2014; Vigeesh et al., 2017, 2019; Vigeesh & Roth, 2020; Vigeesh et al., 2021). Krijger et al. (2001), utilizing the 1700 Å and 1600 Å intensity observations obtained from the Transition Region and Coronal Explorer (TRACE) instrument of a quiet region observed in the disk centre, identified gravity waves in the $k_h - \nu$ phase diagram (c.f. Figure 24, Krijger et al. (2001)). Subsequently, Rutten & Krijger (2003) using the simultaneous UV intensities (1700 Å and 1600 Å intensity images) obtained from the TRACE also detected the gravity waves in $k_h - \nu$ phase diagram (c.f., Figure 3, Rutten & Krijger (2003)). They have also found the signature of gravity waves in the $k_h - \nu$ phase diagram constructed from white light and 1700 Å intensity images (c.f., Figure 5, Rutten & Krijger (2003)). Using $V - V$ observations along with 3D numerical simulations, Straus et al. (2008) detected the upward propagating atmospheric gravity waves. They also estimated that the energy flux carried by gravity waves was comparable to the radiative losses of the entire chromosphere. Using observations of Fe I 5576 Å and Fe I 5434 Å lines, Kneer & Bello González (2011) studied acoustic and atmospheric gravity waves in the quiet Sun and estimated their energy transport to the chromosphere. They concluded that gravity waves also contribute in the chromospheric heating. Using multi-height velocity extractions from the Fe I 6173 Å line filtergrams provided by the HMI/SDO, Nagashima et al. (2014) also reported the presence of atmospheric gravity waves in the solar atmosphere. More recently, using realistic 3D numerical simulations of the solar atmosphere to investigate the propagation dynamics of acoustic-gravity waves, Vigeesh et al. (2017) conclude that IGWs are absent or partially reflected back into the lower layers in the presence of the magnetic fields. They further argue that the suppression is due to the coupling of IGWs to slow magnetoacoustic waves still within the high plasma-β region of the upper photosphere. Vigeesh et al. (2019) found that the propagation properties of IGWs depend on the average magnetic field strength in the upper photosphere and therefore these waves can be potential candidates for magnetic field diagnostics of these layers.

In this article, we report our results from a detailed study of the atmospheric gravity wave dispersion diagrams utilizing intensity observations that cover photospheric to chromospheric heights over regions of different magnetic configurations: quiet-Sun (magnetic network regions), plage, and sunspot. Additionally, we have used two-height velocities estimated within Fe I 6173 Å line over a quiet and a sunspot region. In order to investigate the propagation characteristics, we construct two-height intensity - intensity and velocity - velocity cross-spectra and study the phase and coherence signals in the wavenumber - frequency ($k_h - \nu$) dispersion diagrams and their association with background magnetic fields, utilizing long duration data sets situated at different locations on the solar disc. We compare the derived signatures of the interaction between the IGWs and magnetic fields with those reported using numerical simulations by Vigeesh et al. (2017, 2019), and Vigeesh & Roth (2020). The article is structured as follows: Section 2 discusses the observations, data sets, and analysis procedures, Section 3 presents the results obtained in this investigation, followed by Section 4 that presents discussions and conclusions.

2. Observational Data and Analyses

We employ two-height cross-spectra of intensities and velocities observed over regions of interest to study the height evolution of wave phases and interaction with the background magnetic fields. Intensity - intensity ($I - I$) cross spectra utilise observations obtained from the Helioseismic and Magnetic Imager (HMI; Schou et al. (2012) instrument onboard the Solar Dynamics Observatory (SDO; Pesnell et al. (2012)) for the photosphere using the Fe I 6173 Å line, and from the Atmospheric Imaging Assembly (AIA; Lemen et al. (2012)) onboard the SDO for the 1700 Å and 1600 Å UV channels that sample the photosphere - chromosphere. Velocity - Velocity ($V - V$) cross spectra utilise observation obtained using photospheric Fe I 6173 Å line from the Interferometric BI-dimensional Spectrometer (IBIS; Cavallini (2006)) instrument installed at the Dunn Solar Telescope (DST) at Sacramento Peak, New Mexico. We analyze observations of three large regions, identified as data set 1, 2, and 3, of widely differing magnetic configurations. These regions are also situated on the different locations on the Sun. The data set 1 covers quiet or weak magnetic patches identified by red dashed boxes and labelled $M1$ and $M2$, a plage and sunspot (NOAA AR 11092) areas identified by green and white dashed boxes labelled P, S, respectively (c.f., Figure 1). This whole region was situated near the disk centre ($63'', 150''$ solar coordinates) and was observed on August 03, 2010. The observables include photospheric line-of-sight magnetograms (B_{LOS}), continuum intensity (I_c), UV intensities in 1700 (I_{uv1}) and 1600 (I_{uv2}) Å filters, and the data have been tracked and remapped for a duration of 14 hours; this data set has previously been used for a study of high-frequency acoustic

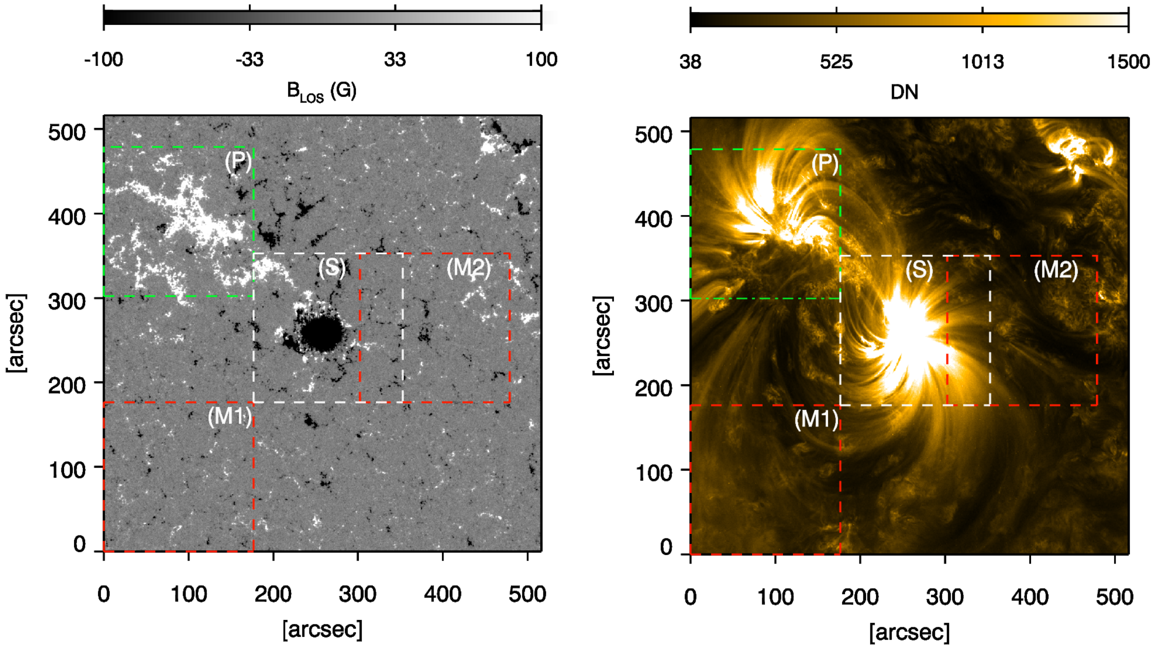

Fig. 1. *Left panel*: HMI line-of-sight magnetic field of a large region observed on August 3, 2010 corresponding to the start time of data used in this work. The colored dashed regions mark the boundaries of sub-regions studied in this work: regions enclosed in red, white and green colored boxes mark the quiet magnetic network, sunspot and plage regions, and also denoted by $M1$, $M2$, S, P, respectively. The magnetic field grey scale has been saturated at ± 100 G to view better the small scale magnetic fields. *Right panel*: Same as left panel but from AIA 171 Å channel.

halos by Rajaguru et al. (2013) and also for a study of the propagation of low-frequency acoustic waves into the chromosphere by Rajaguru et al. (2019). The data set 2 includes a quiet patch identified by red dashed square box labelled Q, and two further sub-regions near the sunspot (NOAA AR 12186) demarcated by green square boxes labelled $R1$ and $R2$ (c.f. Figure 2). This large region was away from the disk centre (-309″,-418″ solar coordinates) and was observed on October 11, 2014, and the same observables as for data set 1 are tracked and remapped for a duration of 12 h 47 minutes. The data set 3 covers a quiet and a sunspot (NOAA AR 10960) region demarcated as black square box and labelled A and B (c.f. Figure 3), which are identified from the field-of-view of the IBIS instrument. The observed region was also located close to the disk centre (276″,-227″ solar coordinates) on June 8, 2007. The identified regions (quiet (A) and sunspot (B)) comprise 3 hours 44 minutes duration and utilized two height velocities within Fe I 6173 Å line formation region. This IBIS data set has been previously used for various studies (Rajaguru et al., 2010; Couvidat et al., 2012; Zhao et al., 2022). The values of average of absolute line-of-sight magnetic fields integrated over whole observation period in the $M1$, $M2$, P, S, Q, $R1$, $R2$, A, and B region are tabulated in Table 1. Brief descriptions of the instruments and data reductions done for the above observations are provided in the following sub-sections.

2.1. *HMI and AIA Observations*

The HMI instrument observes the photosphere of the Sun in Fe I 6173 Å absorption spectral line at six different wavelength positions. It provides full disk (4096×4096 pixel^2) continuum intensity, line depth, Dopplergrams, and line-of-sight magnetograms at a spatial sampling of 0.504″ per pixel and at a temporal cadence of 45 s. It also provides full-disk vector magnetic field at a slightly lower cadence (12 minutes) as a standard product, although it can also be obtained at a cadence of 135 s (Hoeksema et al., 2014). The AIA instrument observes the outer atmosphere of the Sun in seven extreme ultraviolet (EUV) filters at 94, 131, 171, 193, 211, 304 and 335 Å, two ultraviolet (UV) filters at 1600 and 1700 Å and one white light filter at 4500 Å wavelengths. It provides full disc images (4096×4096 pixel^2) at a spatial sampling of 0.6″ per pixel. The temporal cadence is 12 s for EUV, 24 s for UV, and 3600 s for the white light filter. Here, we have used photospheric continuum intensity (I_c), and line-of-sight magnetograms (B_{LOS}) from the HMI at a cadence of 45 s and UV observations in 1700 (I_{uv1}) and 1600 (I_{uv2}) Å at a cadence of 24 s obtained from the AIA instrument, respectively. We have tracked and remapped the images of all these observables to the same spatial and temporal sampling as HMI observations. The sub-regions $M1$, $M2$, P, and S from data set 1 are of size 176×176 arcsec^2, as shown in the Figure 1, gives us a wavenumber resolution (Δk_h) of 0.049 rad Mm^{-1}. The total time duration of data set 1 is 14 hours and cadence (45 s), gives us a frequency resolution ($\Delta\nu$) of 19.8 μHz, and Nyquist frequency (ν_{Ny}) of 11.11 mHz. The spatial resolution $\delta x = 0.504''$ per pixel corresponds to Nyquist wavenumber ($k_{Ny} = \pi/\delta x$) of 8.55 rad Mm^{-1}. The data set 2 comprise of Q, $R1$, and $R2$ regions of 100×100 arcsec^2 shown in the Figure 2, gives us a wavenumber resolution (Δk_h) of 0.0859 rad Mm^{-1}. The total time duration of data set 2 is 12 h 47 minutes, spatial sampling and temporal cadence are same as data set 1. Hence,

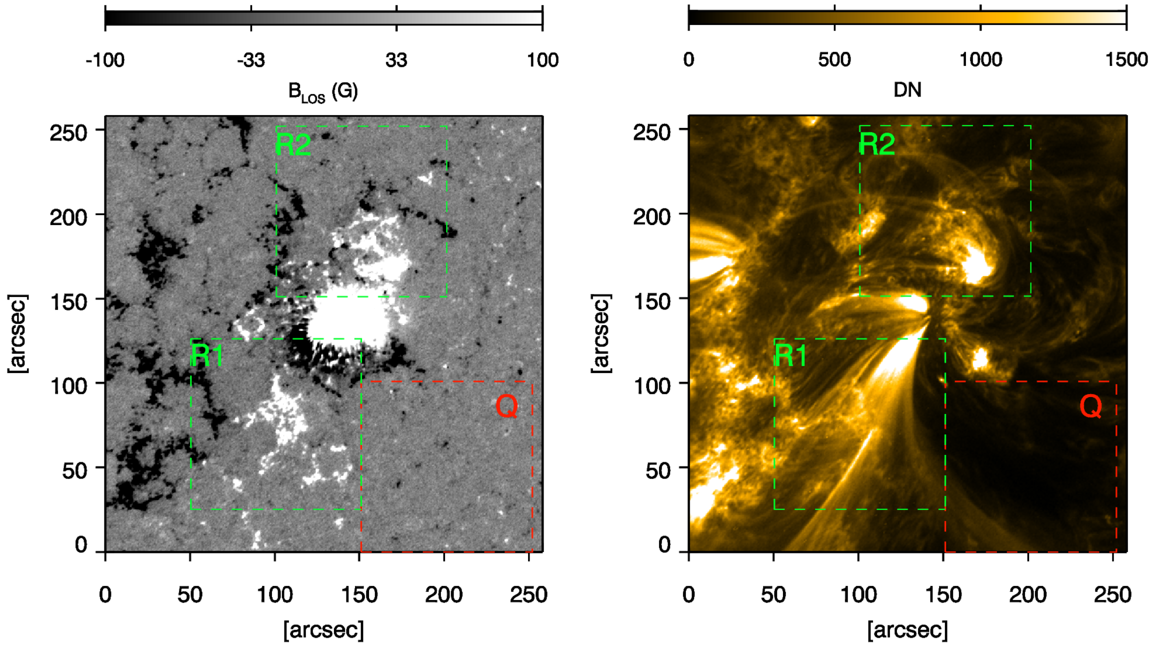

Fig. 2. *Left panel*: HMI line-of-sight magnetic field of a large region observed on October 11, 2014 corresponding to the start time of data used in this work. The colored dashed regions mark the boundaries of sub-regions studied in this work: regions enclosed in red, and green colored boxes mark the quiet magnetic network, canopy regions, and also denoted by Q, $R1$, and $R2$, respectively. The magnetic field grey scale has been saturated at ± 100 G to view better the small scale magnetic fields. *Right panel*: Same as left panel but from AIA 171 Å channel.

Table 1. Table represents the values of average of absolute line-of-sight magnetic fields over selected locations.

Location	$< \lvert B_{LOS} \rvert >$ (G)
$M1$	3.3
$M2$	5.5
P	37.0
S	53.2
Q	2.7
$R1$	32.2
$R2$	32.8
A	5.8
B	74.2

it gives us a frequency resolution ($\Delta\nu$) of 21.7 μHz.

2.2. IBIS Observations

The imaging spectropolarimetry data were acquired on June 08, 2007 utilizing the IBIS instrument installed at the DST. The IBIS has a circular FOV of 80″ in diameter (≈ 60 Mm). The observed region covers a medium size sunspot and surrounding quiet-Sun situated near the disk center, with full Stokes (I,Q,U,V) images scanned over 23 wavelength positions along the Fe I 6173.3 Å line at a spectral resolution of 25 mÅ. The spatial resolution of these observations is 0.33″ (0.165″ per pixel) at a temporal cadence of 47.5 s. From these observations Rajaguru et al. (2010) have estimated 10 bisector line-of-sight Doppler velocities starting from line core (level 0) to line wing (level 9). Here, we have used two height velocities at 10% (V_{10}) and 80% (V_{80}) intensity levels in our analysis, in which V_{80} corresponds to lower height, whereas V_{10} corresponds to upper height within the Fe I 6173 Å line. The data set 3 comprises of a quiet (A) and a sunspot (B) region of 24×24 arcsec^2 as shown in Figure 3. The total time duration of data set 3 is 3 hours 44 minutes, and temporal cadence (47.5 s), gives us a frequency resolution ($\Delta\nu$) of 74.4 μHz, and Nyquist frequency (ν_{Ny}) of 10.5 mHz. The spatial resolution $\delta x = 0.165''$ per pixel corresponds to Nyquist wavenumber ($k_{Ny} = \pi/\delta x$) of 26.2 rad Mm^{-1}.

2.3. Height Coverage of HMI and AIA Observations

The HMI and AIA observables, as described above, are chosen to cover the photospheric to mid-chromospheric layers of the solar atmosphere. The formation height of Fe I 6173 Å line in the solar photosphere was investigated by Norton et al. (2006), who derived a height range of h = 16 – 302 km above the continuum optical depth at 5000 Å(τ_c = 1, which corresponds to z = 0) in the quiet region. However, the formation

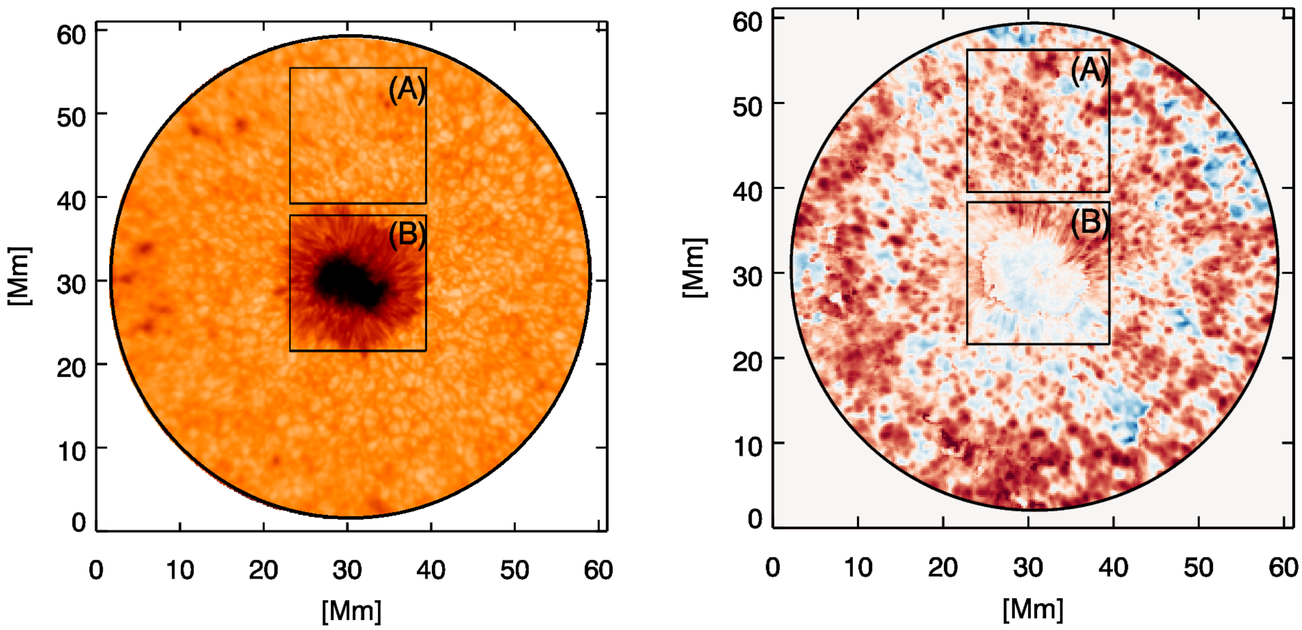

Fig. 3. *Left panel*: A sample image of continuum intensity showing the field of view of the observation obtained from the IBIS/DST with a sunspot at the center. The black square regions mark the boundaries of sub-regions of a quiet and a sunspot region studied in this work, also denoted by *A*, and *B*, respectively. *Right panel*: A sample image of line-of-sight Doppler velocity estimated by bisector method at 10% intensity levels i.e. V_{10} velocity map.

height of Fe I 6173 Å line in the magnetized region i.e. umbra is lower compare to quiet region. Norton et al. (2006) utilizing the Maltby-M umbral atmosphere model reported that core of Fe I 6173 Å line form around 270 km, while wings form around 20 km above $\tau_c = 1$ continuum optical depth. Non-LTE radiation hydrodynamic simulations done by Fossum & Carlsson (2005) show that the average formation heights of 360 and 430 km for the 1700 and 1600 Å passbands, respectively, although the 1600 Å passband has contributions from a wider height-range extending into upper chromosphere.

2.4. Cross-Spectral Analysis of Wave Propagation

We investigate the cross-spectra of IGWs utilizing different observables covering heights from photosphere (20 km) to chromosphere (430 km). We form two-height intensity - intensity $(I - I)$ and velocity - velocity $(V - V)$ pairs and study their cross-spectra. Cross-spectra of two observables $f_1(x, y, t)$ and $f_2(x, y, t)$ are defined as the complex-valued product of their three dimensional Fourier transforms (Vigeesh et al., 2017),

$$X_{12}(\boldsymbol{k}, \nu) = \boldsymbol{f}_1(\boldsymbol{k}, \nu)\boldsymbol{f}^*{}_2(\boldsymbol{k}, \nu) \tag{1}$$

where $\boldsymbol{f}$'s are the Fourier transforms, with a superscript $*$ representing the complex conjugate, $\boldsymbol{k} = \boldsymbol{k_h} = (k_x, k_y)$ is the horizontal wave vector and ν is the cyclic frequency. Here, subscripts 1 and 2 in f_1 and f_2 denote the two heights z_1 and z_2 of the observables. The phase spectrum, $\delta\phi(\boldsymbol{k}, \nu)$, that captures the phase evolution between heights of the two observables is then given by the phase of the complex cross-spectrum $X_{12}(\boldsymbol{k}, \nu)$,

$$\delta\phi(\boldsymbol{k}, \nu) = \tan^{-1}[Im(X_{12}(\boldsymbol{k}, \nu))/Re(X_{12}(\boldsymbol{k}, \nu))] \tag{2}$$

The normalised magnitude of $X_{12}(\boldsymbol{k}, \nu)$ is used to calculate the coherence,

$$C(\boldsymbol{k}, \nu) = \frac{|X_{12}(\boldsymbol{k}, \nu)|}{\sqrt{|\boldsymbol{f}_1|^2|\boldsymbol{f}_2|^2}}, \tag{3}$$

We focus on studying $\delta\phi(k_h, \nu)$ from the different $I-I$ and $V-V$ cross-spectra that trace photospheric - chromospheric height ranges, viz. the HMI continuum I_c, AIA UV intensities I_{uv1} (1700 Å) and I_{uv2} (1600 Å) offer pairs of heights from among 20, 360, and 430 km, respectively and two height velocities estimated within Fe I 6173 Å line formation region i.e. V_{80} and V_{10} are correspond to within 16 – 300 km height range above $\tau_c = 1$. In all our analyses, we azimuthally average the three-dimensional spectra in the $k_x - k_y$ plane to derive $k_h - \nu$ diagrams of $\delta\phi(k_h, \nu)$ and $C(k_h, \nu)$, where $k_h = \sqrt{k_x^2 + k_y^2}$.

To guide the analysis, we employ the well known dispersion relation, derived under the Cowling approximation that neglects perturbations in the gravitational potential for adiabatic acoustic-gravity waves in the solar interior and atmosphere (Leibacher & Stein, 1981),

$$k_z^2 = \frac{(\omega^2 - \omega_{ac}^2)}{c_s^2} - \frac{(\omega^2 - N^2)}{\omega^2}k_h^2 \tag{4}$$

where $\omega = 2\pi\nu$ is the angular frequency, ω_{ac} is the acoustic cutoff frequency and N is the Brunt-Väisälä frequency. In a $k_h - \nu$ diagram, regions where $k_z^2 > 0$ demarcates vertically propagating acoustic-gravity waves from the evanescent ($k_z^2 < 0$) ones. In all our two-height $\delta\phi(k_h, \nu)$ that we derive from observations, we mark such propagation boundaries by evaluating the $k_z^2 = 0$ condition using the dispersion relation given by Eqn. 4 for the upper height using the VAL-C model of the solar chro-

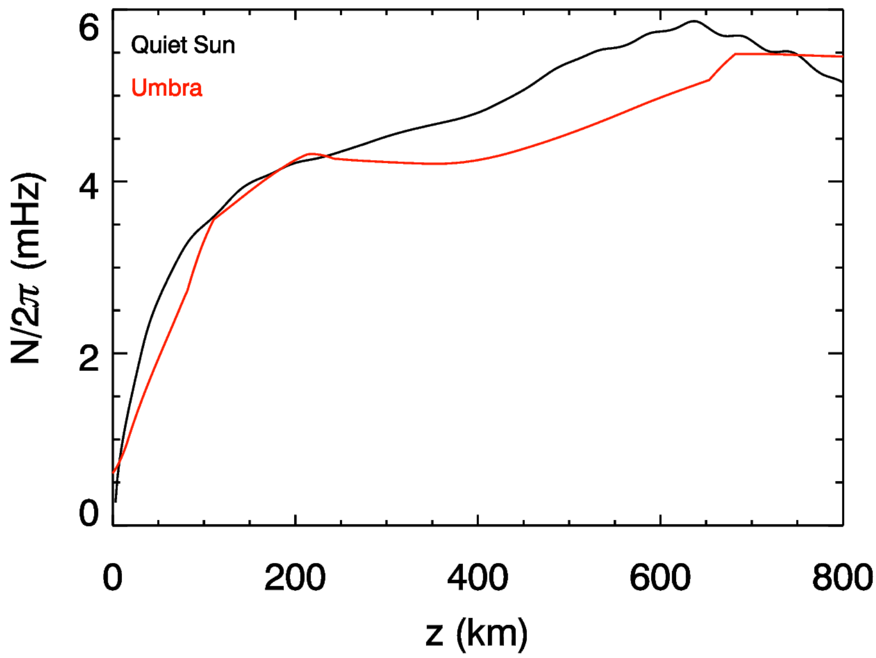

Fig. 4. Height evolution of Brunt-Väisälä frequency (N) for quiet-Sun (black) of a realistic solar atmosphere using the VAL-C model and umbra (red) of a sunspot using Maltby-M model.

mosphere (Vernazza et al., 1981). The expressions for ω_{ac} and N applicable for a gravitationally stratified atmospheres are,

$$\omega_{ac}^2 = \frac{c_s^2}{4H_\rho^2}(1 - 2\frac{dH_\rho}{dz}) \tag{5}$$

$$N^2 = \frac{g}{H_\rho} - \frac{g^2}{c_s^2} \tag{6}$$

We have two solutions for $k_z^2 = 0$, and hence two propagation boundaries separating vertically propagating waves from the evanescent ones in the $k_h - \nu$ diagram: the higher frequency boundary corresponds to the cut-off frequency for acoustic waves while the lower frequency one, typically falling lower than the f-mode frequencies, is that for the internal or atmospheric gravity waves. The locations of these boundaries in the $k_h - \nu$ plane depends on height in the atmosphere, and we typically overplot these boundaries for upper heights (solid black line) involved in each pair of variables for which the cross-spectral phases, ($\delta\phi$), coherences, (C) are derived. We also overplot the dispersion curve of the surface gravity mode (f-mode) and that of acoustic Lamb mode in each diagrams.

3. Results

The IGWs in the solar atmosphere have their sources in the photospheric granular convection, which overshoots into the stable layers above. As alluded to earlier, the IGWs have the characteristics of transporting energy upward while their phases propagate downward, hence exhibit negative phase in the gravity wave regime of $k_h - \nu$ cross-spectral phase diagram. We first present and analyse the phase and coherence signals in the $I - I$ cross-spectra that we obtain for the two large regions covering different magnetic configurations, viz. quiet magnetic network, plage, and sunspots, which are shown in Figures 1 and 2. Next, we analyse the phase and coherence diagrams constructed from $V - V$ pair over a quiet and a sunspot region. The wave propagation boundary corresponding to $k_z^2 = 0$ for the IGWs is set by the Brunt-Väisälä frequency, N, which is a function of height in the solar atmosphere and is given by equation 6. Using the VAL-C model (Vernazza et al., 1981) for quiet Sun and the Maltby-M model (Maltby et al., 1986) for sunspot umbra, we have calculated N and plotted in Figure 4. It shows that N increases upto a height of $\approx$ 600 km and then it starts decreasing, and it also indicates that there is no significant difference between the variation of N in the quiet-Sun and umbra of a sunspot. For the mean height of formation of intensity I_{uv2}, N approaches $\approx$ 5 mHz.

As the primary objective of this work is to study the effect of magnetic fields on the propagation of IGWs, we first discuss the phase spectra of gravity waves in the quiet magnetic network regions followed by a comparision between the phase obtained for strongly magnetized regions and quiet regions. Results on effects of magnetic fields on the coherence of IGWs are presented at the end.

3.1. Phase Spectra of IGWs in Quiet-Sun Regions

The region labelled $M1$ in Figure 1 has the average absolute LOS magnetic field of $\approx$ 3 G (integrated over whole observation period) and is chosen to represent the quiet-Sun. The cross-spectral phase difference, $\delta\phi$, and coherence, C, diagrams obtained for this region (from data set 1) are shown in Figure 5:

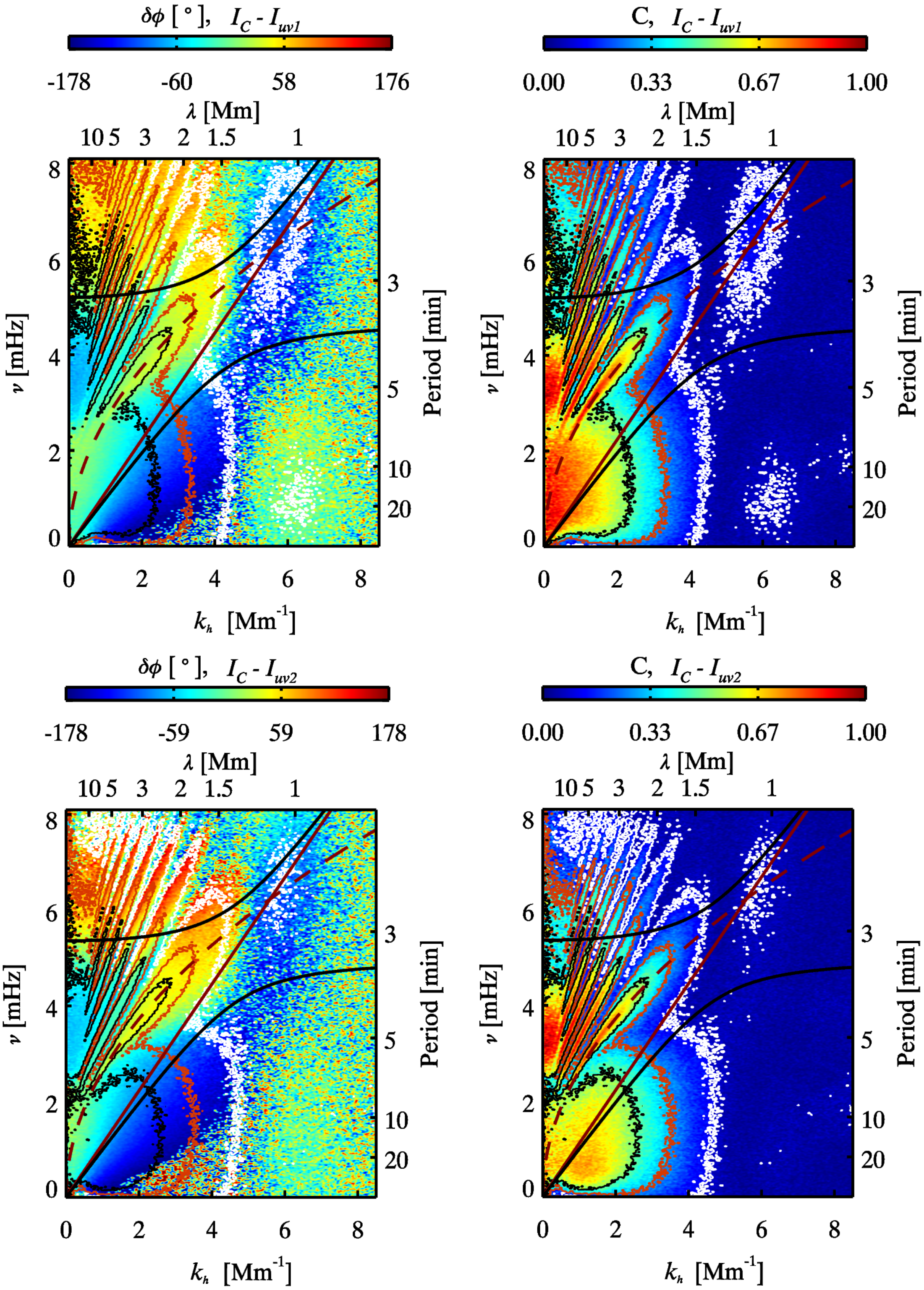

Fig. 5. *Top panel*: Cross-spectral phase difference, $\delta\phi(k_h, \nu)$ (*top left panel*), and coherence, $C(k_h, \nu)$ (*top right panel*), diagrams of $M1$ region constructed from $I_c - I_{uv1}$ pair of photospheric continuum intensity (HMI) and UV 1700 Å channel of AIA, which correspond to 20 – 360 km above z = 0 in the solar atmosphere. *Bottom panel*: same as *top panel*, but from $I_c - I_{uv2}$ pair of photospheric continuum intensity (HMI) and UV 1600 Å channel of AIA, which correspond to 20 – 430 km above z = 0 in the solar atmosphere. The solid black lines separate vertically propagating waves ($k_z^2 > 0$) from the evanescent ones ($k_z^2 < 0$) at upper height. The dashed red line is the f-mode dispersion curve and solid red line is the Lamb mode. The overplotted black, red and white contours represent the coherence at 0.5, 0.3 and 0.1 levels, respectively.

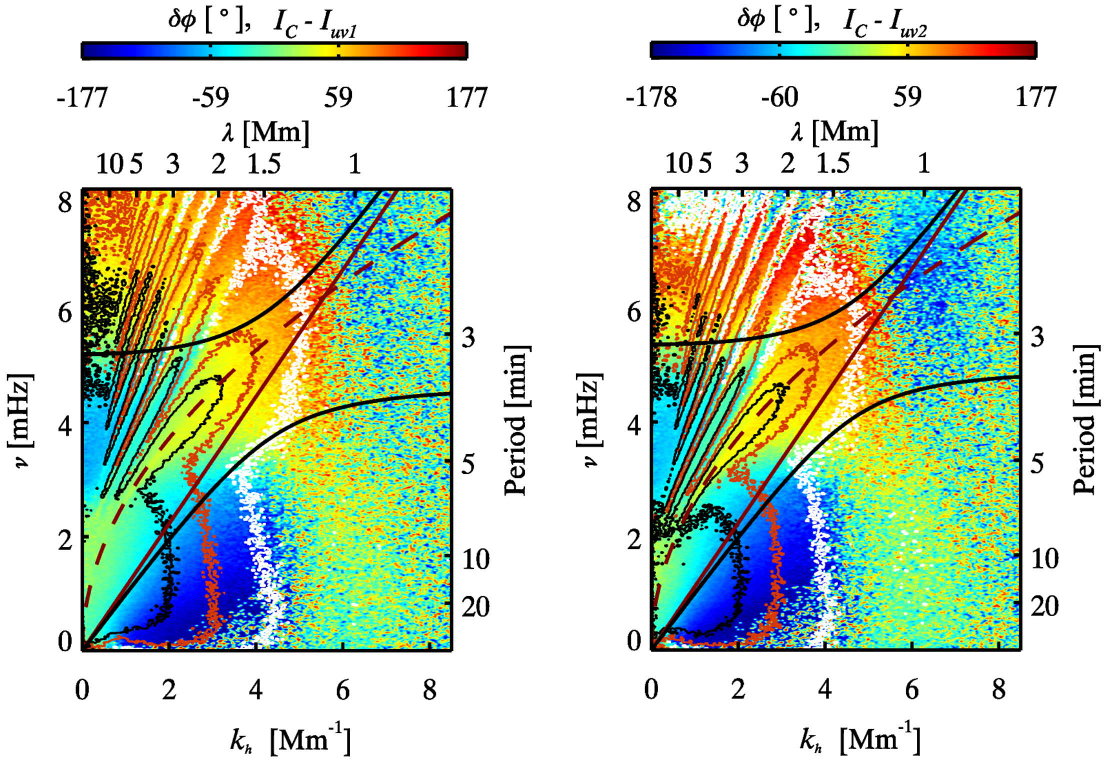

Fig. 6. Cross-spectral phase difference, $\delta\phi(k_h, \nu)$ diagrams of $M2$ region as indicated by $M2$ in Figure 1 constructed from $I_c - I_{uv1}$, and $I_c - I_{uv2}$ intensity pairs, respectively. The overplotted black, red and white contours represent the coherence at 0.5, 0.3 and 0.1 levels, respectively.

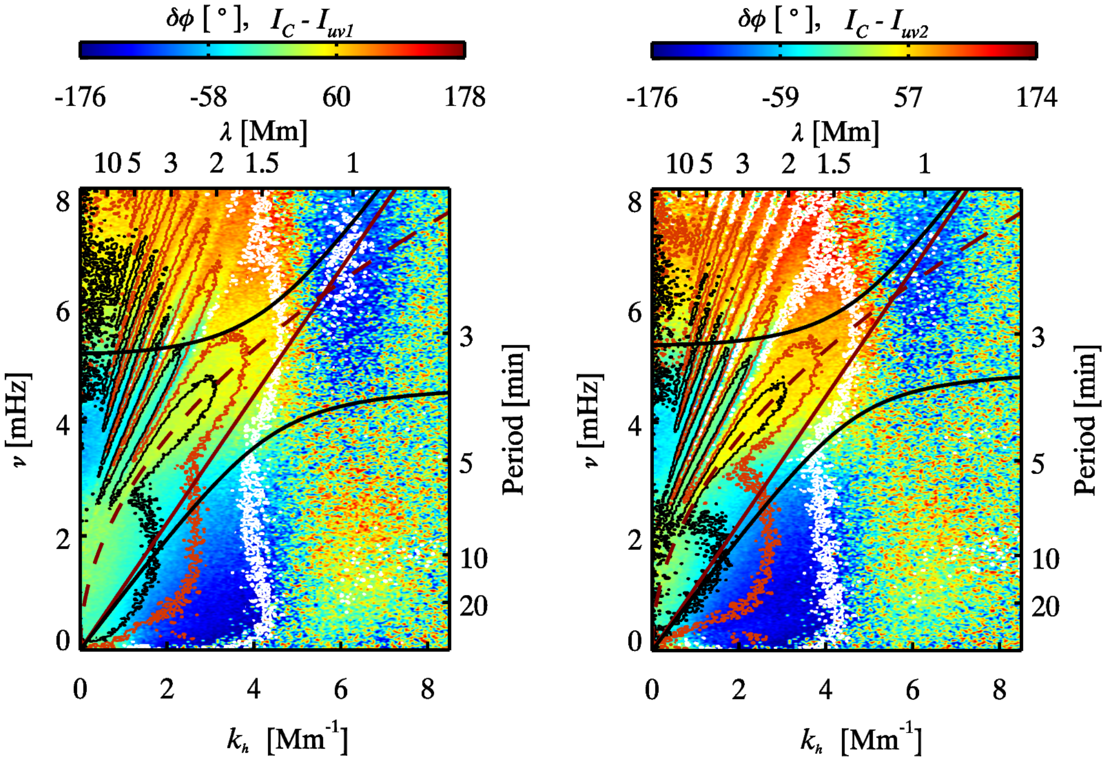

Fig. 7. Same as Figure 6, but for plage region as indicated by P in Figure 1.

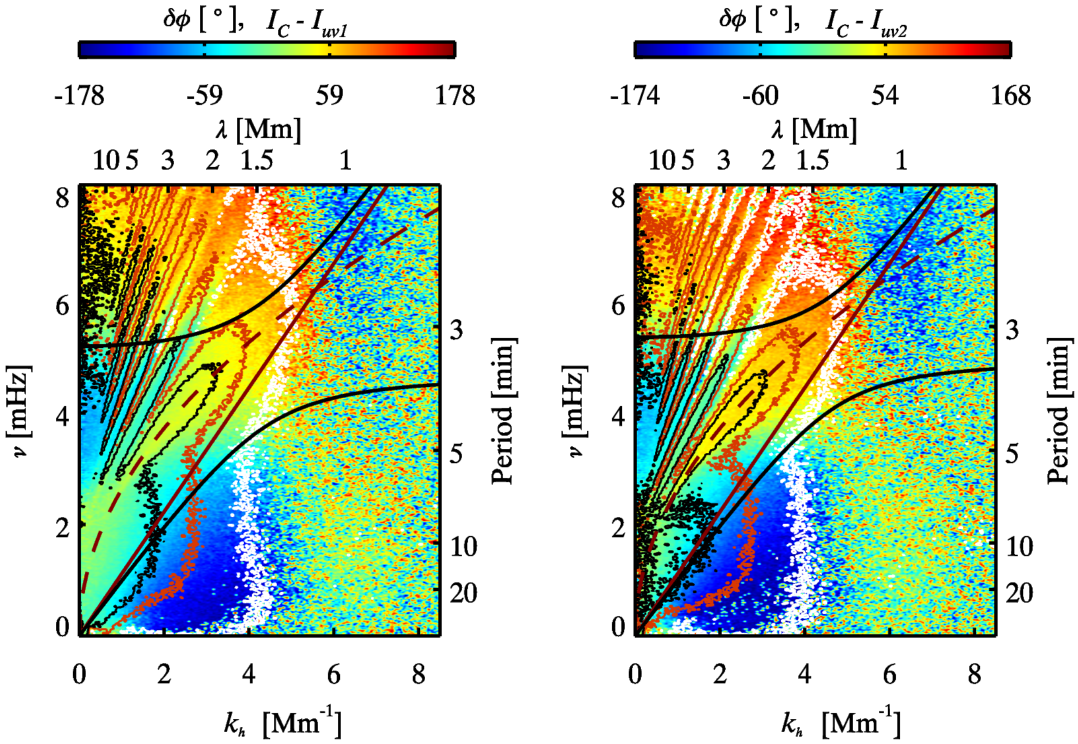

Fig. 8. Same as Figure 6 but for sunspot region as indicated by symbol S in the Figure 1.

top panels are for the $I_c - I_{uv1}$ pair, and bottom panels are for the $I_c - I_{uv2}$ pair.

We mainly focus on the effect of magnetic fields on the gravity waves, and hence are not discussing the acoustic wave regimes. In the gravity wave region of the diagnostic diagrams (c.f. Figure 5), we observe the well known negative phase as expected for IGWs, whose phase and group velocities have opposite signs. In general, in all our $\delta\phi(k_h, \nu)$ diagrams, we observe noisy phase signals with very low coherence C for $k_h > 5.5$ Mm^{-1} and also even at lower k_h when $\nu < 0.5$ mHz. We avoid such regions in (k_h, ν) and focus only on IGWs that have $\nu \geq 0.5$ mHz and $k_h < 5.5$ Mm^{-1}. The magnitudes and wavenumber-extents of IGWs depend on the height separation in the solar atmosphere, and also vary significantly from region to region or location even in the quiet-Sun. For the quiet-Sun region $M1$, interestingly, the negative $\delta\phi(k_h, \nu)$ (c.f. left panel of Figure 5) corresponding to IGWs extend over, along a curved band, to the evanescent region and beyond into higher frequency domain, over the $k_h = 4.1 - 6.8$ Mm^{-1} and over ν beyond 4 mHz. This seems to indicate that there are IGW-like waves extending beyond the classical gravity wave boundary expected from the simple dispersion relation given by Equation 4. Interestingly, exactly such a behaviour is seen in the numerical simulations of IGWs performed by Vigeesh & Roth (2020) and as seen in their Figure 5(b), where they also synthesised spectral lines and derived $\delta\phi(k_h, \nu)$ from line core intensities of Fe 5576 Å and Fe 5434 Å lines. However, the coherence $C(k_h, \nu)$ (c.f. right panel of Figure 5) is less than 0.1 in $k_h = 4.1 - 5.5$ Mm^{-1} & $\nu >$ 3.5 mHz, corresponding to the negative phase observed in the evanescent wave regimes of $\delta\phi$ diagrams. Hence the reality of these seemingly high frequency IGWs, in the evanescent region and beyond, is doubtful despite their resemblance to the simulation results of Vigeesh & Roth (2020). Nevertheless, there are several factors which can affect the coherence; for example, results of Vigeesh & Roth (2020) from synthetic observations show that coherence decreases as height separation increases, and we also see such behaviour for the $I_c - I_{uv2}$ intensity pair, which corresponds to higher height (h = 20 – 430 km). Additionally, they suggested that the angle of wave propagation with respect to normal for a given wave of a given frequency can also influence the coherence, which is governed by the local Brunt-Väisälä frequency (N). A wave launched at a particular frequency, without any non-linear interaction, will eventually follow a curved trajectory if the local N changes with height. Therefore, the coherency of the waves propagating between two heights for a given Fourier frequency may locally change over the field of view (Vigeesh & Roth, 2020).

We show the $\delta\phi$, and C diagrams constructed from another quiet-Sun sub-region labelled as Q within a larger region including a small sunspot and neighbouring plage region (c.f. data set 2 shown in Figure 2) in Figure 9. Here, we see the negative $\delta\phi(k_h, \nu)$ in the gravity wave region extending upto $k_h = 6.2$ Mm^{-1} and also exhibiting 180 deg. wrapping of phase at low frequencies (less than 0.8 mHz), especially for the higher height pair $I_c - I_{uv2}$ (c.f. bottom left panel of Figure 9). Comparing the two quiet-Sun regions Q and $M1$ in left panels of Figures 9 and 5, respectively, also reveals significant differences, especially in regard to the curved band of negative $\delta\phi(k_h, \nu)$ that extends through the evanescent region to higher frequencies in the $M1$ region – it is absent in the Q region. Furthermore, the $\delta\phi(k_h, \nu)$ and $C(k_h, \nu)$ diagrams of $M1$ region shows reduced extent of negative phase and coherence over k_h and ν corresponding to Q region. The observed phase difference of gravity waves in $M1$ region is similar to the earlier estimation by Rutten & Krijger (2003) utilizing white light and 1700 Å intensity as shown in their Figure 5, where the overplotted contours at C = 0.5, 0.2 and 0.1 demonstrate that contour of C = 0.5 is extended only upto k_h = 1.3 arcsec^{-1}, which in Mm^{-1} would be approximately 1.8 Mm^{-1}. However, in our analysis the contour of C = 0.5 is extended upto around k_h = 2.0 Mm^{-1} (c.f. Figure 5) and k_h = 4.0 Mm^{-1} (c.f. Figure 9). The extent of contour of C = 0.5 in our investigation is better than that earlier reported by Rutten & Krijger (2003). In the $M1$ region negative $\delta\phi$ and contour of coherence at $C = 0.1$ is extended only upto k_h = 4.1 Mm^{-1} whereas Q region occupies bigger extent than $M1$, upto k_h = 6.2 Mm^{-1}. This is possibly associated with the slanted propagation of gravity waves in the solar atmosphere. Thus, as we are going away from the disk center, we are probably detecting more and more gravity wave signals compared to that of disk center location. In addition to that, the phase and coherence diagrams constructed from $V - V$ pair i.e. $V_{80} - V_{10}$ over a quiet region (A) as depicted in the Figure 3 are shown in the Figure 12. The gravity wave regime shows the well known negative phase extending upto k_h = 6 Mm^{-1} with a very high coherence (c.f. Figure 12). Interestingly, the observed phase difference in the gravity wave regime over a quiet region (A) (c.f. Figure 12) is consistent with the earlier phase difference diagram constructed between two height $V - V$ pair estimated within Fe I 7090 Å line as reported in the Figure 1 of Straus et al. (2008).

3.2. Phase Spectra of IGWs in Magnetic Regions and Comparisons with Quiet Regions

From the data of three large regions (data set 1, 2, and 3), we have several strongly magnetised regions of different configurations, P, S, $R1$, $R2$, and B and the $\delta\phi(k_h, \nu)$ and $C(k_h, \nu)$ diagrams of these regions are shown in Figures 7, 8, 10, 11, and 13 respectively. The region $M2$ is close to the sunspot in data set 1 and has one side of the sunspot canopy field covered within it, and it is clear from the left panels of Figure 6 that the extent of gravity wave regime in the $M2$ region is reduced over ν and k_h as compared to that seen in the quiet network region (c.f. Figure 5): while it occupies ν= 0 – 4 mHz range extending up to about k_h = 5.5 Mm^{-1} in $M1$, the negative phases taper off and become positive over ν > 3 mHz and k_h > 4.41 Mm^{-1}. In their synthetic observations based on numerical simulations, Vigeesh & Roth (2020) have shown that the magnitude and wavenumber-extent of negative phase reduces as the magnetic field strength increases. We observe a similar trend in the $\delta\phi$ diagrams obtained from magnetized regions. In the phase diagrams of $M2$, P and S regions negative $\delta\phi$ tapers off at approximately ν = 2.5 mHz and at k_h = 4.82 Mm^{-1}. Similarly, the phase diagrams of $R1$, and $R2$ regions of data set 2 indicate that negative phase is extended upto only ν = 3.0 mHz, and k_h = 5.8 Mm^{-1} (c.f. Figures 10, and 11); these two regions also exhibit reduced coherence as compared to that in the Q region. The above general reducing extents of negative $\delta\phi$ of IGWs in magnetic regions have to be compared with those observed in the quiet-Sun regions $M1$ (c.f. Figure 5) and Q (c.f. Figure 9), where they extend upto about ν = 4 mHz, and k_h = 6.2 Mm^{-1}. It is to be noted that the coherence diagrams constructed from $I - I$ pair over quiet regions ($M1$ and Q) show that coherence is samll i.e., contour of C at 0.5 extends upto k_h = 2 Mm^{-1} and k_h = 4 Mm^{-1} as shown in the Figure 5, and Figure 9, respectively. Despite the low coherence over the quiet regions (c.f. see extent of contours in Figure 5 and Figure 9), coherence estimated over magnetized regions ($M2$, P, S, $R1$ and $R2$) is further reduced (c.f. see extent of contours in Figures 6, 7, 8, 10, and 11). Moreover, the phase and coherence diagrams constructed from $V_{80} - V_{10}$ velocity pair from a high magnetic concentrations over a sunspot (B) are shown in the Figure 13. The $\delta\phi(k_h, \nu)$ and $C(k_h, \nu)$ diagrams (c.f. Figure 13) over B region show that phase and coherence both are reduced in the sunspot over k_h and ν extent, compared to quiet (A) region as shown in the Figure 12.

In order to better understand the effect of magnetic fields on the IGWs, we have averaged $\delta\phi$ over k_h = 1.0 – 3.0, 2.75 – 4.1, and 4.1 – 5.5 Mm^{-1} in $M1$, $M2$, P, and S regions of data set 1 and have plotted them in Figure 14. The left panels [(a), (c), and (e)] correspond to intensity $I_c - I_{uv1}$ pair, while right panels [(b), (d), and (f)] are from higher height intensity $I_c - I_{uv2}$ pair. We have smoothed $< \delta\phi >$ by taking a smoothing window of 13 point to reduce the noise. In our analysis, the IGWs mostly lie up to k_h = 7.0 Mm^{-1}, and ν up to about 3.5 mHz. The panels (a), (b), (c), and (d) of Figure 14, in the k_h = 1.0 – 3.0, and 2.75 – 4.1 Mm^{-1} demonstrate that there is a change in the phase of the order of 30 – 40 and 20 – 30 degrees in the ν = 2.5 – 3 mHz band estimated over $M2$, P, and S regions, respectively corresponding to $M1$ region. Additionally, panels (e) and (f) of Figure 14 indicate that there is a change in the phase of the order of 30 – 70, and 80 – 100 degrees in 2.5 – 3.0 mHz as estimated for the k_h = 4.1 – 5.5 Mm^{-1} wavenumber over $M2$, P, and S regions with respect to $M1$ region. Interestingly, we find that the phase is reduced in large amount in the higher wavenumber (k_h = 4.1 - 5.5 Mm^{-1}) in magnetized regions compared to quiet region, almost changing from negative to positive sign as shown in the panel (e) and (f) of Figure 14. We also notice that the $< \delta\phi >$ estimated from $M2$ region, which is very close to the sunspot is notably affected in k_h = 1.0 – 3.0, 2.75 – 4.1, and 4.1 – 5.5 Mm^{-1} (c.f. Figure 14) compared to $M1$ region. Similarly, the $< \delta\phi >$ vs ν plots over k_h = 1.0 – 3.0, 2.75 – 4.1, and 4.1 – 5.5 Mm^{-1} for Q, $R1$, and $R2$ regions of data set 2 as shown in the Figure 15 also demonstrate the reduction in phase over $R1$, and $R2$ regions upto ν = 4.0 mHz band. The panels (a), (b), (c), and (d) of Figure 15 for k_h = 1.0 – 3.0, and 2.75 – 4.1 Mm^{-1} indicate the change in $< \delta\phi >$ over ν = 2.5 – 3 mHz band of the order of 10 – 20 degrees, while for panels (e) and (f) for k_h = 4.1 – 5.5 Mm^{-1} show the change in $< \delta\phi >$ of the order of 25 – 50 degree in 2.5 – 3 mHz band (c.f. Figure 15) concerning to Q region. The bottom panel [(e), and (f)] of Figure 15 also shows that phase of gravity waves are reduced in larger amount in the higher wavenumber k_h = 4.1 –

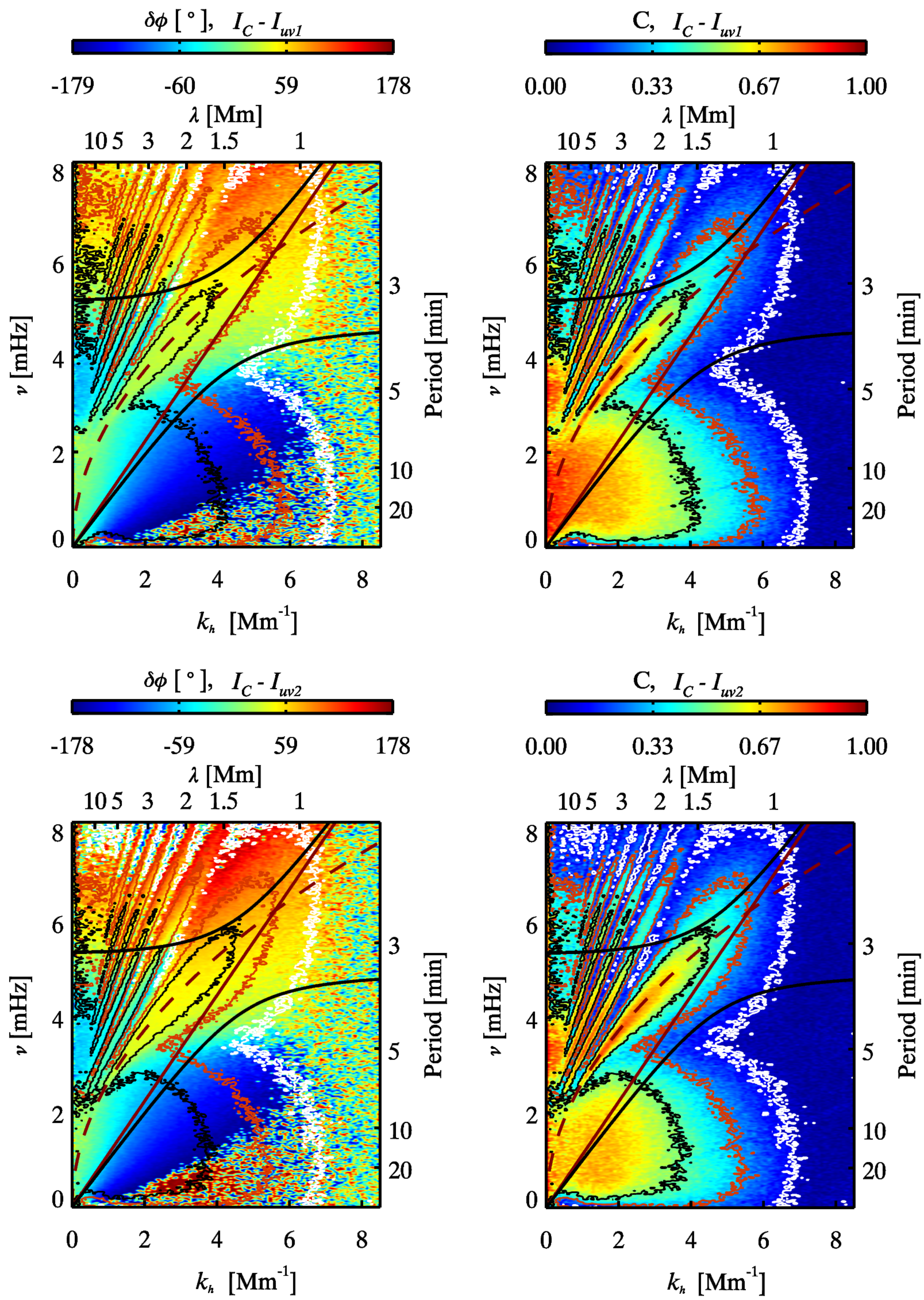

Fig. 9. *Top panel*: Cross-spectral phase difference, $\delta\phi(k_h, \nu)$ (*top left panel*), and coherence, $C(k_h, \nu)$ (*top right panel*), diagrams of Q region constructed from $I_c - I_{uv1}$ pair of photospheric continuum intensity (HMI) and UV 1700 Å channel of AIA, which correspond to 20 – 360 km above z = 0 in the solar atmosphere. *Bottom panel*: same as *top panel*, but from $I_c - I_{uv2}$ pair of photospheric continuum intensity (HMI) and UV 1600 Å channel of AIA, which correspond to 20 – 430 km above z = 0 in the solar atmosphere. The black solid lines separate vertically propagating waves ($k_z^2 > 0$) from the evanescent ones ($k_z^2 < 0$) at upper height. The dashed red line is the f-mode dispersion curve and solid red line is the Lamb mode. The over plotted black, red and white contours represent the coherence at 0.5, 0.3 and 0.1 levels, respectively.

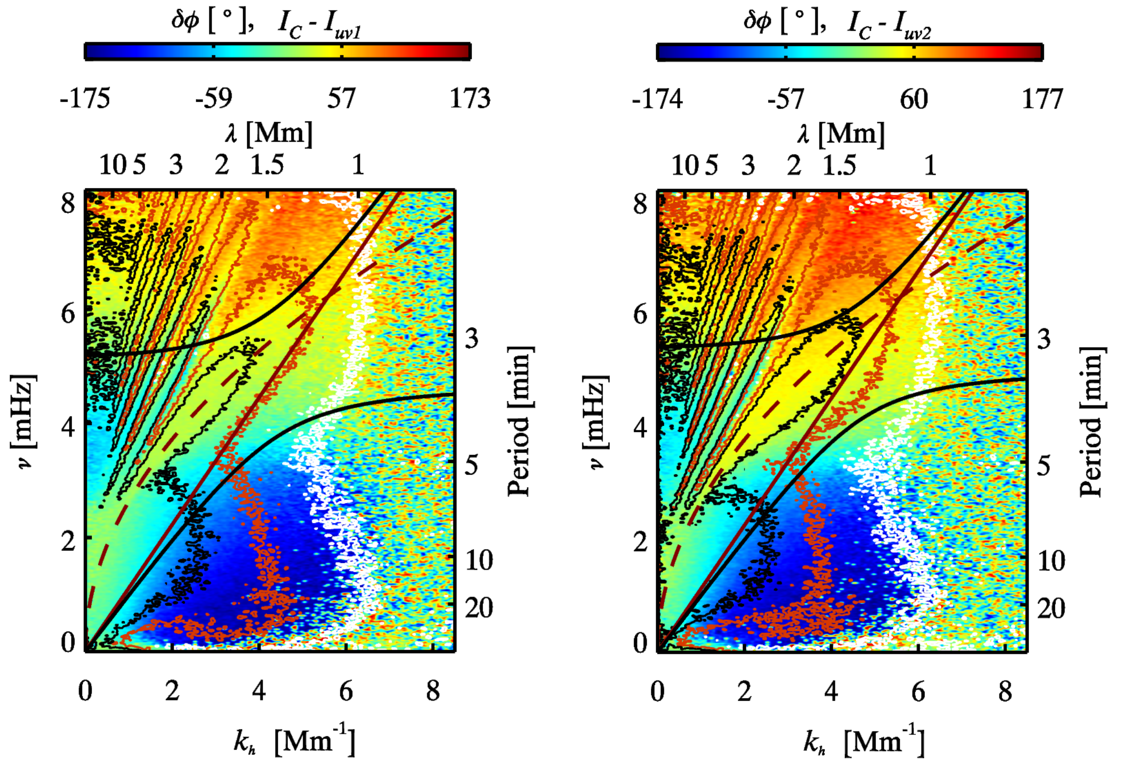

Fig. 10. Cross-spectral phase difference, $\delta\phi(k_h, \nu)$ diagrams of $R1$ region as indicated in the Figure 2 constructed from $I_c - I_{uv1}$, and $I_c - I_{uv2}$ intensity pairs, respectively. The over plotted black, red and white contours represent the coherence at 0.5, 0.3 and 0.1 levels, respectively.

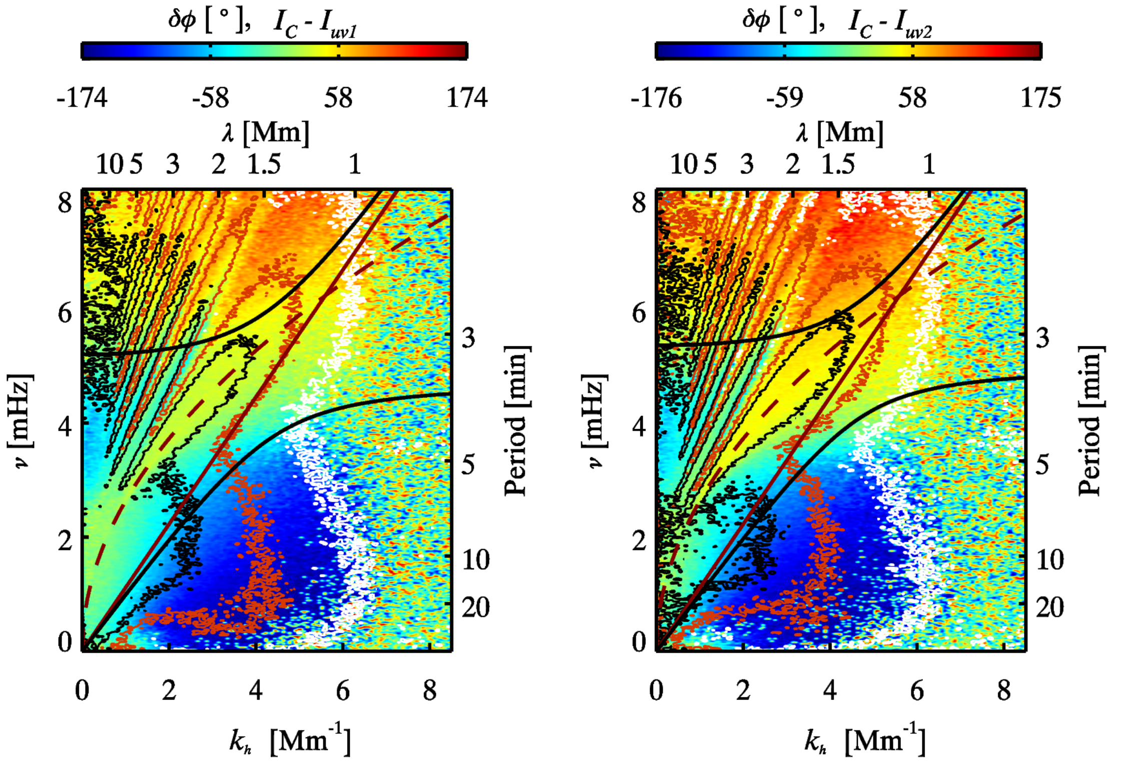

Fig. 11. Same as Figure 10, but for $R2$ region as indicated in the Figure 2.

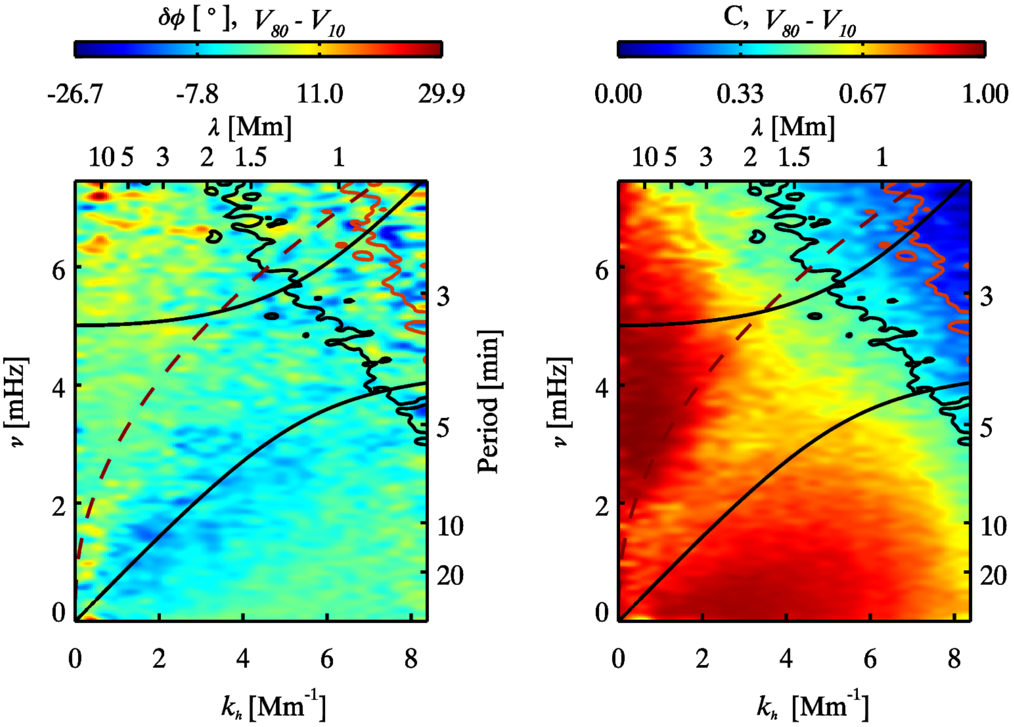

Fig. 12. Cross-spectral phase difference, $\delta\phi(k_h, \nu)$ (*left panel*), and coherence, $\mathrm{C}(k_h, \nu)$ (*right panel*), diagrams of quiet (A) region constructed from $V_{80} - V_{10}$ velocity pair of photospheric Fe I 6173 Å line observations obtained from the IBIS instrument, which correspond to different heights within 16 – 302 km above z = 0 in the solar atmosphere. The black solid lines separate vertically propagating waves ($k_z^2 > 0$) from the evanescent ones ($k_z^2 < 0$) at upper height. The dashed red line is the f-mode dispersion curve. The overplotted black, red and white contours represent the coherence at 0.5, 0.3 and 0.1 levels, respectively.

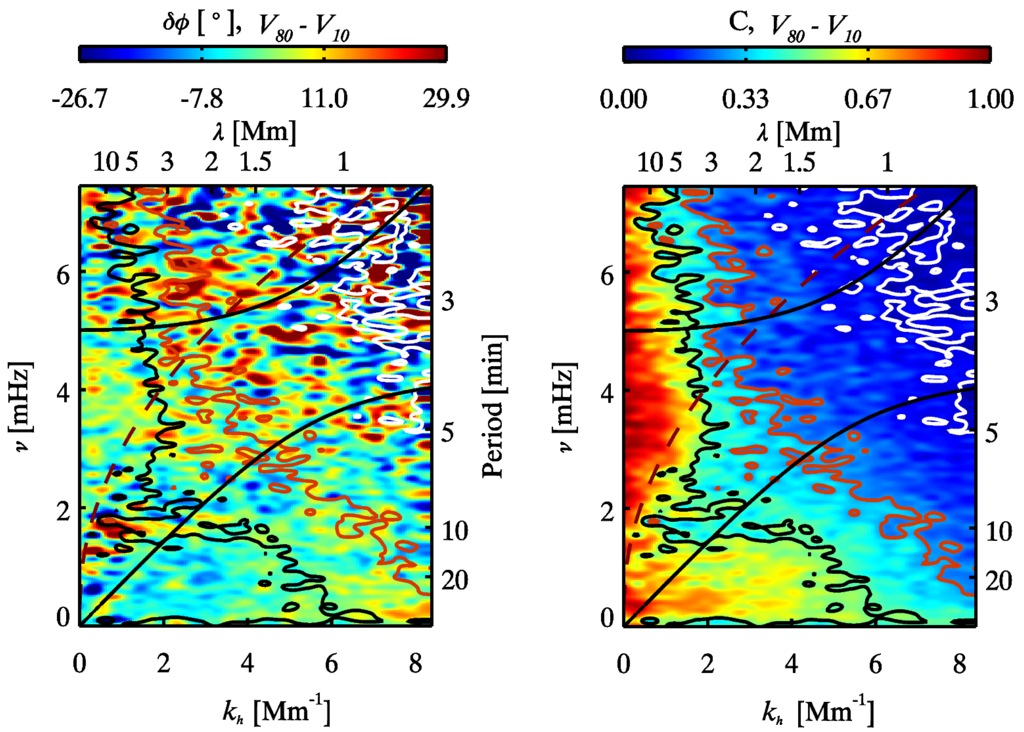

Fig. 13. Same as Figure 12, but for sunspot (B) region as indicated in the Figure 3.

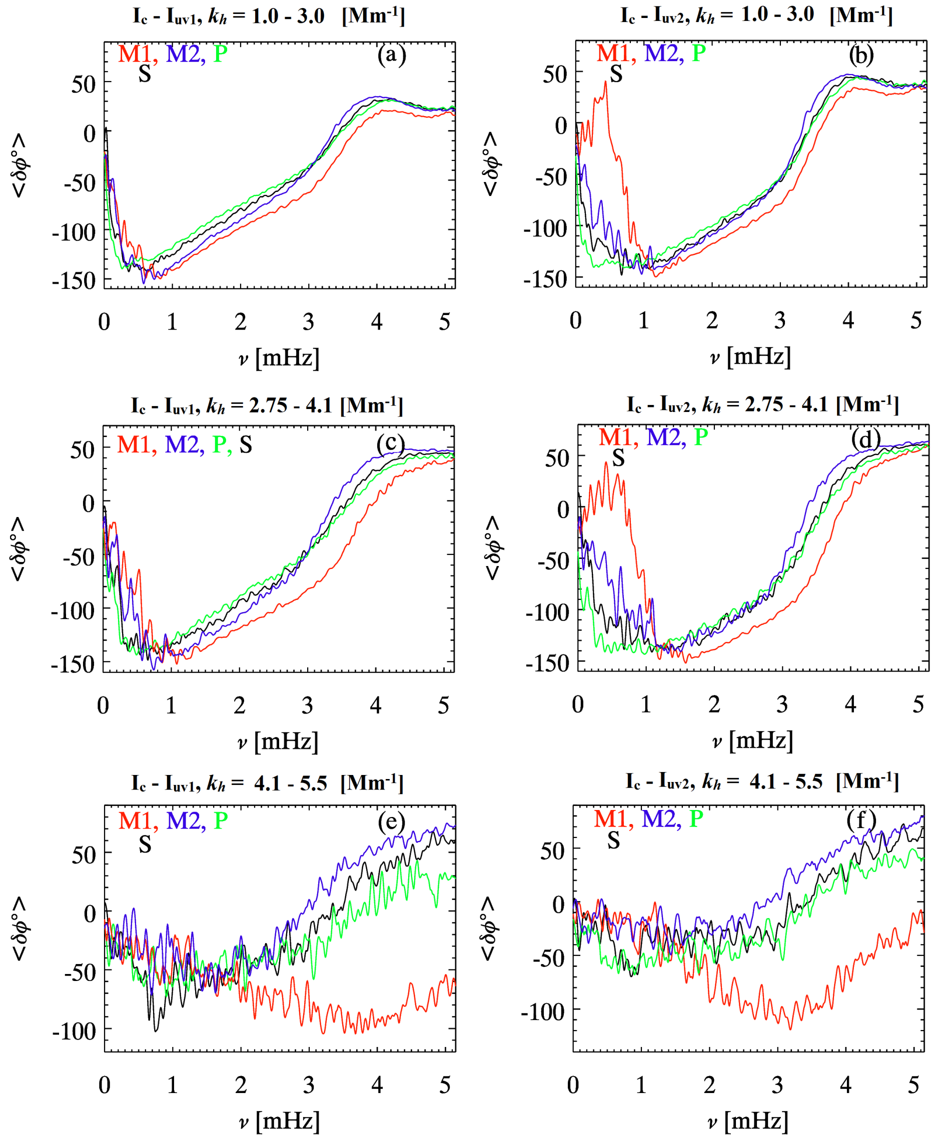

Fig. 14. Plots indicate average phase over k_h = 1.0 – 3.0, 2.75 – 4.1, and 4.1 – 5.5 Mm^{-1}, estimated from $I_c - I_{uv1}$, and $I_c - I_{uv2}$ intensity pairs, over $M1$, $M2$, P, and S regions, respectively, as indicated in Figure 1.

5.5 Mm^{-1} as compared to quiet region (Q). Further, it is to be noted that $M2$, and $R1$ regions cover a large amount of looping magnetic fields, hence they are largely horizontal, as can be seen in the AIA 171 Å passband (c.f. right panel of Figures 1 and 2), respectively. We also find that suppression of phase is more in these regions ($M2$, and $R1$) as compared to others.

Additionally, we also estimate and plot $< \delta\phi >$ over quiet (A) and sunspot (B) region over k_h = 2 – 4 Mm^{-1} from $V_{80} - V_{10}$ velocity pair as shown in the Figure 18. It indicates that $< \delta\phi >$ is positive in the sunspot (B) region, while it is negative over the quiet (A) region around ν = 1.5 mHz. Further, we also estimate $< \delta\phi >$ over A and B region from pixel by pixel calculation after removing the acoustic wave regime part from $k_h - \nu$ diagram i.e. above the f-mode in the diagnostic diagram utilizing a 3D FFT filter. The $< \delta\phi >$ over A and B regions are shown in the Figure 19 shows that there is a change in sign of the $< \delta\phi >$ estimated over sunspot (B) region compare to quiet (A) region. It is to be noted that we have used velocity V_{80} and V_{10} estimated within the Fe I 6173 Å line at two heights. The formation height of Fe I 6173 Å line is different in quiet and magnetized region i.e. sunspot. In the quiet region, Fe I line forms within h = 16 – 300 km, whereas in umbra it is around h = 20 – 270 km above the τ_c = 1. Thus, we estimate the percentage change in the formation height of quiet and sunspot region. There is an approximately 12% change in the formation height of Fe I line with respect to a quiet region. However, the percentage change in the $< \delta\phi >$ estimated from Figure 19 at ν = 1.5 mHz are found to be of the order of 114.3% compare to quiet region. Nevertheless, the $< \delta\phi >$ estimated over a quiet (A) and a sunspot (B) region from Figure 18 in ν = 1.5–3.5 mHz and k_h = 2–4 Mm^{-1} are of the order of -5.35 degree and 0.255 degree, respectively. Thus,

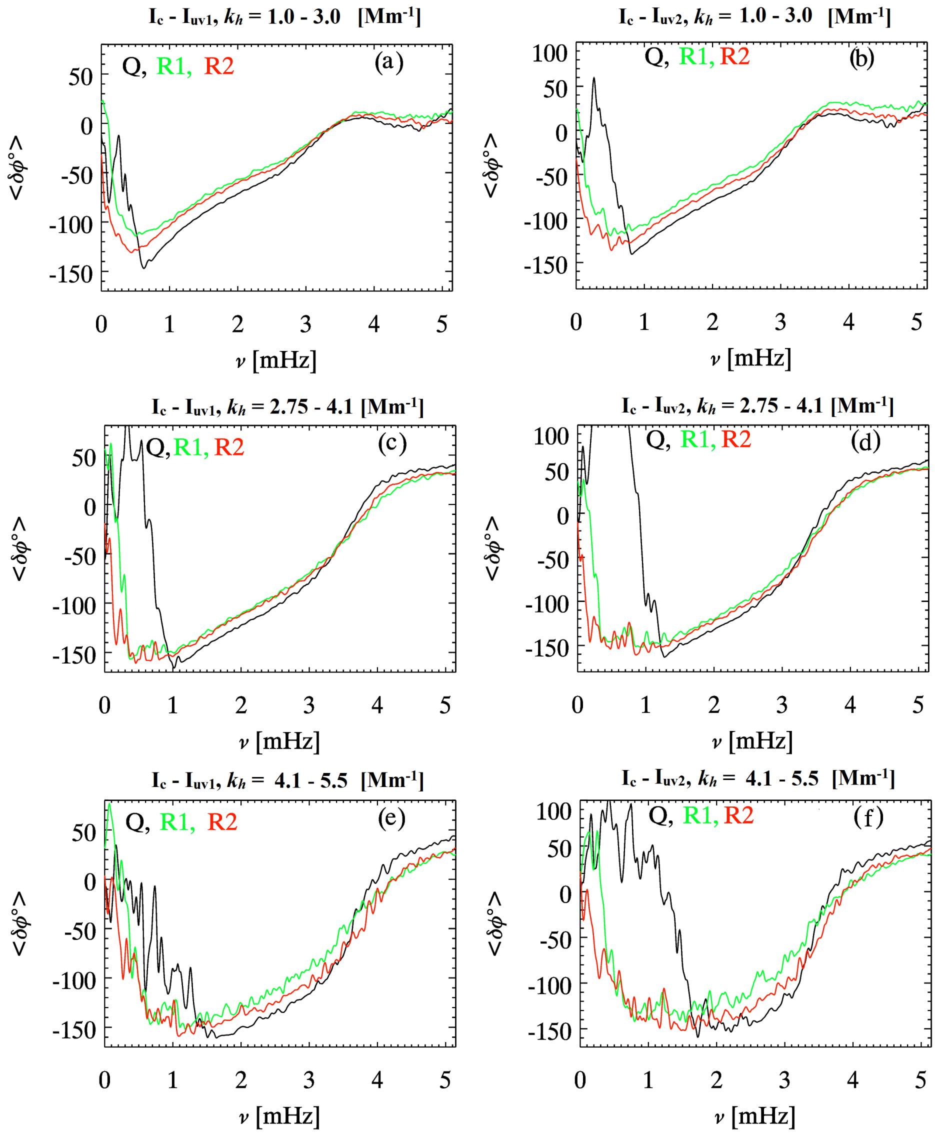

Fig. 15. Same as Figure 14 but, over Q, $R1$, and $R2$ regions, respectively, as indicated in Figure 2.

such a change in $<\delta\phi>$ and change in sign is not possibly due to the lowering in the formation height of Fe I 6173 Å line in sunspot, indicating that it is due to the suppression or reflection of gravity waves in the magnetized regions. The formation height of I_{uv1} and I_{uv2} might be decrease in the magnetized regions. However, the observed percentage change in phase over the highly magnetized regions, are more than 50%–100% at ν = 2.0 – 2.5 mHz and change in sign between quiet and magnetic regions near 3 mHz (c.f. Figure 14), and their similarities with the phase analysis of $V - V$ spectrum, indicate that it is not due to change in formation heights of observables used but due to the direct effect of magnetic fields on their propagation. This is because, a sign change in phase shifts between quiet and magnetic regions cannot come from the formation height differences, however big they are.

3.3. Coherence and Effects of Magnetic Fields

We analyzed the average coherence on two different wavenumber ranges i.e. k_h = 1.0 – 3.0 Mm^{-1} (pale blue line), and k_h = 2.75–4.1 Mm^{-1} (black line) integrated over ν = 1 – 2 mHz band from dataset 1, over $M1$, $M2$, P, and S regions and plotted them in Figure 16. The plots of $<C>$ versus $<|B_{LOS}|>$ obtained from $I_c - I_{uv1}$ (dashed line) and $I_c - I_{uv2}$ (solid line) pair as shown in the Figure 16 demonstrate that as magnetic field strength increases coherence decreases. From the dataset 2, we also estimate $<C>$ on k_h = 1.0 – 3.0 Mm^{-1} (pale blue line), k_h = 2.75–4.1 Mm^{-1} (black line), and k_h = 4.1 – 5.5 Mm^{-1} (blue line) integrated over ν = 1 – 2 mHz over $Q1$, $R1$, and $R2$ from $I_c - I_{uv1}$ (dashed line) and $I_c - I_{uv2}$ (solid line) pairs, which are depicted in the Figure 17. These also demonstrate that as magnetic field strength increases coherence decreases. It is to be noted that in k_h = 2.75–4.1 Mm^{-1} range in Figure 16 and k_h

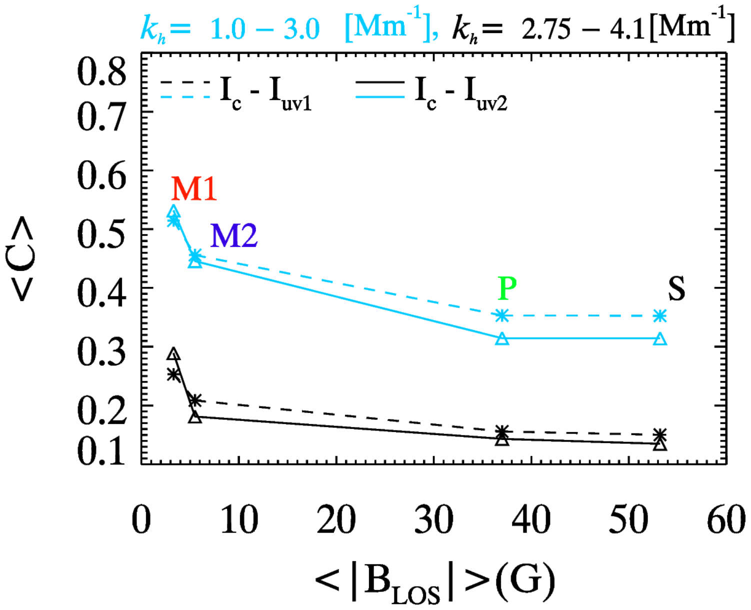

Fig. 16. Plots show $< C >$ versus $< |B_{LOS}| >$ over k_h = 1.0 – 3.0, 2.75 – 4.1 Mm^{-1}, and ν = 1 – 2 mHz, estimated from $I_c - I_{uv1}$, and $I_c - I_{uv2}$ intensity pairs, over $M1$, $M2$, P and S regions, respectively, as indicated in Figure 1.

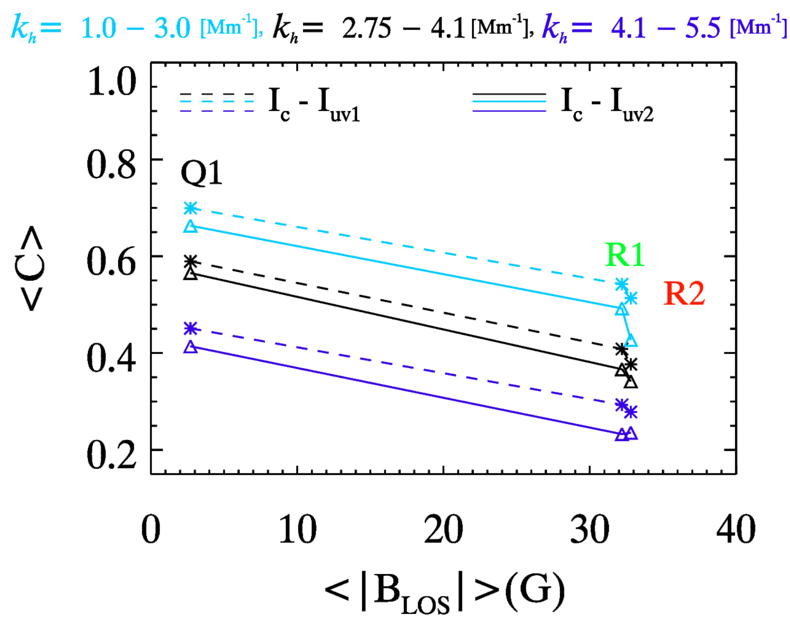

Fig. 17. Plots show $< C >$ versus $< |B_{LOS}| >$ over ν = 1 – 2 mHz, and k_h = 1.0 – 3.0, 2.75 – 4.1, and 4.1 – 5.5 Mm^{-1}, estimated from $I_c - I_{uv1}$, and $I_c - I_{uv2}$ intensity pairs, over Q, $R1$ and $R2$ regions, respectively, as indicated in Figure 2.

= 4.1–5.5 Mm^{-1} regime in the Figure 17 coherence is below 0.5. However, despite the low coherence in quiet regions ($M1$ and $Q1$), coherence is further reduced in magnetized regions. Similar reduction in coherence is also observed in the $< C >$ versus ν plot constructed over quiet (A) and sunspot (B) regions as shown in the right panel of Figure 18. Figures 16, 17, and right panel of Figure 18 suggest that magnetic fields also affect coherence apart from other factors as suggested by Vigeesh & Roth (2020).

4. Discussion and Conclusions

The IGWs in the solar atmosphere, which are thought to be generated by the turbulent convection penetrating locally into a stably stratified medium are believed to dissipate their energy by radiative damping just above the solar surface (Lighthill, 1967). Earlier studies (Mihalas & Toomre, 1981, 1982) suggest that IGWs can reach upto the middle chromosphere, before breaking of these waves due to nonlinearities resulting in a complete dissipation. Recent simulations done by Vigeesh

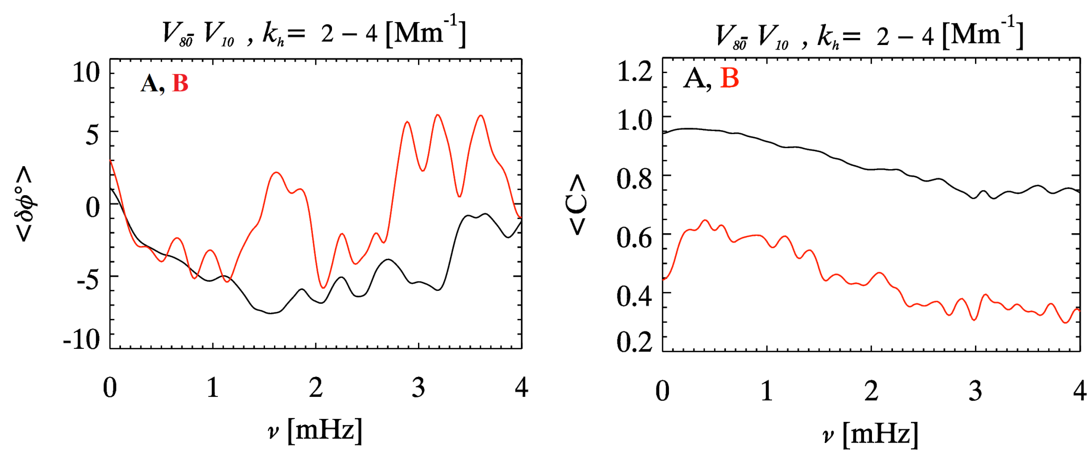

Fig. 18. Plots indicate average phase (left panel) and coherence (right panel) over k_h = 2.0 – 4.0 Mm^{-1}, estimated from $V_{80} - V_{10}$ velocity-velocity pairs, over *A*, and *B* regions, respectively, as indicated in Figure 3.

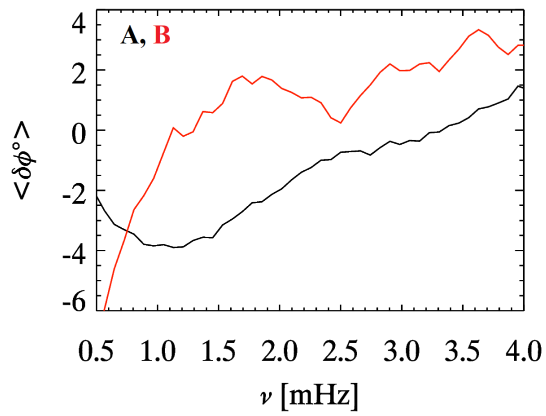

Fig. 19. Plots indicate average phase estimated over *A* and *B* regions from $V_{80} - V_{10}$ pairs from pixel-by-pixel calculation, after removing the acoustic wave regime part above the f-mode region in the $k_h - \nu$ diagram.

et al. (2017), Vigeesh et al. (2019), and (Vigeesh & Roth, 2020) have shown that these waves are still present in the higher atmosphere, where the radiative damping time scale is high, and that magnetic fields suppress or scatter IGWs in the solar atmosphere.

Our investigations of $k_h - \nu$ phases and coherences of IGWs within the photosphere and from photospheric to lower chromospheric height ranges over a varied levels of background magnetic fields and their configurations have brought out clear signatures of reduced extent of negative phase and coherence and a change of sign in phases in the gravity wave regime due to the magnetic fields as compared to quiet regions – as demonstrated in Figures 5, 6, 7, 8, 9, 10, 11. The above finding from intensity observations is also strengthened from the phase and coherence diagrams estimated from velocity - velocity cross-spectral pairs observed over a quiet (*A*) and a sunspot (*B*) region (c.f. Figure 12, and 13). Further, from the comparison of average phase in k_h = 1.0 – 3.0, 2.75 – 4.1, and 4.1 – 5.5 Mm^{-1} over quiet and magnetic regions from data set 1 and 2 as shown in the Figures 14, and 15, we find that the phase of IGWs are much reduced in the magnetized regions. Moreover, this effect is more prominent in the higher wavenumber regions i.e. for the waves of lower wavelength (λ = 2.175 – 2.75 Mm) suggesting that these gravity waves are scattered by the background magnetic fields or partially reflecting from the upper atmospheric layers leading to positive phase in the gravity wave regime. The average phase estimated from $V - V$ pair in k_h = 2 – 4 Mm^{-1} (c.f. Figure 18) also indicate change in sign at ν = 1.5 mHz in sunspot (*B*) compare to quiet (*A*) region. Moreover, the average phase estimated from $V - V$ pair from pixel-by-pixel analysis over quiet (*A*) and sunspot (*B*) regions also demonstrate the change in sign of the phase. Furthermore, the observed percentage change in phase in the sunspot (*B*) compared to quiet (*A*) region is much higher than percentage change in the formation height of Fe I line in sunspot compared to quiet region, strongly favouring the suppression or reflections of gravity waves in the high magnetized region i.e. sunspot (c.f. Figur 19). It is to be noted that the observed differences in the *B* region compared to the *A* region could be due to lack of excitation of gravity waves over sunspot in the photosphere, but there is still a possibility of scattering/suppression of gravity waves that propagate from the surrounding quiet Sun over the sunspot location. Importantly, we also find a reduction in coherence in the presence of background magnetic fields as shown in the Figures 16, and 17 as well as shown in the right panel of Figure 18. Previously, Straus et al. (2008) showed that the rms wave velocity fluctuations due to IGWs were suppressed at locations of magnetic flux. Here, we have provided further observational evidence in the $k_h - \nu$ diagrams for the suppression or scattering or partial reflection of gravity waves in the magnetized regions of the solar atmosphere.

In general, the above nature of IGWs in magnetized regions are broadly consistent with the simulation results of Vigeesh et al. (2017) and Vigeesh et al. (2019); Vigeesh & Roth (2020) suggesting the suppression of gravity waves in magnetized regions. This led to identifying our reported differences between quiet and magnetic regions as observational evidences for such influences of magnetic fields. We anticipate that several of our analyses and findings reported here will be examined in more detail in the near future containing bigger FOV, involving coordinated simultaneous multi-height observations of photosphere and chromosphere utilising Dopplergrams data from the newer Daniel K Inouye Solar Telescope (DKIST; Rimmele et al. (2020)) (National Solar Observatory USA) facility along with MAST (Mathew, 2009; Venkatakrishnan et al., 2017) and HMI, AIA onboard SDO spacecraft.

Acknowledgments

We acknowledge the use of data from the HMI and AIA instruments onboard the *Solar Dynamics Observatory* spacecraft of NASA. We are thankful to SDO team for their open data policy. The SDO is NASA's mission under the Living With a Star (LWS) program. At the time IBIS observation was acquired, Dunn Solar Telescope at Sacramento Peak, New Mexico, was operated by National Solar Observatory (NSO). NSO is managed by the Association of Universities for Research in Astronomy (AURA) Inc. under a cooperative agreement with the National Science Foundation. The research work being carried out at Udaipur Solar Observatory, Physical Research Laboratory is supported by the Department of Space, Govt. of India. S.P.R. acknowledges support from the Science and Engineering Research Board (SERB, Govt. of India) grant CRG/2019/003786. We thank two anonymous referees for critical and constructive comments and suggestions which significantly improved the presentation and discussion of results in this paper.

References

Cavallini, F. (2006). IBIS: A New Post-Focus Instrument for Solar Imaging Spectroscopy. *Solar Phys.*, *236*(2), 415–439. doi:10.1007/s11207-006-0103-8.

Couvidat, S., Rajaguru, S. P., Wachter, R. et al. (2012). Line-of-Sight Observables Algorithms for the Helioseismic and Magnetic Imager (HMI) Instrument Tested with Interferometric Bidimensional Spectrometer (IBIS) Observations. *Solar Phys.*, *278*(1), 217–240. doi:10.1007/s11207-011-9927-y.

Deubner, F. L., & Fleck, B. (1989). Dynamics of the solar atmosphere. I - Spatio-temporal analysis of waves in the quiet solar atmosphere. *Astron. Astrophys.*, *213*(1-2), 423–428.

Fossum, A., & Carlsson, M. (2005). Response Functions of the Ultraviolet Filters of TRACE and the Detectability of High-Frequency Acoustic Waves. *Astrophys. J.*, *625*(1), 556–562. doi:10.1086/429614.

Goldreich, P., & Kumar, P. (1990). Wave Generation by Turbulent Convection. *Astrophys. J.*, *363*, 694. doi:10.1086/169376.

Hoeksema, J. T., Liu, Y., Hayashi, K. et al. (2014). The Helioseismic and Magnetic Imager (HMI) Vector Magnetic Field Pipeline: Overview and Performance. *Solar Phys.*, *289*(9), 3483–3530. doi:10.1007/s11207-014-0516-8. arXiv:1404.1881.

Kneer, F., & Bello González, N. (2011). On acoustic and gravity waves in the solar photosphere and their energy transport. *Astron. Astrophys.*, *532*, A111. doi:10.1051/0004-6361/201116537.

Krijger, J. M., Rutten, R. J., Lites, B. W. et al. (2001). Dynamics of the solar chromosphere. III. Ultraviolet brightness oscillations from TRACE. *Astron. Astrophys.*, *379*, 1052–1082. doi:10.1051/0004-6361:20011320.

Leibacher, J. W., & Stein, R. F. (1981). Oscillations and pulsations. In S. Jordan (Ed.), *NASA Special Publication* (pp. 263–287). volume 450.

Lemen, J. R., Title, A. M., Akin, D. J. et al. (2012). The Atmospheric Imaging Assembly (AIA) on the Solar Dynamics Observatory (SDO). *Solar Phys.*, *275*(1-2), 17–40. doi:10.1007/s11207-011-9776-8.

Lighthill, J. (1978). *Waves in Fluids*. Cambridge: Cambridge University Press.

Lighthill, M. J. (1952). On Sound Generated Aerodynamically. I. General Theory. *Proceedings of the Royal Society of London Series A*, *211*(1107), 564–587. doi:10.1098/rspa.1952.0060.

Lighthill, M. J. (1967). Predictions on the Velocity Field Coming from Acoustic Noise and a Generalized Turbulence in a Layer Overlying a Convectively Unstable Atmospheric Region. In R. N. Thomas (Ed.), *Aerodynamic Phenomena in Stellar Atmospheres* (p. 429). volume 28.

Maltby, P., Avrett, E. H., Carlsson, M. et al. (1986). A New Sunspot Umbral Model and Its Variation with the Solar Cycle. *Astrophys. J.*, *306*, 284. doi:10.1086/164342.

Mathew, S. K. (2009). A New 0.5m Telescope (MAST) for Solar Imaging and Polarimetry. In S. V. Berdyugina, K. N. Nagendra, & R. Ramelli (Eds.), *Solar Polarization 5: In Honor of Jan Stenflo* (p. 461). volume 405 of *Astronomical Society of the Pacific Conference Series*.

Mihalas, B. W., & Toomre, J. (1981). Internal gravity waves in the solar atmosphere. I - Adiabatic waves in the chromosphere. *Astrophys. J.*, *249*, 349–371. doi:10.1086/159293.

Mihalas, B. W., & Toomre, J. (1982). Internal gravity waves in the solar atmosphere. II - Effects of radiative damping. *Astrophys. J.*, *263*, 386–408. doi:10.1086/160512.

Mihalas, D., & Mihalas, B. W. (1995). *Foundations of Radiation Hydrodynamics*. Oxford University Press.

Nagashima, K., Löptien, B., Gizon, L. et al. (2014). Interpreting the Helioseismic and Magnetic Imager (HMI) Multi-Height Velocity Measurements. *Solar Phys.*, *289*(9), 3457–3481. doi:10.1007/s11207-014-0543-5. arXiv:1404.3569.

Norton, A. A., Graham, J. P., Ulrich, R. K. et al. (2006). Spectral Line Selection for HMI: A Comparison of Fe I 6173 Å and Ni I 6768 Å. *Solar Phys.*, *239*(1-2), 69–91. doi:10.1007/s11207-006-0279-y. arXiv:astro-ph/0608124.

Pesnell, W. D., Thompson, B. J., & Chamberlin, P. C. (2012). The Solar Dynamics Observatory (SDO). *Solar Phys.*, *275*(1-2), 3–15. doi:10.1007/s11207-011-9841-3.

Rajaguru, S. P., Couvidat, S., Sun, X. et al. (2013). Properties of High-Frequency Wave Power Halos Around Active Regions: An Analysis of Multi-height Data from HMI and AIA Onboard SDO. *Solar Phys.*, *287*(1-2), 107–127. doi:10.1007/s11207-012-0180-9. arXiv:1206.5874.

Rajaguru, S. P., Sangeetha, C. R., & Tripathi, D. (2019). Magnetic Fields and the Supply of Low-frequency Acoustic Wave Energy to the Solar Chromosphere. *Astrophys. J.*, *871*(2), 155. doi:10.3847/1538-4357/aaf883.

Rajaguru, S. P., Wachter, R., Sankarasubramanian, K. et al. (2010). Local Helioseismic and Spectroscopic Analyses of Interactions Between Acoustic Waves and a Sunspot. *Astrophys. J. Lett.*, *721*(2), L86–L91. doi:10.1088/2041-8205/721/2/L86. arXiv:1009.2350.

Rimmele, T. R., Warner, M., Keil, S. L. et al. (2020). The Daniel K. Inouye Solar Telescope - Observatory Overview. *Solar Phys.*, *295*(12), 172. doi:10.1007/s11207-020-01736-7.

Rutten, R. J., & Krijger, J. M. (2003). Dynamics of the solar chromosphere IV. Evidence for atmospheric gravity waves from TRACE. *Astron. Astrophys.*, *407*, 735–740. doi:10.1051/0004-6361:20030894.

Schou, J., Scherrer, P. H., Bush, R. I. et al. (2012). Design and Ground Calibration of the Helioseismic and Magnetic Imager (HMI) Instrument on the Solar Dynamics Observatory (SDO). *Solar Phys.*, *275*(1-2), 229–259. doi:10.1007/s11207-011-9842-2.

Schwarzschild, M. (1948). On Noise Arising from the Solar Granulation. *Astrophys. J.*, *107*, 1. doi:10.1086/144983.

Stein, R. F. (1967). Generation of Acoustic and Gravity Waves by Turbulence in an Isothermal Stratified Atmosphere. *Solar Phys.*, *2*(4), 385–432. doi:10.1007/BF00146490.

Straus, T., Fleck, B., Jefferies, S. M. et al. (2008). The Energy Flux of Internal Gravity Waves in the Lower Solar Atmosphere. *Astrophys. J. Lett.*, *681*(2), L125. doi:10.1086/590495.

Venkatakrishnan, P., Mathew, S. K., Srivastava, N. et al. (2017). The Multi Application Solar Telescope. *Current Science*, *113*(4), 686. doi:10.18520/cs/v113/i04/686-690.

Vernazza, J. E., Avrett, E. H., & Loeser, R. (1981). Structure of the solar chromosphere. III. Models of the EUV brightness components of the quiet sun. *Astrophys. J. Suppl.*, *45*, 635–725. doi:10.1086/190731.

Vigeesh, G., Jackiewicz, J., & Steiner, O. (2017). Internal Gravity Waves in the Magnetized Solar Atmosphere. I. Magnetic Field Effects. *Astrophys. J.*, *835*(2), 148. doi:10.3847/1538-4357/835/2/148. arXiv:1612.04729.

Vigeesh, G., & Roth, M. (2020). Synthetic observations of internal gravity waves in the solar atmosphere. *Astron. Astrophys.*, *633*, A140. doi:10.1051/0004-6361/201936846. arXiv:1912.06435.

Vigeesh, G., Roth, M., Steiner, O. et al. (2021). On the influence of magnetic topology on the propagation of internal gravity waves in the solar atmosphere. *Philosophical Transactions of the Royal Society of London Series A*, *379*(2190), 20200177. doi:10.1098/rsta.2020.0177. arXiv:2010.06926.

Vigeesh, G., Roth, M., Steiner, O. et al. (2019). Internal Gravity Waves in the Magnetized Solar Atmosphere. II. Energy Transport. *Astrophys. J.*, *872*(2), 166. doi:10.3847/1538-4357/ab020c. arXiv:1901.08871.

Zhao, J., Rajaguru, S. P., & Chen, R. (2022). Phase Shifts Measured in Evanescent Acoustic Waves above the Solar Photosphere and Their Possible Impacts on Local Helioseismology. *Astrophys. J.*, *933*(1), 109. doi:10.3847/1538-4357/ac722d.